University of Alberta

SINGLE SIDEBAND MODULATION FOR DIGITAL FIBER OPTIC COMMUNICATION SYSTEMS

by

Michael James Sieben ©

A thesis submitted to the College of Graduate Studies and Research
in partial fulfillment of the requirements for the degree of Doctor of Philosophy

Department of Electrical and Computer Engineering

Edmonton, Alberta

Fall 1998

National Library
of Canada

Acquisitions and
Bibliographic Services

395 Wellington Street
Ottawa ON K1A 0N4
Canada

Bibliothèque nationale
du Canada

Acquisitions et
services bibliographiques

395, rue Wellington
Ottawa ON K1A 0N4
Canada

Your file Votre référence

Our file Notre référence

The author has granted a non-exclusive licence allowing the National Library of Canada to reproduce, loan, distribute or sell copies of this thesis in microform, paper or electronic formats.

The author retains ownership of the copyright in this thesis. Neither the thesis nor substantial extracts from it may be printed or otherwise reproduced without the author's permission.

L'auteur a accordé une licence non exclusive permettant à la Bibliothèque nationale du Canada de reproduire, prêter, distribuer ou vendre des copies de cette thèse sous la forme de microfiche/film, de reproduction sur papier ou sur format électronique.

L'auteur conserve la propriété du droit d'auteur qui protège cette thèse. Ni la thèse ni des extraits substantiels de celle-ci ne doivent être imprimés ou autrement reproduits sans son autorisation.

0-612-34832-6

Canada

University of Alberta

Library Release Form

Name of Author: **Michael James Sieben**

Title of Thesis: **Single Sideband Modulation for Digital Fiber Optic Communication Systems**

Degree: **Doctor of Philosophy**

Year this Degree Granted: **1998**

Permission is hereby granted to the University of Alberta Library to reproduce single copies of this thesis and to lend or sell such copies for private, scholarly or scientific research purposes only.

The author reserves all other publication and other rights in association with the copyright in the thesis, and except as hereinbefore provided, neither the thesis nor any substantial portion thereof may be printed or otherwise reproduced in any material form whatever without the author's prior written permission.

Mike Sieben

Michael James Sieben
8923 - 19th Avenue
North Battleford, Saskatchewan
Canada S9A 2V8

Date: May 11, 1998

University of Alberta

Faculty of Graduate Studies and Research

The undersigned certify that they have read, and recommend to the Faculty of Graduate Studies and Research for acceptance, a thesis entitled Single Sideband Modulation for Digital Fiber Optic Communication Systems submitted by Michael James Sieben in partial fulfillment of the requirements for the degree of Doctor of Philosophy.

Jan Conradi

Dr. Jan Conradi, *Supervisor*

David E Dodds

David Dodds, *Supervisor*

JM McMullin

Dr. Jim McMullin, *Supervisor*

Robert Jopson

Dr. Robert Jopson, *External*

Dr. Ioannis Nikolaidis

A. Elezzabi

Dr. Abdul Elazzabi

I. Filanovsky

Dr. Igor Filanovsky

Date: May 8, 1998

ABSTRACT

This thesis investigates the potential of optical single sideband signaling at 10 Gb/s for increasing the transmission distance of digital lightwave communication systems. The primary bit rate/distance limitation in digital fiber optic systems operating on standard single mode fiber at the 1.55 μm wavelength is chromatic dispersion. Optical single sideband modulation offers an alternative to reducing the impact of chromatic dispersion in these optical systems.

A number of novel approaches for transmitting a digital optical single sideband signal in a self-homodyne detection system were developed. Two approaches showed to be beneficial and practically implementable. The first approach was based on driving each arm of a dual arm drive Mach-Zehnder modulator with a combination of a baseband digital signal and the Hilbert transform of that signal respectively to create an optical single sideband signal. The second approach was based on driving each arm of a dual arm drive Mach-Zehnder modulator in the conventional push-pull manner while driving a subsequent phase modulator with the Hilbert transform of that signal to create an optical single sideband signal. In terms of reducing the effects of chromatic dispersion, transmitting the signal in a single sideband format has two advantages over a double sideband format. First, the optical bandwidth of the transmitted single sideband signal is approximately half of a conventional double sideband signal. Second, an optical single sideband signal can be self-homodyne detected and the majority of the phase information preserved since no spectrum

back folding occurs upon detection thus allowing the received signal to be partially equalized in the electrical domain.

Simulation results showed that 10 Gb/s data could be transmitted at the 1.55 µm wavelength on standard single mode fiber over distances beyond 1000 km with post-detection electrical dispersion compensation. Experimental results showed transmission of 10 Gb/s up to 320 km. Critical parameters in the experiment included frequency modulation to amplitude modulation noise due to the laser source linewidth interacting with the chromatic dispersion in the fiber and the nonideal frequency response of a number of the electrical components used at the transmitter and receiver including the signaling source and the equalizer.

To my wife, Esther

ACKNOWLEDGMENTS

The author thanks his primary supervisors, Dr. Jan Conradi at Corning Inc. and David Dodds at the University of Saskatchewan, for their guidance and instruction throughout the course of this work. Their advice and assistance throughout the course work, research and in the preparation of this thesis are gratefully appreciated. The author also thanks Dr. Jim McMullin for assuming the role of supervisor at the University of Alberta when Dr. Conradi returned to industry in January of 1998.

The author also thanks the additional members of his examining committee Dr. Robert Jopson, Dr. Ioanis Nikolaidis, Dr. Abdul Elazzabi and Dr. Igor Filanovsky for their time and effort.

The author also thanks Sheldon Walklin of Telecommunication Research Labs (TR Labs) for initiating the design of the fiber optic digital communication simulation program, for his help and advice in assembling the initial experimental circuits, and for many additional helpful theoretical discussions.

The author also thanks David Clegg of TR Labs for his tremendous help and speedy response in assembling many of the power supplies, lasers and other equipment used in the experiments.

The author also thanks Jason Lamont, Raymond Semeniuk and Antony Roth of TR Labs for their help during the assembly of the experimental circuits.

The author also thanks his colleagues, Rajkumar Nagaranjan, David Moore, Ping Wan, Geoff Hayward, Gary Hassell, Alan Hnatiw, Dave Boertjes, Tom Young, Sing Cheng, Heng Foo, Ray DeCorby and Bob Davies for many interesting and stimulating discussions. They along with the rest of the students and staff at TR Labs have created an excellent research environment.

The author also thanks Nortel for allowing additional research to be carried out at their Skyline lab in Ottawa. Special thanks goes out to Terry Taraschuk and Yuanmin Cai for their tremendous help at the Nortel site. The author also thanks the other Nortel employees that helped out at the Nortel site.

The author also thanks Siecor of Saskatoon, Saskatchewan and Photonetics of Wakefield, Massachusetts for temporary loan of 150 km of standard single mode fiber and a tunable narrow linewidth laser respectively.

Finally, the author thanks his family, friends, coaches and teammates for their interest in his work and encouragement to continue.

This research was supported in part by TR Labs, the Province of Alberta, the University of Alberta, Nortel and the Natural Sciences and Engineering Research Council of Canada (NSERC).

TABLE OF CONTENTS

1. INTRODUCTION 1

1.1 Fiber Optic Applications 1

1.2 Thesis Objectives 4

1.3 Thesis Organization 5

2. BACKGROUND TO CHROMATIC DISPERSION 6

2.1 Dispersion and Attenuation 6

2.2 Previous Approaches to Limit the Effects of Chromatic Dispersion 12

2.2.1 Optical Methods 12

2.2.2 Post Detection Methods 22

2.2.3 Transmission Format Methods 25

3. THEORY OF OPTICAL SINGLE SIDEBAND 28

3.1 Benefits of Optical Single Sideband 28

3.2 Prior Art in Optical Single Sideband Systems 30

3.3 Theoretical Development of New Optical Single Sideband Systems 37

3.4 Hilbert Transforms of Broadband Baseband Signals 48

3.5 Comparison of Optical Single Sideband and Composite Single Sideband Techniques 58

3.6 Optical Single Sideband and Duobinary Signaling 62

4. SIMULATION OF DIGITAL OPTICAL SINGLE SIDEBAND SYSTEMS 64

4.1 Simulated System Models and Parameters 64

4.2 Noise Modeling 75

4.2.1 Normal Detection with Gaussian Noise 76

4.2.2 Normal Detection with Square-Root Operation and non-Gaussian Noise 82

4.3 Simulation Results 85

4.3.1 Comparison of Designs 1, 2 and 3 85

4.3.2 Variations on the Hilbert Transform Filter 93

4.3.3 Variations on the Modulation Depth and Bias Angle 97

4.3.4 Comparison of Single and Double Sideband Systems 106

4.3.5 Variations on the Pattern Length 111

4.3.6 Comparison of Normal Single Sideband with Composite Single Sideband 112

4.3.7 Comparison of Design 2 with and without Square-Root Function 115

4.3.8 Single Sideband with Non-Zero Source Linewidth 119

4.3.9 Modeled Microstrip Equalizer 122

5. DIGITAL OPTICAL SINGLE SIDEBAND EXPERIMENTAL RESULTS 125

5.1 Introduction to the Experiments 125

5.2 Optical Spectrum Analyzers 126

5.3 Experiments at TR Labs 129

5.3.1 Supporting Circuits 129

5.3.2 Electrical Magnitude Spectra 134

5.3.3 System Layouts and Results 136

5.3.3.1 BNR III-V Module in DSB and SSB Design 3 Configurations 136

5.3.3.2 Lucent Modulator in SSB Design 2 Configuration 144

5.3.3.3 Lucent Modulator in DSB and SSB Design 3 Configurations 148

5.3.4 Comparison of Simulated and Experimental Results 169

5.4 Experiments at Nortel 178

6. CONCLUSION 185

6.1 Conclusion 185

6.2 Future Work 187

6.3 Additional Comments 189

REFERENCES 191

APPENDIX A: Parameters and Losses of Optical Components used in the Experiments at TR Labs 199

APPENDIX B: Pictures of Components and the Full System used in the Experiments at TR Labs 202

APPENDIX C: The Erbium Fiber Laser 205

LIST OF TABLES

Table A.1 Fiber Loss at 1533 nm 199

Table A.2 Isolator Loss at 1533 nm........ 200

Table A.3 Band Pass Filter Loss at 1533 nm 200

Table A.4 Wavelength Division Multiplexer Loss at 1533 nm........ 200

Table A.5 Erbium Doped Fiber Amplifier Parameters at 1533 nm 201

LIST OF FIGURES

Figure 2.1 Wavelength dependence of the dispersion coefficient for silica glass .. 10

Figure 2.2 Wavelength dependence of loss for silica glass 10

Figure 2.3 Energy level diagram for a typical EDFA 11

Figure 2.4 Gain versus wavelength for a typical EDFA................................ 11

Figure 2.5 Phase delay versus frequency for standard single mode fiber and dispersion compensating fiber.. 13

Figure 2.6 Fiber optic system using dispersion compensating fiber to minimize chromatic dispersion 13

Figure 2.7 Fiber optic system using midspectral inversion to perform chromatic dispersion compensation... 14

Figure 2.8 Fiber optic system using chirped fiber gratings to perform chromatic dispersion compensation... 15

Figure 2.9 Fiber optic system using birefringent crystals to perform chromatic dispersion compensation... 18

Figure 2.10 Fiber optic system using a PLC to perform chromatic dispersion compensation... 19

Figure 2.11 Dual arm Mach Zehnder modulator... 19

Figure 2.12 Fiber optic system using differential time delay of the upper and lower sidebands to perform chromatic dispersion compensation 22

Figure 2.13 Magnitude and phase of DSB (a) baseband, (b) optical, (c) detected baseband and (d) detected IF signals.......................... 23

Figure 2.14 Fiber optic system using electronic equalization at an IF to perform chromatic dispersion compensation........ 24

Figure 2.15 Multilevel signaling system........ 26

Figure 3.1 Magnitude and phase of DSB, (a) and (b), and SSB, (c) and (d), signals........ 29

Figure 3.2 Magnitude and phase of a Hilbert transform filter........ 31

Figure 3.3 First integrated optical SSB transmitter........ 32

Figure 3.4 Optical spectrum of RF carriers in (a) DSB form and (b) SSB form... 34

Figure 3.5 Relative RF power at 17.35 GHz versus fiber length........ 35

Figure 3.6 Optical filter to generate SSB........ 36

Figure 3.7 Design 1 for optical SSB transmission........ 38

Figure 3.8 Design 2 for optical SSB transmission........ 39

Figure 3.9 Design 3 for optical SSB transmission........ 40

Figure 3.10 Phase modulator........ 40

Figure 3.11 Ratio of $\hat{m}(t)$ to $m(t)$ versus bias angle θ........ 47

Figure 3.12 Normalized output electric field and power versus bias angle θ for a dual arm MZ modulator........ 48

Figure 3.13 Weaver's method to generate a SSB RF signal........ 49

Figure 3.14 Modified Weaver approach used to generate the Hilbert transform of a broadband signal........ 49

Figure 3.15 Magnitude spectra of the signals in Figure 3.14........ 52

Figure 3.16 Alternate version of the modified Weaver approach used to generate the Hilbert transform of a broadband signal........ 54

Figure 3.17 Generation of the combination signals........ 54

Figure 3.18 Tapped delay approach to generate the Hilbert transform of a broadband signal........ 55

Figure 3.19 Impulse response of the Hilbert transform.................................. 56

Figure 3.20 Circuit to generate independent driving signals 56

Figure 3.21 Magnitude spectra of signals shown in Figure 3.20....................... 57

Figure 3.22 Circuit to generate driving signals for Design 2........................... 57

Figure 3.23 Circuit to detect optical SSB signal 58

Figure 3.24 Design for optical CSSB transmission.. 60

Figure 4.1 Block diagram of the simulated optical SSB system....................... 65

Figure 4.2 Optical modulator configurations for (a) Design 1 and Design 2 and (b) Design 3 65

Figure 4.3 Effective relative permitivity versus frequency for a microstrip design with ε_r=10.2, h=1 mm and $w\approx$ 1 mm 71

Figure 4.4 Second order phase response of fiber and microstrip for (a) USB and (b) LSB optical transmission 72

Figure 4.5 Second derivative of microstrip propagation constant versus frequency for a microstrip design with ε_r=10.2, h=1 mm and $w\approx$ 1 mm 73

Figure 4.6 Microstrip attenuation per meter versus frequency......................... 74

Figure 4.7 Normal optical receiver... 75

Figure 4.8 Optical receiver employing square-root function.......................... 76

Figure 4.9 Optical receiver circuit with pin detector and amplifier................... 78

Figure 4.10 Optical link with three EDFAs and two sections of fiber................. 82

Figure 4.11 Probability distributions (a) Gaussian and (b) non-Gaussian 84

Figure 4.12 Time domain plots of (a) $m(t)$, (b) $\hat{m}(t)$, (c) $m(t)+\hat{m}(t)$ and (d) $-m(t)+\hat{m}(t)$ 86

Figure 4.13 Receiver sensitivity versus fiber length for Designs 1 and 2 87

Figure 4.14 Simulated optical spectrums (a) DSB, (b) SSB - Design 2 and (c) SSB - Design 1 89

Figure 4.15 Eye diagrams of a standard DSB signal for (a) 0 km, (b) 75 km and (c) 150 km 90

Figure 4.16 Eye diagrams of an unequalized SSB signal using Design 2 for (a) 0 km, (b) 150 km and (c) 300 km 90

Figure 4.17 Eye diagrams of an equalized SSB signal using Design 2 for (a) 0 km, (b) 300 km and (c) 800 km 90

Figure 4.18 Eye diagrams of an equalized SSB signal using Design 1 for (a) 0 km, (b) 300 km and (d) 800 km 91

Figure 4.19 Equalized received eye diagram using Design 2 for (a) 3,000 km and (b) 6,000 km 91

Figure 4.20 Receiver sensitivity versus fiber length for Design 2 92

Figure 4.21 General phase response of tap delay filter 93

Figure 4.22 Magnitude response of (a) 2 tap, (b) 4 tap and (c) 6 tap delay filter with a time delay T of 0.375 ns 93

Figure 4.23 Transmitted optical electric field magnitude spectrums of (a) 2 tap, (b) 4 tap and (c) 6 tap delay filter with a time delay T of 0.375 ns 94

Figure 4.24 Magnitude response of (a) 0.2 ns, (b) 0.375 ns and (c) 0.5 ns unit delay with a four tap filter configuration 94

Figure 4.25 Transmitted optical electric field magnitude spectra of (a) 0.2 ns, (b) 0.375 ns and (c) 0.5 ns unit time delay with a four tap filter configuration 95

Figure 4.26 Transmitted optical electric field magnitude spectrum using Hilbert filter with an infinite number of taps 96

Figure 4.27 Receiver sensitivity versus distance for Design 2 implementing a Hilbert filter with four taps and with an infinite number of taps 97

Figure 4.28 Schematic of optical pulse sequence for a modulation parameter *P* of 0.2 98

Figure 4.29 Receiver sensitivity versus bias angle θ for Design 2 for a fiber length of 400 km, modulation ratio $\hat{m}(t)$ to $m(t)$ of 1 and a modulation parameter of 0.2.......... 99

Figure 4.30 Receiver sensitivity versus bias angle θ for Design 2 at 200 km allowing the ratio of $\hat{m}(t)$ to $m(t)$ to vary 100

Figure 4.31 Receiver sensitivity versus bias angle θ for Design 2 at 400 km allowing the ratio of $\hat{m}(t)$ to $m(t)$ to vary 101

Figure 4.32 Receiver sensitivity versus bias angle θ for Design 2 at 600 km allowing the ratio of $\hat{m}(t)$ to $m(t)$ to vary 102

Figure 4.33 Insertion loss due to the modulation signal versus the modulation parameter.......... 102

Figure 4.34 BER versus launched optical power into the fiber for different values of modulation parameter *P* at 200 km 104

Figure 4.35 BER versus launched optical power into the fiber for different values of modulation parameter *P* at 400 km 105

Figure 4.36 BER versus launched optical power into the fiber for different values of modulation parameter *P* at 600 km 105

Figure 4.37 BER versus input power for 600 km fiber length for EDFA configuration with P_{SAT} of 6 dBm and a G_o of 30 dB with 50 km spacing between EDFAs.......... 107

Figure 4.38 BER versus input power for 600 km fiber length with EDFA configuration with P_{SAT} of 6 dBm and a G_o of 30 dB and 50 km spacing between EDFAs.......... 108

Figure 4.39 BER versus input power for EDFA configuration with a fixed gain of 28 dB at 560 km with 80 km spacing between EDFAs 109

Figure 4.40 BER versus input power for EDFA configuration with P_{SAT} of 10 dBm and a G_o of 25 dB and 80 km spacing between EDFAs at 320 km 110

Figure 4.41 Receiver sensitivity versus pattern length for a fiber length of 1000 km... 112

Figure 4.42 Optical electric field spectrum for CSSB................................ 113

Figure 4.43 Receiver sensitivity versus fiber length for SSB and CSSB............ 114

Figure 4.44 Received eyes at 1000 km for (a) normal square-law detection and (b) square-law detection followed by a square-root function....... 115

Figure 4.45 Receiver sensitivity versus fiber length for normal square-law detection and square-law detection followed by a square-root function 116

Figure 4.46 Receiver sensitivity for square-root with Gaussian and non-Gaussian noise processes.. 117

Figure 4.47 Receiver sensitivity versus bias angle for 600 km with square-root function at the receiver 118

Figure 4.48 BER versus bias angle for 600 km with square-root function at the receiver.. 119

Figure 4.49 Required laser linewidth for a BER of 10^{-9} versus fiber length for a SSB system 121

Figure 4.50 BER versus launched optical power into the fiber for 540 km fiber length for different values of source linewidth...................... 122

Figure 4.51 Received eye diagram using Design 2 for (a) 300 km and (b) 800 km and (c) 1000 km using the modeled microstrip equalizer 123

Figure 4.52 Receiver sensitivity versus fiber length using an ideal and a modeled microstrip equalizer 124
Figure 4.53 Microstrip length versus fiber length using Design 2........ 124
Figure 5.1 Optical spectrum analyzer using a FFP, a pin diode and an oscilloscope........ 127
Figure 5.2 Optical spectrum analyzer using a FFP and an optical power meter.... 128
Figure 5.3 Circuit to generate 10 Gb/s data from 2.5 Gb/s data supplied by the BERT 130
Figure 5.4 Circuit to generate 10 GHz clock from 2.5 GHz clock supplied by the BERT........ 131
Figure 5.5 Receiver and decision circuit 132
Figure 5.6 Clock recovery circuit to regenerate 2.5 GHz clock from the received data at the receiver........ 133
Figure 5.7 Electrical magnitude spectrum of the signal $m(t)$ 134
Figure 5.8 Electrical magnitude spectrum of the signal $\hat{m}(t)$ with the magnitude response of the four tap Hilbert filter overlayed as a dashed line........ 134
Figure 5.9 Optical DSB system using the BNR III-V module........ 137
Figure 5.10 Electrical layout for the DSB system using the BNR III-V module..... 138
Figure 5.11 Optical SSB transmitter using the BNR III-V module and the UTP PM 139
Figure 5.12 Electrical layout for the SSB system using the BNR III-V module and the UTP PM 140
Figure 5.13 Optical spectra for the carrier (a) without and (b) with DSB modulation using the BNR III-V module 141

Figure 5.14 Optical spectra for the carrier (a) without modulation, (b) with DSB modulation and (c) with SSB modulation using the BNR III-V module 142

Figure 5.15 Receiver sensitivity versus fiber length for BNR III-V module 143

Figure 5.16 BER versus received optical power for SSB case at 75 km with the BNR III-V module and the UTP PM 144

Figure 5.17 Optical SSB system using Lucent modulator in the Design 2 configuration 145

Figure 5.18 Electrical layout using the Lucent modulator in the Design 2 configuration 147

Figure 5.19 Optical DSB system using the Lucent modulator 149

Figure 5.20 Electrical layout for the DSB system using the Lucent modulator 150

Figure 5.21 Optical SSB transmitter using the Lucent modulator and UTP PM 151

Figure 5.22 Electrical layout for the SSB system using the Lucent modulator and the UTP PM 152

Figure 5.23 Optical spectra for the carrier with (a) no modulation and (b) with DSB modulation using the Lucent modulator 153

Figure 5.24 Optical spectra for the carrier with (a) DSB modulation and (b) SSB modulation using the Lucent modulator 153

Figure 5.25 Optical signal spectra for (a) carrier, (b) DSB and (c) SSB 154/155

Figure 5.26 Deconvolved optical signal spectra for (a) DSB and (b) SSB modulation 155/156

Figure 5.27 Receiver sensitivity versus fiber length for the four EDFA link 157

Figure 5.28 BER versus received optical power for SSB Design 3 at 270 km of fiber and 32 cm of microstrip 158

Figure 5.29 BER versus received optical power at 200 km with two different source linewidths 159

Figure 5.30 Experimental DSB eyes at (a) 0 km, (b) 100 km and (c) 170 km...... 160

Figure 5.31 Experimental SSB eyes at (a) 0 km, (b) 120 km and (c) 195 km...... 160

Figure 5.32 Experimental SSB eyes at 270 km for (a) unequalized and (b) equalized using 32 cm microstrip...... 160

Figure 5.33 Phase response of the Veritech (VMA3K10C-232) amplifier and 100 km of standard single mode fiber...... 161

Figure 5.34 320 km SSB optical system...... 163

Figure 5.35 Receiver sensitivity versus fiber length for six EDFA link...... 164

Figure 5.36 BER versus received optical power for fiber lengths of 0 km, 100 km, 210 km with 8 cm microstrip and 320 km with 32 cm microstrip equalization for six EDFAs...... 165

Figure 5.37 BER versus received optical power for 270 km with and without 24 cm microstrip equalization for six EDFAs...... 166

Figure 5.38 BER versus microstrip length for an optical SSB system with six EDFAs in the link...... 167

Figure 5.39 Experimental DSB eyes at fiber lengths of (a) 0 km, (b) 100 km and (c) 175 km...... 168

Figure 5.40 Experimental SSB eyes at fiber lengths of (a) 0 km, (b) 100 km and (c) 175 km...... 168

Figure 5.41 Experimental SSB eyes at fiber lengths of (a) 210 km with 8 cm microstrip, (b) 270 km with 24 cm microstrip and (c) 320 km with 32 cm microstrip...... 168

Figure 5.42 Experimental SSB eyes at fiber lengths of (a) 270 km with no equalization (b) 270 km with 24 cm microstrip with the old source linewidth of 3.8 MHz and (c) 330 km with 32 cm microstrip...... 169

Figure 5.43 Simulated DSB eyes at fiber lengths of (a) 0 km, (b) 100 km and (c) 175 km...... 170

Figure 5.44 Simulated SSB eyes at fiber lengths of (a) 0 km, (b) 100 km and (c) 175 km 170

Figure 5.45 Simulated SSB eyes at fiber lengths of (a) 210 km with 8 cm microstrip, (b) 270 km with 24 cm microstrip and (c) 320 km with 32 cm microstrip 171

Figure 5.46 Simulated SSB eyes at fiber lengths of (a) 270 km with no equalization (b) 330 km with 32 cm microstrip 171

Figure 5.47 Simulated DSB and SSB optical spectra 172

Figure 5.48 Receiver sensitivity versus fiber length for the experimental and the simulated optical SSB system with four EDFAs 173

Figure 5.49 Receiver sensitivity versus fiber length for the experimental and the simulated optical SSB system with six EDFAs 173

Figure 5.50 BER versus launched optical power into the fiber for the ideal system with nonideal components at 540 km with 45 km EDFA spacings 175

Figure 5.51 Attenuation versus microstrip length at 10 Ghz 176

Figure 5.52 Phase delay versus microstrip length at 10 Ghz 177

Figure 5.53 Optical signal spectra for (a) DSB and (b) SSB 179

Figure 5.54 Nortel 290 km optical SSB system 180

Figure 5.55 BER versus received optical power for SSB systems at 0, 155, 215 and 290 km (with 24 cm microstrip equalization) 181

Figure 5.56 BER versus pattern length for the optical SSB system at 290 km 183

Figure B.1 Hilbert Transform Circuit (showing splitters, delay lines, attenuators, broadband combiner, amplifier and phase modulator) 202

Figure B.2 16 cm microstrip equalizer 202

Figure B.3 Erbium doped fiber amplifiers and fiber reels 203

Figure B.4 System layout showing Bit Error Ratio Test set 204

Figure C.1 Erbium Fiber Laser 206

LIST OF ABBREVIATIONS

AM-PSK	Amplitude Modulate - Phase Shift Key
ASE	Amplified Spontaneous Emission
AT&T	American Telegraph and Telephone
B	Bandwidth
BER	Bit Error Ratio
BERT	Bit Error Ratio Test (Set)
BPF	Band Pass Filter
CSSB	Composite Single Sideband
D-FF	D - Flip Flop
DSB	Double Sideband
EDFA	Erbium Doped Fiber Amplifier
FFP	Fiber Fabry Perot
FFT	Fast Fourier Transform
FM-AM	Frequency Modulation/Amplitude Modulation
FSR	Free Spectral Range
HP	Hewlett Packard
IF	Intermediate Frequency
IFFT	Inverse Fast Fourier Transform
LED	Light Emitting Diode
$LiNbO_3$	Lithium Niobate
LO	Local Oscillator

LPF	Low Pass Filter
LSB	Lower Sideband
MUX	Multiplexer
MZ	Mach Zehnder
NRZ	Non-Return to Zero
OC-192	9.95328 Gb/s data rate
PLC	Planar Lightwave Circuit
PM	Phase Modulator
PR	Pseudo Random
PS	Phase Shifter
RF	Radio Frequency
RIN	Relative Intensity Noise
SNR	Signal to Noise Ratio
SSB	Single Sideband
TO	Thermo Optic
TR Labs	Telecommunications Research Laboratories
USB	Upper Sideband
VOA	Variable Optical Attenuator
VSB	Vestigial Sideband
WDM	Wavelength Division Multiplex

1. INTRODUCTION

1.1 Fiber Optic Applications

Fiber optic communications has a number of advantages which makes it attractive in a wide range of applications. Two advantages offered by optical fibers are very low attenuation and large bandwidth. Other advantages offered by optical fibers over coaxial cables include being smaller and lighter and the elimination of electrical ground loops. As a result of the advantages offered by optical fibers, fiber optic communications have allowed the transmission of the highest data rates over the longest distances of any closed channel system.

To date, the most extensive application of fiber optic communications has been in the telephone industry. The rapid advances in the 1970's led to a series of field experiments and early applications in North America [1]. One of the first commercial long distance optical fiber telephone systems was put into service by the American Telephone and Telegraph Company (AT&T) in 1983 [2]. Today, many major cities throughout North America are linked by an optical fiber system. In addition, many developed countries are linked by transoceanic optical systems. Fiber optic systems in the telephone industry are almost exclusively digital due to the digital switching, multiplexing and transmission technology currently in use.

More recently, video transmission is progressing from an analog format to a digital one thus increasing the need for digital optical links. Further, with the additional requirements of computer networks, integrating video, telephone and internet applications for each user on one line is an attractive option. As a result, the bandwidth requirement for one user can grow quite quickly. When multiple users are multiplexed on one line in an integrated system, the total data rate capability of the system can grow even faster. If the distance between these multiple users is stretched from city to city, the high data rate link must now cover hundreds if not thousands of kilometers.

The types of optical systems used to transmit the information have evolved as a direct result of this growth in capacity and distance requirement. From the first optical systems to today's high speed transoceanic links, the speed of commercially available optical systems has been quadrupling every five years. Fiber optic systems have gone through four generations [3] on the road to increased capacity and transmission distance.

First generation systems used light emitting diodes (LED) and semiconductor lasers operating at the 0.85 μm wavelength with multimode fiber. These systems were limited in their transmission distance by high loss and also suffered from modal dispersion in the fiber. Despite this, these initial fiber systems still outperformed existing coaxial cable systems.

Second generation systems began with advances in fiber technology where reductions in core size made single mode fiber available. The improved single mode fiber had a core diameter of 8 μm which was significantly smaller than 50 μm for the multimode fiber. This reduction in core size reduced modal dispersion in the fiber but also required more precise mechanical specifications. Eventual advances were also made in laser and detector technology to shift the wavelength of operation to 1.3 μm where the fiber loss was lower.

Third generation systems came from a shift of the operating wavelength to 1.55 μm where the loss in silica fibers reaches the absolute minimum. This helped extend the transmitter to receiver distance. Mode partition noise resulting from multiple modes being created within the laser was still a problem though. Pulse dispersion was generated from the information traveling down the fiber in more than one mode created by the laser source. The development of the distributed feedback laser resulted in single mode sources which reduced this effect and extended that transmission distance of high bit rate systems even further.

Fourth generation systems have not been clearly defined yet, however, the use Erbium doped fiber amplifiers (EDFA) and integrated optics such as lithium niobate

($LiNbO_3$) which operate in the 1.55 μm wavelength region have been suggested as major factors in defining the next generation. With the invention of optical amplifiers, the loss in fiber could be compensated at regular intervals and thus the span between transmitter and receiver could be extended to hundreds and even thousands of kilometers. These systems are state of the art and have provided the highest data rate transmission systems to date.

Achieving high speed digital transmission in an optical system over short distances, such as a few kilometers, is limited more by the electrical technology than the optical technology. Optical carriers at wavelengths of 1.55 μm have significantly large information carrying capacity. For example, the equivalent carrier frequency of 1.55 μm is approximately 200 THz. Thus, theoretically, 200 THz of binary information could be transmitted at this frequency. The limitation is that current transmitter and receiver technology has not developed to the point where they can transmit digital information on a single channel at terabit rates. Current single channel data rates are commercially available at 10 Gb/s with research based systems demonstrating 40 Gb/s and higher per channel [4]. One approach to utilizing more of the optical spectrum and to increase the total capacity of the fiber is to wavelength division multiplex (WDM) a number of separate electrical channels onto a number of separate optical carriers creating a multichannel system. This way, more of the optical spectrum is utilized without increasing the capacity of the electrical components. WDM systems have now been demonstrated which transmit 2.6 Tb/s of data over a single optical fiber [5].

While WDM systems help to increase the overall transmission capacity of a fiber, maximizing the single channel data rate of each WDM channel is still an important item. The useful range over which optical wavelengths can be transmitted is limited by factors such as the loss and EDFA gain windows and thus this range must be used efficiently. Tradeoffs exist between the number of carriers and the single channel data rate, however, the overall throughput is generally maximized in conventional systems using high single channel data rates.

For long distance single channel and WDM systems, the limitation is not always the end electronics but can be the fiber itself. For single mode fiber systems which require both high data rate capability and long transmission distances on a single channel, problems arise due to the effects of chromatic dispersion in single mode fiber [6]. For long haul optical trunking links between major cities and between continents, the effects of chromatic dispersion have great importance.

For systems with single mode sources that have narrow linewidths, the modulated information on an optical carrier is carried down the fiber in a range of optical frequencies. Chromatic dispersion results from these optical frequencies traveling down the fiber at different group velocities. The effect on a digital pulse in the time domain is to disperse or smear the pulse. The effect on a stream of digital data is to distort the quality of the signal such that the inherent noise in the system causes errors in the received bits. The higher the data rate or the longer the distance, the more distortion in the signal and thus more errors received in the data.

Chromatic dispersion is higher in some types of fiber than others. Some types of fiber are specifically designed to have low dispersion such that high data rates can be transmitted over long distances. However, standard single mode fiber, which is currently installed in 75% of North America's optical networks, has a high level of chromatic dispersion at 1.55 μm which can severely limit the performance of high speed long distance systems. The price to replace standard single mode fiber already installed was quoted in 1998 at $100,000 US per mile [7].

As previously mentioned, the negative impact of chromatic dispersion in standard single mode fiber at 1.55 μm increases both with bit rate and fiber length. Consequently, one major goal in installed long haul high speed digital optical systems using standard single mode fiber is to limit or reverse the effects of chromatic dispersion so that the bit rate distance product can be increased. This corresponds to higher data rates over longer distances for single and multiple wavelength systems.

1.2 Thesis Objectives

There were four main objectives of the research described in this thesis. The first objective was to review published approaches which have been either developed or proposed to reverse or limit the effects of chromatic dispersion on standard single mode fiber in the 1.55 μm wavelength region on digital systems operating at the OC-192 data rate

(9.95328 Gb/s). The second objective was to develop a new method or technique which could be used in baseband digital optical systems which would reverse or limit the effects of chromatic dispersion. The focus of the research was on single sideband (SSB) modulation of an optical carrier with a digital signal. The third objective was to simulate this technique by modeling the optical SSB system on a computer and verify its effectiveness. The fourth and final objective was to build and test the new optical SSB system and verify experimentally the effectiveness of this new technique in combating the effects of chromatic dispersion in standard single mode fiber.

1.3 Thesis Organization

Chapter 2 presents a brief review on the background of the problems created by chromatic dispersion in standard single mode fiber. In addition, the previous approaches used to reverse or limit the effects of chromatic dispersion are reviewed.

Chapter 3 presents a theoretical analysis of optical SSB modulation for digital systems. Through this analysis, previous optical SSB systems are reviewed and the new optical SSB systems are introduced.

Chapter 4 presents the simulation results of the new optical SSB systems. The performance of these systems in terms of extending the transmission distance of the OC-192 data rate is the focus. Simulations are performed for ideally modeled components.

Chapter 5 presents the experimental results of the new optical SSB systems that were tested. Again, performance of these systems in terms of extending the transmission distance of the OC-192 data rate is the focus. A comparison of some of the simulated and experimental results is also given with comments given on similarities and differences between the two results.

The conclusion of the thesis is given in Chapter 6. In addition, recommendations for improvements and future experiments are also given.

2. BACKGROUND TO CHROMATIC DISPERSION

2.1 Dispersion and Attenuation

Chromatic dispersion is a major factor limiting the maximum distance and/or bit rate of many current long haul fiber optic systems. Chromatic dispersion results from the frequencies associated with the information sidebands traveling down the fiber at different group velocities. In the frequency domain, chromatic dispersion results in an equivalent transfer function with a flat magnitude response but a nonlinear phase response. In the time domain, if the source linewidth is smaller than the information bandwidth, chromatic dispersion has the effect of broadening a received pulse of light into an adjacent pulse interval. Chromatic dispersion generally refers to dispersion in a fiber that is wavelength dependent. Chromatic dispersion is the dominant form of dispersion in standard single mode fiber in most cases, however, other forms of dispersion do exist. Four general sources of dispersion in optical fibers are modal dispersion, waveguide dispersion, nonlinear dispersion and material dispersion [8].

Modal dispersion occurs in multimode fibers as a result of the differences in group velocities in the modes [8]. More specifically, the information is dispersed throughout a number of modes and each mode propagates down the fiber with a different velocity such that they arrive at the receiver at different times. This type of dispersion is critical in an amplitude modulated optical system since the varying arrival times of each mode at the receiver can distort the quality of the received signal. However, modal dispersion is not significant in modern long haul digital systems since they use single mode fiber.

Waveguide dispersion results from the difference in distribution in optical power in the core and in the cladding with optical frequency [8]. Since the phase velocity in the core and in the cladding are different, the group velocity is altered for each wavelength. Each wavelength has a different distribution of optical power in the core and cladding.

Nonlinear dispersion results from the fiber refractive index being intensity dependent [8]. The phase shift incurred on the spectral components constituting the information is dependent on both frequency and optical power. An optical signal launched at a high intensity can be subjected to nonlinear phase distortion more so than a low intensity signal. This can become critical if the launched optical power into the fiber is set at a very high level for the purposes of maintaining an acceptable signal to noise ratio (SNR) at the receiver or in a WDM system where the combined power of all of the carriers is higher than that of a single channel.

Material dispersion results from the fact that the refractive index of glass is a function of wavelength [8]. Material dispersion is the dominant form of dispersion that causes problems for current long haul digital optical systems operating on standard single mode fiber. The other forms of dispersion are generally smaller. Material dispersion affects systems differently if the source spectral width is smaller or larger than the information spectrum. The effects are more severe in systems where the source linewidth is larger than the information spectral width. Recent developments in source quality have allowed long distance systems to use sources with very narrow spectral widths to reduce these negative effects, however, the material dispersion can still have a significant impact on the information spectrum.

For systems using a source with a spectral width smaller than the information bandwidth, material dispersion can be modeled as phase distortion operating on the electric field of the light in the fiber representing the information. A simplified version of the fiber transfer function representing this phase change can be written as [9]:

$$H(\omega, z) = \exp(-j\beta(\omega)z) \tag{2.1}$$

where z is the fiber length and β is the frequency dependent propagation constant. The term β can be expanded in a Taylor series about the carrier wavelength ω_o to give:

$$\beta(\omega) = \beta_o + \frac{d\beta}{d\omega}(\omega - \omega_o) + \frac{1}{2}\frac{d^2\beta}{d\omega^2}(\omega - \omega_o)^2 + \frac{1}{6}\frac{d^3\beta}{d\omega^3}(\omega - \omega_o)^3 \cdots \tag{2.2}$$

The first term on the right hand side of equation 2.2, which is related to a phase delay, does not provide any nonlinear phase distortion that would result in a corrupted received signal. The second term on the right hand side of equation 2.2, which is related to the group velocity, also does not provide any nonlinear phase distortion that would result in a corrupted received signal since the phase delay for this term is linear with frequency. Linear phase delay results in preservation of the relative phase relationship of all of the frequencies within the relevant spectral range. The most significant term on the right hand side of equation 2.2 is the third term, which is related to the first order group velocity dispersion. This is the most significant term in optical systems operating at the 1.55 μm wavelength on standard single mode fiber since it provides a nonlinear phase distortion. This nonlinear phase distortion is significant in systems since it distorts the original information by the time it has reached the receiver.

Examining the third term on the right hand side of equation 2.2 in more detail, a common form of the first order group velocity dispersion can be derived. This term is commonly identified with material or chromatic dispersion. We expand on this term by first letting τ be the group delay per unit length in the fiber and write its relationship to the propagation constant β as:

$$\tau = \frac{d\beta}{d\omega} \tag{2.3}$$

Taking the first derivative of equation 2.3 with respect to frequency ω gives:

$$\frac{d\tau}{d\omega} = \frac{d^2\beta}{d\omega^2} \tag{2.4}$$

Further, letting λ be the wavelength, $\frac{d\tau}{d\omega}$ can be expanded in the form:

$$\frac{d\tau}{d\omega} = \frac{d\tau}{d\lambda}\frac{d\lambda}{d\omega} \tag{2.5}$$

If $\frac{d\lambda}{d\omega}$ is evaluated using the relationship of the speed of light with wavelength and frequency, $c = f\lambda$, a new representation for $\frac{d^2\beta}{d\omega^2}$ can be given as:

$$\frac{d^2\beta}{d\omega^2} = -\frac{\lambda^2}{2\pi c}\frac{d\tau}{d\lambda} \tag{2.6}$$

The dispersion coefficient D is defined as the first derivative of the group delay with respect to wavelength:

$$D = \frac{d\tau}{d\lambda} \tag{2.7}$$

Thus, using equations 2.6 and 2.7, the third term on the right hand side of equation 2.2 representing the most significant material dispersion at 1.55 μm can be written as:

$$\beta_{disp} = -\frac{1}{2}\left[\frac{\lambda_o^2}{2\pi c}\right]D(\omega-\omega_o)^2 \tag{2.8}$$

where λ_o is the wavelength of the optical carrier.

Examining equation 2.8, it can be seen that the frequency components in the information spectrum which are farthest away from the carrier are phase distorted the most due to the second order dependence on frequency. Further, looking back at equation 2.1, it can be seen that as the fiber length z increases, the product of the propagation constant and the fiber length also increases. Thus, the total phase coefficient increases with both frequency and fiber length. This relationship is often called a bandwidth/length product where if a given amount of penalty due to dispersion is specified either the fiber length or transmission bandwidth cannot be increased without decreasing the other.

For silica in single mode optical fibers, the dispersion coefficient D is wavelength dependent. This wavelength dependence is shown in Figure 2.1. From Figure 2.1, it can be seen that the dispersion minimum is around 1.3 μm. At 1.55 μm, the dispersion coefficient is significant at 17 ps/km-nm. This is primarily a result of material dispersion although small effects from waveguide dispersion are reflected in this value.

The optical attenuation of silica glass is also wavelength dependent. An example of the loss of single mode fiber as a function of wavelength is shown in Figure 2.2. From Figure 2.2, it can be seen that the loss minimum is in the 1.55 μm region. Short wavelengths are limited by Rayleigh scattering while longer ones by infrared absorption.

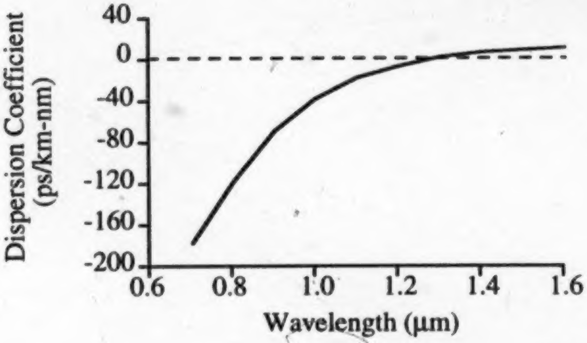

Figure 2.1 Wavelength dependence of the dispersion coefficient for silica glass (Adapted from [8])

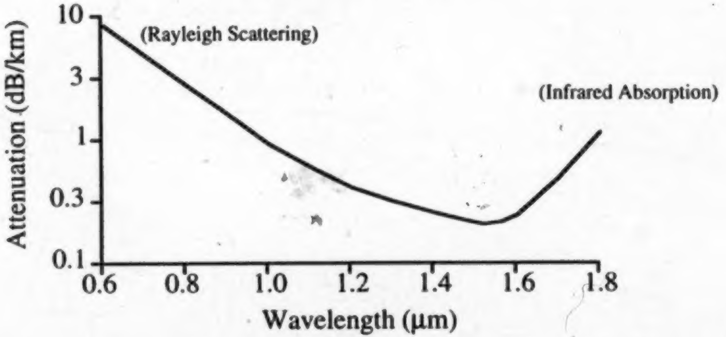

Figure 2.2 Wavelength dependence of loss for silica glass (Adapted from [8])

The loss minimum of single mode fiber also corresponds to the effective operating region of EDFAs. An EDFA is an optical gain medium which at the basic level, consists of a section of Erbium doped fiber which is pumped with a light of a shorter wavelength and provides gain at a longer wavelength. The gain mechanism is similar to a laser cavity with the pumped electrons residing in a metastable state for an adequate period of time, however, there is no feedback in the EDFA like there is in a laser. The energy level diagram of an EDFA is shown in Figure 2.3. In Figure 2.3, an electron in energy level E_1 is pumped with an external source to energy level E_3. The electron decays to energy level E_2 where, with high probability, it remains until it is stimulated down to energy level E_1 by an input signal. The output signal is an amplified version of the input signal. This amplification process within the EDFA is also wavelength dependent. The gain versus wavelength for a typical EDFA is shown in Figure 2.4.

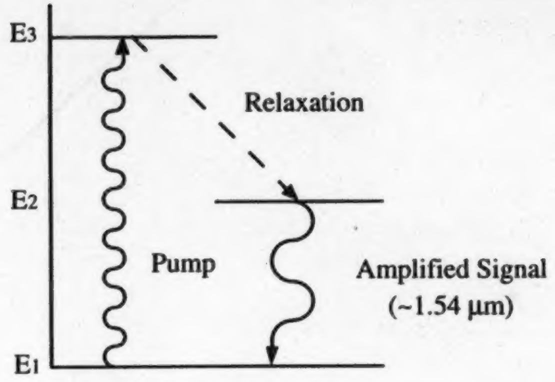

Figure 2.3 Energy level diagram for a typical EDFA (Adapted from [9])

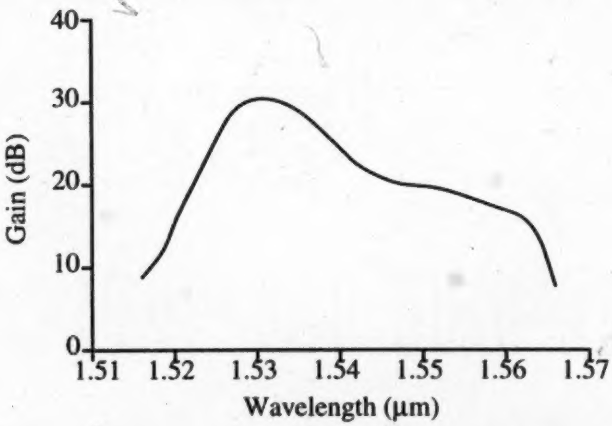

Figure 2.4 Gain versus wavelength for a typical EDFA

In most long haul digital optical systems, attenuation limits are overcome by operating in the 1.55 µm region. However, the penalty is high chromatic or material dispersion. Currently, most systems are cost effective by operating at the loss minimum. Attempts are then made to try to reverse the effects of chromatic dispersion. The alternative is to operate at the dispersion minimum and attempt to overcome the higher losses at the 1.3 µm wavelength. Currently, there is work being carried out to develop optical amplifiers at the 1.3 µm wavelength, however, systems still perform better when operating at the 1.55 µm wavelength using Erbium amplifiers. The combination of loss minimum and optical gain from Erbium doped fiber outweigh any benefits from reduction in chromatic dispersion seen at 1.3 µm.

2.2 Previous Approaches to Limit the Effects of Chromatic Dispersion

Three general approaches have been used to reduce the effects of chromatic dispersion. The first is based purely on optical methods where the phase distortion incurred in the fiber at the optical electric field level is reversed in the optical domain at the electric field level by inserting an element in the optical path before detection. The second is based on post detection electronic equalization methods where the phase distortion incurred by the fiber is reversed in the electrical domain after detection of the optical power. The third is based on modifying the transmission format in order to reduce the effective bandwidth required to transmit or receive the data. By reducing the transmitted bandwidth of the signal at the optical electric field level, the effects of chromatic dispersion are reduced since the difference between the highest and the lowest frequency components in the signal spectrum is less.

The distinction between optical electric field and optical power is important. Photodetectors used at the receiver in optical systems have a linear relationship between received optical power and output current. The electric field, which the dispersion level is evaluated at, is not generally measurable. Since the detector measures the optical power which is the square of the electric field, the process can be called square-law detection.

2.2.1 Optical Methods

The first optical method used to reverse the effects of chromatic dispersion is to add dispersion compensating fiber to the transmission path containing the standard single mode fiber. Dispersion compensating fiber uses a step or graded index core with a refractive index profile selected such that at 1.55 μm the waveguide dispersion dominates over material dispersion [8]. When light propagates in dispersion compensating fiber, longer wavelengths reside more in the cladding than in the core and thus the shorter wavelengths encounter more delay. The refractive index profile of the dispersion compensating fiber is specifically designed to reverse the effects of material dominated dispersion in standard single mode fiber. An example of the phase delay versus frequency of chromatic dispersion in standard single mode fiber and that of an appropriate amount of dispersion compensating fiber is shown in Figure 2.5.

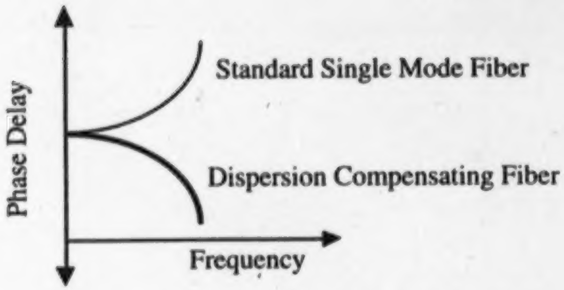

Figure 2.5 Phase delay versus frequency for standard single mode fiber and dispersion compensating fiber

The dispersion compensating fiber can be added to the transmission path at one point in the optical path or can be placed at multiple points throughout the path. The amount of dispersion compensating fiber added to the system depends on the amount of standard single mode fiber used; the proportion is approximately 4:1 where for every 4 units of standard single mode fiber used, 1 unit of dispersion compensating fiber is needed.

Using dispersion compensating fiber in a digital optical system was proposed by Lin *et al.* [10] and Onishi *et al.* [11] and was implemented by Dugan *et al.* [12] and Goel *et al.* [13]. An example of an optical system which uses dispersion compensating fiber at the end of the transmission path is shown in Figure 2.6. Placing the dispersion compensating fiber at multiple points along the path can vary the systems performance since the dispersion compensating fiber has a high loss requiring strategic placement of EDFAs.

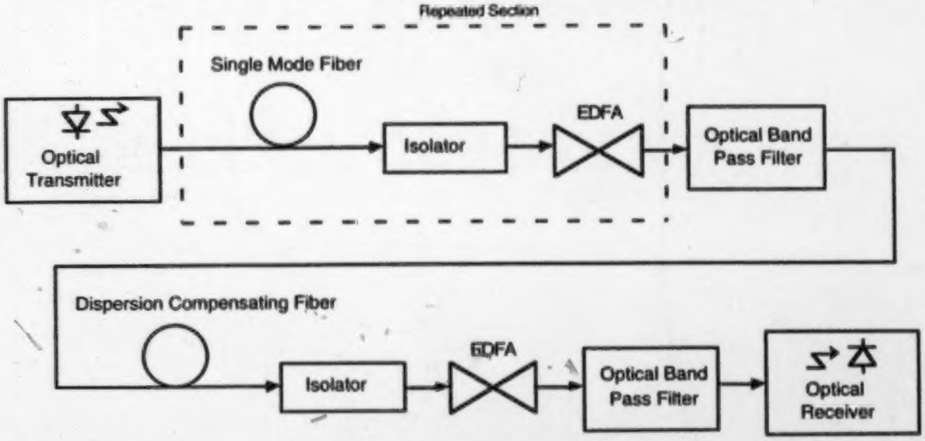
Repeated Section
Single Mode Fiber
Optical Transmitter
Isolator
EDFA
Optical Band Pass Filter
Dispersion Compensating Fiber
Isolator
EDFA
Optical Band Pass Filter
Optical Receiver

Figure 2.6 Fiber optic system using dispersion compensating fiber to minimize chromatic dispersion

Work has also been done to create dispersion shifted fiber where the dispersion minimum for the fiber is shifted to 1.55 μm such that if the entire fiber link was composed of this type of fiber, chromatic dispersion would be minimized [13]-[16]. However, this type of fiber is generally more expensive to fabricate than standard single mode fiber since a more elaborate refractive index profile is required for the core and it also has a slightly higher loss than standard single mode fiber. The bending losses of cores with elaborate refractive index profiles is also a strong concern since some refractive index profiles are more susceptible to bending losses than others. Bending losses are important in maintaining the ruggedness of installed systems. In addition, this type of fiber offers no correction for the standard single mode fiber used in currently installed systems which has its dispersion minimum at 1.3 μm.

A second optical method which can be used to reverse the effects of chromatic dispersion is to spectrally invert the signal at the midpoint of the fiber span. By inverting the information signal, the phase distortion incurred by the first half of the fiber is equalized by the phase distortion incurred by the second half of the fiber and thus the signal's original phase alignment is restored prior to detection. The experimental system demonstrated by Jopson *et al.* [17] is shown in Figure 2.7.

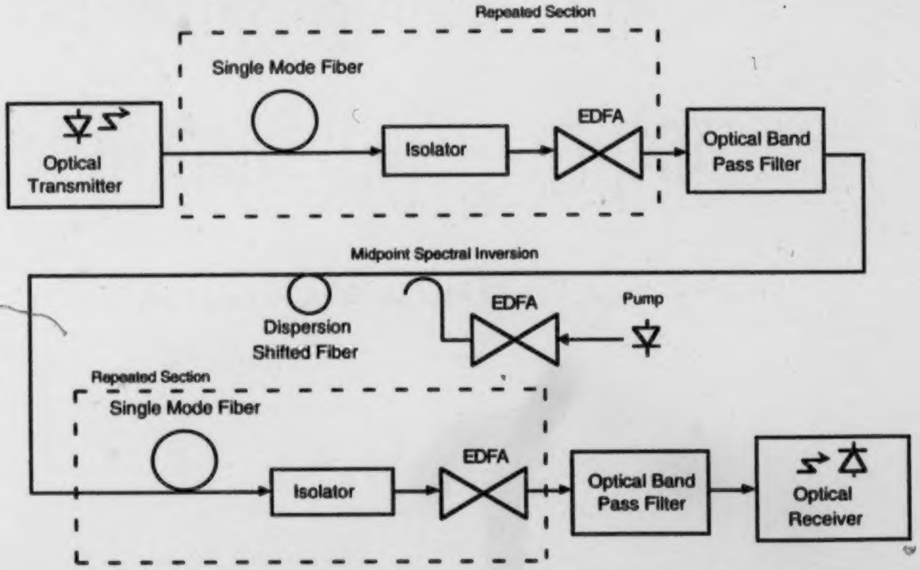
Repeated Section
Single Mode Fiber
Optical Transmitter
Isolator
EDFA
Optical Band Pass Filter
Midpoint Spectral Inversion
Dispersion Shifted Fiber
EDFA
Pump
Repeated Section
Single Mode Fiber
Isolator
EDFA
Optical Band Pass Filter
Optical Receiver

Figure 2.7 Fiber optic system using midspectral inversion to perform chromatic dispersion compensation (Adapted from [17])

The information spectrum is inverted at the midpoint through optical-phase conjugation. More specifically, the conjugate of the information signal is created and transmitted via a nonlinear process called four wave mixing. In this case, the four wave mixing occurs by externally pumping a section of dispersion compensated fiber with a powerful source at a wavelength offset from the original source wavelength.

A third optical method which can be used to reverse the effects of chromatic dispersion is to use a chirped fiber Bragg grating in the optical path. The fiber grating reverses the effects caused by chromatic dispersion by providing an inverse second order phase characteristic to that created by the standard single mode fiber. Its phase response is similar to the dispersion compensating fiber shown in Figure 2.5. A grating is formed in a length of optical fiber and the grating period is reduced linearly down the length of the device. When compared with long wavelength light, shorter wavelengths propagate further into the device before being reflected and are therefore delayed more. Due to the reflective mode of operation of the gratings, circulators are required in the system. An example of the optical system tested by Loh *et al.* [18] is shown in Figure 2.8. As in the dispersion shifted fiber case, the gratings can be placed at the beginning of the fiber path, at the end, or at multiple points throughout. The position of the gratings along the optical path has varying effects due to the insertion loss of the circulators.

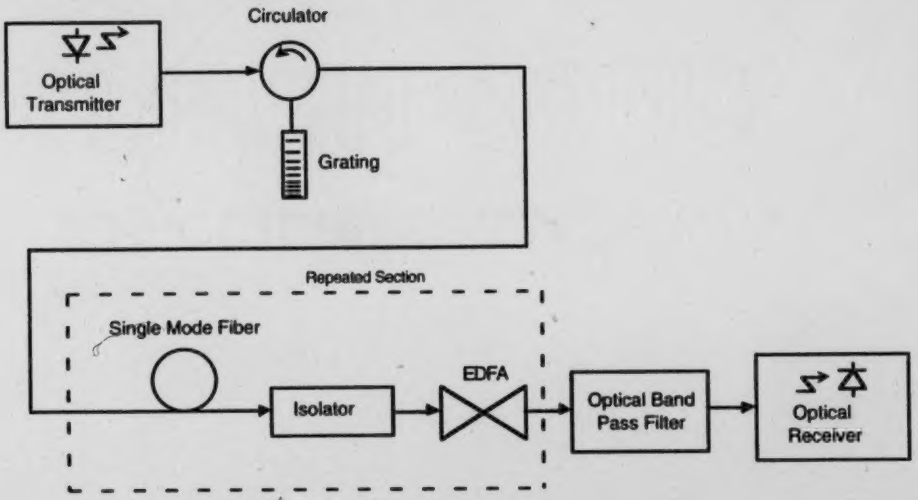

Figure 2.8 Fiber optic system using chirped fiber gratings to perform chromatic dispersion compensation (Adapted from [18])

Currently, chirped gratings fabricated with silicon masks that are fixed over the fiber section during the writing process have a fixed amount of compensation that they can provide over a given optical bandwidth. Thus, the gratings cannot be made long enough to compensate standard 10 Gb/s systems longer than a few hundred kilometers. These fiber gratings are limited in the amount of compensation they can provide for a given bandwidth by the maximum silicon wafer size that can be grown. The silicon wafer is used in the grating writing process. With a fixed wafer size, there is a limit to the optical bandwidth/dispersion compensation product. If the bandwidth of the grating is to be increased, the amount of compensation is correspondingly reduced. Currently, maximum wafer sizes are around 10 cm in diameter thus limiting a grating with a 0.12 nm bandwidth to 5000 ps/nm of dispersion compensation. To help increase the dispersion compensation limit, multiple gratings with different phase characteristics can be cascaded to increase the maximum compensatible distance [18], however, the cost is added optical insertion loss due to the additional gratings.

Recently, work has been done [19] to write the grating into the fiber through a dynamic process where the mask is no longer chirped, but has a constant period and is moved at a controlled rate along the fiber. In this scenario, chirped gratings as long as 1.3 m have been fabricated. These gratings have greatly increased the optical bandwidth/ dispersion compensation product. One important problem with these longer gratings is their high loss.

Systems using slightly different designs of chirped gratings have also been tested by Okamoto *et al.* [20], Ouellette *et al.* [21] and Litchinitser *et al.* [22]. All systems showed the ability to partially equalize the effects of chromatic dispersion. Nonidealities in the grating designs have generally been the limiting factor in extending the transmission distance. Figure 2.8 shows a grating that operates on the basis of reflection. However, some work has also been done by Litchinitser *et al.* [23] in creating Bragg gratings that can be used in a transmissive mode thus reducing the added optical insertion loss created by the optical circulator.

In order to make the dispersion compensation by the chirped grating adaptable to varying fiber lengths, Garthe *et al.* [24] looked at adjusting the strain and Laming *et al.* [25]

looked at adjusting the temperature gradient along the grating length. By adjusting either of these parameters, the amount of compensation provided by a fixed grating length could be varied. This type of equalizer could be used in a system with varying fiber lengths such as in a switched optical network where the fiber length between a transmitter node and a receiver node can vary depending on the transmission path through the network.

The periodic nature of the gratings was also investigated by Ouellette *et al.* [26]. In the investigation, it was shown that the compensation characteristic is periodic in wavelength due to the nature of the grating and could be utilized to equalize the dispersion at multiple wavelengths such as would be required in a WDM system.

Gnauck *et al.* [27] showed that an alternative to using a chirped grating was to use a Fabry Perot cavity. This device has a reflective type operation similar to the grating and thus a circulator or coupler is required to use it effectively in the transmission path. The Fabry Perot cavity has a phase response which is second order over a select range of frequencies. This characteristic is tailored to be the inverse of the fiber dispersion by adjusting the cavity length. Limitations exist in that the range of frequencies over which a proper phase response is generated is very limited with this type of operation.

A fourth method which can be used to limit the effects of dispersion is to use birefringent crystals in the optical path. The birefringent crystals can be aligned in the optical path so as to partially compensate the effects of chromatic dispersion created by the standard single mode fiber. Ozeki [28] showed through simulations that optical circuits could be synthesized for equalizing the dispersion of standard single mode fiber. The polarized crystals served to separate the frequencies of interest, delay portions of the frequencies by different amounts, and subsequently recombine the new frequencies. Further, the periodic nature of the equalizer resulted in periodic dispersion free bands in the optical spectrum. Thus, the author proposed this method for WDM systems as well. A short distance system under 30 km that was tested by Sharma *et al.* [29] which used a crystal equalizer as shown in Figure 2.9. Sharma's results are controversial though since the dispersion shown over 30 km of standard single mode fiber is extremely high. Sharma's system operated at 10 Gb/s. At 10 Gb/s, a 1 dB eye closure penalty due to chromatic dispersion is not typically measured until 65 km.

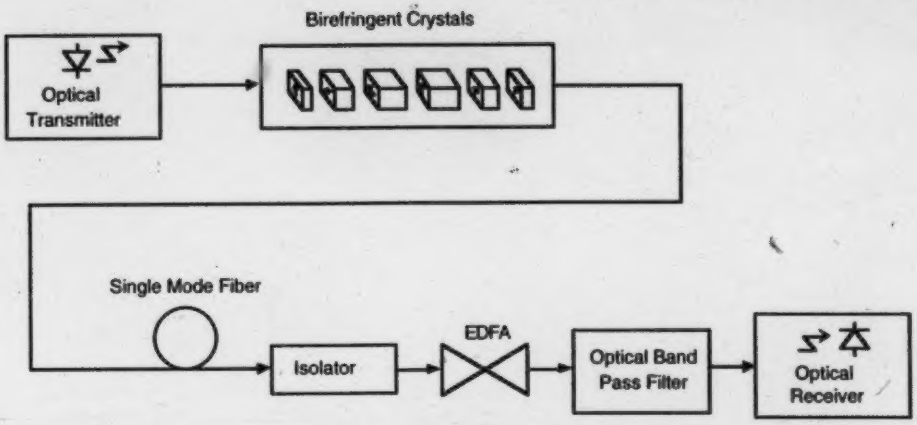

Figure 2.9 Fiber optic system using birefringent crystals to perform chromatic dispersion compensation (Adapted from [29])

A fifth optical method which can be used to limit the effects of dispersion is to use a planar lightwave circuit (PLC) in the optical path. Takiguchi *et al.* [30] proposed using a PLC which consisted of 12 couplers with asymmetric arm lengths cascaded in series. This design is analogous to a cascade of dual arm modulators with control of the delay in each arm. A short distance system using a PLC is shown in Figure 2.10.

In Figure 2.10, the relative path difference ΔL can be achieved through a fixed delay or with a thermo-optic (TO) phase shifter on the optical waveguide. Thermal control of the waveguide changes the light's effective path length. It was suggested by Takiguchi that the chromatic dispersion of the equalizer could be varied from negative to positive values by TO phase control in the optical waveguides. By varying these parameters, a desirable magnitude and phase response for the equalizer could be formulated. Thus, using this adaptive effect, a particular length of single mode fiber with a given dispersion characteristic could be equalized by generating a PLC device which matched the magnitude and reversed the sign of the dispersion generated by the single mode fiber. This type of system could also be used in a switched optical network where the fiber lengths vary. In this scenario, the amount of dispersion induced on a signal may vary depending on the originating point of the signal. To adapt to this change, the electrical signals applied to the TO controls would be adjusted to provide a magnitude and phase response appropriate for equalizing the incurred dispersion.

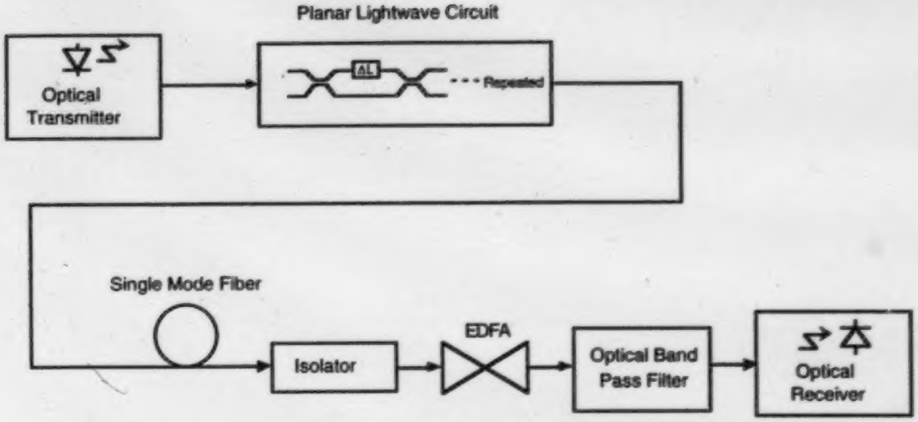
Planar Lightwave Circuit
Optical Transmitter
ΔL
Repeated
Single Mode Fiber
Isolator
EDFA
Optical Band Pass Filter
Optical Receiver

Figure 2.10 Fiber optic system using a PLC to perform chromatic dispersion compensation (Adapted from [30])

A sixth method which can be used to limit the effects of chromatic dispersion is to frequency chirp an external Mach Zehnder (MZ) modulator. MZ modulators are often used to modulate a lightwave carrier with high speed digital information. MZ modulators allow faster modulation of coherent laser light than is achievable by modulating the laser directly. Frequency chirping is a method by which small shifts in frequency of the optical carrier within the pulse offset the effects of chromatic dispersion. An example of a dual arm MZ modulator is shown in Figure 2.11.

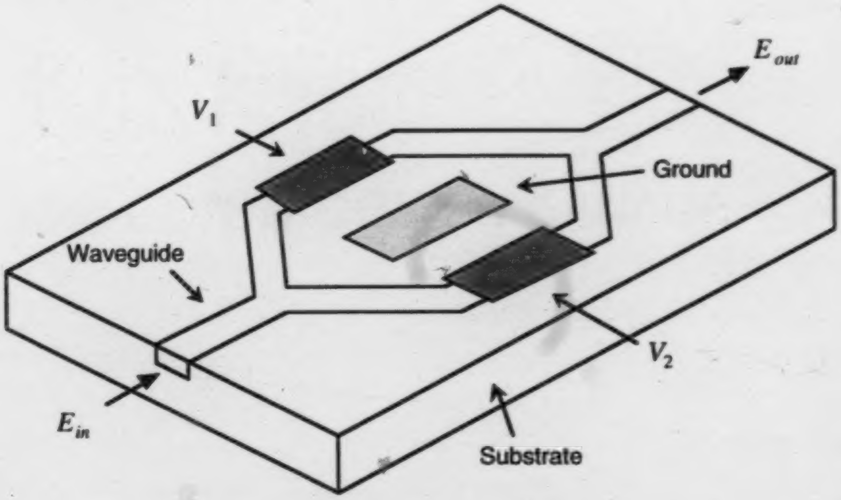
E_{out}
V_1
Ground
Waveguide
V_2
E_{in}
Substrate

Figure 2.11 Dual arm Mach Zehnder modulator

In this device, light is split equally into the two arms through a Y junction, is delayed independently in each arm, and is then recombined through another Y junction. The light in each arm is phase delayed relative to applied electrical signals on each arm. The MZ modulator makes use of the Pockels effect in the optical waveguide to create the phase delay in each arm. The nature of this effect is where the refractive index of the waveguide changes linearly with applied electric field. Careful choice of the applied electrical signals to each arm of the modulator provides an optical intensity pattern at the output of the modulator which contains the desired information in an amplitude modulated form.

In order to see how a MZ modulator can be chirped, consider the complex external modulator transfer function given by:

$$E_{out} = \frac{E_{in}}{2}\exp\left(j\pi\frac{V_1}{V_\pi}\right) + \frac{E_{in}}{2}\exp\left(j\pi\frac{V_2}{V_\pi}\right) \qquad (2.9)$$

where V_π is the modulator's switching voltage, also defined as the required voltage to induce a 180 degree phase shift of the light in a waveguide, V_1 and V_2 are the driving voltage signals on each arm of the modulator, E_{out} is the output electric field and E_{in} is the input electric field which can be written as:

$$E_{in} = \exp(j\omega_o t) \qquad (2.10)$$

where ω_o is the optical carrier frequency and t is time.

Through algebraic manipulations, equation 2.9 can be rewritten as [31]:

$$E_{out} = E_{in}\cos\left(\frac{\pi}{2V_\pi}(V_2 - V_1)\right)\exp\left(j\frac{\pi}{2V_\pi}(V_2 + V_1)\right) \qquad (2.11)$$

In equation 2.11, it can be seen that the transfer function between the input electric field and the output electric field contains an amplitude modulating term (cos) and a phase modulating term (exp). Chirping is generally defined as a nonzero value for the phase term. For small-signal drive conditions with mathematically similar waveforms and an appropriate dc bias, the chirp parameter of a MZ modulator is roughly constant and determined by the peak-to-peak values of the ac electrical drive signals for each arm [31]. The chirp parameter α is given by:

$$\alpha \approx \frac{V_2 + V_1}{V_2 - V_1} \tag{2.11}$$

In some cases, it is ideal to drive a MZ modulator in a chirp free manner such that $\alpha = 0$ which can be achieved by driving the MZ modulator with balanced drive signals such that $V_1 = -V_2$. In this case, the phase term in equation 2.11 is zero and the amplitude modulation is maximized.

It was shown in by Gnauck *et al.* [32] and Cartledge *et al.* [33] that choosing a nonzero value for the chirp parameter can be advantageous depending on the fiber dispersion coefficient and the fiber length. By operating the MZ modulator with small negative chirp (i.e. $\alpha = -1$), the dispersion limited distance can be slightly extended over chirp free transmission. Prechirping essentially predistorts the phases of the frequencies in each pulse before it encounters the chromatic dispersion caused by the fiber. This effect has been called pulse compression since in space, negative dispersion imparts a red shift on the rising edge of a prechirped digital pulse and a blue shift on the falling edge. The result is the rising edge travels slower than the falling edge because of the difference in group velocity in the fiber. Therefore, as a digital pulse propagates down the fiber, it will become compressed for a given distance giving it an anti-dispersive property. The correcting effect supplied by prechirping a pulse is limited since after a certain fiber length, the pulse will be fully compressed and will then begin to decompress.

A seventh method which can be used to limit the effects of chromatic dispersion is to differentially delay the upper and lower sideband of the modulated optical signal. It was reported by Djupsjöbacka *et al.* [34] that this method is beneficial but does not accomplish complete dispersion compensation. However, they claim that this technique is superior to the common prechirp technique. An example of an optical system implementing this technique is shown in Figure 2.12. Djupsjöbacka stated that the differential delay device could be placed at any point along the fiber path; it is shown following the optical transmitter in Figure 2.12.

The incoming optical signal to the differential time delay circuit is split by a 3 dB splitter. In each branch there is an optical narrowband filter. The bandwidth is chosen so as to allow only the upper or lower sideband modulation sideband to pass through. In one of the branches the corresponding sideband is delayed a time T relative to the other sideband to compensate for the different propagation times in the dispersive fiber. This type of delay is similar to that provided by the Fabry Perot design presented by Gnauck [27] since only a select range of frequencies related to the delay time are properly corrected for the effects of chromatic dispersion induced by the fiber. This method is susceptible to temperature fluctuations in the two branches resulting in an effective path length difference for each sideband.

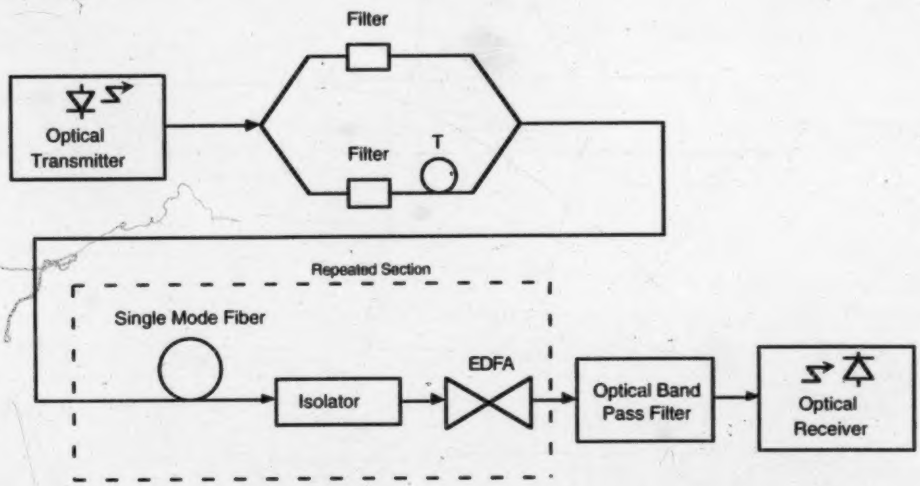

Figure 2.12 Fiber optic system using differential time delay of the upper and lower sidebands to perform chromatic dispersion compensation (Adapted from [34])

2.2.2 Post Detection Methods

A second general method to compensate for the effects of chromatic dispersion is post detection electronic equalization [35]. Electrical equalization after detection cannot be performed on a regular transmitted optical double sideband (DSB) signal since the phase distortion incurred by the fiber on the information sidebands is different for each sideband and thus the phase delay incurred by the fiber is no longer reversible due to the backfolding of the upper and lower sidebands upon detection. Electrical equalization can be performed on a coherently received optical DSB signal if the equalization is done at an intermediate frequency (IF) which is higher than the highest frequency in the baseband signal. This can be accomplished by using a local oscillator (LO) at the photodetector and mixing the received optical signal to an IF, electrically equalizing the signal, and then mixing the IF signal down to baseband. An example of this type of operation is shown in Figure 2.13.

In Figure 2.13, f_o represents the optical carrier frequency while f_b represents the bandwidth required to transmit the data; for binary signals, this is approximately the bit rate. In Figure 2.13 (a), a baseband DSB signal is shown before modulation. In Figure 2.13 (b), an optical DSB signal is shown after modulation onto the optical carrier with the phase information incurred by the chromatic dispersion represented with a hatching of the magnitude spectrum. The corresponding square law detected baseband signal is shown in Figure 2.13 (c). In Figure 2.13 (c), the cross hatching from the lower sideband (LSB) and the upper sideband (USB) overlap representing a destruction of the phase information incurred by the chromatic dispersion. Thus, the chromatic dispersion incurred on the received signal in the form of a frequency dependent phase delay is not readily reversible. However, if the DSB signal in Figure 2.13 (b) is coherently detected with a LO of a frequency different from the source, the phase information represented by the cross hatching is primarily preserved as shown in Figure 2.13 (d) and can generally be reversed through post-detection electronic equalization. The IF signal is then subsequently mixed down to baseband for further signal processing.

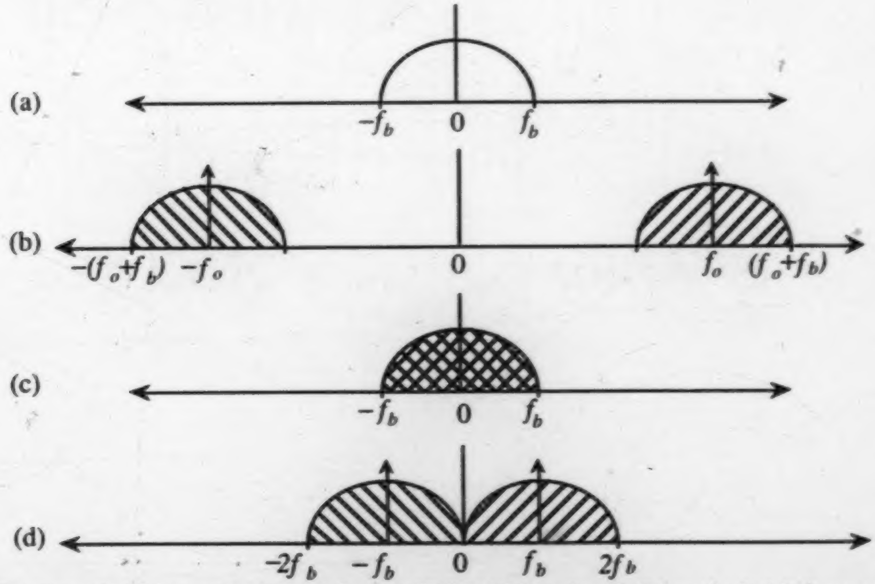

Figure 2.13 Magnitude and phase of DSB (a) baseband, (b) optical, (c) detected baseband and (d) detected IF signals

An example of a system which uses electronic equalization with a LO at the receiver is shown in Figure 2.14.

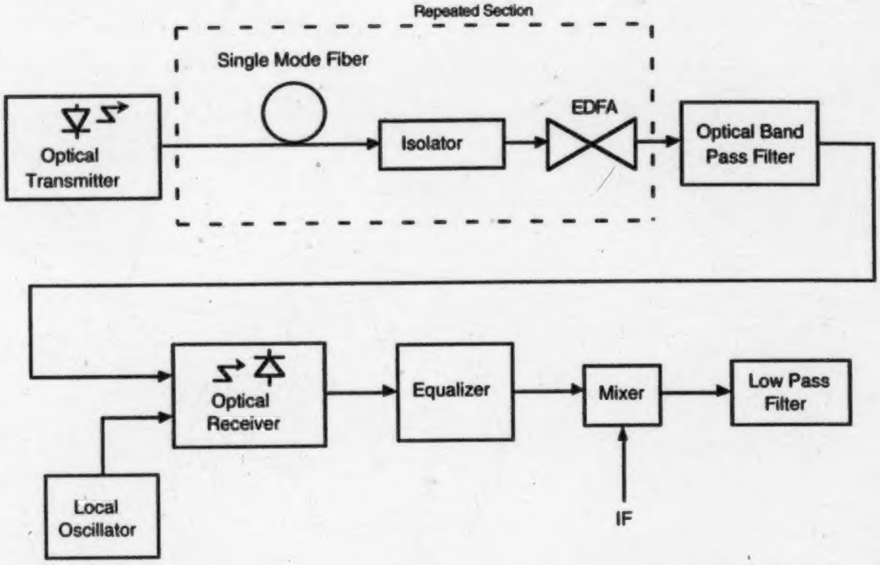
Repeated Section
Single Mode Fiber
Optical Transmitter
Isolator
EDFA
Optical Band Pass Filter
Optical Receiver
Equalizer
Mixer
Low Pass Filter
Local Oscillator
IF

Figure 2.14 Fiber optic system using electronic equalization at an IF to perform chromatic dispersion compensation (Adapted from [35])

One approach to electronic equalization demonstrated by Takachio *et al.* [36], [37] was to use a microstrip line on the received electrical signal. The section of microstrip used for the equalization has the approximate inverse nonlinear phase characteristics of the chromatic dispersion induced by the fiber. Generally, for a given length of fiber, a certain amount of microstrip was required to compensate. Detecting the optical signal at an IF was required in this case since an optical DSB signal was transmitted. One of the drawbacks of using microstrip equalizers is their frequency dependent attenuation.

Winters [38] proposed using a microwave waveguide instead of a microstrip line to perform the equalization. The suggested advantages of the waveguide over the microstrip were lower radiation from the device into other parts of the receiver and lower signal attenuation while the disadvantages included a higher IF frequency in the waveguide and possibly more expensive construction when compared to a microstrip line.

Winters [39] also created a fractionally spaced equalizer which was implemented with an analog tapped delay line. This equalizer had the advantage of being adaptive and could thus equalize chromatic dispersion over varying distances making it also applicable to optically switched networks. By varying the tap weights, the amount of equalization could be varied.

2.2.3 Transmission Format Methods

A third general approach which reduces the effects of chromatic dispersion but does not eliminate it is to modify the transmission format such that the baseband signal spectrum is compressed. For example, coding a binary signal in a duobinary format reduces the required transmission bandwidth by a factor of two. By reducing the bandwidth (B) by a factor of two, the difference between the highest and lowest frequency in the information spectrum is less. Thus, examining equation 2.8, it can be seen that the dispersion is reduced if the difference between the highest and the lowest frequencies is reduced. It is important to note that if the required transmission bandwidth has been reduced, the transmitted signal must be filtered down to the minimum required transmission bandwidth. If the signal is not filtered, even though a duobinary signal is transmitted, the spectral content above the minimum required bandwidth will still corrupt the received signal and no improvement in the transmission distance will be measured.

A duobinary receiver was shown by May *et al.* [40] and a duobinary transmitter was shown by Yonenaga *et al.* [41]. It is interesting to note that in Yonenaga's implementation, the transmission is in an amplitude modulated - phase shift keyed (AM-PSK) format where the electrical information is encoded in a duobinary format at the optical electric field level, however, the MZ modulator used to modulate the information on the carrier is biased such that upon square-law detection, the received electrical signal is in a binary format at the optical power level. This type of signaling sees the benefits of reduced effects of chromatic dispersion since the bandwidth of the signal at the electric field level is reduced by the duobinary format and also sees the benefits of improved noise immunity of binary signaling since the detected optical signal is two level and not three.

A duobinary transmitter in conjunction with chirped fiber gratings was demonstrated by Loh *et al.* [42] and also Ennser *et al.* [43]. This approach has a dual benefit in that the optical transmission bandwidth is effectively reduced and optical compensation in the form of the grating both help reduce the effects of chromatic dispersion. By reducing the effective bandwidth at the electric field level, more dispersion compensation could be obtained out of the gratings. As was mentioned before, due to the fixed size of gratings created with a stationary mask, there is a bandwidth-dispersion product limit. Thus, reducing the optical bandwidth requirements allows for the increase of grating dispersion compensation.

Duobinary signaling is one example of multilevel signaling. Higher order multilevel signaling formats can also be used to reduce the required transmission bandwidth further for a given bit rate. In general, with multilevel signaling, the amplitude of the carrier is switched between multiple levels where each level represents two or more bits of information [44]. If q is the number of bits represented by each symbol, then the number of levels required for each symbol is 2^q. For example, if a two level binary signal was coded into a four level format, the required transmission bandwidth would be reduced by a factor of two. Consequently, the transmission length could be increased by a factor of four to maintain the same dispersion penalty. A multilevel decoder is generally required in these systems. An example of a multilevel system is shown in Figure 2.15. In this case, the multilevel electrical signal must be filtered down to B/4 before optical transmission.

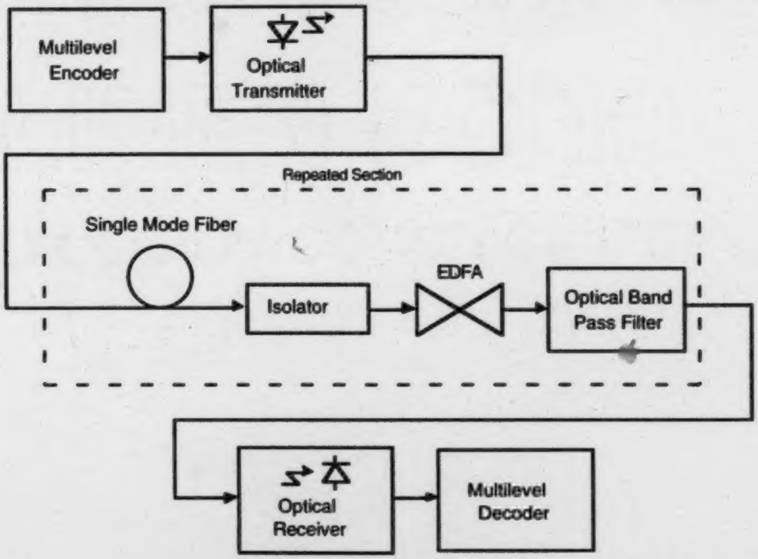

Figure 2.15 Multilevel signaling system

One hybrid of multilevel signaling is polybinary signaling. It also offers a benefit with regards to dispersion immunity, also due to a type of reduced spectral width. Polybinary signals are multilevel signals developed by introducing correlation among the bits in a binary sequence. This process is referred to as correlative-level coding or partial response signaling [44]. The interesting property of binary signals is that power is redistributed such that there is more relative power at lower frequencies (frequencies closer to the carrier in the modulated signal). Since phase distortion of the information increases for frequencies farther away from the carrier when transmitting over dispersive fiber, polybinary signals are more immune to dispersion. Polybinary signaling also requires proper electrical filtering at the transmitter and receiver as is done in the multilevel case.

3. THEORY OF OPTICAL SINGLE SIDEBAND

3.1 Benefits of Optical Single Sideband

The generation, transmission and detection of SSB signals has been used in the radio frequency (RF) and microwave regions of the electromagnetic spectrum to reduce the bandwidth of the signal by a factor of two and to improve the signal to noise ratio at the receiver [45]-[49]. The primary purpose behind SSB systems in the RF domain has been to allow closer channel spacing in a multichannel RF system. When a RF carrier is modulated with a binary information signal, a DSB spectrum results. Thus, the closest that the RF carriers can be spaced, theoretically, is $2f_{\max}$ where $f_{\max}$ is the maximum frequency in the information signal. When the information signal is transmitted on the RF carriers in a SSB format, the carriers can be spaced by $f_{\max}$. Thus, in a RF system where the overall available bandwidth is limited by physical limitations or by regulation, the number of separate transmitted channels can be doubled if SSB is used instead of DSB.

An optical carrier can also be modulated with a binary information signal to result in a SSB output spectrum. The first benefit, due to the fact that the transmitted signal spectrum is SSB, is that the multiple optical carriers could be spaced by $f_{\max}$ instead of $2f_{\max}$ which is required for DSB information signals. This is analogous to the RF case. Additional advantages of optical SSB transmission arise from reducing the effects of chromatic dispersion. First, a dispersion benefit would accrue due to the fact that the bandwidth of the transmitted signal spectrum has been reduced by a factor of two. As was shown in Chapter 2, the chromatic dispersion from the first order group velocity dispersion increases with the square of the frequency. Thus, if the difference between the highest and lowest frequency in the optical signal is reduced by a factor of two, the dispersion penalty decreases by approximately a factor of four. A second and even more significant advantage of optical SSB transmission is that upon square-law detection, we end up with a dispersed baseband signal where the information of the relative arrival time of the various signal frequencies remains as part of the electrical output signal. Hence, the fiber dispersion can be compensated in the electrical domain after detection. This advantage is similar to that for heterodyne detection of DSB signals, but with SSB transmission and detection, it is the electrical baseband signal that has the phase or delay information incurred by the fiber primarily preserved.

An example of a heterodyne detection system was originally shown in Figure 2.13. In a heterodyne detection system, a LO is required at the detector in order to mix the received signal to an IF. At the IF, frequency equalization can be done with subsequent mixing down to baseband. One inherent problem with heterodyne detection is stabilizing the LO so that fluctuations in the IF are minimal. If an optical DSB signal were square-law detected in the conventional manner, the baseband signal could not be equalized.

To better show how an optical DSB signal that is square-law detected cannot be equalized, but an optical SSB signal that is square-law detected can, the phase information incurred by chromatic dispersion on an optical signal is shown again by hatching the magnitude spectra in Figure 3.1.

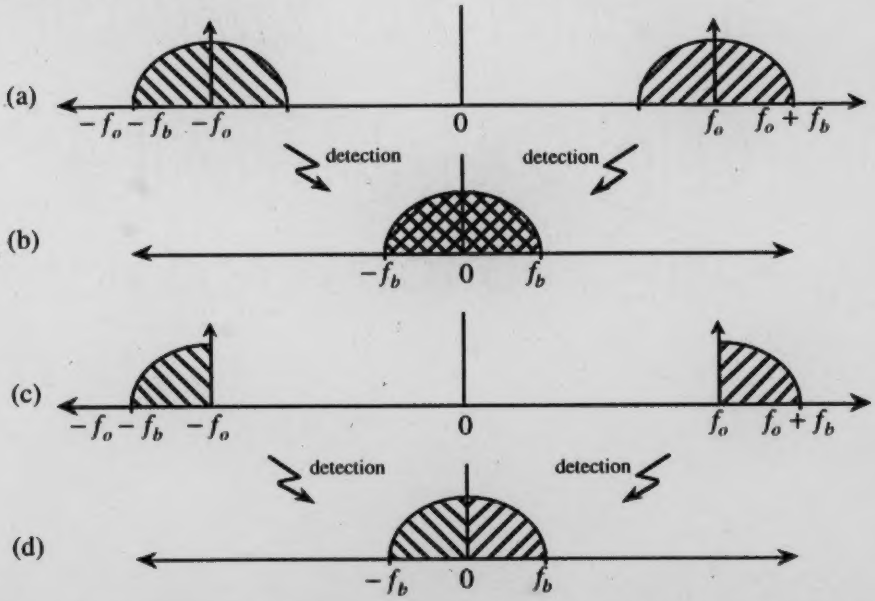

Figure 3.1 Magnitude and phase of DSB, (a) and (b), and SSB, (c) and (d), signals

In Figure 3.1, f_o represents the optical carrier frequency while f_b represents the bandwidth required to transmit the data. In Figure 3.1 (a), an optical DSB signal is shown while the square law detected baseband signal is shown in Figure 3.1 (b). In Figure 3.1 (b), the hatching from the LSB and the USB overlap representing a destruction of the phase information incurred by the chromatic dispersion. Thus, the chromatic dispersion incurred on the received signal is not readily reversible. However, if the SSB signal in Figure 3.1 (c) is square law detected, the phase information represented by the hatching is primarily preserved as shown in Figure 3.1 (d) and can be compensated (reversed) through post-detection electronic equalization. The purpose of the spectra in Figure 3.1 are to better explain the difference in phase information of received DSB and SSB signals. Higher order spectra resulting from distortion in the square-law detection process have been omitted in this figure for clarity.

Heterodyne detection systems use a LO to mix the optical signal down to an IF. The DSB and SSB systems shown in Figure 3.1 are also mixed down to baseband through the square-law detection process. The LO is the optical carrier itself. The process can be described as a sort of self-homodyne detection process. In multi-gigabit transmission systems, MZ modulators similar to the one shown in Figure 2.11 are used to modulate the digital information onto the optical carrier. Proper biasing of this modulator ensures a significant carrier remains in the transmitted signal which provides the LO for self-homodyne detection at the receiver.

Modulating optical carriers with multi-gigabit per second binary information in a DSB format is the standard approach used today. The goal then is to formulate a method or methods which would allow the modulation of the information onto the optical carrier in a SSB format. The information should be recoverable through square-law detection.

3.2 Prior Art in Optical Single Sideband Systems

A SSB signal is a mathematical version of a DSB signal. For a normal DSB signal $m(t)$, the analytic SSB form of it can be obtained by [50]:

$$m_{SSB}(t) = m(t) \pm j\hat{m}(t) \tag{3.1}$$

where the ± gives the LSB/USB.

$\hat{m}(t)$ is the Hilbert transform of $m(t)$ where the Hilbert transform is defined as shown in Figure 3.2 with $|H(\omega)|$ the magnitude and $\theta_H(\omega)$ the phase of the Hilbert transform.

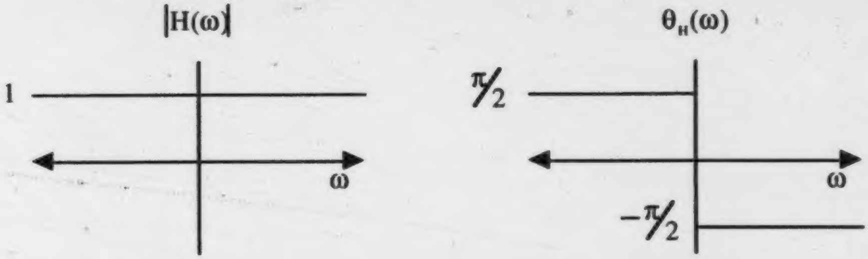

Figure 3.2 Magnitude and phase of a Hilbert transform filter

If the SSB signal is modulated onto a carrier, the SSB signal would be of the form:

$$m_{SSB}(t) = m(t)\cos(\omega_c t) \pm \hat{m}(t)\sin(\omega_c t) \tag{3.2}$$

where ω_c is the carrier frequency. In the case of an optical system, the carrier ω_c is the optical carrier and $m(t)$ is the modulating information.

Foreseeing the benefits of optical SSB, the first optical SSB transmitter was designed by Izutsu *et al.* [51]. Their integrated optical SSB modulator, shown in Figure 3.3, was fabricated using $LiNbO_3$ waveguides. The system is comprised of four guided wave phase modulators (PM) and three phase shifters (PS). A PS is a device which imparts a constant phase offset to the incoming carrier while a PM is a device which modulates the phase of the incoming carrier with an applied electrical signal.

Izutsu *et al.* demonstrated optical SSB with a single frequency tone ϕ as the modulating signal. This made generating the Hilbert transform, ϕ', of the modulating signal relatively easy since the Hilbert transform of a carrier with a cosine type phase is just the 90 degree phase shifted version, sine.

The operation of Izutsu's design is such that the PS in arm b in Figure 3.3 allows the modulators to be fed optically in quadrature. This provides the cosine and sine carriers to be modulated as shown in equation 3.2. The PMs and PS in arms c and d are used to amplitude modulate the cosine carrier with information ϕ. The PMs and PS in arms e and f are used to amplitude modulate the sine carrier with the Hilbert transform of the information

ϕ'. The resultant output is a optical SSB version of equation 3.2 with the information essentially being tones.

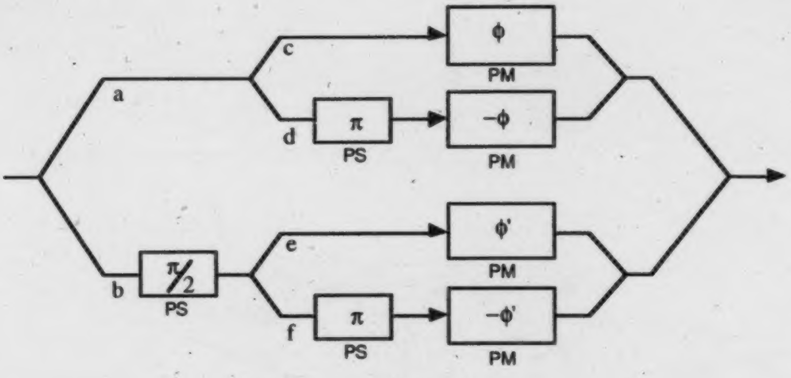

Figure 3.3 First integrated optical SSB transmitter (Adapted from [51])

Olshansky [52] also designed an optical SSB system using a MZ modulator as the SSB modulating device. The SSB modulator was designed for narrowband applications for the purpose of transmitting two or more optical signals with different optical carrier frequencies on a single fiber. Optical carriers could thus be spaced by f_{max} instead of $2f_{max}$ as in the DSB case where f_{max} is the maximum frequency in the modulating signal. This design can be classified as an example of a narrowband application since each baseband signal was modulated onto a RF carrier before driving the modulator. A schematic of the MZ modulator similar to the one used in Olshansky's design was shown in Figure 2.11.

In Olshansky's design and in the ones that follow, it is important to note that the MZ modulator has two separately accessible arms. This is important in certain types of optical SSB generation since the signals driving each arm are generally different. Some MZ modulators do exist where only one signal drives one arm of the MZ and the other arm is grounded. This type of MZ modulator will not work alone for optical SSB, although it does provide a type of amplitude modulation. A MZ modulator that has a configuration such that one signal can drive both arms in a chirp free manner would work in one type of SSB modulation as will be shown later.

In Figure 2.11, E_{in} and E_{out} represent the input and output optical electric fields. In Olshansky's design, the signals V_1 and V_2 required to make E_{out} SSB are of the form:

$$V_1(t) = \Sigma\beta_i \sin(\omega_i t + \delta_i) \qquad (3.3)$$

$$V_2(t) = \Sigma\beta_i \cos(\omega_i t + \delta_i) - V\pi/2 \qquad (3.4)$$

where β_i, ω_i and δ_i are the magnitude, frequency and phase respectively of the *i*th subcarrier and $V\pi/2$ represents half of the switching voltage for the modulator. Again, $V\pi$ is defined as the modulator's switching voltage. In Olshansky's design, the bias is used as a means of generating orthogonal carriers.

The electric field at the output of the MZ modulator in Olshansky's design is in an optical SSB form. However, as Olshansky found out, a LO at the receiver with an optical frequency equivalent to the *i*th subcarrier optical frequency and proper phase is required in order to properly detect the information signal in the *i*th subcarrier. If a LO is not added to the received signal, a portion of the non-modulated light must be leaked into the transmitted optical signal. This allows the information spectra to be properly self-homodyne detected at the receiver. Self-homodyne detection, as previously mentioned, is a method by which unmodulated carrier is included in the transmitted signal such that the unmodulated carrier acts as a LO at the receiver so that the information signal is properly mixed to baseband upon square-law detection. The problem with self-homodyne detection is that only the *i*th subcarrier with the non-modulated light is mixed down to baseband. The other information signals still sit on IF carriers and must subsequently be mixed down to baseband electrically. Consequently, usually only one information signal is transmitted in a system that uses self-homodyne detection.

Olshansky's design was composed mainly for the purpose of more closely spacing RF carriers with information. However, as was also determined, transmitting RF carriers in an optical SSB form showed higher immunity to the effects of chromatic dispersion from fiber than ones in DSB form.

Park *et al.* [53] and Smith *et al.* [54] both implemented a version of Olshansky's design and demonstrated experimentally an optical SSB signal using a single external modulator. In both of these experiments, the modulating signals were single channel narrowband RF signals in the 18 GHz region. What they showed is that RF signals modulated onto an optical carrier in a DSB format experience detected nulls at points down the fiber where as the ones modulated in a SSB format did not.

When RF signals are modulated onto an optical carrier in a DSB format such as shown in Figure 3.4 (a), the spacing between the upper and the lower RF carrier on either side of the optical carrier is quite large. As a signal of this nature propagates down the fiber, the chromatic dispersion imparts a phase shift on each subcarrier such that after a certain distance, the sidebands would be 180 degrees out of phase. If the optical signal were detected at this point, no significant electrical signal would be measured because the sidebands would cancel upon square law detection. This null would occur repeatedly down the fiber at another length as the dispersion shifted the sidebands come into phase and out of phase. The first null for a RF carrier of 18 GHz is less than 15 km on standard single mode fiber.

This cyclical dependence can be shown by combining the fiber transfer function shown in equation 2.1 with the first order group velocity dispersion term represented in equation 2.8 to give:

$$H(\omega,z) = \exp\left(j\frac{1}{2}\left[\frac{\lambda_o^2}{2\pi c}\right] D(\omega-\omega_o)^2 z \right) \qquad (3.5)$$

Examining equation 3.5, it can be seen that if ω is a RF signal represented by a tone, there will be a phase difference of π between the upper and lower sideband tone for a given frequency difference between the sidebands, a given dispersion coefficient D and a given fiber length z.

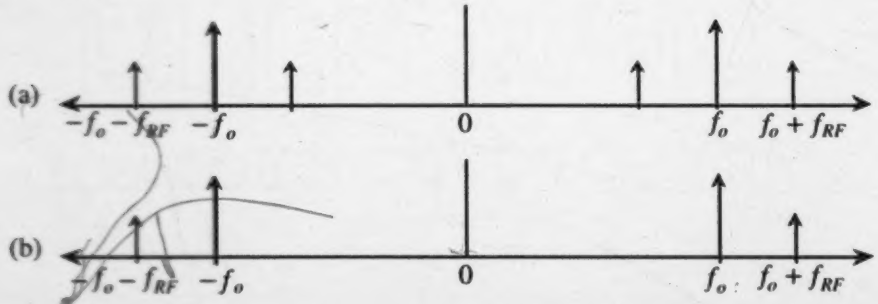

Figure 3.4 Optical spectrum of RF carriers in (a) DSB form and (b) SSB form

Alternatively, if the RF carrier is modulated onto the optical carrier is a SSB form as shown in Figure 3.4 (b), there are no detected nulls since only one signal carrier sideband beats against the optical carrier at the receiver and there is no other sideband to cancel with.

Experimental results of these detected nulls are shown in Figure 3.5 [55]. In this case, a 17.35 GHz carrier was modulated onto an optical carrier in first a DSB format to show that there is a detected null at around 13 km and then SSB modulated onto an optical carrier to show how this null can be reduced. There were two modulator structures used, one using a single MZ modulator and a second using a cascade of one MZ modulator and one PM. These two different designs will be elaborated upon later. Wale [56] designed a MZ modulator specifically for this application. The waveguides and microstrip within a MZ modulator were specifically designed for this type of application where the driving signals are in the 18 GHz region.

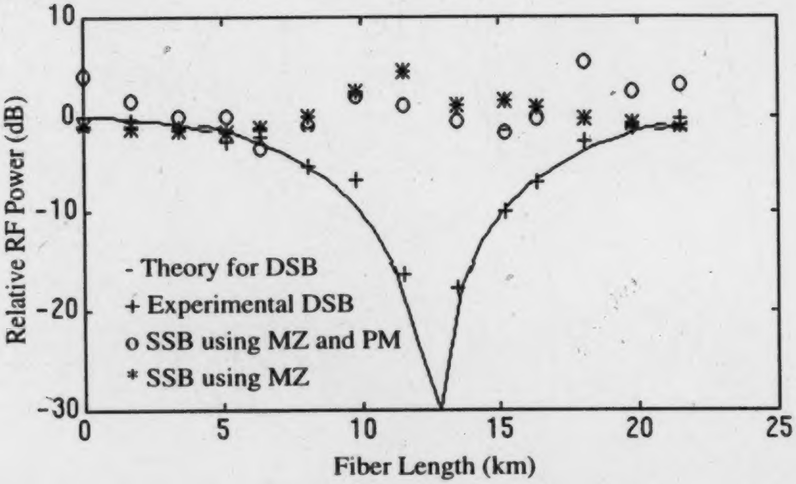

Figure 3.5 Relative RF power at 17.35 GHz versus fiber length (Adapted from [55])

Generating an optical SSB signal for a broadband signal such as a baseband digital signal is much more complicated than for a narrowband signal. The complication lies in generating the Hilbert transform of the broadband signal. The number of frequency octaves covered by a baseband digital signal is much larger than for a baseband signal modulated onto a RF carrier. For the narrowband signal, the Hilbert transform can be accurately approximated by integration's or differentiation which phase shifts all signal components by 90 degrees and introduces a small distortion in amplitude.

To circumvent this problem, Yonenaga *et al.* [57], [58] created an approximate SSB signal by first amplitude modulating an optical carrier in a DSB format and then subsequently optically filtering the DSB signal. The optical filter was a MZ type optical filter with a ring resonator in one arm. This provided an adequate optical filter, however, the roll-off characteristic was less than ideal. As a result, the optical SSB signal degraded to an optical vestigial sideband (VSB) signal. The system is shown in Figure 3.6.

In the systems implemented by Yonenaga *et al.*, unmodulated light was leaked into the modulated optical signal at the transmitter in order to properly self-homodyne detect the optical SSB signal at the receiver. The systems implemented by Yonenaga *et al.* were phase shift keyed (PSK) and as such, if there was no extra unmodulated carrier added to the transmitted information, the square-law detection process would not restore the modulated information to it's proper form at the receiver. Further, the optical filter partially attenuates the power in the optical carrier limiting the self-homodyne capability of the signal.

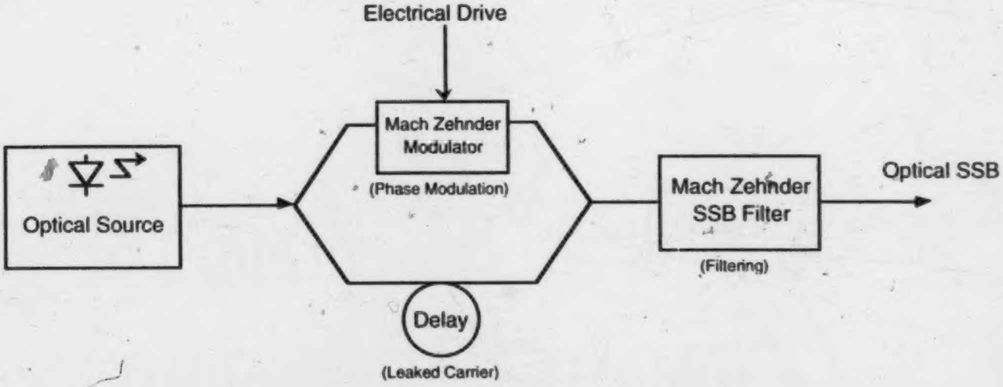

Figure 3.6 Optical filter to generate SSB (Adapted from [57])

This system of optical SSB generation for a baseband digital signal was the first of it's kind. It combats chromatic dispersion in two ways. First it reduces the bandwidth of the transmitted signal since the difference between the highest and lowest frequency components in the information is reduced. Second, the relative arrival time of the various signal frequencies remains as part of the electrical output signal and hence the chromatic dispersion can be compensated in the electrical domain after detection. Yonenaga *et al.* used electrical equalization in the form of microstrip to compensate the phase distortion created through the effects of chromatic dispersion.

The problems that arise with the optical filtering method are that filters with infinitely steep roll-off are hard to make and thus, optical VSB is the best achievable result. Second, the cost of fabricating custom MZ filters is high. Yonenaga fabricated the filter with $LiNbO_3$ waveguides. These waveguides are created with a precise fabricating process. Third, the frequency of the laser source is not allowed to vary since the MZ filter is designed to filter at one specific wavelength. Fourth and finally, additional non-modulated light must be externally added to the transmitted signal. This light must be in phase with the modulated light and thus accurate control of the nonmodulated light's phase is required. This is not a simple task considering the long path length of the nonmodulated light around the MZ modulator, the short optical wavelength of transmission and variations in the path refractive index with temperature.

The direction of this thesis project is to implement SSB without using an optical filter but rather some variation of Olshansky's approach to direct generation of an optical SSB signal. The system must have the capability to handle broadband signals, particularly, baseband digital signals on the order of 10 Gb/s. Further, it would be beneficial if unmodulated carrier would not have to be added to the transmitted signal in order to properly square law detect the baseband signal at the receiver. The result would be an easily implementable baseband optical SSB system which would limit and allow for the reversal of the effects of chromatic dispersion. Further, the source could drift in wavelength and the temperature could vary with no significant impact.

3.3 Theoretical Development of New Optical Single Sideband Systems

The goal is to create an optical SSB signal as in equation 3.2 where the information source is baseband binary data which is on the order of 10 Gb/s and the optical carrier has a wavelength at 1.55 μm. This type of system would allow operation at the attenuation minimum of standard single mode fiber. It would also allow operation within the EDFA gain window. Further, by the nature of the optical SSB electric field, this method would allow for significant equalization post detection in the electrical domain of the chromatic dispersion incurred by the fiber at the 1.55 μm wavelength. Proposed are three designs which try to achieve direct optical SSB transmission for this purpose.

Design 1 for the optical transmitter is shown in Figure 3.7. In this design, the baseband signal $m(t)$ and the Hilbert transform of that signal $\hat{m}(t)$ each drive one arm of a dual arm drive MZ modulator similar to the one shown in Figure 2.11. A dc bias, equivalent to $V_\pi/2$, is added to the Hilbert transform signal in order to create a phase difference of 90 degrees between the light in each arm of the MZ modulator. As previously mentioned, V_π is the modulator's switching voltage where V_π is the applied voltage to one arm required to phase shift the light in that arm by 180 degrees. The absolute dc bias added to each arm can be varied, but the relative difference between the dc bias values in each arm must be $V_\pi/2$. If a relative difference of $-V_\pi/2$ were used, the alternate USB or LSB would be transmitted depending on the orientation of $\hat{m}(t)$. Either the USB or LSB can be transmitted, however, the choice would depend on both the phase response of the fiber and that of any electrical equalizer used at the receiver to reverse the effects of the fiber phase response. In this design, additional unmodulated optical carrier must be added to the transmitted signal. The power of this additional optical signal should be large enough to properly self-homodyne detect the optical SSB signal. The phase of this additional optical signal must be inphase with the light in the path in the MZ modulator which is driven by the signal $m(t)$.

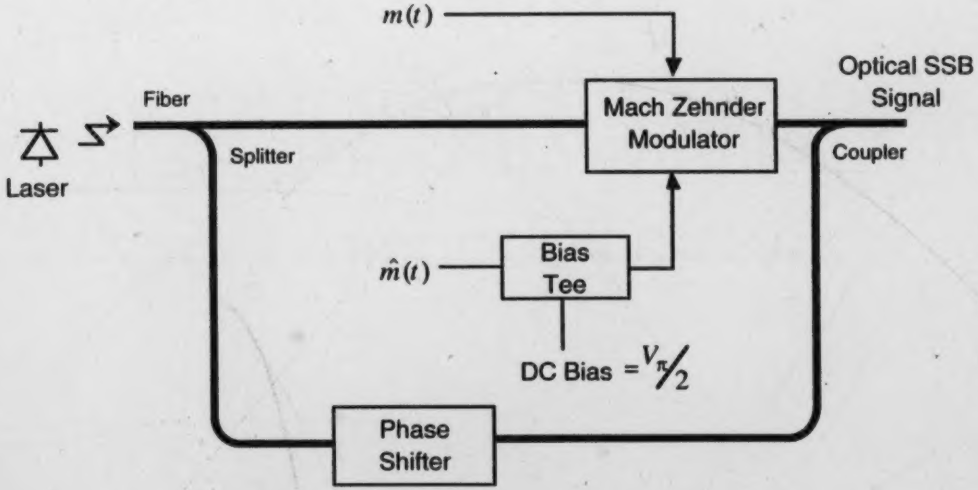

Figure 3.7 Design 1 for optical SSB transmission

Design 2 for the optical transmitter is shown in Figure 3.8. In this design, a combination of the baseband signal $m(t)$ and the Hilbert transform of that signal $\hat{m}(t)$ drive one arm and a different combination of the baseband signal and the Hilbert transform signal drive the second arm of the dual arm drive MZ modulator also similar to the one shown in Figure 2.11. The first combination signal consists of $m(t)+\hat{m}(t)$ while the second combination signal consists of $-m(t)+\hat{m}(t)$. A dc bias is added to one or both arms of the MZ modulator in order to create a phase difference of 90 degrees between the light in each arm of the MZ modulator. In the design shown in Figure 3.8, the dc bias added to the arm driven by $m(t)+\hat{m}(t)$ is equivalent to $-V_\pi/4$ while the dc bias added to the arm driven by $-m(t)+\hat{m}(t)$ is equivalent to $V_\pi/4$. Again, the relative difference between the dc bias in each arm is $V_\pi/2$ or $-V_\pi/2$ depending on which sideband is to be transmitted. In this design, additional unmodulated optical carrier does not have to be added to the transmitted signal in order to properly self-homodyne detect the optical signal. There is enough unmodulated carrier left in the signal to maintain proper self-homodyne detection. This combination of drive signals allows the MZ to be amplitude modulated by $m(t)$ and phase modulated by $\hat{m}(t)$ such that the optical electric field is SSB. Consequently, Design 2 presents an improvement over Design 1 in that extra unmodulated carrier does not have to be phased and added to the modulated light. Thus, existing MZ modulator designs can be used without optical modifications at the transmitter.

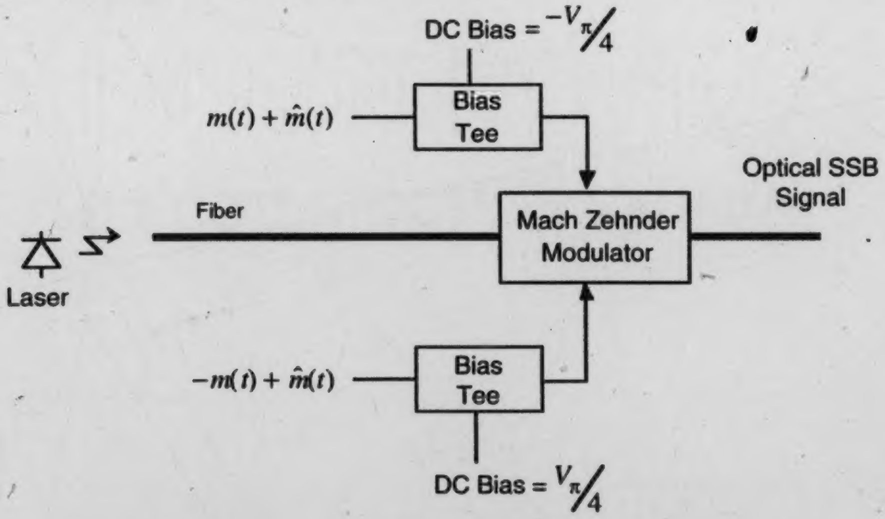

Figure 3.8 Design 2 for optical SSB transmission

Design 3 is a modified version of Design 2. In Design 2, the driving signals $\hat{m}(t)$ on each arm of the MZ modulator operate effectively as a PM on the light. Since the system is linear in the optical domain, the $\hat{m}(t)$ signals can be moved to a separate PM as shown in Figure 3.9 with no difference in terms of the mathematics. It is important to note, however, that the timing of the signals $m(t)$ and $\hat{m}(t)$ is critical in both cases. In Design 2 it seems obvious that when $m(t)$ and $\hat{m}(t)$ are combined that $\hat{m}(t)$ represents the Hilbert transform of $m(t)$ at all instances of time t. However, in Design 3, the signal $\hat{m}(t)$ must be delayed with respect to $m(t)$ by a time equal to the delay in the optical signal between the MZ modulator and the PM. A schematic of the PM is shown in Figure 3.10. It's operation is similar to that of one arm of a MZ modulator. The PM also uses the Pockels effect in phase modulating the input carrier with the applied electrical signal.

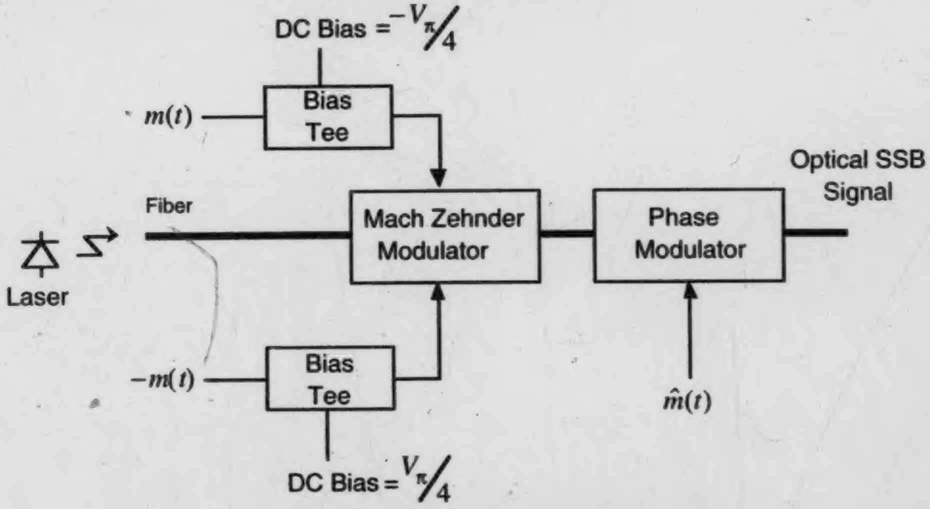
DC Bias = $-V_\pi/4$
$m(t)$
Bias Tee
Optical SSB Signal
Fiber
Mach Zehnder Modulator
Phase Modulator
Laser
$-m(t)$
Bias Tee
$\hat{m}(t)$
DC Bias = $V_\pi/4$

Figure 3.9 Design 3 for optical SSB transmission

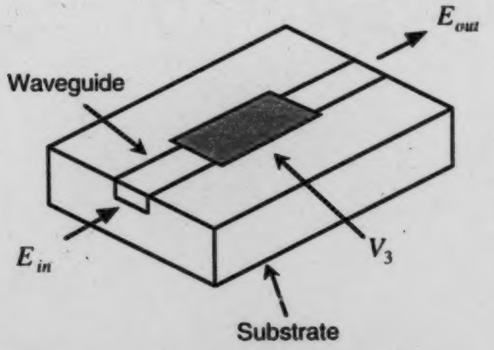
E_{out}
Waveguide
E_{in}
V_3
Substrate

Figure 3.10 Phase modulator

To demonstrate the exact nature of the SSB signals, the mathematical form of each design is derived below.

For all of the designs, the MZ transfer function can be written in a complex form:

$$E_{out} = \frac{E_{in}}{2}\exp\left(j\pi\frac{V_1}{V_\pi}\right) + \frac{E_{in}}{2}\exp\left(j\pi\frac{V_2}{V_\pi}\right) \tag{3.6}$$

where V_π is the modulator's switching voltage and V_1 and V_2 are the driving voltage signals on each arm of the modulator.

The optical electric field of the light entering the modulator is:

$$E_{in} = \exp(j\omega_o t) \tag{3.7}$$

where ω_o is the optical carrier frequency and t is time.

The transfer function in the electric field domain for the PM is simply:

$$E_{out} = E_{in}\exp\left(j\pi\frac{V_3}{V_\pi}\right) \tag{3.8}$$

where V_3 is the applied voltage to the PM arm.

The driving signals for Design 1, the unbalanced drive case, are:

$$V_1 = PV_\pi m(t) \tag{3.9}$$

$$V_2 = PV_\pi \hat{m}(t) + \frac{V_\pi}{2} \tag{3.10}$$

where $m(t)$ is the ac coupled binary data with magnitude of one, $\hat{m}(t)$ is the Hilbert transform of the modulating signal and P is an amplification factor of the modulation signal.

Thus, substituting equations 3.7, 3.9 and 3.10 into equation 3.6 gives:

$$E_{out} = \frac{1}{2}\exp(j\omega_o t)\left[\exp\left(j\pi P(m(t))\right) + \exp\left(j\pi P(\hat{m}(t)) + j\frac{\pi}{2}\right)\right] \tag{3.11}$$

If we let $x = \pi P$ in equation 3.11 and expand into a Taylor Series showing up to the third order we get:

$$E_{out} = \frac{1}{2}\exp\left(j\omega_o t\right)\left[\begin{array}{l}\left(1 + jxm(t) - \frac{1}{2}x^2m^2(t) - j\frac{1}{6}x^3m(t) + \cdots\right) \\ +j\left(1 + jx\hat{m}(t) - \frac{1}{2}x^2\hat{m}(t) - j\frac{1}{6}x^3\hat{m}(t) + \cdots\right)\end{array}\right] \tag{3.12}$$

which can be rearranged in the form:

$$E_{out} = \exp\left(j\omega_o t\right)\left[\begin{array}{l}\left(\frac{1}{2} - \frac{1}{2}x\hat{m}(t) - \frac{1}{4}x^2m^2(t) + \frac{1}{12}x^3\hat{m}^3(t) + \cdots\right) \\ +j\left(\frac{1}{2} + \frac{1}{2}xm(t) - \frac{1}{4}x^2\hat{m}^2(t) - \frac{1}{12}x^3m^3(t) + \cdots\right)\end{array}\right] \tag{3.13}$$

From equation 3.13, it can be seen that the optical electric field is single sideband to the first order for the information signal $m(t)$, however, the carrier is partially in phase with both the information signal $m(t)$ and the Hilbert transform signal $\hat{m}(t)$. Thus, extra carrier C must be added in phase with $m(t)$ to limit the distortion created by $\hat{m}(t)$ after detection.

$$E_{out} = \exp\left(j\omega_o t\right)\left[\begin{array}{l}\left(\frac{1}{2} - \frac{1}{2}x\hat{m}(t) - \frac{1}{4}x^2m^2(t) + \frac{1}{12}x^3\hat{m}^3(t) + \cdots\right) \\ +j\left(C + \frac{1}{2} + \frac{1}{2}xm(t) - \frac{1}{4}x^2\hat{m}^2(t) - \frac{1}{12}x^3m^3(t) + \cdots\right)\end{array}\right] \tag{3.14}$$

If the effects of dispersion are ignored, the square-law detected optical power or the square of the optical electric field is:

$$\begin{aligned}\left|E_{out}^2\right| &= \frac{1}{4} + \frac{1}{4}x^2\hat{m}^2(t) + \left(C + \frac{1}{2}\right)^2 + \frac{1}{4}x^2m^2(t) \\ &-\frac{1}{2}x\hat{m}(t) - \frac{1}{4}x^2m^2(t) + \frac{1}{12}x^3\hat{m}^3(t) + \left(C + \frac{1}{2}\right)xm(t) - \left(C + \frac{1}{2}\right)\frac{1}{2}x^2\hat{m}^2(t) \\ &-\left(C + \frac{1}{2}\right)\frac{1}{6}x^3m^3(t) + \frac{1}{4}x^3\hat{m}(t)m^2(t) - \frac{1}{4}x^3m(t)\hat{m}^2(t) + \cdots\end{aligned} \tag{3.15}$$

which simplifies to:

$$\begin{aligned}\left|E_{out}^2\right| &= \frac{1}{4} + \left(C + \frac{1}{2}\right)^2 + \left(C + \frac{1}{2}\right)xm(t) - \frac{1}{2}x\hat{m}(t) - \frac{C}{2}x^2\hat{m}^2(t) \\ &+\frac{1}{12}x^3\hat{m}^3(t) - \left(C + \frac{1}{2}\right)\frac{1}{6}x^3m^3(t) + \frac{1}{4}x^3\hat{m}(t)m^2(t) - \frac{1}{4}x^3m(t)\hat{m}^2(t) + \cdots\end{aligned} \tag{3.16}$$

From equation 3.16, it can be seen that the information signal $m(t)$ is now recovered from the single sideband format with minimal distortion if x remains less than 1 and C is large with respect to $\frac{1}{2}$.

If dispersion from a nonzero fiber length is to be included in the analysis, the detected signal cannot be represented in a closed time domain form as it is for a fiber length of zero. Since the fiber is a distributed line, it is more easily represented by the frequency domain transfer function shown in equation 2.1. Thus, a fast Fourier transform (FFT) of the input optical electric field is done, the resultant is multiplied by the fiber transfer function , and then the inverse fast Fourier transform (IFFT) of the product is performed to obtain a representation of the optical electric field at the output of the fiber. This new time domain signal can then be square-law detected to obtain the resultant electrical signal. This process is shown in equation form as:

$$E_{out-fiber} = \mathrm{IFFT}(H(\omega,z) * \mathrm{FFT}(E_{in-fiber})) \tag{3.17}$$

$E_{in-fiber}$ would be the same as E_{out} in equation 3.14. The square-law detected signal would then be $\left|E_{out-fiber}\right|^2$.

Considering now Design 2, the driving signals for this balanced drive case are:

$$V_1 = PV_\pi\left(m(t) + \hat{m}(t)\right) - \frac{V_\pi}{4} \tag{3.18}$$

$$V_2 = PV_\pi\left(-m(t) + \hat{m}(t)\right) + \frac{V_\pi}{4} \tag{3.19}$$

Substituting equations 3.8, 3.18 and 3.19 into equation 3.6 gives:

$$E_{out} = \frac{1}{2}\exp(j\omega_o t)\left[\exp\left(j\pi P\left(m(t) + \hat{m}(t)\right) - j\frac{\pi}{4}\right) + \exp\left(j\pi P\left(-m(t) + \hat{m}(t)\right) + j\frac{\pi}{4}\right)\right] \tag{3.20}$$

If we let $x = \pi P$ in equation 3.20 and expand into a Taylor Series showing up to the third order:

$$E_{out}=\frac{1}{2\sqrt{2}}\exp(j\omega_o t)\left[\begin{array}{l}(1-j)\left(\begin{array}{l}1+jx(m(t)+\hat{m}(t))-\frac{1}{2}x^2(m(t)+\hat{m}(t))^2\\-j\frac{1}{6}x^3(m(t)+\hat{m}(t))^3+\cdots\end{array}\right)\\+(1+j)\left(\begin{array}{l}1+jx(-m(t)+\hat{m}(t))-\frac{1}{2}x^2(-m(t)+\hat{m}(t))^2\\-j\frac{1}{6}x^3(-m(t)+\hat{m}(t))^3+\cdots\end{array}\right)\end{array}\right] \tag{3.21}$$

which can be expanded to:

$$E_{out}=\frac{1}{2\sqrt{2}}\exp(j\omega_o t)\left[\begin{array}{l}1+jx(m(t)+\hat{m}(t))-\frac{1}{2}x^2(m(t)+\hat{m}(t))^2-j\frac{1}{6}x^3(m(t)+\hat{m}(t))^3+\cdots\\-j+x(m(t)+\hat{m}(t))+j\frac{1}{2}x^2(m(t)+\hat{m}(t))^2-\frac{1}{6}x^3(m(t)+\hat{m}(t))^3+\cdots\\+1+jx(-m(t)+\hat{m}(t))-\frac{1}{2}x^2(-m(t)+\hat{m}(t))^2-j\frac{1}{6}x^3(-m(t)+\hat{m}(t))^3+\cdots\\+j-x(-m(t)+\hat{m}(t))-j\frac{1}{2}x^2(-m(t)+\hat{m}(t))^2+\frac{1}{6}x^3(-m(t)+\hat{m}(t))^3+\cdots\end{array}\right] \tag{3.22}$$

which simplifies to:

$$E_{out}=\exp(j\omega_o t)\left[\begin{array}{l}\left(\begin{array}{l}\frac{1}{\sqrt{2}}+\frac{1}{\sqrt{2}}xm(t)-\frac{1}{2\sqrt{2}}x^2m^2(t)-\frac{1}{2\sqrt{2}}x^2\hat{m}^2(t)\\-\frac{1}{6\sqrt{2}}x^3m^3(t)-\frac{1}{2\sqrt{2}}x^3\hat{m}^2(t)m(t)+\cdots\end{array}\right)\\+j\left(\begin{array}{l}\frac{1}{\sqrt{2}}x\hat{m}(t)+\frac{1}{\sqrt{2}}x^2m(t)\hat{m}(t)-\frac{1}{6\sqrt{2}}x^3\hat{m}^3(t)\\-\frac{1}{2\sqrt{2}}x^3\hat{m}(t)m^2(t)+\cdots\end{array}\right)\end{array}\right] \tag{3.23}$$

Thus, from equation 3.23, it can be seen that the optical electric field is single sideband to the first order for the information signal $m(t)$ and there is a carrier in phase with $m(t)$ for self-homodyne detection.

If the effects of dispersion are ignored, the detected signal is:

$$\left|E_{out}^2\right| = \frac{1}{2} + \frac{1}{2}x^2m^2(t) + \frac{1}{2}x^2\hat{m}^2(t) - \frac{1}{2}x^2m^2(t) - \frac{1}{2}x^2\hat{m}^2(t) - \frac{1}{6}x^3m^3(t)$$
$$-\frac{1}{2}x^3\hat{m}^2(t)m(t) + xm(t) - \frac{1}{2}x^3m^3(t) - \frac{1}{2}x^3\hat{m}^2(t)m(t) + x^3\hat{m}^2(t)m(t) + \cdots \tag{3.24}$$

Equation 3.24 simplifies to:

$$\left|E_{out}^2\right| = \frac{1}{2} + xm(t) - \frac{2}{3}x^3m^3(t) + \cdots \tag{3.25}$$

From equation 3.25, it can be seen that the information signal $m(t)$ is recovered with minimal distortion if x remains less than 1. Further, the phase modulation from $\hat{m}(t)$ cancels. If the effects of the fiber dispersion are not ignored, the recovered optical power is calculated in the same format as shown in equation 3.17 with the fiber transfer function.

It is interesting to note that for Design 2, at zero fiber length, the second order information terms generated by the MZ modulator in the electric field mixing against the carrier cancel with the second order terms generated by the squaring process of the first order electric field terms. However, if the fiber is anything longer than zero, the fiber transfer function, which acts on the electric field, distorts the phase of the second order components differently such that they no longer cancel in the final detected power.

Design 3, using one MZ modulator and one PM, is mathematically equivalent to Design 2. In Design 2, both arms of the MZ modulator are modulated with $\hat{m}(t)$, thus, this is equivalent to modulating the combined output of the MZ modulator with $\hat{m}(t)$. Design 3 creates the same optical SSB signal using the driving signals:

$$V_1 = PV_\pi m(t) - \frac{V_\pi}{4} \tag{3.26}$$

$$V_2 = -PV_\pi m(t) + \frac{V_\pi}{4} \tag{3.27}$$

$$V_3 = PV_\pi \hat{m}(t) \tag{3.28}$$

where V_1 and V_2 drive the MZ modulator and V_3 drives the PM.

Equation 3.23, which represents the electric field output for Design 2, is equivalent to the electric field for Design 3.

The electric field for both Design 2 and Design 3 can also be written in another form as:

$$E_{out} = \exp(j\omega_o t)\exp(jx\hat{m}(t))\cos\left(xm(t) - \pi/4\right) \tag{3.29}$$

From equation 3.29 it can be seen that the electric field is amplitude modulated and phase modulated. The amplitude modulation is similar to that used for DSB modulation. Thus, phase modulating the optical DSB signal with the Hilbert transform of the information creates an optical SSB signal.

If a more general case is analyzed for Design 2 and 3 where the phase angle between the two arms is allowed to vary, we see that the electric field will remain single sideband if the ratio between $m(t)$ and $\hat{m}(t)$ is no longer restricted to a value of one and is also allowed to vary.

For example, let the driving signals for Design 2 be:

$$V_1 = PV_\pi m(t) + QV_\pi \hat{m}(t) + V_\theta \tag{3.30}$$

$$V_2 = -PV_\pi m(t) + QV_\pi \hat{m}(t) - V_\theta \tag{3.31}$$

where P and Q are independent modulation parameters and V_θ is the dc bias which provides for a phase difference of θ between the two arms.

Substituting equations 3.8, 3.30, 3.31 into equation 3.6 and letting $x = \pi P$ and $y = \pi Q$; the new optical electric field equation can be written as:

$$E_{out} = \exp(j\omega_o t)\exp(jy\hat{m}(t))\cos(xm(t) + \theta) \tag{3.32}$$

Expanding equation 3.32 into a Taylor series gives:

$$\begin{aligned} E_{out} &= \exp(j\omega_o t)\left[1 + jy\hat{m}(t) - y^2\hat{m}^2(t) - jy^3\hat{m}^3(t) + \cdots\right] \\ &\left[\cos(\theta) - x\sin(\theta)m(t) - x^2\frac{\cos(\theta)}{2}m^2(t) + x^3\frac{\sin(\theta)}{6}m^3(t) + \cdots\right] \end{aligned} \tag{3.33}$$

which can be simplified to:

$$E_{out} = \exp(j\omega_o t)\begin{bmatrix} \cos(\theta) - x\sin(\theta)m(t) + jy\cos(\theta)\hat{m}(t) - x^2\dfrac{\cos(\theta)}{2}m^2(t) \\ -x^2\cos(\theta)\hat{m}(t) - jxy\sin(\theta)m(t)\hat{m}(t) - y^2\cos(\theta)\hat{m}^2(t) + \cdots \end{bmatrix} \quad (3.34)$$

From equation 3.34, it can be seen that the signal E_{out} is SSB if the coefficients of the first order $m(t)$ term and the first order $\hat{m}(t)$ term follow a $\tan(\theta)$ ratio as determined by:

$$y = \frac{x\sin(\theta)}{\cos(\theta)} \quad (3.35)$$

The ratio is plotted on a log scale in Figure 3.11. As can be seen, if θ is 45 degrees or $V_\pi/4$, the ratio is one as originally discussed.

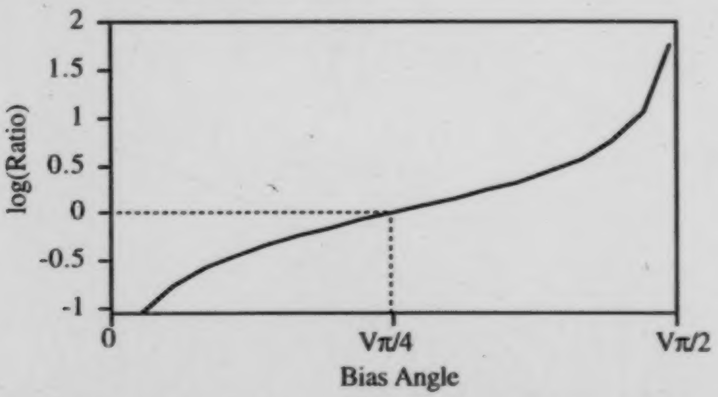

Figure 3.11 Ratio of $\hat{m}(t)$ to $m(t)$ versus bias angle θ

The general dual arm MZ transfer characteristic showing the output electric field and power versus the bias angle θ is plotted in Figure 3.12. In the original derivations, the operating point was always $\theta = V_\pi/4$ with small signal modulation around that point. In Figure 3.12, this bias angle corresponds to the most linear power point. However, the most linear electric field point is at $\theta = V_\pi/2$. However, at $\theta = V_\pi/2$, the optical carrier would be extinguished and would eliminate the capability for self-homodyne detection in Design 2 and 3. In addition, the larger the modulation depth on the MZ modulator, the more distortion that becomes present in the optical SSB signal in the form of unwanted sideband and unequalizable distortion terms generated by the square law detection process. On the other hand, the MZ modulator cannot be driven with too low a modulation depth or else there is too small a difference between light levels for a 0 and a 1 for the purposes of noise immunity. Thus, an optimal condition for bias point and modulation depth should exist which minimizes distortion from both the MZ modulator and the square-law detection process as well as maximizes noise immunity.

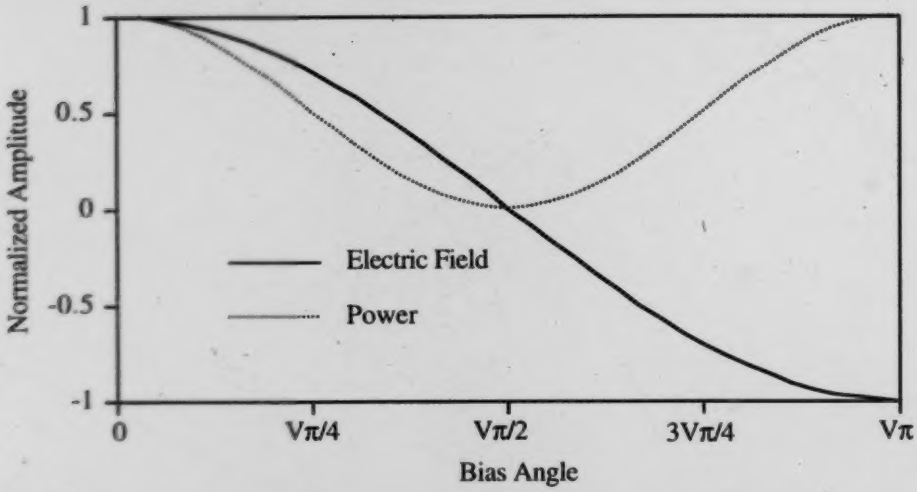

Figure 3.12 Normalized output electric field and power versus bias angle θ for a dual arm MZ modulator

3.4 Hilbert Transforms of Broadband Baseband Signals

Generating an accurate Hilbert transform of a broadband signal such as a baseband 10 Gb/s digital signal is not a trivial task. A method for generating an electrical SSB signal that could be applied to a broadband case was first disclosed by Weaver [59]. In this method, the information signal first simultaneously modulates in-phase and quadrature sinusoids at a carrier frequency f_b. In each of the two resulting branches there is a lowpass filter with cutoff at f_b followed by second respective inphase and quadrature modulation at a higher carrier frequency. This is illustrated in Figure 3.13. The resulting signals in the two branches are combined to form a SSB modulated carrier signal. In Weaver's method, the frequency f_b is equal to 0.5 B which is one half the bandwidth B (10 GHz) required to transmit the information. The carrier frequency applied to the second inphase and quadrature pair of modulators has frequency f_c which is greater than f_b.

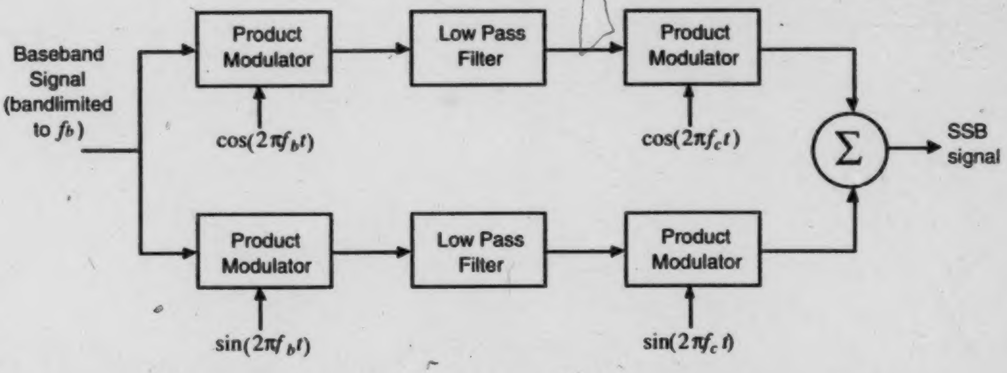
Baseband Signal (bandlimited to f_b)
Product Modulator
Low Pass Filter
Product Modulator
$\cos(2\pi f_b t)$
$\cos(2\pi f_c t)$
Σ
SSB signal
Product Modulator
Low Pass Filter
Product Modulator
$\sin(2\pi f_b t)$
$\sin(2\pi f_c t)$

Figure 3.13 Weaver's method to generate a SSB RF signal (Adapted from [59])

If Weaver's method were to be used to generate a Hilbert transform in one of the previous designs in order to generate an optical SSB signal, some modifications would have to be made. In the modified approach, an optical modulator could be used in place of the second inphase and quadrature carrier frequency modulators disclosed by Weaver. Weaver's method could be implemented in the modified form shown in Figure 3.14.

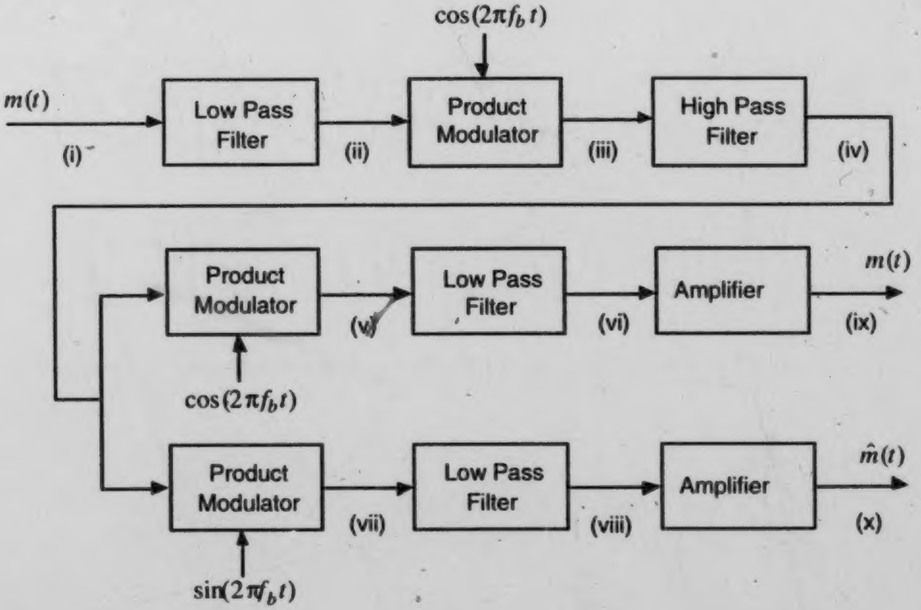
$\cos(2\pi f_b t)$
$m(t)$
(i)
Low Pass Filter
(ii)
Product Modulator
(iii)
High Pass Filter
(iv)
Product Modulator
(v)
Low Pass Filter
(vi)
Amplifier
$m(t)$
(ix)
$\cos(2\pi f_b t)$
Product Modulator
(vii)
Low Pass Filter
(viii)
Amplifier
$\hat{m}(t)$
(x)
$\sin(2\pi f_b t)$

Figure 3.14 Modified Weaver approach used to generate the Hilbert transform of a broadband signal

In order to explain how this design generates the Hilbert transform of the information $m(t)$, we examine the modified Weaver approach in more detail. We will examine each point in the system from a frequency domain prospective in a written and graphical form. To aid in this explanation, the magnitude spectra of the signals at various stages in the system using the Hilbert transform generator shown in Figure 3.14 are shown in Figure 3.15. An arbitrary binary baseband signal is chosen for illustrative purposes.

To start, the input signal $m(t)$ at (i) in Figure 3.14 is first bandlimited to frequencies less than the first null in the power spectral density of the signals which, for binary signals, is at the bit rate. Figure 3.15 (a) represents the original ideal binary baseband signal which corresponds to a perfect nonreturn to zero (NRZ) signal. Figure 3.15 (b) represents the lowpass filtered version of this ideal binary baseband signal. One way to achieve this filtering is to use a third order Butterworth filter with a 3 dB cutoff frequency of 0.65B (6.5 GHz). The baseband information can be represented in the frequency domain as a lower (M_L) and upper (M_U) sideband centered around 0 Hz as shown in Figure 3.15 (b). In the frequency domain, the filtered baseband signal could be written as:

$$M_L + M_U \tag{3.36}$$

Subsequently, in Figure 3.14, the bandlimited signal at point (ii) amplitude modulates, in double sideband form, a cosine carrier whose frequency is equal to bit rate f_b to form the signal at point (iii). Figure 3.16 (c) represents the magnitude spectrum after the modulation by the first carrier. To show how the modulated signal is written, we first show that the Fourier transform of cosine and sine carriers can be represented as:

$$\text{cosine} = \frac{1}{2}\left[\delta(f - f_o) + \delta(f + f_o)\right] \tag{3.37}$$

$$\text{sine} = \frac{1}{2}\left[\delta(f - f_o) - \delta(f + f_o)\right] \tag{3.38}$$

where δ represents a delta function. Thus, since the modulating carrier is at f_b, the resultant signal spectrum can be now be written as:

$$\frac{1}{2}M_L(f + f_b) + \frac{1}{2}M_U(f + f_b) + \frac{1}{2}M_L(f - f_b) + \frac{1}{2}M_U(f - f_b) \tag{3.39}$$

This spectrum is subsequently highpass filtered to leave the upper sideband at point (iv) in Figure 3.14. It is possible to use a lowpass filter in place of the highpass filter at his point; however, there is an implementation advantage to a highpass or a bandpass design at frequencies above 10 GHz since the highpass filter results in a larger gap between wanted and unwanted frequencies at points (v) and (vi) in Figure 3.14 and this reduces the required complexity of the lowpass filters which follow. Figure 3.15 (d) represents the highpass filtered version of Figure 3.15 (c). The better the quality of the highpass filter, the better the cancellation of one sideband. If the filter has unity gain, the filtered modulated signal spectrum can be written as:

$$\frac{1}{2}\mathrm{M_L}(f-f_b)+\frac{1}{2}\mathrm{M_U}(f+f_b) \tag{3.40}$$

Subsequently, in Figure 3.14, the bandlimited signal at point (iv) is split and both signals are amplitude modulated, in double sideband form, by a cosine and sine carrier respectively whose frequencies are again equal to bit rate f_b to form the signals at points (v) and (vii). Figure 3.15 (e) represents the magnitude spectrum after the modulation by either carrier. The difference between the two spectra is now contained in the phase information as shown in the new written representation of each spectrum. The signal at point (v) can be written as:

$$\frac{1}{8}\mathrm{M_U}(f+2f_b)+\frac{1}{8}\mathrm{M_U}+\frac{1}{8}\mathrm{M_L}(f-2f_b)+\frac{1}{8}\mathrm{M_L} \tag{3.41}$$

and the signal at point (vii) can be written as:

$$\frac{1}{8}\mathrm{M_U}(f+2f_b)e^{j\pi/2}+\frac{1}{8}\mathrm{M_U}e^{-j\pi/2}+\frac{1}{8}\mathrm{M_L}(f-2f_b)e^{-j\pi/2}+\frac{1}{8}\mathrm{M_L}e^{j\pi/2} \tag{3.42}$$

After low pass filtering, the signals at point (vi) in Figure 3.14 can be written as:

$$\frac{1}{8}\mathrm{M_L}+\frac{1}{8}\mathrm{M_U} \tag{3.43}$$

and the signal at point (viii) can be written as:

$$\frac{1}{8}\mathrm{M_L}e^{j\pi/2}+\frac{1}{8}\mathrm{M_U}e^{-j\pi/2} \tag{3.44}$$

The spectral representation shown in equation 3.43 matches the original information signal spectrum $m(t)$ and the spectral representation shown in equation 3.44 is the Hilbert transform of the original information.

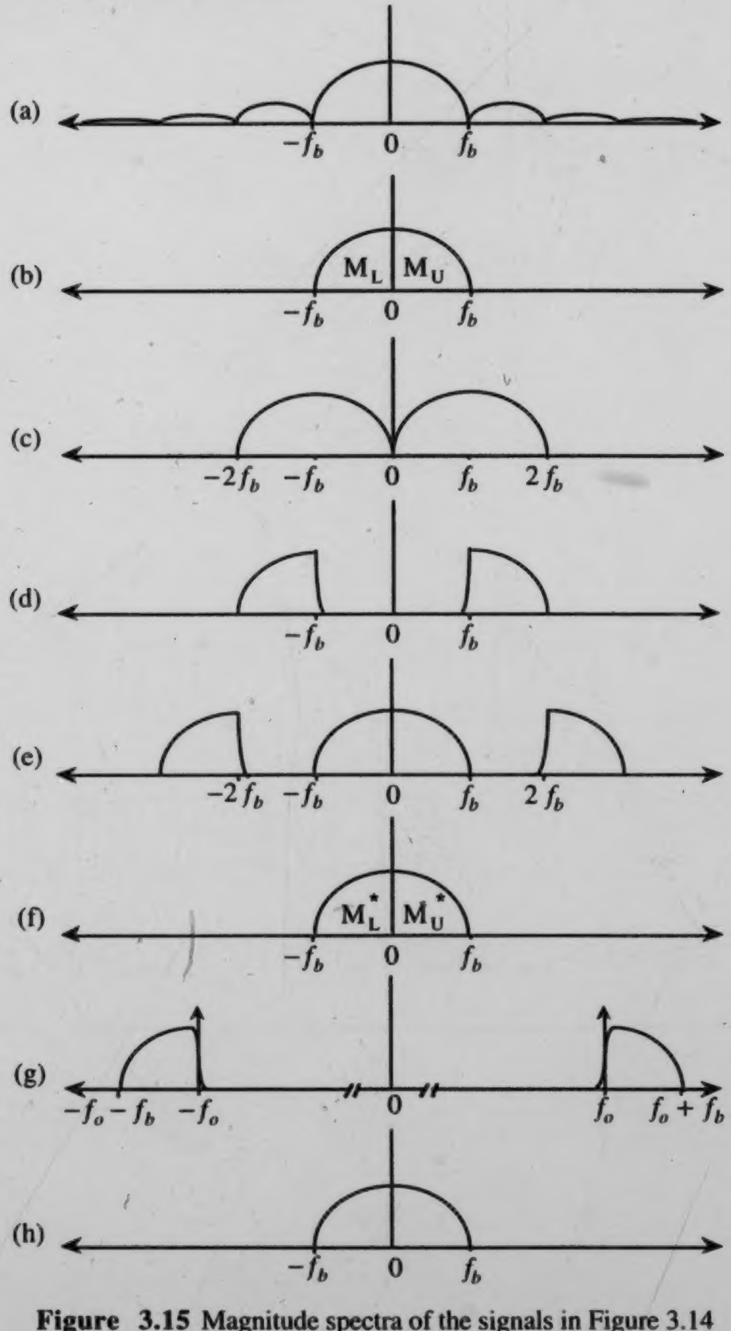
(a)
$-f_b$
0
f_b
(b)
M_L
M_U
$-f_b$
0
f_b
(c)
$-2f_b$
$-f_b$
0
f_b
$2f_b$
(d)
$-f_b$
0
f_b
(e)
$-2f_b$
$-f_b$
0
f_b
$2f_b$
(f)
M_L^*
M_U^*
$-f_b$
0
f_b
(g)
$-f_o-f_b$
$-f_o$
0
f_o
f_o+f_b
(h)
$-f_b$
0
f_b

Figure 3.15 Magnitude spectra of the signals in Figure 3.14

Figure 3.15 (f) shows the new magnitude spectra for either the original information or the Hilbert transform of that information. The difference between these two spectra lies in the phase information. Thus, the upper and lower sidebands now have an asterisk in Figure 3.15 (f) to denote that this magnitude spectral representation can be for both the information and it's Hilbert transform.

After appropriate amplification for driving a MZ modulator, the first inphase modulator and filter has output $m(t)$ at point (ix) and the first quadrature modulator and filter has output $\hat{m}(t)$ at point (x) which is the Hilbert transform of $m(t)$ in Figure 3.14.

Finally, the output of the optical transmitter which results in an optical SSB or VSB signal, depending on the sharpness of the filtering, is shown in Figure 3.15 (g). This is the resultant optical SSB signal. At the receiver, self-homodyne detection by a square-law optical detector results in the recovered baseband spectrum shown in Figure 3.15 (h). Electrical filtering of the received signal should be implemented to limit the noise equivalent bandwidth.

In contrast to Weaver's original method, the modified Weaver design uses lowpass filters and first quadrature modulators operating at f_b equal to B (10 GHz) as opposed to 0.5B as in the original Weaver design. Further, the modified method does not require RF heterodyne detection of the signal at the receiver to bring it down to baseband. This eliminates extra circuitry at the receiver. Finally, the orientation of the final optical SSB spectrum is correct such that self-homodyne detection results in the proper received baseband signal.

In Figure 3.16, an alternate version of the implementation shown in Figure 3.14 is shown. In Figure 3.14, the signals at points (ii) and (ix) are essentially the same so the redundant components can be removed. The original components are still required for the path which generates $\hat{m}(t)$. An important note in this application is that the delay of the signals $m(t)$ and $\hat{m}(t)$ must be properly bit aligned. This is of note in this design especially since circuitry layout is no longer symmetric.

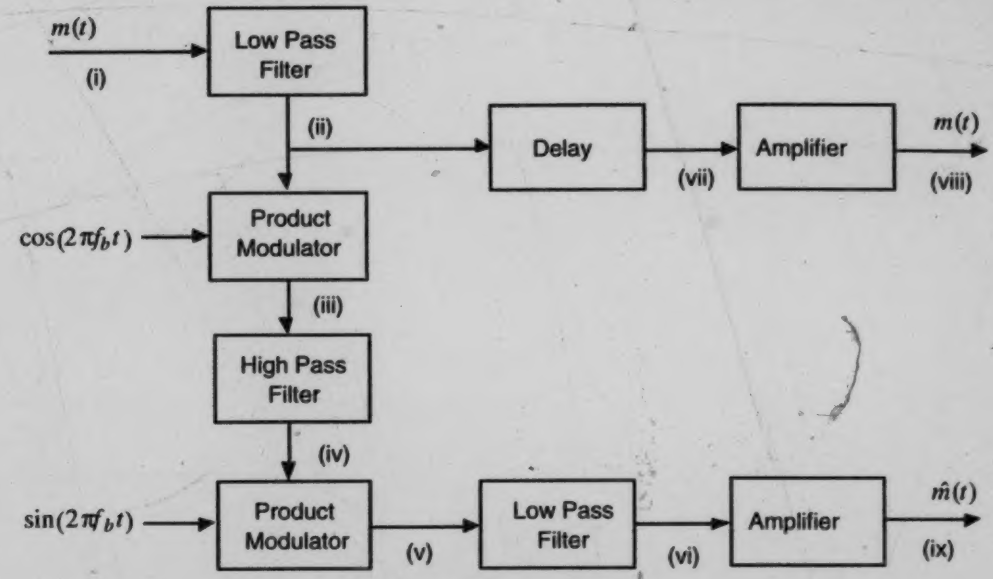
$m(t)$
(i)
Low Pass Filter
(ii)
Delay
(vii)
Amplifier
$m(t)$
(viii)
$\cos(2\pi f_b t)$
Product Modulator
(iii)
High Pass Filter
(iv)
$\sin(2\pi f_b t)$
Product Modulator
(v)
Low Pass Filter
(vi)
Amplifier
$\hat{m}(t)$
(ix)

Figure 3.16 Alternate version of the modified Weaver approach used to generate the Hilbert transform of a broadband signal

In order to generate the combination signals $m(t)+\hat{m}(t)$ and $-m(t)+\hat{m}(t)$ which are required for Design 2, the designs shown in Figure 3.14 and Figure 3.16 can be modified to include the addition of the design shown in Figure 3.17. In both modified designs, each signal $m(t)$ and $\hat{m}(t)$ is split, appropriately amplified and then recombined to form the combination signals.

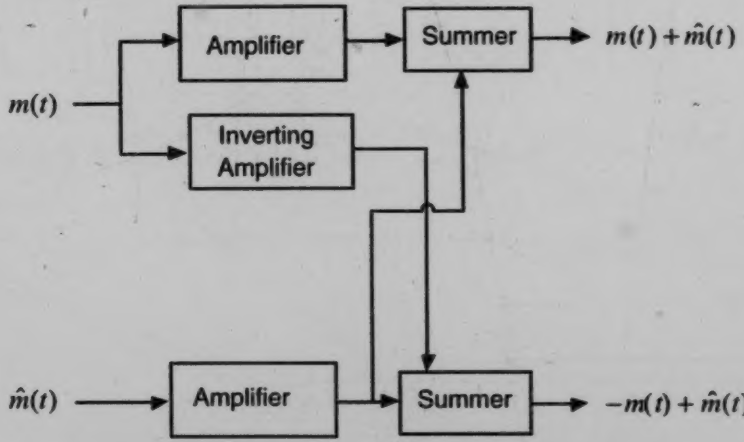
Amplifier
Summer
$m(t)+\hat{m}(t)$
$m(t)$
Inverting Amplifier
$\hat{m}(t)$
Amplifier
Summer
$-m(t)+\hat{m}(t)$

Figure 3.17 Generation of the combination signals

In the third design to generate the Hilbert transform signal, the Hilbert transforming function is carried out by a simple tapped delay filter. An example of a general tapped delay filter is shown in Figure 3.18. This generalized tapped delay approach to modeling a Hilbert transform is presented in [60]. Tapped delay elements serve to take a time derivative of the signal and apply a frequency dependent weighting such that each frequency component has the same amplitude before and after time differentiation. The length of the tapped delay line determines the lowest frequency which will have the output amplitude equal to the input amplitude while the spacing between the taps determines the highest frequency which can be differentiated with respect to time.

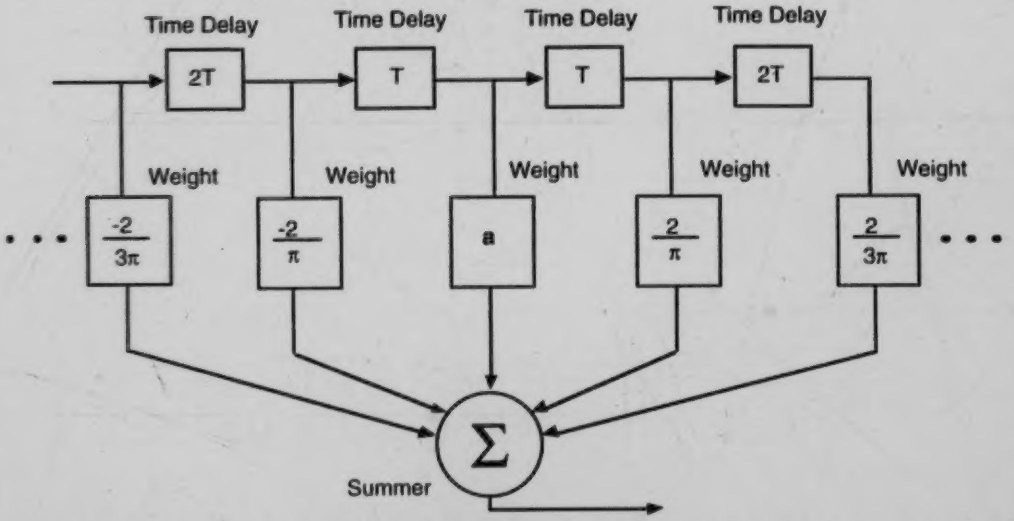

Figure 3.18 Tapped delay approach to generate the Hilbert transform of a broadband signal (Adapted from [60])

This tapped delay approach is derived from determining the time domain impulse response of the Hilbert transform frequency response. Using the frequency domain description of a Hilbert transform shown in Figure 3.2, the impulse response is as [60]:

$$\begin{aligned} h_k &= 2\sin^2(\pi k/2)/\pi n \quad &\text{for} \quad n \neq 0 \\ h_k &= 0 & n = 0 \end{aligned} \tag{3.45}$$

which is shown graphically in Figure 3.19.

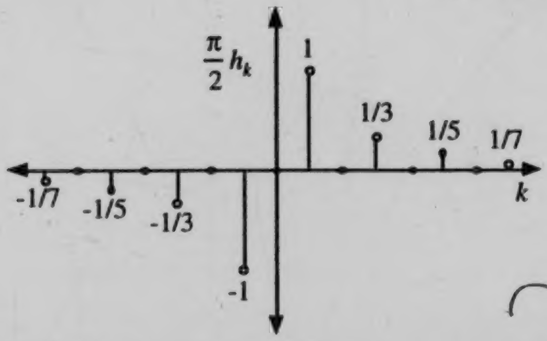

Figure 3.19 Impulse response of the Hilbert transform (Adapted from [60])

In order to generate the proper signals for the optical modulator designs, Design 1 and Design 3, the layout show in Figure 3.20 is used. The signal $m(t)$ is time delayed in order to properly phase align it with the Hilbert signal $\hat{m}(t)$. In Figure 3.20, the Hilbert transform is shown as being created from Tapped Delay Element 1. Tapped Delay Element 1 would employ the tapped delay element shown in Figure 3.18 with coefficient **a** equal to 0. If a filter with four taps were used as an example, a time delay of 3T is required for $m(t)$ in order to properly phase align it with the Hilbert signal $\hat{m}(t)$. The value of T is generally less than one bit period for a digital signal. For example, T can be of the order of 0.4 ns for a 10 Gb/s binary source with a four tap filter.

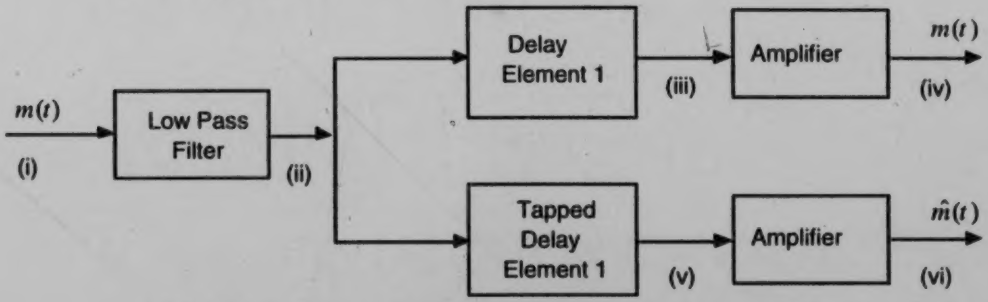

Figure 3.20 Circuit to generate independent driving signals

The magnitude spectrum of the signals at various stages in the system using the Hilbert transform generator shown in Figure 3.20 are shown in Figure 3.21. An arbitrary binary baseband signal is again chosen for illustrative purposes. Figure 3.21 (a) represents the original binary baseband signal while Figure 3.21 (b) represents the lowpass filtered version of Figure 3.21 (a). The output of the optical modulator which results in an optical SSB signal is shown in Figure 3.21 (c). The signal can at times be VSB because since, as will be shown later, using less than an infinite number of taps results in a vestige in the transmitted SSB signal. At the receiver, self-homodyne detection by a square law optical detector results in the recovered baseband spectrum shown in Figure 3.21 (d).

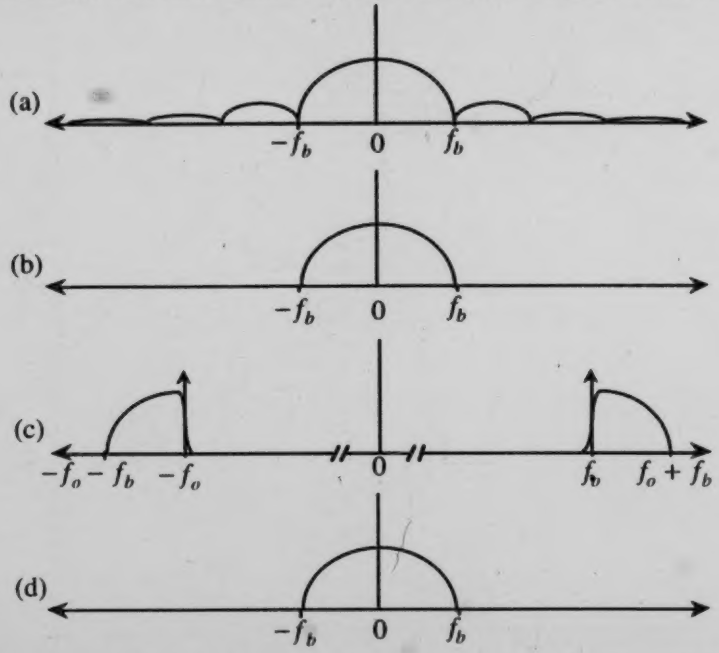

Figure 3.21 Magnitude spectra of signals shown in Figure 3.20

In order to generate the combination modulating signals for Design 2, the layout shown in Figure 3.22 is used. Tapped Delay Element 2 would employ the tapped delay element shown in Figure 3.18 with coefficient **a** equal to 1 thus generating the signal $m(t)+\hat{m}(t)$. Tapped Delay Element 3 would employ the tapped delay element shown in Figure 3.18 with coefficient **a** equal to -1 thus generating the signal $-m(t)+\hat{m}(t)$.

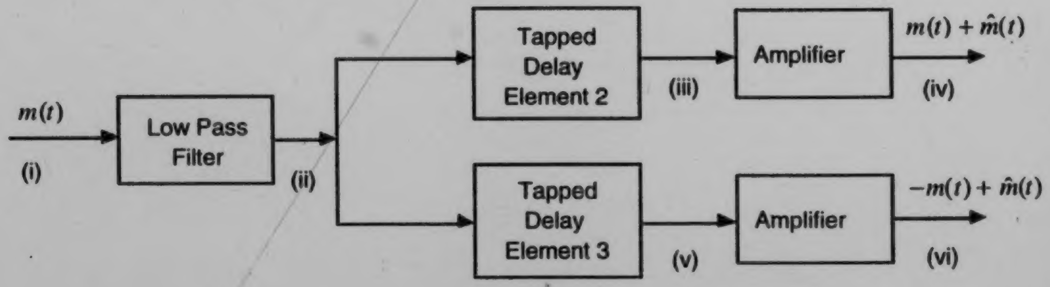
$m(t)$
(i)
Low Pass Filter
(ii)
Tapped Delay Element 2
(iii)
Amplifier
$m(t) + \hat{m}(t)$
(iv)
Tapped Delay Element 3
(v)
Amplifier
$-m(t) + \hat{m}(t)$
(vi)

Figure 3.22 Circuit to generate driving signals for Design 2

Depending on the application and the number of taps, the configuration shown in Figure 3.18 can be created with splitters, delay lines and combiners or each entire filter can be fabricated in microstrip form.

Consequently, optical SSB for 10 Gb/s can be created by using any of the three optical modulator designs, Design 1, 2 or 3, in conjunction with any of the three methods to generate the Hilbert transform of the baseband digital signal. All of the optical signals generated would be converted to electrical baseband signals in an optical receiver using the general design shown in Figure 3.23. The received optical signal would be detected by a simple photodetector employing the common square-law detection operation. The subsequent electrical signal is filtered to reduce the noise equivalent bandwidth and equalized to restore the phase information of the transmitted electrical signal. The equalization can be performed with a microstrip equalizer or other types of equalizers which have the inverse nonlinear phase characteristic of the fiber used for transmission. Electrical amplifiers are added in the receiver where appropriate to restore the amplitude of the data signal before entering a decision circuit.

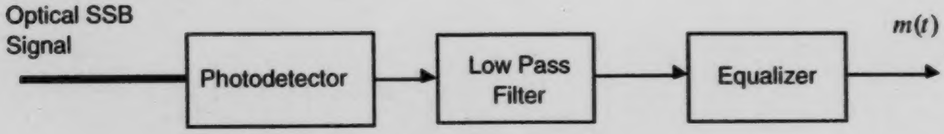

Figure 3.23 Circuit to detect optical SSB signal

3.5 Comparison of Optical Single Sideband and Composite Single Sideband Techniques

One reason that the resultant optical signal in the previous designs is not necessarily a pure optical SSB signal in the strict sense but is an optical VSB is due to the imperfect Hilbert transform generated by a tapped delay line with a limited number of taps or the modified Weaver approach using filters without infinitely steep roll-off characteristics. For example, using a tapped delay filter with a small number of taps results in only partial cancellation of one sideband. It has also been shown that this is not the only cause of imperfect sideband generation. As outlined by Powers [45], hybrid modulation, analogous to the designs previously presented, consisting of amplitude and phase modulation, in the best case, results in a good VSB signal. Pure SSB can only be achieved in a hybrid approach if complicated signal processing is performed on the information signals before they modulate the light. However, the system is still useful in combating chromatic dispersion if the vestige is kept relatively small compared to the transmitted sideband. The frequencies subjected to the most dispersion are the ones furthest away from the carrier and not the ones close to the carrier lying within the vestige. If a good approximation to the Hilbert transform is generated, a small vestige can be achieved. For our purposes, this is sufficient and the system can be called a single sideband one in the general sense since it provides the benefits of one. Further, as will be shown later, the vestige is not the largest inhibitor of successful experimental implementation.

For the purpose of completeness, perfect SSB generation is still examined in this context. Examining the electric field of the transmitted signal for Designs 2 and 3 in equation 3.23, it can be seen that even if a perfect Hilbert transform signal $\hat{m}(t)$ is generated from $m(t)$, the resultant electric field is not purely SSB because there are higher order terms from $m(t)$ and $\hat{m}(t)$. Part of this is due to the nonlinear transfer function of the MZ modulator. The nonlinearity from the MZ modulator transfer is partially limited by reducing the amplitude of the driving signals so as to approximate a linear transfer function, however, they are not completely eliminated. A second limitation of self-homodyne detecting a SSB signal is the distortion introduced by the squaring effect on the information. A type of autocorrelation term exists from the information signal beating against itself upon square-law detection. The nonlinearity created by the square-law detection process on the data is an unavoidable hazard since a pure SSB signal still has to be square-law detected at the receiver. To try and overcome this difficulty, Powers [45] developed a SSB method for RF signals which is called Composite Single Sideband (CSSB). According to Powers, the complex envelope of the transmitted signal which best approximated a SSB signal and was recovered with minimal distortion through square-law detection was of the form:

$$E(t) = a(t)\cos\left(\omega_c t + k_p \overline{\overline{\ln(a(t))}}\right) \tag{3.46}$$

where $\overline{\overline{\ln(a(t))}}$ is the Hilbert transform of the natural log of $a(t)$. In this case, $a(t) = \sqrt{m(t)}$ where $m(t)$ is the information.

As was previously shown, the electric field for Designs 2 and 3 could be written as:

$$E_{out} = \exp(j\omega_o t)\exp(jx\hat{m}(t))\cos(xm(t)-\theta) \tag{3.47}$$

Comparing equation 3.47 with equation 3.46, we see that they are similar in nature since the amplitude terms are $\cos(xm(t)-\theta)$ and $a(t)$ respectively and the phase modulating terms are $x\hat{m}(t)$ and $k_p\ln(a(t))$ respectively.

The designs are similar since there is a type of amplitude modulation by the information and a type of phase modulation involving the Hilbert transform of that information. However, they are obviously not exactly the same. Design 3 could be modified to be a CSSB system if the output of the amplitude modulated signal were used in the phase modulation process. An example of how Design 3 could be modified to become CSSB is shown in Figure 3.24.

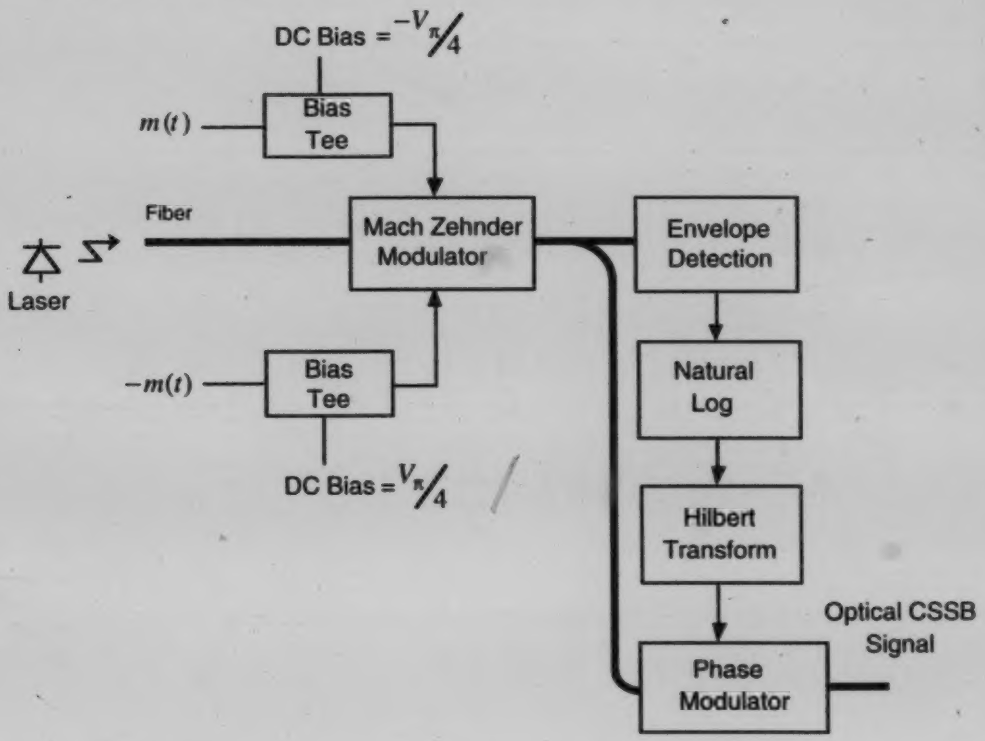
DC Bias = $-V_\pi/4$
$m(t)$
Bias Tee
Fiber
Laser
Mach Zehnder Modulator
Envelope Detection
$-m(t)$
Bias Tee
DC Bias = $V_\pi/4$
Natural Log
Hilbert Transform
Optical CSSB Signal
Phase Modulator

Figure 3.24 Design for optical CSSB transmission

Theoretically, in order to make a CSSB modulator, the envelope of the electric field created by the MZ modulator must be detected, the natural log of it taken and then a perfect Hilbert transform of it must be created so that the resultant electrical signal can modulate the PM. This would provide a CSSB signal where $\cos(xm(t)-\theta)$ represented the square root of the information. This would mathematically create a perfect optical SSB signal.

In a 10 Gb/s digital system, it is a detailed and complex task to obtain the Hilbert transform of the baseband signal. Thus, it is even more complicated to obtain the Hilbert transform of the natural log of the baseband signal. If the baseband signal $m(t)$ were an analog signal, this would be impossible with existing technology. Further, detecting the magnitude of the electric field out of the MZ modulator is practically hard to do. However, if we make the assumption that $m(t)$ is strictly digital with only two levels and eliminate the detection of the magnitude of the electric field, a comparison can be made.

Consider the case where digital values of $m(t)=\pm 0.5$ and $x=0.2\pi$ in equation 3.47. This value for x was determined in simulation to be the optimal drive condition for the SSB system. Thus, the magnitude of the amplitude of equation 3.47 is evaluated at 0.89 for $m(t)=+0.5$ and 0.45 for $m(t)=-0.5$. The measured value after square law detection is 0.79 for $m(t)=+0.5$ and 0.21 for $m(t)=-0.5$. For these values, the phase term of equation 3.47 gives an equivalent k_p value of 0.2π or 0.63.

Based on Powers derivation, for an $a(t)$ value of 0.89 and 0.45, the natural log of $a(t)$ is -0.11 and -0.79 which is a difference of 0.68. Thus, according to Powers, the value of k_p in equation 3.46 should be 0.68 instead of 0.63.

The difference between Powers value and the optimal value found in simulation is small showing that the existing system by nature of the digital information is close to approximating Powers CSSB design without actually performing the natural log of the baseband signal. This small difference is likely accountable by the fact that the baseband signal is bandlimited and thus is not strictly two level and still is analog in the precise sense. A drawback of this approximation is that the signal $\hat{m}(t)$ used to modulate the PM is not the Hilbert transform of the amplitude signal that modulates the optical carrier out of the MZ modulator, it is the Hilbert transform of the electrical signal into the MZ modulator.

This difference is subtle but essential since the best CSSB signal is created when the output of the MZ modulator is used.

3.6 Optical Single Sideband and Duobinary Signaling

As was previously mentioned in Chapter 2, one method for limiting the effects of chromatic dispersion is to reduce the effective transmission bandwidth required to transmit a given data rate. As has already been found, transmitting the digital information in a duobinary form reduces the effective transmission bandwidth from B for conventional binary transmission to B/2 for duobinary transmission.

Converting a binary signal into a duobinary signal changes the two level signal into a three level signal where a 0 is transmitted as no pulse and a 1 is transmitted by a pulse p(t) or -p(t), depending upon the polarity of the previous pulse and the number of 0's between them.

Implementing a duobinary signaling scheme in SSB is possible if the bias point for the MZ modulator is chosen such that the integrity of the three level signal is maintained through to the receiver. In this manner, the three level signal would still have to be decoded at the receiver. Examining equation 3.47, $m(t)$ would represent the three level signal in this case.

With this implementation, the benefits of reducing the transmission bandwidth are gained from both the coding format and the SSB nature of the optical electric field. However, because $m(t)$ is now three level and the amplification x of $m(t)$ in equation 3.29 must be small (less than 1) in order to maintain good sideband cancellation in the signal and limit distortion upon detection, the optical extinction between levels degrades from small for the binary case to extremely small for the three level case. Thus, the duobinary signaling in the SSB form becomes extremely susceptible to noise.

One way to overcome the problem of detecting three optical power levels is to transmit three levels at the electric field level, but bias the MZ modulator such that only two optical power levels are detected. In this manner, a zero is still transmitted and received as no pulse, but a 1 is transmitted as a 1 or -1 at the electric field level but received only as a 1 at the power level. The polarity of a 1 is determined by a precoding formula. This format, called AM-PSK duobinary was effectively demonstrated by Price *et al.* [61]-[62]. In this format, the optical extinction between a 1 and a 0 could be increased because only two levels are being detected.

What makes this method effective is that even though the optical power spectrum has bandwidth B, the optical electric field spectrum, which the chromatic dispersion effect acts on, has only bandwidth B/2. Thus, the effects on chromatic dispersion have been reduced over the conventional binary DSB case.

The question then arises, can AM-PSK duobinary which provides partial improvements in dispersed systems be implemented in a SSB form like regular duobinary to obtain even more improvements? The answer is no.

As previously shown, the optical electric field for Design 2 and 3 can be written as:

$$E_{out} = \exp(j\omega_o t)\exp(jy\hat{m}(t))\cos(xm(t)+\theta) \tag{3.48}$$

Assuming that $m(t)$ is a three level signal, the detected optical power $|E_{out}|^2$ can be made two level if θ is chosen to be $\frac{\pi}{2}$ and the mid signal level is still 0. This the basic concept used in AM-PSK duobinary transmission.

Now, what value of y in equation 3.48 is required to make the AM-PSK duobinary system SSB? As previously shown, the ratio of the signal and Hilbert terms follows the $\tan(\theta)$ function which, under the AM-PSK bias conditions gives:

$$y = x\tan\left(\frac{\pi}{2}\right) = \infty \tag{3.49}$$

From equation 3.49, it can be seen that there is no realistic coefficient for the Hilbert signal $\hat{m}(t)$ to make the AM-PSK duobinary signal SSB. The benefits of SSB and AM-PSK duobinary are mutually exclusive in a self-homodyne detection system.

4. SIMULATION OF DIGITAL OPTICAL SINGLE SIDEBAND SYSTEMS

4.1 Simulated System Models and Parameters

In order to demonstrate the capability of the three designs previously presented, the designs were modeled and simulated and their system performance was characterized. The system performance was measured in a number of ways including received bit error rate (BER) for varying transmitted and received optical powers. These measures of performance provided information on design issues and system parameters.

Designs 1 through 3, described in detail in Chapter 3, were simulated using the optical system shown in Figure 4.1. Figure 4.2 (a) shows the simulated modulator configurations for Designs 1 and 2 while the modulator configuration used for Design 3 is shown in Figure 4.2 (b).

Two different types of simulations of the optical system were used. These are classified as ideal and detailed. In the ideal simulations, all of the optical system components were modeled through mathematical equations derived from the characteristic operation of each component. These simulation results are shown here in Chapter 4. Detailed simulations used measured frequency responses of the experimental system components. These frequency responses were measured with a network analyzer. Measured EDFA parameters were also added to the simulation. These simulations aided in the analysis of the experimentally measured results. Detailed simulation results are shown later in Chapter 5 where they are useful in understanding experimental phenomenon.

As previously mentioned, Designs 2 and 3 are mathematically equivalent in terms of the optical SSB signal created at the transmitter. Thus, with regards to the ideal simulations, provided that the optical path after each transmitter is the same, there is no difference in the received results. Consequently, although both Design 2 and Design 3 were simulated, only one set of results needs to be presented. These results are labeled in Chapter 4 as Design 2 but are applicable to Design 3 as well.

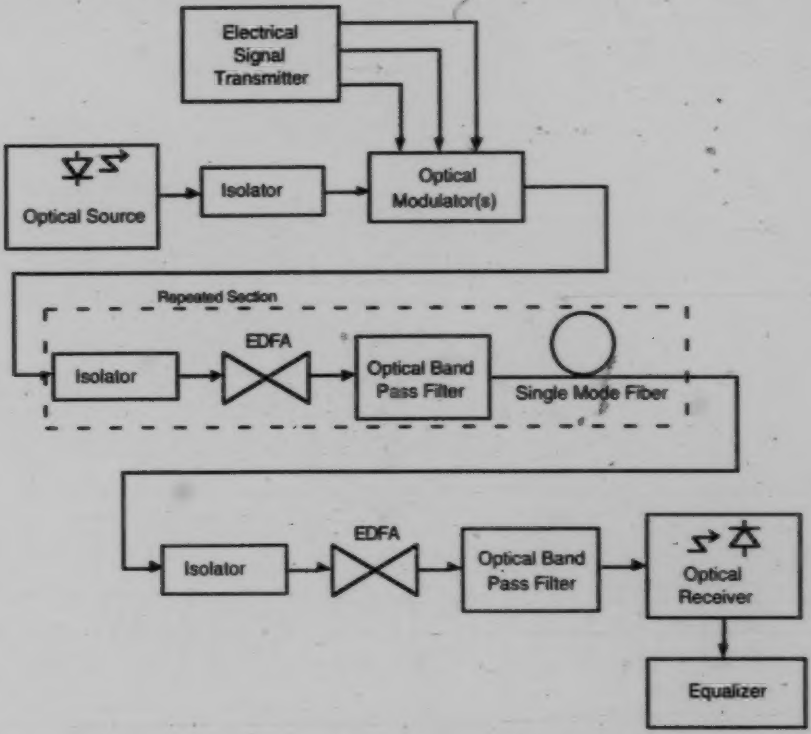
Electrical Signal Transmitter
Optical Source
Isolator
Optical Modulator(s)
Repeated Section
Isolator
EDFA
Optical Band Pass Filter
Single Mode Fiber
Isolator
EDFA
Optical Band Pass Filter
Optical Receiver
Equalizer

Figure 4.1 Block diagram of the simulated optical SSB system

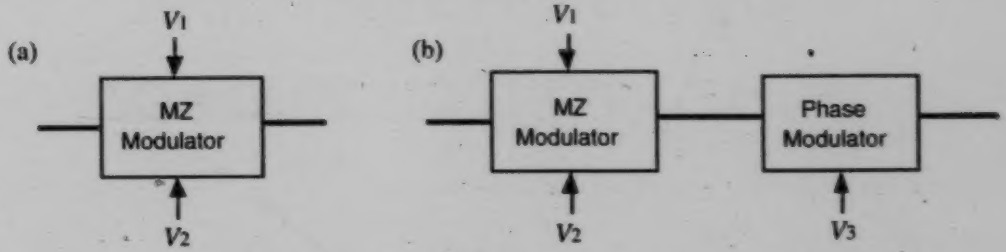
(a)
V_1
MZ Modulator
V_2
(b)
V_1
MZ Modulator
Phase Modulator
V_2
V_3

Figure 4.2 Optical modulator configurations for (a) Design 1 and Design 2 and (b) Design 3

Describing the system in Figure 4.1 on a general level, the optical source consisted of a single mode laser which provided the continuous wave light. It was a narrow linewidth laser biased with a dc current such that the laser was providing light created primarily by stimulated emission. The central wavelength of the laser was constant and was assumed not to vary. The information was modulated onto the optical carrier by driving the external drive modulator(s) with signals from the electrical signal transmitter. The electrical signals consisted of the appropriately amplified and combined versions of $m(t)$ and $\hat{m}(t)$. The MZ modulator was a dual arm drive one with independently accessible arms as shown in Figure 2.11. The PM was as shown in Figure 3.10. Repeated optical amplifiers and single mode fiber links covered the distance. Each optical amplifier was comprised of an isolator, an EDFA, and a band pass filter (BPF). The isolator eliminated Rayleigh backscattered noise that would result if amplified spontaneous emission (ASE) from the EDFA were allowed to migrate in the direction of the transmitter. The BPF reduced the amount of broadband ASE transmitted on to the following EDFA. The fiber was standard single mode fiber with its attenuation minimum near 1.55 μm and its dispersion minimum near 1.3 μm. Detection was carried out at the receiver with a photodiode. As previously mentioned, this type of detector measured the square of the optical electric field so it is often called a square-law detector. The photodiode converted the received optical power into a photocurrent related to the responsivity R.

More specifically, the input signal to the system was an ideal NRZ binary sequence which was pulse shaped at the transmitter with a 3rd order Butterworth low pass filter (LPF) with a cutoff frequency at 0.65B where B is the bit rate (10 Gb/s).

The Hilbert transform signal $\hat{m}(t)$ used in the simulations was created by the tapped delay element shown in Figure 3.18. This tapped delay element was assembled from resistive splitters, attenuators, delay lines and power combiners all assumed to operate ideally (*i.e.* flat magnitude response and linear phase delay when plotted versus frequency). For the simulations, the total number of taps was truncated to a finite number since it was impossible to build a filter with an infinite number of taps. This is what is required if a perfect Hilbert transform was to be obtained from a tapped delay filter. Initial simulations truncated the number of taps to four, however, other configurations were examined. The weight of coefficient **a** in Figure 3.18 was 1 and -1 in order to generate the signals $m(t)+\hat{m}(t)$ and $-m(t)+\hat{m}(t)$ for Design 2 and 0 in order to generate the signal $\hat{m}(t)$ for Design 1 and 3.

At the transmitter, the laser source was modeled as a continuous wave device with single mode operation. The wavelength of the simulated laser was set to 1.55 μm with a relative intensity noise (RIN) value of -155 dB/Hz. Initially, the linewidth of the laser was set to 0 Hz, but was increased to realistic values in later simulations.

The external modulator was modeled as a optical Mach-Zehnder modulator. The transfer function in the electric-field domain for the external modulators was based on a modified version of equation 3.6. The new transfer function for the external modulator used in the simulations is shown in equation 4.1. It is similar to equation 3.6 except for the addition of a correction factor for the optical extinction ratio [63]. The optical extinction ratio for the external modulator was set to 30 dB in the simulations.

$$E_{out} = \frac{E_{in}}{2}\exp\left(j\pi\frac{V_1}{V_\pi}\right) + \frac{E_{in}}{2}\exp\left(j\pi\frac{V_2}{V_\pi}\right) - \frac{E_{in}}{2}(1-A)\exp\left(\frac{j\pi V_2}{V_\pi}\right) \tag{4.1}$$

where:

$$A = \frac{1-2\sqrt{\chi(1-\chi)}}{1-2\chi} \tag{4.2}$$

where:

$$\chi = \frac{1}{1+10^{\frac{ER}{10}}} \tag{4.3}$$

where *ER* is the specified extinction ratio in dB.

In equation 4.1, the correction term includes the drive voltage V_2. This value is used in the correction term because it is assumed that arm two has an electric field amplitude differing by a factor of A with arm one. In other words, there is a nonideal split of light into the two arms such that there is more light in arm one than arm two. If this assumption is reversed so that the electric field amplitude in arm one is smaller than in arm two, then a value of V_1 would be used in equation 4.1 instead. In a real MZ, equal division of light into the two arms is unlikely and it is hard to predict which arm will receive more light. Either way, an unequal split of light will result in an imperfect extinction ratio regardless of the drive signals used.

The PM was also modeled with a transfer function in the electric field domain as shown in equation 3.8.

The single-mode fiber was modeled as a bandpass filter with flat amplitude response and a nonlinear phase response. Based on derivations in [64], a low-pass equivalent model for the single-mode fiber transfer function was used:

$$H(f) = \exp\left[\frac{j\pi DL\lambda^2 f^2}{c}\right] \tag{4.4}$$

where D is the fiber dispersion factor, L is the fiber length, λ is the operating wavelength, f is the low-pass equivalent frequency and c is the group velocity in the fiber. This transfer function is representative of the third term shown in equation 2.2. This transfer function does not include any fiber nonlinearities outside of the effect of chromatic dispersion and only the effects of first order group velocity dispersion are modeled since the higher order effects are negligible at the 1.55 μm wavelength. The dispersion coefficient D was set to 17 ps/km·nm which corresponded to the value for standard single mode fiber with a zero dispersion minimum near 1.3 μm. Again, it is important to note that this transfer function operates on the electric field of the light and not the optical power.

Each optical amplifier in the system model consisted of an isolator, an EDFA and an optical BPF. The isolator was modeled as an ideal unidirectional device and thus the effects of Rayleigh backscattered ASE noise were primarily eliminated. Isolators do not have an infinite isolation so there can be a small amount of backreflected noise but it was negligible with the isolators that will be used. The optical BPF was modeled as an ideal rectangular bandpass characteristic centered at the signal wavelength. The optical bandwidth of the simulated optical BPF was approximately 1.28 nm for all of the simulations. This number was a result of the method by which the noise model for the optical system was derived and implemented in software. The method, which will be described in more detail later on, was based on a theory developed by Cartledge [65]. In all cases, within the simulations, each bit in the 10 Gb/s stream was sampled 16 times. This corresponded to a 160 GHz sampling frequency. This bandwidth was the noise equivalent bandwidth of each BPF according to the noise theory. This bandwidth translated to wavelength at 1.55 μm gave 1.28 nm.

The EDFA was modeled as a system block with a single optical input and a single optical output with a gain between the input and the output defined by the following transcendental equation [66]:

$$G = G_o \exp\left[(1-G)\frac{P_{IN}}{P_{SAT}}\right] \tag{4.5}$$

where G is the internal gain of the EDFA, G_o is the small signal gain of the EDFA, P_{SAT} is the saturation power of the EDFA and P_{IN} is the power of the optical signal at the input of the EDFA. P_{SAT} is defined as the output power when the gain is reduced by a factor of 1/e or approximately 4.3 dB. The value G in equation 4.5 is evaluated in linear units, however, the variables are commonly referred to in dB units. The spontaneous emission noise factor N_{SP} was set to 2 for all of the EDFAs used in the ideal simulations. Further, each optical amplifier was considered to have a 4 dB loss due in part to the insertion loss of the isolator and the bandpass filter and due in part to the input and output coupling efficiencies of the EDFA.

The optical receiver was modeled as an ideal square-law detector, LPF and equalizer. In the detector, the received optical power is linearly converted to a current with a value of responsivity or photodiode quantum efficiency R equal to 0.8 Amp/Watt. The received optical power is the square magnitude of the received optical electric field. Thus, if the electric field is E, the received photocurrent i, can be written as:

$$i = R\left|E^2\right| \tag{4.6}$$

The baseband receiver shaping filter following the detector was a simple 3rd order Butterworth LPF with cutoff frequency at 0.65B.

The electrical equalizer following the receiver filter was modeled with two different methods. In the ideal simulation, the equalizer was represented as the inverse phase function of the fiber. Thus, if the transfer function at the optical electric field level representing the chromatic dispersion is as in equation 4.4, the equalizer transfer function at the electrical level in the frequency domain is represented as:

$$H_{if}(f) = \exp\left[\frac{-j\pi D L \lambda^2 f^2}{c}\right] \tag{4.7}$$

In the a more detailed simulation, the equalizer was modeled as a microstrip delay line which approximates equation 4.7. The microstrip was a transmission waveguide where the dispersion characteristics of the microstrip were used to reverse the effects of the optical fiber. For each distance of fiber, a corresponding length of microstrip was chosen to compensate the dispersion effects.

Modeling the microstrip was a much more complex process than simply letting the equalizer have an inverse phase function of the fiber. In modeling the microstrip line as an equalizer, the transfer function of the microstrip line is written as [67]:

$$H_{ms}(f) = \exp(-j\theta(f)) \tag{4.8}$$

where:

$$\theta(f) = \frac{l_m 2\pi f}{c}\sqrt{\varepsilon_{r\_eff}(f)} \tag{4.9}$$

where f is the frequency, c is the speed of light, l_m is the length of the microstrip and $\varepsilon_{r\_eff}(f)$ is the frequency dependent effective relative permitivity which is representative of the dispersive properties of the microstrip. The value of $\varepsilon_{r\_eff}(f)$ is modeled using the model presented by Hammerstad and Jensen [68]. The equations used to determine the dependence of ε_{r_eff} on frequency are as follows:

$$\varepsilon_{r\_eff} = \varepsilon_r - \frac{\varepsilon_r - \varepsilon_e}{1 + G\left(f/f_p\right)^2} \tag{4.10}$$

where:

$$G = \frac{\pi^2}{12}\frac{(\varepsilon_r - 1)}{\varepsilon_e}\sqrt{\frac{2\pi Z_o}{\eta_o}} \tag{4.11}$$

$$f_p = \frac{Z_o}{2\mu_o h} \tag{4.12}$$

$$\varepsilon_e = \frac{\varepsilon_r + 1}{2} + \frac{\varepsilon_r - 1}{2}\left(1 + \frac{10}{u}\right)^{-ab} \tag{4.13}$$

where:

$$a = 1 + \frac{1}{49}\ln\left(\frac{u^4 + \left(u/52\right)^2}{u^4 + 0.432}\right) + \frac{1}{18.7}\ln\left(1 + \left(\frac{u}{18.1}\right)^3\right) \tag{4.14}$$

$$b = 0.564\left(\frac{\varepsilon_r - 0.9}{\varepsilon_r + 3}\right)^{0.053} \tag{4.15}$$

where:

$$u = \frac{w}{h} \tag{4.16}$$

$$Z_o = \frac{\eta_o}{2\pi}\ln\left(\frac{f_u}{u} + \sqrt{1 + \left(\frac{2}{u}\right)^2}\right) \tag{4.17}$$

where:

$$f_u = 6 + (2\pi - 6)\exp\left(-\left(\frac{30.666}{u}\right)^{0.7528}\right) \tag{4.18}$$

$$\eta_o = \frac{376.73}{\sqrt{\varepsilon_e}} \tag{4.19}$$

For the values of relative permitivity of the substrate ε_r=10.2, substrate height h=1 mm and a microstrip width w= 1 mm, the value of ε_{r_eff} versus frequency is shown in Figure 4.3. The width is chosen so that the characteristic impedance of the microstrip is 50 ohms. This is beneficial when the microstrip must be connectorized and used in an experimental system where the line impedance of all of the components is 50 ohms.

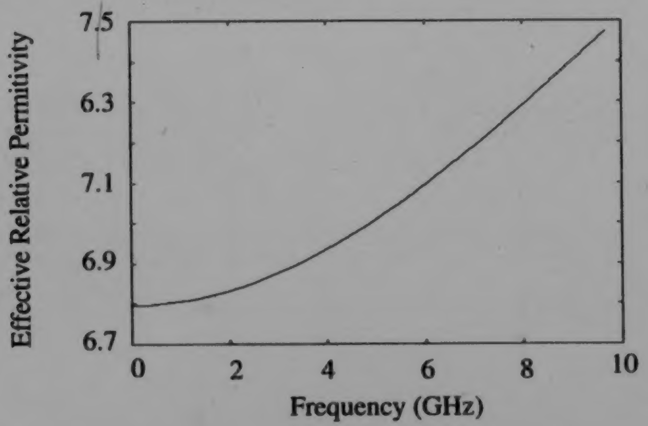

Figure 4.3 Effective relative permitivity versus frequency for a microstrip design with ε_r=10.2, h=1 mm and w= 1 mm

The frequency dependence of the effective relative permitivity of the substrate was the factor which was exploited for the purposes of reversing the effects of chromatic dispersion in the fiber. The frequency dependence causes a phase response in the microstrip which is the approximate inverse of the fiber, provided that the optical USB is transmitted. The dependence of transmitted sideband is shown in Figure 4.4. If the USB is transmitted, upon square law detection, the phase delay incurred by the fiber can be corrected by the microstrip as shown in Figure 4.4 (a). If the LSB is transmitted, the phase information incurred by the fiber on the baseband signal is reversed and is in the same orientation as that incurred by the microstrip. This is shown in Figure 4.4 (b). Thus, the phase delay incurred by the microstrip would double the phase delay incurred by the fiber rather than reduce it to approximately zero.

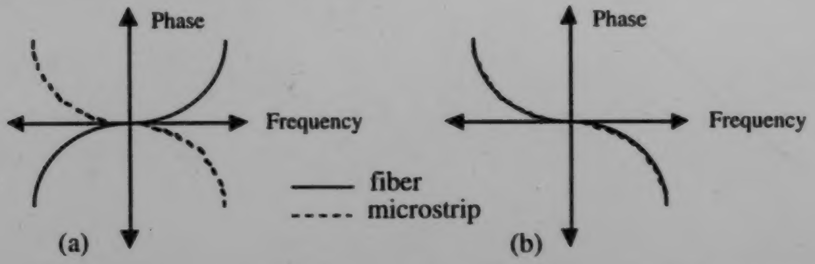

Figure 4.4 Second order phase response of fiber and microstrip for (a) USB and (b) LSB optical transmission

To determine the length of the microstrip needed to equalize a given length of fiber, the propagation constant of the microstrip was analyzed. The propagation constant for the microstrip in units of radians/meter is:

$$\beta(f) = \frac{2\pi f}{c}\sqrt{\varepsilon_{r\_eff}(f)} \tag{4.20}$$

Equation 4.20 assumes the permitivity dominates the frequency dependent effects while the effects from frequency dependent magnetic susceptibility are negligible.

The second order derivative of the propagation constant with respect to frequency $\frac{d^2\beta}{df^2}$ can be determined. Using the effective relative permitivity plot in Figure 4.3, the second derivative versus frequency as defined by equation 4.20 is shown in Figure 4.5.

Utilizing Figure 4.5, the length of the microstrip used for fiber chromatic dispersion equalization can be chosen such that the following equation is satisfied:

$$l_m \frac{d^2\beta}{df^2} + L_f D_1 = 0 \tag{4.21}$$

where D_1 has units of per meter and is a modified version of the previous dispersion coefficient D represented as:

$$D_1 = \frac{\lambda_o^2}{2\pi c} D \tag{4.22}$$

where L_f is the length of the fiber, λ_o is the optical wavelength (1.55 μm), c is the speed of light and D is the dispersion coefficient (17 ps/km·nm).

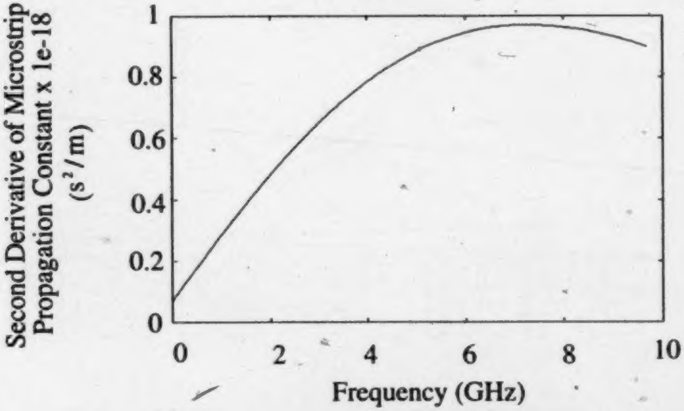

Figure 4.5 Second derivative of microstrip propagation constant versus frequency for a microstrip design with ε_r=10.2, h=1 mm and $w\approx$ 1 mm

As can be seen from Figure 4.5, the value of $\frac{d^2\beta}{df^2}$ for the microstrip is frequency dependent. D_1 for the fiber can be considered to be frequency independent since even though the dispersion coefficient for the fiber changes with frequency, it changes very little over the frequencies occupied by the information bandwidth around the optical carrier. If $\frac{d^2\beta}{df^2}$ was constant for the microstrip, there would be an optimum length of microstrip to compensate for fiber dispersion. However, there is a variation in $\frac{d^2\beta}{df^2}$ with frequency which will ultimately degrade the received eye and therefore it must be included in the simulation. As a result, to determine the best length of microstrip for a given distance of fiber, the microstrip was modeled with the frequency dependence of $\frac{d^2\beta}{df^2}$ included in the model. Subsequently, for each given distance of fiber, the length of microstrip was optimized based on maximizing the eye opening of the received signal after equalization. This way, a more detailed model for the microstrip was used with better predictions of experimental performance.

The attenuation of the microstrip was also added into the model since this is also a realistic effect of microstrip transmission lines. The microstrip has length dependent and frequency dependent losses that include conductor loss, a dielectric loss and a leakage loss. The conductor loss dominates over the other losses and as such is the only loss considered in the simulations. The conductor loss can be modeled as a skin effect modeled by the following equation [67]:

$$\alpha_c = -\frac{R_s}{Z_o w} \tag{4.23}$$

where:

$$R_s = \sqrt{\frac{\pi f \mu_o}{\sigma_c}} \tag{4.24}$$

where α_c is in Nepers/m, R_s is the skin resistance and σ_c is the conductivity.

A plot of the attenuation per meter versus frequency for the microstrip using the parameters ε_r=10.2, h=1 mm, w≈ 1 mm and σ_c=5.81e7 S/m is shown in Figure 4.6.

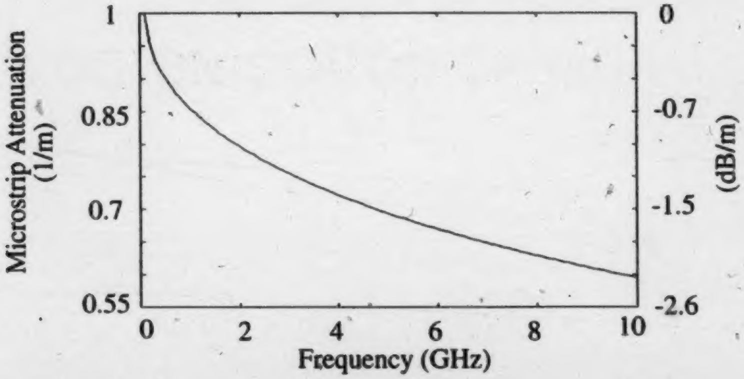

Figure 4.6 Microstrip attenuation per meter versus frequency

As can be seen from Figure 4.6, the attenuation is strongly frequency dependent and will have significant impacts on the system since the binary data covers the frequency spectrum from 0 Hz up to 10 GHz. This attenuation model was used in the simulations of the modeled microstrip in order to foresee any implications of this effect.

4.2 Noise Modeling

In the simulations, the signal input to the system was a binary sequence in a pattern formulated after a pseudo-random (PR) bit sequence. This PR sequence was input to the optical system as an electrical voltage drive signal which was used to drive the MZ modulator and PM in each design. The resultant output signal from the system was also an electrical signal in the form of a photocurrent signal which was representative of the received optical power. Assuming that the optical link functions properly, the information contained in the input voltage signal was reflected in the received current signal.

Within the simulations, two different noise scenarios were examined. The first case was where the receiver consisted of a normal square-law detector and the noise processes in the electrical domain were Gaussian noise currents. Modeling the noise processes in a Gaussian format is the classical approach and is reflective of realistic situations where pin detectors are used that convert the incident optical power into an electrical current. The Gaussian format was the one considered in the majority of the simulations. This type of optical receiver circuit is shown in Figure 4.7. The receiver filter is representative of not only the LPF used to reduce the noise equivalent bandwidth before decision, but also the frequency response of the pin detector.

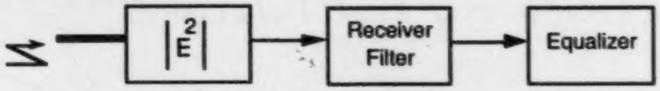

Figure 4.7 Normal optical receiver

The second case was where a square-root operation is performed immediately after the square-law detection and receiver filtering process. This scenario is analogous to a system where the magnitude of the electric field is converted to a current at the receiver. The square-root operation, although not realistic for a broadband signal such as 10 Gb/s data, is shown later in simulations to offer some benefit. In this case, the received information was still in the form of an electrical current and the noises were modeled as noise currents after the receiver filter. However, after the square-root function, the random variable was no longer Gaussian. The new noises are subsequently calculated. This type of optical receiver circuit is shown in Figure 4.8. Thus, two noise models were considered for the simulations.

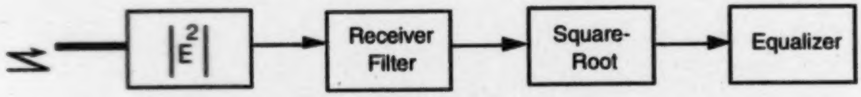

Figure 4.8 Optical receiver employing square-root function

4.2.1 Normal Detection with Gaussian Noise

Within the simulations, calculations of the BER of the received binary signal was a general measure of performance for the system. The calculation of the BER for a received signal was based on the assumption that the received current or photocurrent represented the mean value of a random variable and the noise currents or variance of that mean current followed a Gaussian distribution. The probability of error P_e for a Gaussian variable can be written as:

$$P_e = \frac{1}{2}\operatorname{erfc}\left[\frac{x - x_m}{\sqrt{2}\sigma}\right] \tag{4.25}$$

where erfc is the complimentary error function, x is the sampled value, x_m is the mean and σ^2 is the variance of the sample at a given instant in time.

For the simulations which follow, the P_e for each sample point in a given bit was calculated based on a received mean value and variance. The probability of error P_{ef} for the full bit sequence of length $2^m - 1$ was an average of the P_e calculated for each bit at the optimized clocked decision time and threshold for the entire sequence.

If the received photocurrent is written as i_k for bit k which can be either a transmitted 1 or a transmitted 0, the threshold current is written as i_t which represents a decision level, and the time averaged noise power of the received noise current is written as $\langle i_\sigma^2 \rangle$, the P_{ef} for an entire simulated sequence can be written as:

$$P_{ef} = \frac{1}{2^m - 1} \sum_{k=1}^{2^m - 1} \frac{1}{2} \operatorname{erfc}\left[\frac{i_k - i_t}{\sqrt{2} i_\sigma}\right] \qquad (4.26)$$

The optimum threshold current i_t is determined by optimizing two parameters within the received sequence, time of decision and threshold amplitude. The time within all bits at which the decision is made is chosen at the point where the eye opening of the received sequence is a maximum. The threshold level at which the decision is made is chosen at the point where the P_{ef} is a minimum for the received sequence.

The received photocurrent noise $\langle i_\sigma^2 \rangle$ consists of a number of noise sources including constant and signal dependent sources. The models for the noise sources can be calculated by two different approaches given by Olsson [69] and Cartledge [65]. In Olsson's model, the transmitted optical power is assumed to be constant and thus all noise sources are assumed to be constant over time. In Olsson's model, the signal dependent noises are calculated with bandwidth approximations and do not include the impulse response of the receiver circuit. Thus, the noise currents calculated for a given bit are independent of previous bits in the stream. In Cartledge's model, the transmitted electric field is allowed to vary, like it does in a real system, and thus provides a more accurate model. The noise terms that are signal dependent are calculated based on a receiver impulse response. The impulse response provides interference when calculating the noise current for a bit. In Cartledge's approach, the entire bit sequence is used for this process. As a result, Cartledge's model was used for the signal dependent noise terms in the simulations.

In order to convert the received photocurrent into a voltage for subsequent processing where a decision is made on the orientation of the bit, the detector circuit used is shown as in Figure 4.9. In Figure 4.9, the pin diode is reversed biased and the load resistor R_e converts the current into a voltage at (v). The amplifier is used in experimental circuits to amplify the signal at (v). The amplifier adds additional noise to the signal but this noise was ignored for these simulations. If the system was one in which the optical SSB transmission format was used, the amplified electrical signal was then subjected to electrical equalization. The equalized, or nonequalized, electrical signal was then input to a decision circuit. Since the simulated decision circuit had no amplitude dependence, the amplifier gain was irrelevant within the simulations.

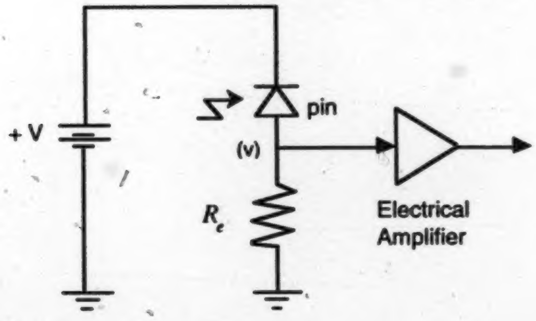

Figure 4.9 Optical receiver circuit with pin detector and amplifier

In the described optical system, the photocurrent noise at point (v) in Figure 4.9 consists of seven noise sources. These noise currents are thermal noise, laser relative intensity noise, dark current shot noise, signal dependent shot noise, ASE shot noise, signal-spontaneous beat noise and spontaneous-spontaneous beat noise.

The thermal noise is due to spontaneous fluctuations of current in the load resistor R_e in the detector circuit. The electrons in a resistor are always in random motion. The intensity of this motion is proportional to temperature. The effect of this motion is to produce a randomly varying current in the circuit. The mean of the squared thermal noise current is given by:

$$\left\langle i_{th}^2 \right\rangle = \frac{4kTB_e}{R_e} \tag{4.27}$$

where k is Boltzman's constant, T is temperature in degrees Kelvin and B_e is the equivalent electrical bandwidth of the receiver.

If the load resistor is matched to the amplifier load, the noise power from the different noise sources, for probability of error purposes, will be reduced by a factor of four since the noise current is split between the two loads. Accordingly, the signal power will also be reduced by a factor a four. As a result, the SNR does not change.

The laser RIN noise is generated from the spontaneous fluctuations in electron to photon conversion in the laser and reflections within the laser cavity. The mean square value of the laser RIN noise current is given by [44]:

$$\left\langle i_{RIN}^2(t)\right\rangle = \frac{R_o^2 RIN_{tot}}{2B_e}\int_{-\infty}^{t} P^2(\tau)h_r^2(t-\tau)d\tau \tag{4.28}$$

where P is the optical power, $h_r(t)$ is the receiver impulse response and R_o is the photodiode responsivity given by:

$$R_o = \frac{\eta\lambda q}{hc} \tag{4.29}$$

and where η is the photodiode quantum efficiency, h is Planck's constant, q is the charge of an electron and λ is the center optical wavelength.

The total RIN value RIN_{tot} is given by:

$$RIN_{tot} = RIN_{laser} + RIN_{fiber} \tag{4.30}$$

where RIN_{laser} is the classic value of RIN specified for a laser times the electrical bandwidth and RIN_{fiber} is due to the frequency modulation to amplitude modulation (FM-AM) noise resulting from the laser linewidth interacting with the fiber chromatic dispersion. The FM-AM noise is generated by laser phase noise being converted to intensity noise due to chromatic dispersion in the fiber. This noise becomes larger with increasing laser linewidth and increasing chromatic dispersion. The amount of chromatic dispersion is obviously proportional to the fiber length. The FM-AM noise due to the laser linewidth is derived by Yamamoto *et al.* [70] and discussed in detail by Walklin [44].

RIN_{fiber} is given by:

$$RIN_{fiber} = \int_{-\infty}^{\infty} N(f)\left|H_r(f)\right|^2 df \tag{4.31}$$

where $H_r(f)$ is the receiver frequency response:

$$N(f) = \frac{2\Delta\upsilon}{\pi f^2}\left(1-\cos\left(8\pi^2 F f^2\right)\right) \tag{4.32}$$

where $\Delta\upsilon$ is the linewidth of the laser in Hz and:

$$F = \frac{LD\lambda^2}{4\pi c} \tag{4.33}$$

where L is the fiber length and D is the dispersion coefficient.

The FM-AM noise results from variations in the instantaneous wavelength of the source originating from an inherent FM noise in the laser. These frequency deviations are generally classified as a source linewidth which is measured as the 3 dB spectral width of the source over a given time interval. Through the interaction of the dispersion and the square-law detection process, the FM noise is converted to an AM noise. This type of noise has minimal effects in DSB systems employing optical equalization for dispersion but it is significant in SSB systems using post detection equalization. In optically equalized systems, the dispersion is essentially zero at the point of detection and thus the FM noise is not detected. In the SSB system where the equalization is post detection, the FM noise added to an information spectral component increases with distance from the optical carrier. This phase deviation incurred by the FM noise is not reversible in a post detection domain. Thus, in any SSB system with post detection dispersion compensation where the laser linewidth is not zero, this type of noise is significant.

The dark current shot noise is a result of the dark current that flows through the photodetector circuit when no light is incident on the photodiode. The mean square value of the dark current shot noise is given by [44]:

$$\left\langle i_{d-sh}^{2}\right\rangle = I_d q \int_{-\infty}^{\infty} h_r^2(\tau)\,d\tau \tag{4.34}$$

where I_d is the dark current for the photodiode.

The signal dependent shot noise arises from the statistical nature of the production and collection of photoelectrons when an optical signal is incident on a photodiode. The mean square value of the signal dependent shot noise is given by [44]:

$$\left\langle i_{sig-sh}^{2}(t)\right\rangle = qR_o \int_{-\infty}^{t} P(\tau)h_r^2(t-\tau)\,d\tau \tag{4.35}$$

The use of EDFAs in the system result in three additional noise terms due to the ASE produced in each amplifier. ASE shot noise is generated in the same manner as the signal dependent shot noise except that the optical noise source originates within the EDFA.

Since isolators are used prior to each EDFA, ASE light only propagates toward the receiver. The mean square ASE shot noise current at the receiver for a single EDFA is [44]:

$$\left\langle i_{ASE-sh}^2 \right\rangle = m_t P_N \eta_o q R_o \int_{-\infty}^{\infty} h_r^2(\tau)d\tau \tag{4.36}$$

where m_t is the number of polarization states and P_N is the ASE noise power given by:

$$P_N = (G-1)h\upsilon N_{sp} B_o \tag{4.37}$$

where G is the internal gain of the EDFA, υ is the optical frequency, N_{sp} is the spontaneous noise factor for the EDFA, and B_o is the bandwidth of the optical BPF following the EDFA.

The spontaneous-spontaneous beat noise results from the beating between various ASE spectral components upon square-law detection of the received optical signal. The mean square spontaneous-spontaneous beat noise current arising from a single EDFA is given by [44]:

$$\left\langle i_{sp-sp}^2 \right\rangle = 2P_N^2 m_t \eta_o^2 R_o^2 \left(\int_{-\infty}^{\infty} h_r(\tau)d\tau \right)^2 \tag{4.38}$$

The signal-spontaneous beat noise arises from the ASE spectral components beating with the signal spectra upon square-law detection of the received optical signal. The mean square signal-spontaneous beat noise current caused by a single EDFA is given by [44]:

$$\left\langle i_{sig-sp}^2(t) \right\rangle = \frac{1}{2} R_o^2 P_N \eta_i \eta_o^2 \left(2\int_{-\infty}^{t} P^{\frac{1}{2}}(\tau) h_r(t-\tau)d\tau \right)^2 \tag{4.39}$$

The $\frac{1}{2}$ term is due to the light being linearly polarized out of the laser. If the light out of the laser is not linearly polarized, this term is omitted.

For the noise terms which were independent of the signal power, the integration limits were between -∞ and ∞. For the noise terms which were dependent on the signal power, the integration limits were between -∞ and time t. The difference is due to the fact the signal independent noise terms are constant over all time, past and future, while the signal dependent terms are dependent only on all of the past bits or the received bits up to time *t*.

Thus, the total noise at the receiver can then be written as:

$$\left\langle i_{\sigma}^{2}(t)\right\rangle = \left\langle i_{th}^{2}\right\rangle + \left\langle i_{RIN}^{2}(t)\right\rangle + \left\langle i_{d-sh}^{2}\right\rangle + \left\langle i_{sig-sh}^{2}(t)\right\rangle + \left\langle i_{ASE-sh}^{2}\right\rangle + \left\langle i_{sp-sp}^{2}\right\rangle + \left\langle i_{sig-sp}^{2}(t)\right\rangle \quad (4.40)$$

It is important to note that the noise terms generated within a particular EDFA such as the ASE shot noise, the spontaneous-spontaneous beat noise and the signal-spontaneous beat noise are amplified by the optical link following that EDFA. The optical link following an EDFA contains losses due to fiber and gain due to subsequent EDFAs. Further, the subsequent EDFAs create their own ASE noise terms thus resulting in an accumulation of noise in the optical signal as it propagates down an optical link.

For example, consider how the ASE noise power accumulates over a three EDFA link with two spans of lossy fiber as sown in Figure 4.10. The total ASE shot noise at the output of the third EDFA is the summation of the shot noises created by all of the amplifiers up to that point.

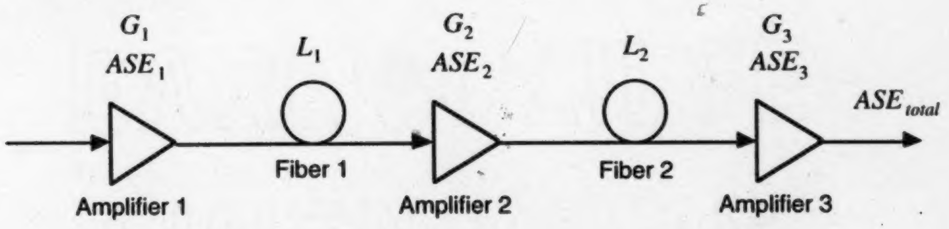

Figure 4.10 Optical link with three EDFAs and two sections of fiber

Thus, the total ASE noise power at the end of the third EDFA can be written as:

$$ASE_{total} = ASE_3 + L_2G_3ASE_2 + L_2G_3\left(L_1G_2ASE_1\right) \quad (4.41)$$

4.2.2 Normal Detection with Square-Root Operation and non-Gaussian Noise

As was previously mentioned, the square-root operation can be implemented at the receiver as shown in Figure 4.8. The random variable at the output of the pin diode is

Gaussian and it's variance is described by the noise currents previously outlined in section 4.2.1. The random variable after the square-root process is no longer Gaussian. This can be shown as follows.

Let the random variable before the square-root process have mean m_x and variance σ_x^2. The random variable following the square-root process has mean m_y and variance σ_y^2. The function relating Y and X is:

$$Y = X^{\frac{1}{2}} \tag{4.42}$$

Thus, it is straight forward to see that the mean of random variable Y is:

$$m_y = m_x^{\frac{1}{2}} \tag{4.43}$$

The variance of Y is not as easily calculated. The variance of Y is derived as follows. Let $F_X(x)$ and $F_Y(y)$ represent the cumulative distributions of X and Y respectively. Then:

$$F_Y(y) = P(Y \le y) = P\left(X^{\frac{1}{2}} \le y\right) \tag{4.44}$$

which can also be written as:

$$F_Y(y) = P(X \le y^2) = F_X\left(y^2\right) \tag{4.45}$$

where P is the probability. By differentiating equation 4.45 with respect to y, we obtain the relationship between the respective probability distribution functions. This relationship can be written as:

$$p_Y(y) = 2y p_X\left(y^2\right) \tag{4.46}$$

Thus, from equation 4.46, it can be seen that if p_X is Gaussian, p_Y is not Gaussian. To show this relationship more clearly, Figure 4.11 (a) shows a Gaussian probability distribution for a random variable and (b) shows the corresponding probability distribution function of a new random variable if the square-root function is taken of the old random variable. Figure 4.11 does not have numbers on the axis, but the central mean of the probability distribution function in (b) would be the square-root of the function in (a). Further, both distributions would have a normalized area of one.

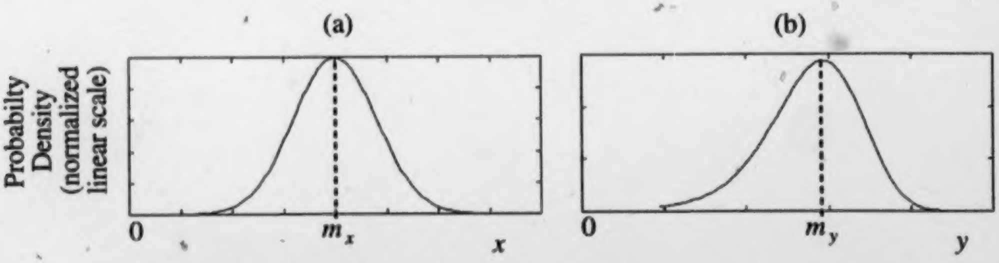

Figure 4.11 Probability distributions (a) Gaussian and (b) non-Gaussian

From Figure 4.11, it can be seen that the probability distribution of the random variable after the square-root function is not Gaussian and is skewed. Thus, the probability of error for 0's and 1's will be different for a given distance away from the mean. As an additional effect, the optimal decision time and/or amplitude will change to optimize the probability of error.

The new variance σ_y^2 can be calculated by taking the second central moment as:

$$\sigma_y^2 = \int_{-\infty}^{\infty} \left(y - m_y\right)^2 p_Y(y)dy \tag{4.47}$$

Knowing that random variable X is Gaussian, the variance of Y in equation 4.47 can be written in terms of mean m_x and variance σ_x^2:

$$\sigma_y^2 = \int_{-\infty}^{\infty} \left(y - \sqrt{m_x}\right)^2 2y\left(\frac{1}{\sigma_x\sqrt{2\pi}}\right)\exp\left({-\left(y^2 - m_x\right)^2} \Big/ {2\sigma_x^2} \right)dy \tag{4.48}$$

As a result, the mean and variance for the new random variable Y can be calculated and a new P_{ef} can be calculated for the system after the square-root process.

Of interest is the possibility of the random variable X going negative. It is assumed in the previous derivation that this does not happen. The assumption is made that the probability distribution function of the new random variable has an impulse at 0 representing the area of negative probabilities. This could be changed accordingly if more information were available on how the square-root function would be implemented in an experimental system. For example, are negative values possible? If they are not, how are they represented. In the simulations that follow, representation by an impulse was satisfactory.

4.3 Simulation Results

In addition to the models previously described for the components and noise sources, some additional parameters are defined for the simulated models. First, the data rate was 10 Gb/s as previously mentioned. Second, V_π for the MZ in Design 1 through 3 was set to 4.5 V (modeled after the Lucent MZ modulator used in the experiments). The V_π for the phase modulator was set to 9 V (modeled after the UTP device used in the experiments). However, as previously mentioned, Design 2 and 3 are equivalent in terms of ideal simulations so only the results for Design 2 are presented in this section and are representative of both designs. The length of the simulation record or pattern length was $2^7 - 1$ unless otherwise noted. The modulation parameter P was set to 0.2 unless otherwise noted. As will be shown later, this is the optimal value for the SSB modulation.

Within the simulations, time domain signals of $m(t)$, $\hat{m}(t)$, $m(t)+\hat{m}(t)$ and $-m(t)+\hat{m}(t)$ were used to drive the modulators. An example of the time domain plots of $m(t)$, $\hat{m}(t)$, $m(t)+\hat{m}(t)$ and $-m(t)+\hat{m}(t)$ for a signal normalized to one Volt peak to peak are shown in Figure 4.12. In these plots, the ideal binary sequence has been dc blocked and low pass filtered with a third order Butterworth LPF with a cutoff frequency at 0.65B. The Hilbert signal was created with a four tap filter with a delay time T of 0.375 ns.

4.3.1 Comparison of Designs 1, 2 and 3

A preliminary comparison was made between Designs 1, 2 and 3. The basis of the comparison was transmission distance over standard single mode fiber. Each design's ability to provide for the reversal of chromatic dispersion was measured in terms of eye opening at the receiver and also receiver sensitivity. Receiver sensitivity is a measure of required optical power at the input to the EDFA at the receiver which is needed to order to maintain a given BER.

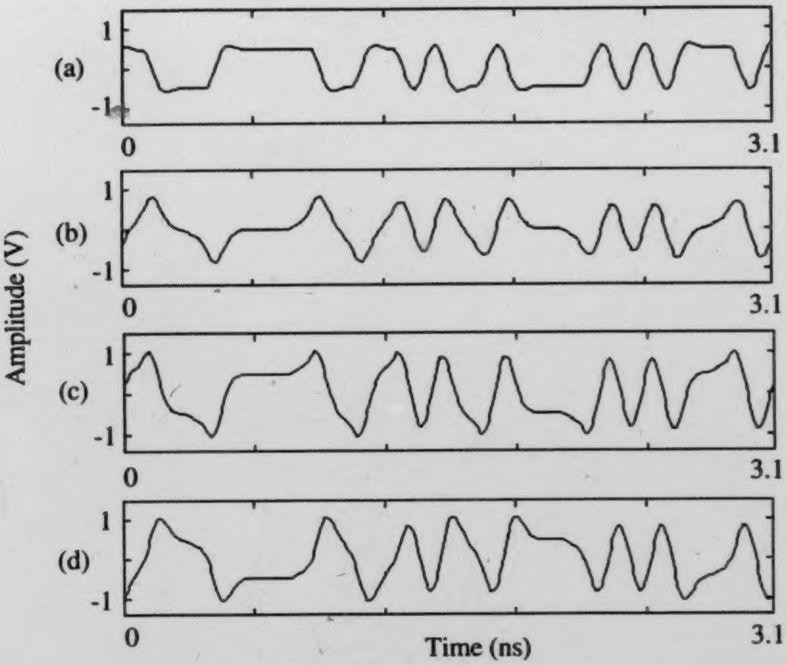

Figure 4.12 Time domain plots of (a) $m(t)$, (b) $\hat{m}(t)$, (c) $m(t)+\hat{m}(t)$ and (d) $-m(t)+\hat{m}(t)$

In the first set of simulations, only one optical amplifier was used in each system. The optical amplifier was placed in front of the photodetector. This optical pre-amplifier had a small signal gain G_o of 30 dB, a N_{SP} of 2 and an output saturation power P_{SAT} of 6 dBm. These values are similar to ones measured for the EDFAs used in some of the experiments. The EDFA was allowed to self-regulate. In addition, the fiber was assumed to be lossless in this initial system. The purpose for this configuration was to isolate the effects of chromatic dispersion. In this configuration, a plot of the receiver sensitivity versus distance shows how chromatic dispersion affects the maximum transmission length without the ASE noise effects from multiple EDFAs in the system. Normally, link EDFAs are required in long distance systems to recover the loss incurred by the fiber. Figure 4.13 shows the receiver sensitivity versus distance for five different cases, standard DSB, SSB without equalization implementing Design 1, SSB with equalization implementing Design 1, SSB without equalization implementing Design 2 and SSB with equalization implementing Design 2. Again, it is noted that Design 2 and Design 3 are equivalent in these ideal simulations. All of the received SSB signals listed as 'with equalization' are equalized with an ideal electrical equalizer which is characterized as the inverse of the fiber transfer function. However, it is important to note that the inverse function is not applied to the received signal until after square-law detection in the electrical domain. The receiver sensitivity shown in Figure 4.13 is the required optical power at the input to the optical amplifier at the receiver required to maintain a BER of 10^{-9}. All of the noise sources other than the effects of in-line EDFAs were included in the simulation.

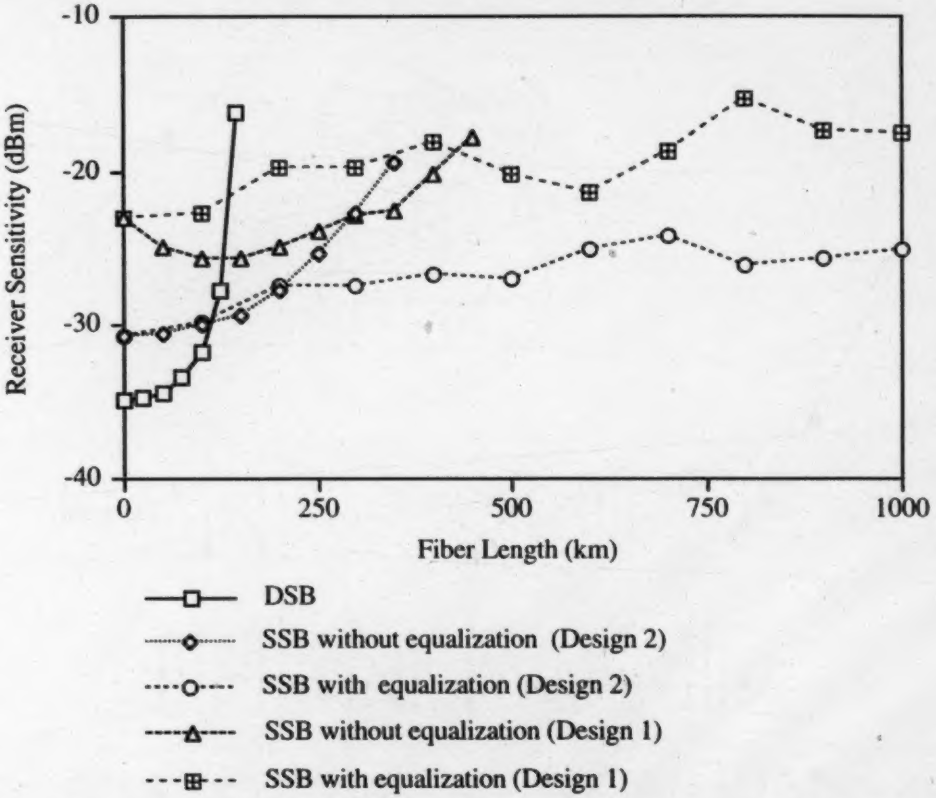

Figure 4.13 Receiver sensitivity versus fiber length for Designs 1 and 2

From Figure 4.13, it can be seen that Design 2 outperforms Design 1 in terms of receiver sensitivity. This is due to the balanced nature of the drive signals in Design 2 and was predicted in Chapter 3 where it was shown that the balanced configuration of Design 2 had less distortion in the square-law detected signal than the nonbalanced configuration of Design 1.

From Figure 4.13, it can also be seen that the SSB case of Design 2 with equalization follows the same curve as the SSB case of Design 2 without equalization for distances less than approximately 200 km. This is due to the second order terms, such as $m^2(t)$ generated from the MZ transfer function, canceling with the second order terms created from the square-law detection process. However, for distances longer than 200 km, chromatic dispersion from the fiber affects each second order term differently thus preventing any meaningful cancellation. Consequently, beyond 200 km, they can both add to the degradation of the signal. This effect at 0 km can be seen in equation 3.25 were the second order terms of $m^2(t)$ from the MZ modulator and the squaring of the first order terms from the square-law detection processes cancel.

In order to show the SSB nature of Design 1 and Design 2, the simulated optical spectrum of the signals generated at the transmitter are shown in Figure 4.14. Figure 4.14 includes a simulated regular DSB spectrum as well for comparative purposes. In the spectral plots of Figure 4.14, the optical carrier component which would be at the zero frequency mark has been removed to better show the information sidebands. This carrier component is required to properly self-homodyne detect the optical signal. As was previously mentioned, the Hilbert transform was approximated with a four tap Hilbert filter where T is 37.5% of the bit period. As a result of the imperfect Hilbert signal, the optical spectrum was, in the strict sense, VSB. This can be seen in Figure 4.14. However, the effects of the vestige can be minimized if the time delay between the taps is appropriately chosen. Thus, the systems can be called SSB in the general sense and VSB in the strict sense. However, since the system exploits the benefits of the nature of SSB, they will be called SSB systems for the most part. The ripples in the SSB spectra are also a result of the 2^7-1 pattern length. The difference between the absolute magnitude of the information spectrum in Design 1 and Design 2 corresponds to the reduced signal power in Design 1 as a result of tapping off carrier for proper self-homodyne detection.

From Figure 4.14, it can be seen that the spectral width of the transmitted optical spectrum for the SSB cases are just more than half of the DSB case. As a result, a dispersion benefit of a factor of just less than two will result form this fact alone. However, as also shown, to improve the transmission distance even further, equalization at the receiver is employed.

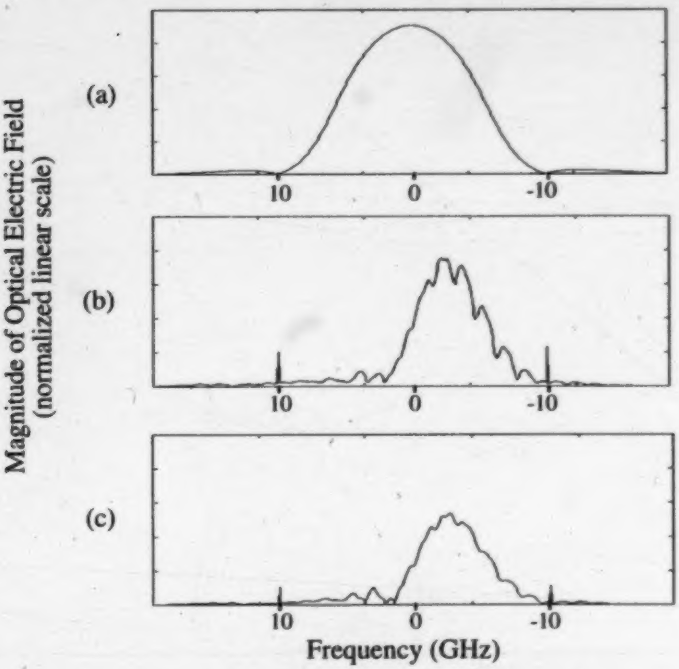

Figure 4.14 Simulated optical spectrums (a) DSB, (b) SSB - Design 2 and (c) SSB - Design 1

Further, comparing the spectral plots of Figure 4.14 (b) and (c), it can be seen that the spectral power contained in the signal for Design 1 is less than Design 2. This is due to part of the transmitted light being used as a non-modulated carrier to properly self-homodyne detect the received signal in Design 1. In these particular simulations, 30% of the transmitted optical carrier was tapped from the source and recombined after modulation to create the final transmitted optical signal in Design 1. This was an optimal situation for Design 1. In Design 2, more power could be used in modulating the signal since the carrier, inherent from the modulation process, is totally in phase with the $m(t)$ term as previously shown.

To show in the time domain, the expected benefits of SSB and equalized SSB over DSB, eye diagrams of the received signal are generated from a simulation of the superior design, Design 2, and are shown in Figures 4.15 through 4.17. In this case, all of the noise processes were omitted from the simulations in order to present cleaner eye diagrams. The eye diagrams of the received signal for a standard DSB signal for distances of 0 km, 75 km and 150 km are shown in Figure 4.15. The eye diagrams of the received signal from Design 2 for an unequalized SSB signal for distances of 0 km, 150 km and 300 km are shown in Figure 4.16. The eye diagrams of the received signal from Design 2 for an equalized SSB signal for distances of 0 km, 300 km and 800 km are shown in Figure 4.17. Again, the equalizer was an ideal equalizer which was represented as the inverse fiber transfer function implemented at the electrical level.

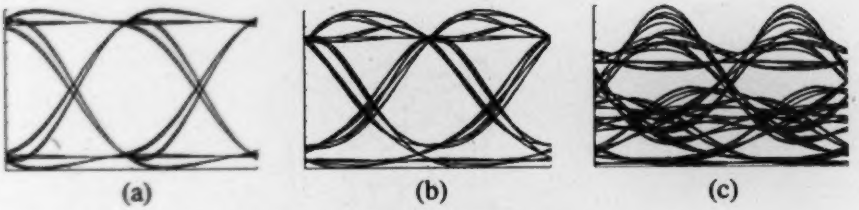
(a) (b) (c)

Figure 4.15 Eye diagrams of a standard DSB signal for (a) 0 km, (b) 75 km and (c) 150 km

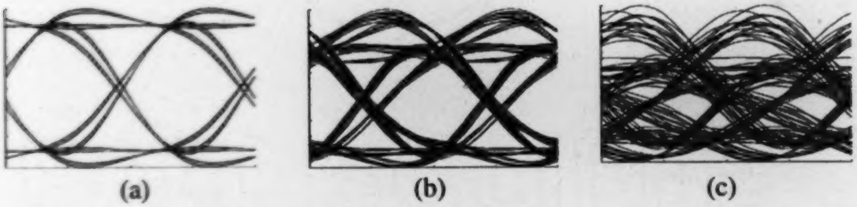
(a) (b) (c)

Figure 4.16 Eye diagrams of an unequalized SSB signal using Design 2 for (a) 0 km, (b) 150 km and (c) 300 km

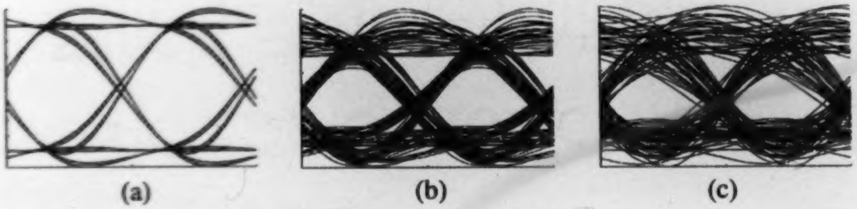
(a) (b) (c)

Figure 4.17 Eye diagrams of an equalized SSB signal using Design 2 for (a) 0 km, (b) 300 km and (c) 800 km

To show in the time domain, the expected benefits of equalized SSB over DSB for the secondary design, Design 1, eye diagrams of the received signal were generated from Design 1 and are shown in Figure 4.18. The eye diagrams of the received signal from

Design 1 for an equalized SSB signal for distances of 0 km, 300 km and 800 km are shown in Figure 4.18.

Comparing the eye diagrams of the received signal for Designs 1 and 2, it can be seen again that Design 2 outperforms Design 1 for all equalized distances. Of considerable note is the degraded performance of Design 1 at the 0 km distance. Consequently, Design 2 will be the only SSB design considered from hereon. This reinforces the results shown in Figure 4.13 where, based on receiver sensitivity, Design 2 outperformed Design 1.

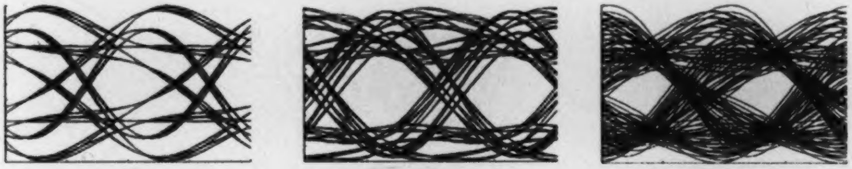
(a) (b) (c)

Figure 4.18 Eye diagrams of an equalized SSB signal using Design 1 for (a) 0 km, (b) 300 km and (d) 800 km

In order to show how Design 2 with a modulation parameter of 0.2 performs over extremely long distances, such as more than 1,000 km, the eye diagrams of a received signal at 3,000 km and 6,000 km are shown in Figure 4.19. The received signal was again equalized with an ideal equalizer which was the inverse of the fiber transfer function implemented at the electrical level. The word length was again $2^7 - 1$.

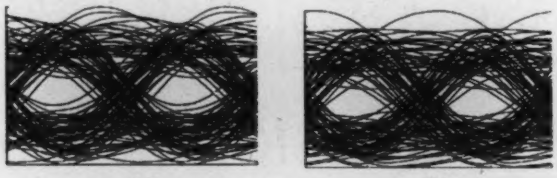
(a) (b)

Figure 4.19 Equalized received eye diagram using Design 2 for (a) 3,000 km and (b) 6,000 km

The receiver sensitivity versus distance for Design 2 is shown in Figure 4.20 for long distances up to 10,000 km. From Figure 4.20, it can be seen that the receiver sensitivity is a measurable value for these conditions which is a result of the fact that a measurable eye exists at each distance. As the fiber length changes, the receiver sensitivity fluctuates. This is a result of the distortion from the second order, third order, etc. effects, which are not compensated for by the equalizer, affecting the system performance in varying degrees. The distortion form the higher order effects cyclically varies and affects some distances more than others thus leading to fluctuations in the received eye opening and thus the receiver sensitivity.

As can be seen from Figure 4.19 and 4.20, there is a discernible eye at the extremely long distances although it is quite small at certain distances. Thus, the distances beyond 1000 km represent the fact that equalization can take place theoretically. However, at these distances, noise accumulation from the large number of in-line EDFAs needed to recover the fiber loss is a very serious concern. Some submarine systems implemented in a DSB format at a lower bit rate [71] with consideration made for dispersion at the optical level have shown successful operation out to 7,200 km. Thus, experimentally, this noise accumulation is not always fatal, however, these SSB systems at 10 Gb/s would suffer a penalty, depending on the amplifier spacing, after an extremely long distance due to ASE noise accumulation in conjunction with a small received eye.

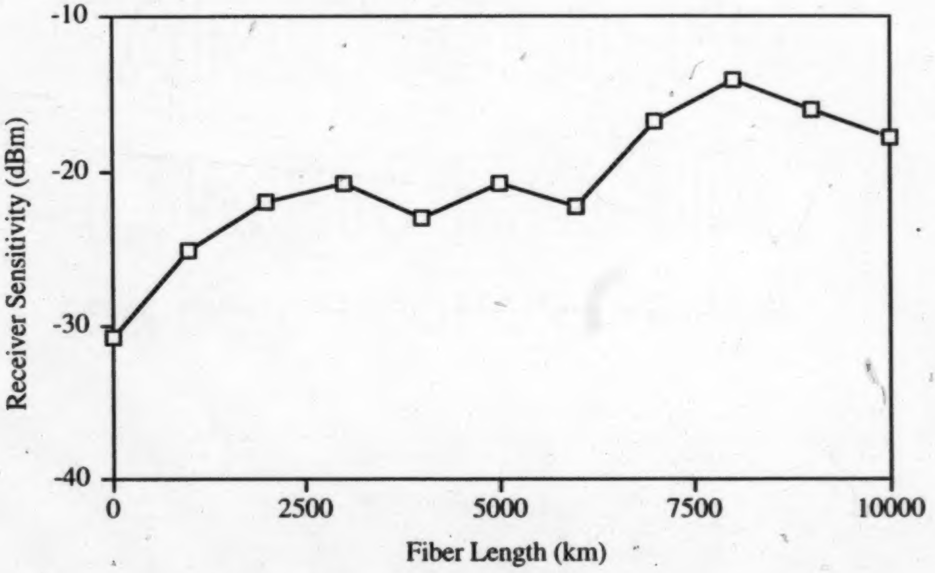

Figure 4.20 Receiver sensitivity versus fiber length for Design 2

4.3.2 Variations on the Hilbert Transform Filter

All of the previous simulations were carried out using a Hilbert transform filter with four taps and a time delay T of 37.5% of the bit period or, for 10 Gb/s data, 0.375 ns. This Hilbert filter was used to create the Hilbert signal $\hat{m}(t)$. This tap number and delay were idealized for this design based on the premise that the Hilbert filter built in the lab would have four taps. However, the number of taps and the delay was altered in simulation, and as a result, the nature of the transmitted optical spectrum changed.

The approximate phase response of the filters simulated is shown in Figure 4.21. This shows an ideal response, however, filters with four or more taps come close to this type of phase response.

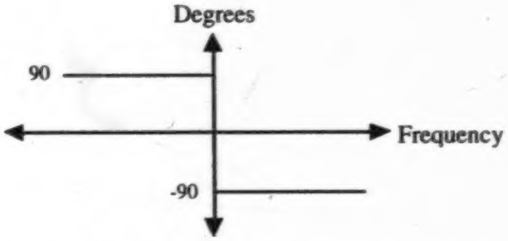

Figure 4.21 General phase response of tap delay filter

In the first case, the delay was fixed and the number of taps was allowed to vary. Figure 4.22 shows the magnitude response of filters with different number of taps, all with a unit delay T of 0.375 ns. The low frequency cutoff in the responses in Figure 4.22 is proportional to the time delay through the filter. The transmitted optical SSB spectra as a result of using each of these filters is shown in Figure 4.23.

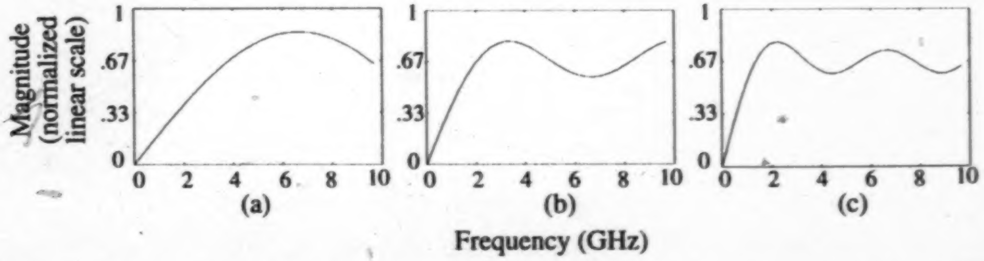

Figure 4.22 Magnitude response of (a) 2 tap, (b) 4 tap and (c) 6 tap delay filter with a time delay T of 0.375 ns

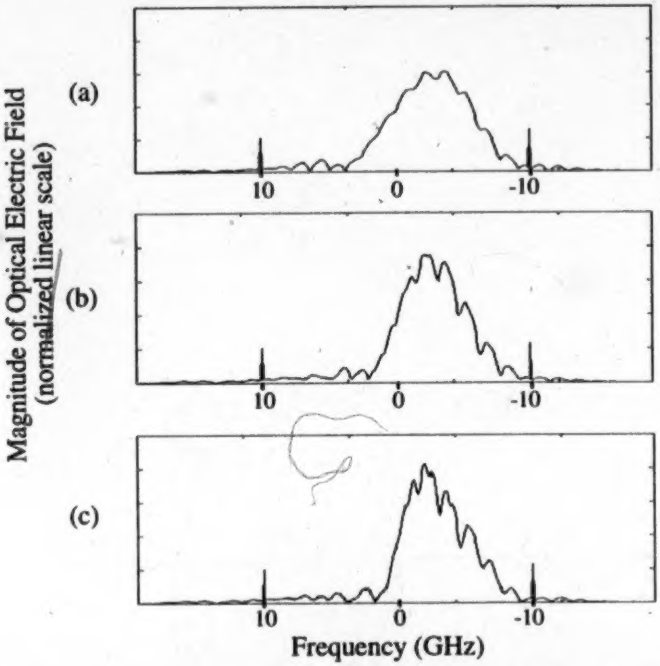

Figure 4.23 Transmitted optical electric field magnitude spectrums of (a) 2 tap, (b) 4 tap and (c) 6 tap delay filter with a time delay T of 0.375 ns

In the second case, the unit time delay T between each tap was altered to give varying magnitude responses of the tapped delay filter. To show how varying tap delay can affect the transmitted optical spectrum, the magnitude response for time delays of 0.2 ns, 0.375 ns and 0.5 ns are shown in Figure 4.24. The total number of taps for all cases in Figure 4.24 is four. The transmitted optical SSB spectrum as a result of using each of these filters is shown in Figure 4.25.

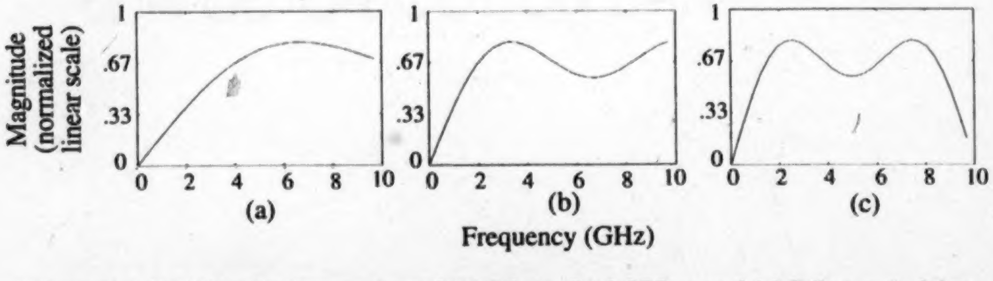

Figure 4.24 Magnitude response of (a) 0.2 ns, (b) 0.375 ns and (c) 0.5 ns unit delay with a four tap filter configuration

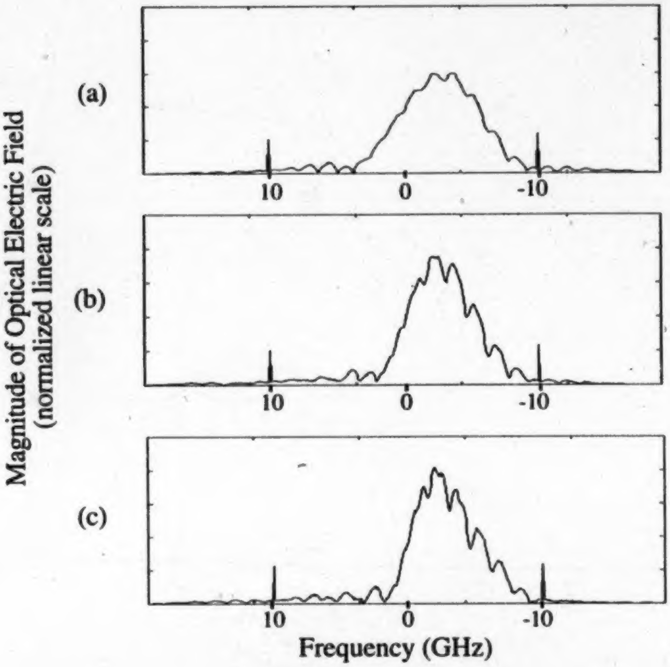

Figure 4.25 Transmitted optical electric field magnitude spectra of (a) 0.2 ns, (b) 0.375 ns and (c) 0.5 ns unit time delay with a four tap filter configuration

Examining the Hilbert filter responses, the transmitted optical spectrum that each response creates and utilizing these Hilbert filters in simulations, two conclusions were drawn. First, increasing the number of taps increases the cancellation of one sideband in the optical signal. As previously mentioned, the low frequency cutoff for the filter is proportional to the time delay through the filter. Thus, more taps for a given time delay or a longer time delay for a given number of taps reduces the vestige. Second, passband ripple can be detrimental to the transmitted signal if the ripple occurs in the high power region of the signal spectrum (i.e. ≈1-5 GHz). Consequently, the best Hilbert filter which had a realistic truncated number of taps had only four taps and a unit time delay of 0.375 ns. Even though this filter created a noticeable vestige, it's distortion of the spectral components in the 1-5 GHz region was minimal. An ideal Hilbert filter with very small ripple and creating a very small vestige could be obtained with a infinite number of taps, but this is realistically impracticable. Thus, a compromise was made to use four taps with an optimized time delay since a four tap combiner/splitter was available in the lab to create the Hilbert filter for the experiments.

If an infinite number of taps were used, the Hilbert transform would be perfect and would have a flat magnitude response. If Design 2 used a Hilbert filter with an infinite number of taps, the simulated optical electric field spectrum at the transmitter would be as shown in Figure 4.26. An infinite number of taps in the time domain can be simulated by representing the Hilbert function in the frequency domain with the response shown in Figure 3.2

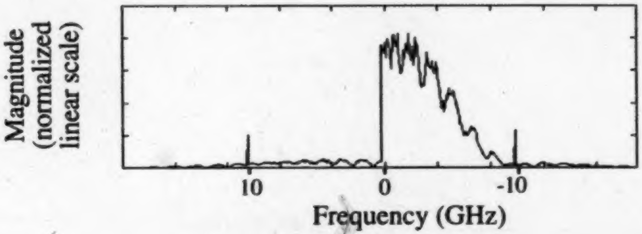

Figure 4.26 Transmitted optical electric field magnitude spectrum using Hilbert filter with an infinite number of taps

From Figure 4.26, it can be seen that an infinite number of taps provides for a better cancellation of the vestige than a filter with a limited number of taps. However, there still are small spectral components present in the canceled sideband. These are due to the higher order terms created by the MZ modulator which are not made SSB by the Hilbert signal since $\hat{m}(t)$ is the Hilbert transform of the signal input to the MZ modulator, not the signal at the output of the MZ modulator.

As a measure of performance of the four tap filter against a filter with an infinite number of taps, the receiver sensitivity versus distance for Design 2 implementing both types of filters is shown in Figure 4.27.

From Figure 4.27, it can be seen that a four tap filter is adequate for this system. The primary reason that the filter with the infinite number of taps does not outperform a filter with four taps is that the major impairment to the system is not the vestige from the first order term but the non-SSB higher order terms created in the MZ modulator. More importantly, the squared terms created after square-law detection limit the ability to equalize the chromatic dispersion at the electrical level.

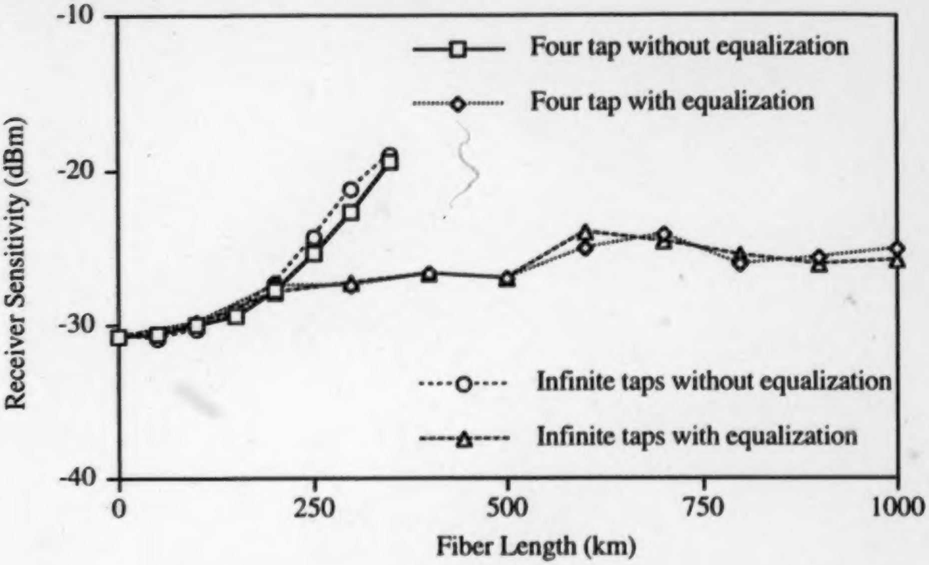

Figure 4.27 Receiver sensitivity versus distance for Design 2 implementing a Hilbert filter with four taps and with an infinite number of taps

4.3.3 Variations on the Modulation Depth and Bias Angle

The general dual arm MZ transfer characteristic showing the electric field and power versus the bias angle θ in equation 3.32 was plotted in Figure 3.12. In the previous simulations, the operating point was always $\theta = V\pi/4$ with small signal modulation around that point. In Figure 3.12, this bias angle corresponds to the most linear power point. However, the most linear electric field point is at $\theta = V\pi/2$. However, by biasing at $\theta = V\pi/2$, the optical carrier would be extinguished and the capability for self-homodyne detection would be eliminated. In addition, the larger the modulation depth on the MZ modulator, the more distortion that becomes present in the optical SSB signal in the form of unwanted sideband and unequalizable distortion terms generated by the square-law detection process. On the other hand, the MZ cannot be driven with too low a modulation depth or else there is too small a difference between light levels for a 0 and a 1 for the purposes of noise immunity. Thus, an optimal condition for bias point and modulation depth should exist which minimizes distortion from both the MZ modulator and the square-law detection process as well as maximizes noise immunity.

In the previous simulations, the modulation parameter P was set to 0.2. This parameter, as will be shown, is the optimal value based on a number of factors including the receiver sensitivity, the insertion loss in the modulator due to the modulation signal (i.e. the reduction in optical power of the modulated signal over unmodulated light) and also the ratio between the Hilbert signal $\hat{m}(t)$ and the original information $m(t)$.

The modulation parameter P can be translated to relative optical power levels for binary levels at zero fiber length. For example, the modulation parameter P of 0.2 with biasing at $\theta = {}^{V\pi}/_{4}$ translates to optical power levels at the output of the MZ modulator between 20% and 80 % of full light. In other words, a zero would be transmitted at 20 % of full light and a one would be transmitted at 80 % full light. This is shown schematically in Figure 4.28.

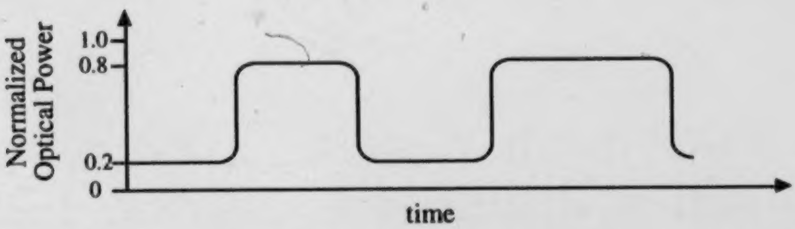

Figure 4.28 Schematic of optical pulse sequence for a modulation parameter P of 0.2

If the modulation parameter was changed to 0.5, the extinction between levels would be close to 0% and 100% of full light. On the other hand, a modulation parameter of 0.01 would translate to levels between 48% and 52% light. The tradeoffs between small and large modulation parameters as they relate to noise immunity and also the ability to equalize post detection were explored further.

As a first test of changing the bias point, the modulation parameter P was left at 0.2, the modulation ratio of $\hat{m}(t)$ to $m(t)$ as determined by equation 3.35 was left at one and only the bias point was varied from the original setting of $\theta = {}^{V\pi}/_{4}$. The receiver sensitivity for Design 2 versus the bias angle θ for a fiber length of 400 km is shown in Figure 4.29.

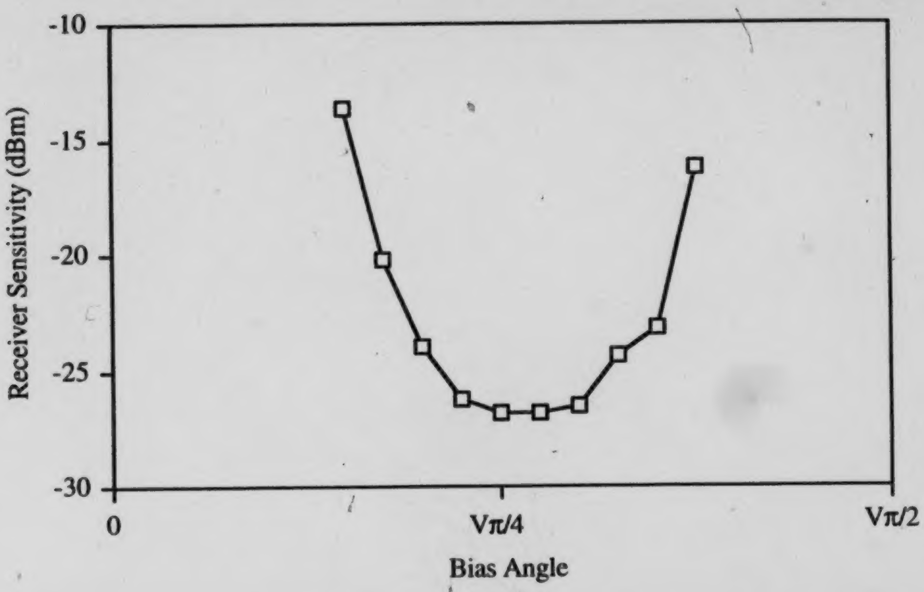

Figure 4.29 Receiver sensitivity versus bias angle θ for Design 2 for a fiber length of 400 km, modulation ratio $\hat{m}(t)$ to $m(t)$ of 1 and a modulation parameter of 0.2

From Figure 4.29, it can be seen that the receiver sensitivity follows a sharp bathtub curve around the bias point $\theta = V\pi/4$ and that this bias point is the best for the modulation parameter of 0.2 and a modulation ratio of $\hat{m}(t)$ to $m(t)$ of one. In this case, the ratio of $\hat{m}(t)$ to $m(t)$ was not allowed to vary, however, as was previously determined by equation 3.35, this ratio must vary with the tangent of the bias angle in order to maintain the maximum sideband cancellation of the optical electric field signal. A different set of results is obtained if the modulation ratio is allowed to vary.

In a second test, the modulation parameter P and the bias angle θ were varied with the ratio between $\hat{m}(t)$ and $m(t)$ allowed to change in order to optimize the receiver sensitivity. In this case, the ratio of $\hat{m}(t)$ to $m(t)$ follows the tangent of the bias angle as defined by equation 3.25. In Figure 4.30, the receiver sensitivity versus the bias angle θ is plotted for a number of different modulation parameters P at a distance of 200 km. Figure 4.31 and Figure 4.32 shown the same scenarios for distances of 400 km and 600 km respectively. The EDFA used at the receiver is modeled with the same parameters as the one used in the previous receiver sensitivity calculations where the EDFA at the receiver or optical preamplifier had a small signal gain G_o of 30 dB, a N_{SP} of 2 and an output saturation power P_{SAT} of 6 dBm.

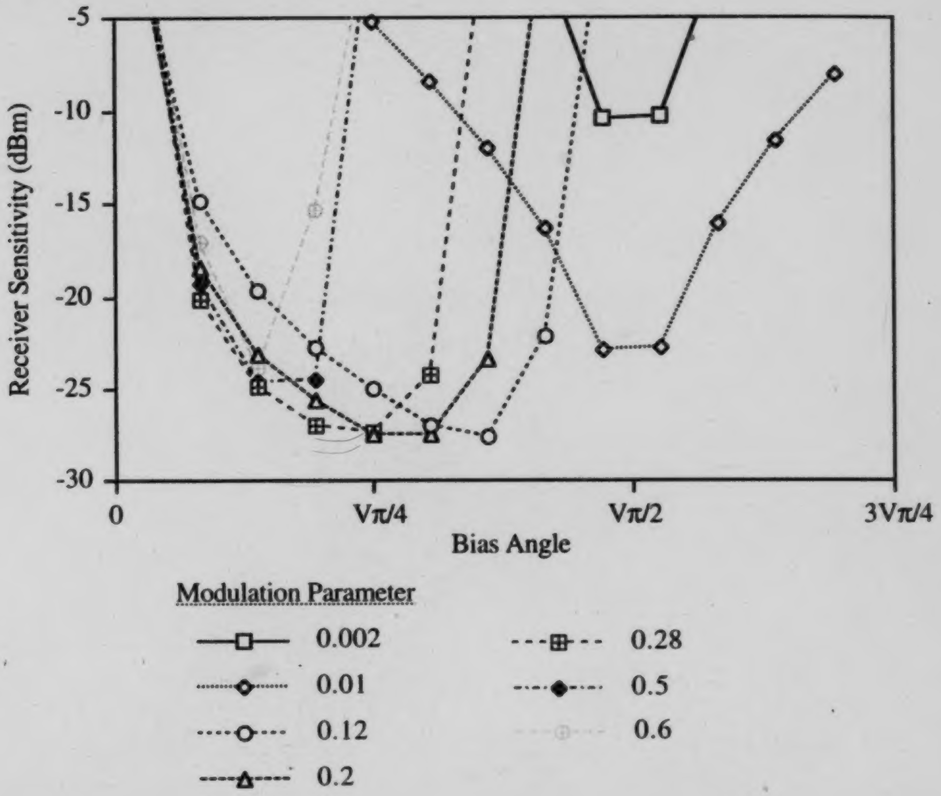

Figure 4.30 Receiver sensitivity versus bias angle θ for Design 2 at 200 km allowing the ratio of $\hat{m}(t)$ to $m(t)$ to vary

From Figures 4.30 through 4.32, it can be seen that for each modulation parameter, there is an optimal bias angle where the receiver sensitivity is maximized. This is due to the combination of minimization of the total distortion terms generated from the MZ transfer function and also the square-law detection process along with the maximizing of the noise immunity process of the received sequence. The general characteristic shown in Figures 4.30 through 4.32 is common for all distances beyond approximately 200 km. However, each modulation parameter has a different bias angle for maximum receiver sensitivity. For example, a modulation parameter of 0.6 has a maximum receiver sensitivity at a bias angle of 10 degrees or 10/180 of V_π while a modulation parameter of 0.002 has a maximum receiver sensitivity at a bias angle near 85 degrees or 85/180 of V_π. The maximum receiver sensitivity generally occurs where the modulation parameter is 0.2 with a bias angle near 45 degrees or $V_\pi/4$. At some distances, the optimal modulation parameter varies from 0.2. However, the general trend is that a modulation parameter of 0.2 was a good compromise since it provided the best, or close to the best performance, for most distances of interest less than 1000 km.

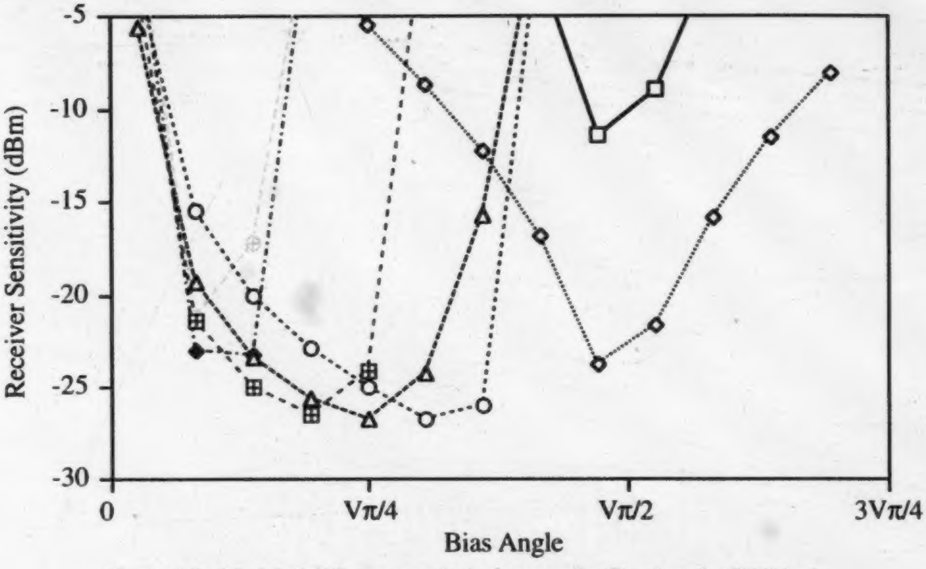

(Legend for Modulation Parameters is the same as for fiber length of 200 km)

Figure 4.31 Receiver sensitivity versus bias angle θ for Design 2 at 400 km allowing the ratio of $\hat{m}(t)$ to $m(t)$ to vary

In Figure 4.33, the insertion loss in the modulator due to the modulation signal is plotted for different modulation parameters *P*. This insertion loss was due to two elements. First, the average optical power is reduced by the nature of the information since a lower power level is transmitted for a zero than for a one. Second, if the bias point is altered, the mean power level between a zero and a one is changed thus altering the average optical power. The insertion loss is calculated as the difference of the optical power of the continuous wave light into the modulator and the output of the modulator at the bias angle θ where the receiver sensitivity is the best for that modulation parameter. From Figure 4.33, it can be seen that for a very small modulation parameter, the insertion loss due to the signaling format is very high since the optimal bias point is near $\theta = V_\pi/2$ where there is a small non-modulated component. It is optimal for higher modulation parameters where the non-modulated component is larger and the average optical power between a zero and a one is also higher.

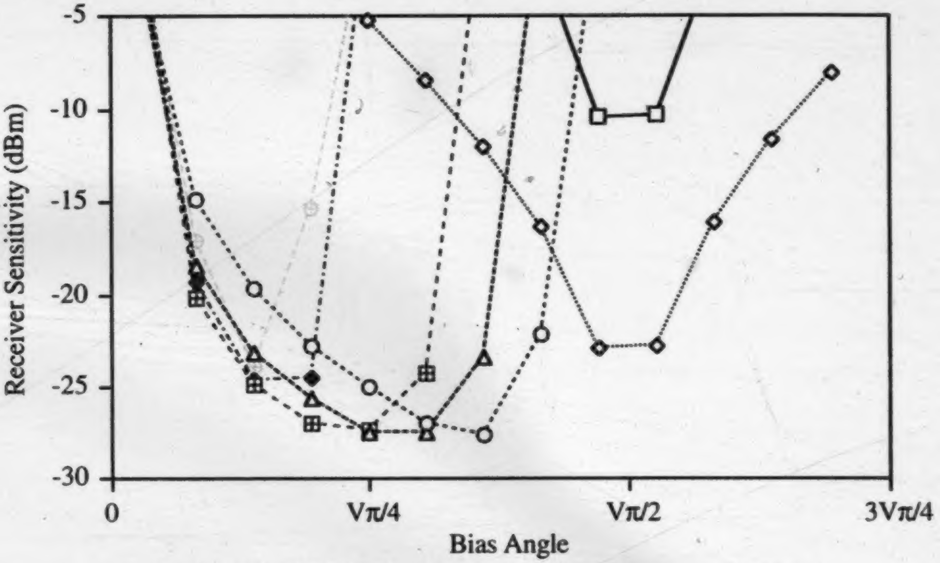

(Legend for Modulation Parameters is the same as for fiber length of 200 km)

Figure 4.32 Receiver sensitivity versus bias angle θ for Design 2 at 600 km allowing the ratio of $\hat{m}(t)$ to $m(t)$ to vary

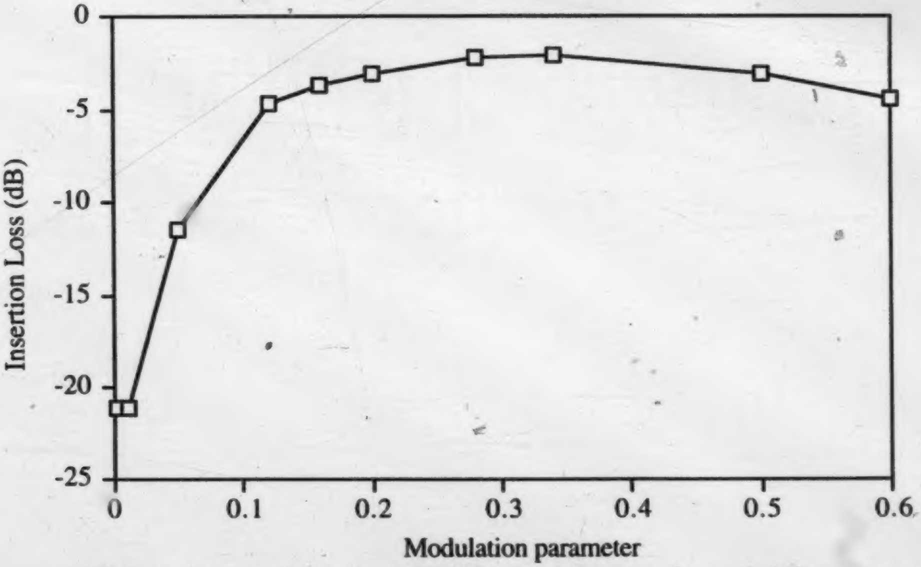

Figure 4.33 Insertion loss due to the modulation signal versus the modulation parameter

What Figures 4.30 through 4.33, along with Figure 3.11 showing the ratio of $\hat{m}(t)$ to $m(t)$, demonstrate is, that on an overall basis, a modulation parameter of approximately 0.2 is a good compromise. This value gives close to the best receiver sensitivity with a modulation insertion loss of 3 dB. Further, the ratio between of $\hat{m}(t)$ to $m(t)$ is only one which is important since from an implementation standpoint, large amplitudes in the actual $\hat{m}(t)$ signal resulting from ratios larger than one can lead to experimental problems such as saturation in amplifiers used to drive the modulator(s).

Initially, variation in the parameter P was evaluated as it pertained to the receiver sensitivity. Subsequently, the variation in the parameter P was evaluated as it pertains to a full EDFA cascade. Thus, the fiber loss, amplifier gain and ASE noise contributions of the multiple EDFAs were added to the simulations. Throughout the initial simulations, the parameter P was found to be optimal at 0.2. To show that this is still the optimal value, the system BER performance is shown with all of the in-line EDFAs included.

In the following simulations, the fiber loss was represented as 0.25 dB/km and splices are assumed to occur, with loss of 0.1 dB/splice, every 2 km. The link EDFAs were modeled the same as the receiver EDFA; they are modeled as self regulating gain blocks with a small signal gain G_o of 30 dB, a N_{SP} of 2 and an output saturation power P_{SAT} of 6 dBm. The EDFAs were separated by 50 km fiber links. The optical insertion loss per link was 19 dB consisting of 12.5 dB fiber loss, 2.5 dB splice loss and 4 dB insertion loss due to an isolator at the input of the EDFA and an optical BPF at the output of the EDFA.

The BER versus launched optical power is shown in Figures 4.34, 4.35 and 4.36 for three distances, 200 km, 400 km and 600 km respectively. The launched optical power is representative of the optical power launched from the first EDFA at the transmitter into the fiber. This power level is important since nonlinear effects in the fiber for these distances or in the EDFA can set in when the optical power in the fiber exceeds approximately +8 to 9 dBm.

A BER curve is plotted for each modulation parameter. The bias point used for each curve was chosen so that the receiver sensitivity for each modulation parameter is maximized.

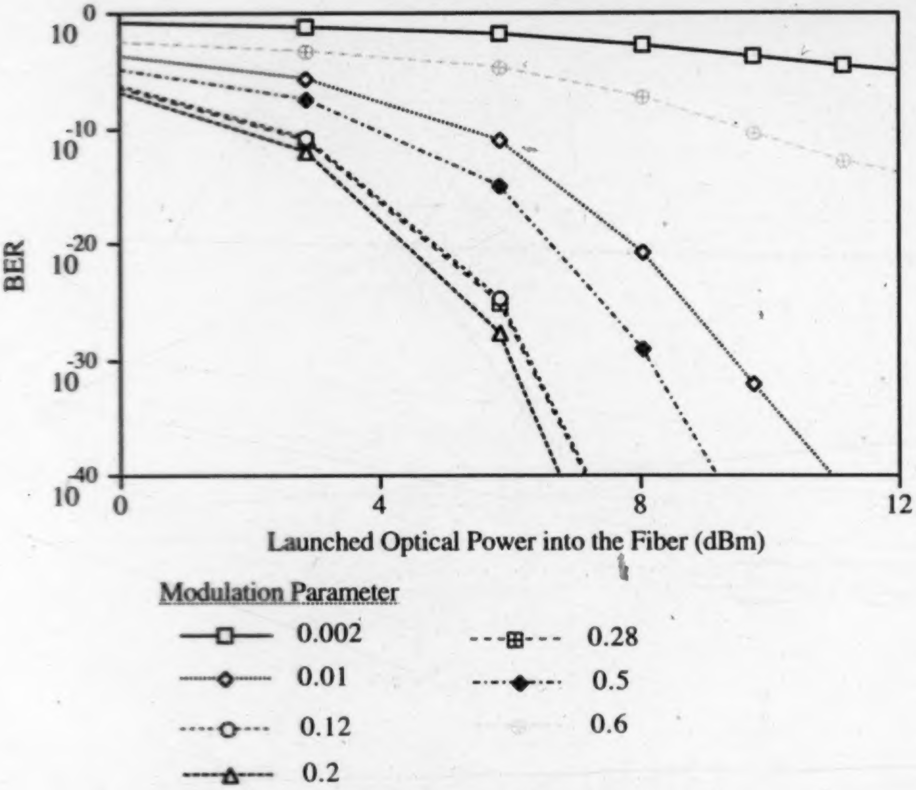

Figure 4.34 BER versus launched optical power into the fiber for different values of modulation parameter *P* at 200 km

From Figure 4.34 through 4.36, it can be seen that a value of 0.2 for *P* provides generally the lowest BER curve. For a *P* value less than 0.2, a high degree of linearity in the transmitted signal is maintained and as a result, the equalized version of $m(t)$ has little distortion. However, the difference in optical power levels between a one and a zero is small and as such, the system is more susceptible to noise. On the other hand, for values of *P* higher than 0.2, the system is not as susceptible to noise because of a larger difference in power levels for a one and a zero. However, the system cannot be equalized as readily beyond approximately 150 km because of distortion from second order and higher terms present in the transmitted signal. Consequently, the BER curves reinforce the conclusions drawn from the corresponding receiver sensitivity curves. A modulation parameter of 0.2 at a bias angle of $\theta = V_\pi/4$ is still the best case.

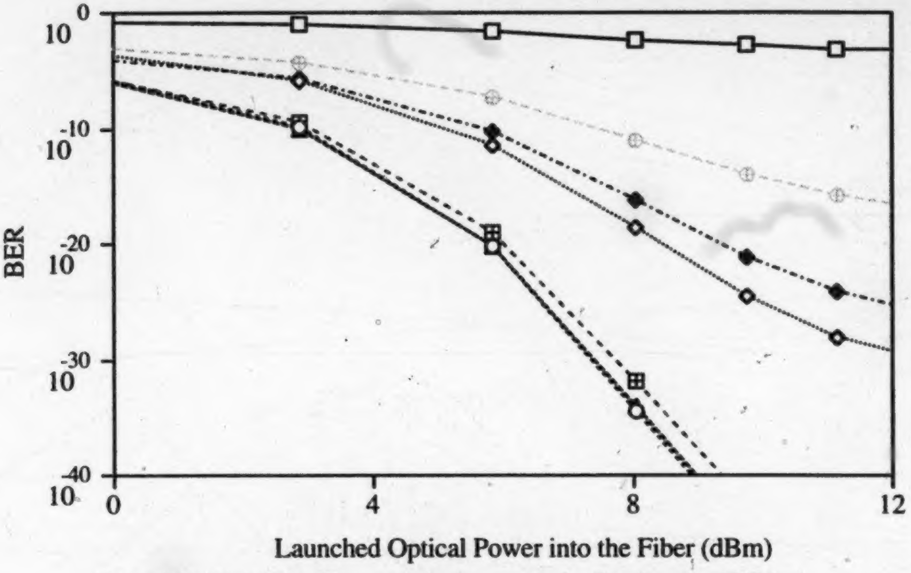

(Legend for Modulation Parameters is the same as for fiber length of 200 km)

Figure 4.35 BER versus launched optical power into the fiber for different values of modulation parameter P at 400 km

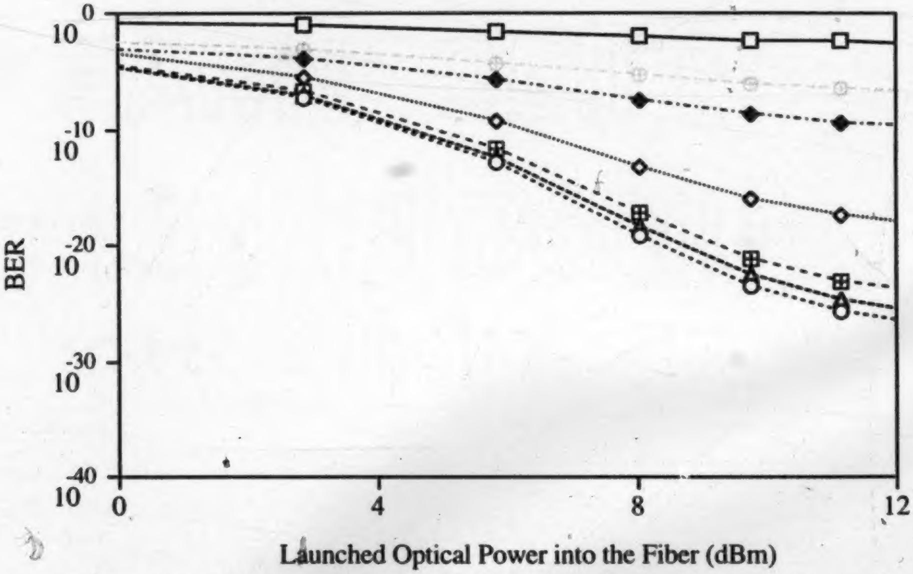

(Legend for Modulation Parameters is the same as for fiber length of 200 km)

Figure 4.36 BER versus launched optical power into the fiber for different values of modulation parameter P at 600 km

4.3.4 Comparison of Single and Double Sideband Systems

In this section, optical SSB and DSB systems were studied with optical equalization and compared to SSB systems with electrical equalization. The designs were modeled in detail by including all of the EDFAs in the optical link. Thus, the fiber loss, amplifier gain and ASE noise contributions of the multiple EDFAs were included in the simulations. This provided two benefits. One, it showed what the baseline case was in terms of noise accumulation through the optical link without the effects of chromatic dispersion disrupting the received eye pattern and two, it showed how well an optical SSB system with electrical compensation compared to a conventional DSB system using ideal optical equalization.

In general, three systems were shown. The first was the regular SSB case which used the implementation shown as Design 2 and used an ideal electrical equalizer which was modeled as the inverse fiber transfer function implemented at the electrical level. The second was the same SSB system but used all optical equalization thus eliminating the need for any electrical equalization. The third system was the regular DSB system which also used full optical equalization. It is important to note that, the DSB case was driven to full extinction. The modulation parameter P for the SSB cases was 0.2 so the MZ modulator was not driven to full extinction in the SSB cases. At the fiber lengths over which the simulations were performed, full optical extinction at the modulator was not possible in the SSB case. At the longer fiber lengths, electrical equalization could only be carried out if the modulation parameter was optimized. This was demonstrated earlier here in Chapter 4.

In the following simulations, the fiber loss was modeled for standard single mode fiber operating in the 1.55 μm window. This loss was represented as 0.25 dB/km and 0.1 dB/splice with the splices occurring every 2 km. The EDFAs were modeled as either fixed gain or self regulating gain blocks with a N_{SP} of 2.

The first case consisted of the system where the fiber length was fixed for all three of the situations: DSB with no dispersion, SSB with no dispersion and SSB with dispersion. The EDFAs in this case were set up in a self gain regulating format. An example of BER versus launched optical power is shown in Figure 4.37 for a fiber length of 600 km. In this case, all of the EDFAs had a P_{SAT} of 6 dBm and a G_o of 30 dB with the link loss at 19 dB for 50 km EDFA separation. Thus, there were 13 EDFAs used in the link. One of these EDFAs served as a postamp at the transmitter and a second served as a preamp at the receiver.

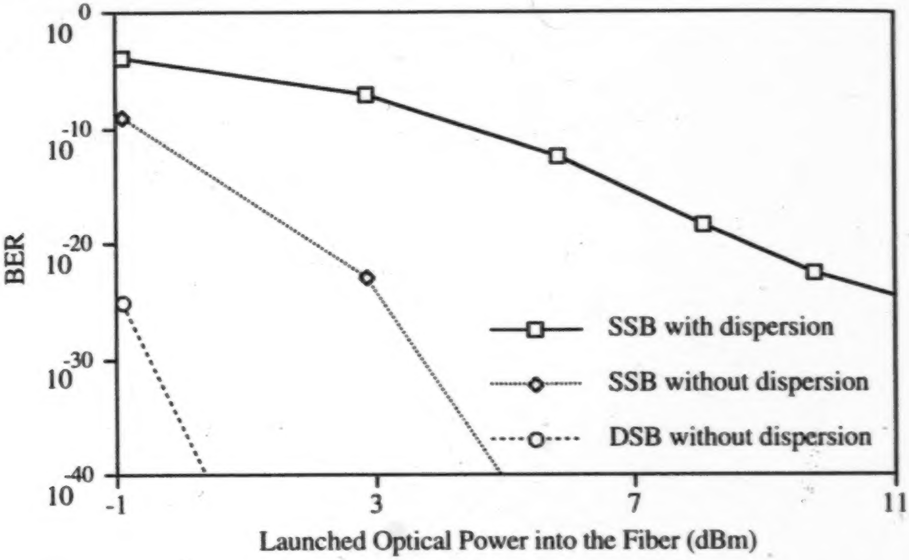

Figure 4.37 BER versus input power for 600 km fiber length for EDFA configuration with P_{SAT} of 6 dBm and a G_o of 30 dB with 50 km spacing between EDFAs

In a real system with DSB modulation, the optical equalization could be performed with dispersion compensating fiber. Dispersion compensating fiber is usually added to the system in a ratio of 4:1 where for every 4 km of standard single mode fiber used, 1 km of dispersion shifted fiber is needed for equalization. Dispersion compensating fiber also has a higher loss than standard single mode fiber at 0.5 dB/km at the 1.55 μm wavelength. Thus, if the previous system is considered where each link had 50 km of fiber, 40 km of it would be standard single mode fiber and 10 km of it would be dispersion compensating fiber. Thus, each link will have an additional 2.5 dB of loss due to the dispersion compensating fiber. In Figure 4.38, two of the same systems are shown again with a new one, DSB with dispersion. This new system is representative of a DSB system with full optical equalization but the link loss is now 21.5 dB representative of the higher loss incurred in each link by the dispersion compensating fiber.

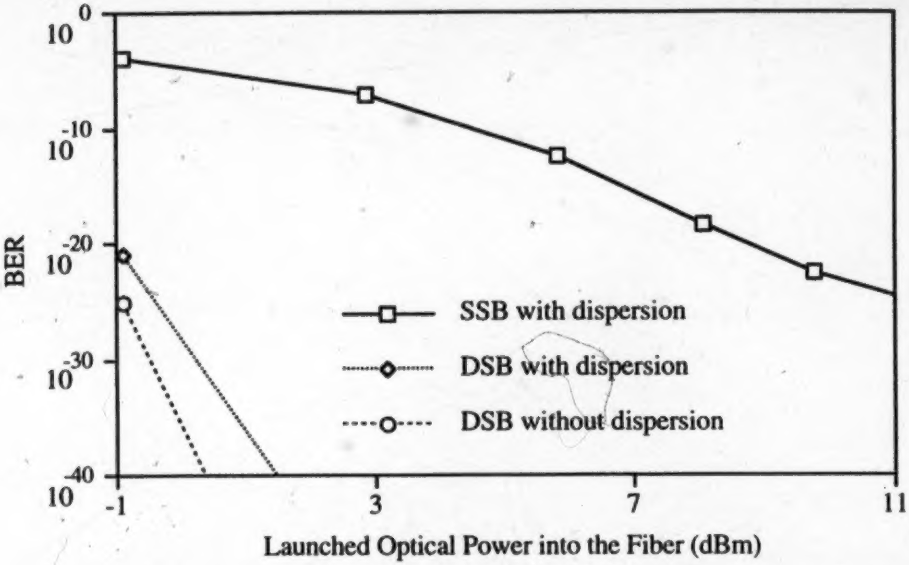

Figure 4.38 BER versus input power for 600 km fiber length with EDFA configuration with P_{SAT} of 6 dBm and a G_o of 30 dB and 50 km spacing between EDFAs

In the third system, all of the EDFAs in the cascade, including the EDFA pre-amplifier at the receiver, were modeled with a P_{SAT} of 15 dBm and a G_o of 28 dB. The EDFA gain in this case was fixed at 28 dB. The EDFAs were separated by 80 km sections of standard single mode fiber. As a result, the optical loss per stage was 28 dB (20 dB fiber loss, 4 dB splice loss and 4 dB insertion loss due to an isolator at the input of the EDFA and optical BPF at the output of the EDFA).

In this simulation, the optical gain of each amplifier was equal to and fixed at the loss of each link. The received BER versus required input optical power to the first EDFA in the system is shown in Figure 4.39. The plot shows the BER versus required input power for three cases, the DSB case with no dispersion, the SSB case with no dispersion and the SSB case where dispersion is included and the received signal is equalized with an ideal equalizer in the electrical domain. The fiber length is 560 km. Thus, eight EDFAs were used in the system. The launched power into the fiber for a given point on the x-axis in Figure 4.39 can be calculated by adding 28 dB to the power input to the EDFA post-amplifier.

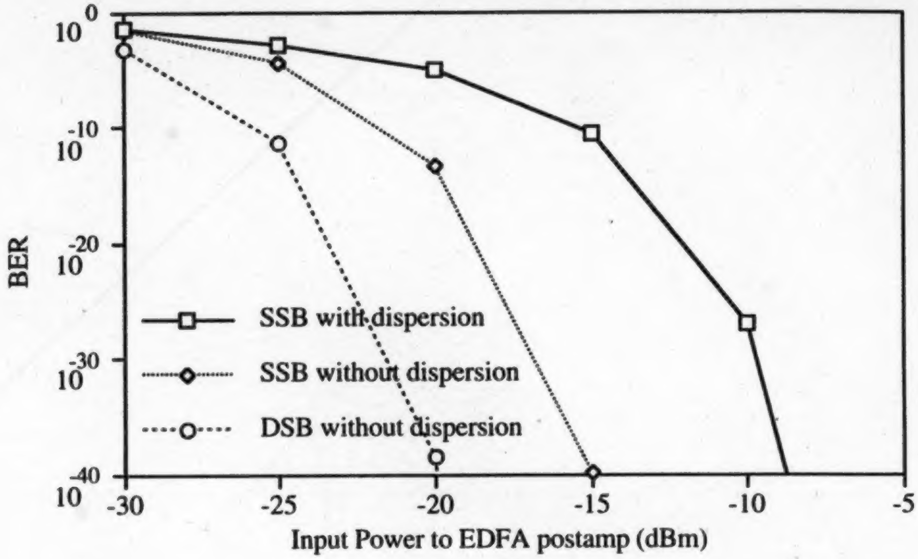

Figure 4.39 BER versus input power for EDFA configuration with a fixed gain of 28 dB at 560 km with 80 km spacing between EDFAs

In the fourth system, all of the EDFAs in the cascade, including the EDFA pre-amplifier at the receiver, were modeled with a P_{SAT} of 10 and a G_o of 25. The EDFAs in this case were allowed to self regulate. The EDFAs were separated by 80 km sections of standard single mode fiber. As a result, the optical loss per stage was 28 dB (20 dB fiber loss, 4 dB splice loss and 4 dB insertion loss due to an isolator at the input of the EDFA and optical BPF at the output of the EDFA).

In this case, the gain of each optical amplifier was less than the loss incurred in each link. As a result, the SNR degraded rapidly as the signal propagated from the transmitter to the receiver. The received BER versus required input optical power to the first EDFA in the system is shown in Figure 4.40. The plot shows the BER versus required input power for three cases at 320 km, the DSB case with no dispersion, the SSB case with no dispersion and the SSB case where dispersion is included and the received signal is equalized with an ideal electrical equalizer.

The differences between the EDFA configurations shown in Figure 4.39 and Figure 4.40 lie primarily in the ratio of available optical gain in each stage to optical loss in each stage. In the first EDFA configuration shown in Figure 4.39, the available optical gain in each stage was equal to the loss in each stage. However, for the EDFA configuration in Figure 4.40, the available optical gain in each stage was less than adequate to cover the loss in each stage. Thus, the SNR of the optical signal degraded very rapidly in Figure 4.40.

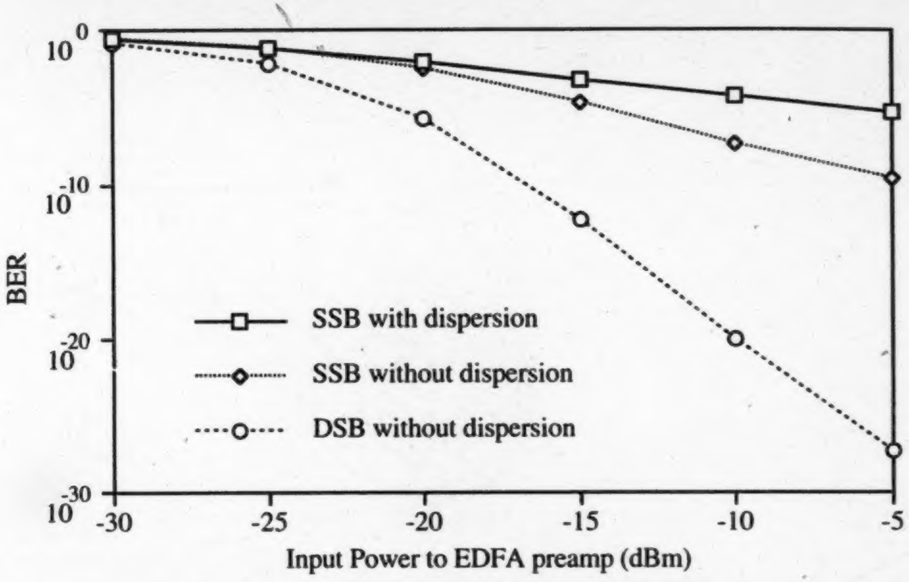

Figure 4.40 BER versus input power for EDFA configuration with P_{SAT} of 10 dBm and a G_o of 25 dB and 80 km spacing between EDFAs at 320 km

In all of the systems simulated, the DSB system with no chromatic dispersion outperformed the SSB case with no chromatic dispersion primarily because the MZ modulator was being driven harder in the DSB case and thus the optical extinction ratio between a zero and a one was larger in the DSB case. The SSB case with chromatic dispersion performed less favorably primarily because the received eye in the last system could not be fully equalized due to the vestige and more significantly to the distortion terms of the information evident after square-law detection. As such, some eye closure occurred in the received signal as the fiber length was increased beyond 200 km.

Comparing the three different EDFA configurations with the system employing electrical equalization and the DSB system employing optical equalization, it can be seen that the margin of improvement of the DSB system over the SSB system grows as the available gain of the EDFAs grows. Thus, as the EDFAs ability to recover the fiber loses decreases, it appears that the systems are more similar in terms of performance. However, this isn't a benefit of the SSB system. The SNR is degrading so fast with distance in all cases that they only look comparable.

From these systems, it can be seen that the DSB system employing realistic optical equalization still outperformed the SSB system employing electrical equalization. However, there are some other issues to be considered as will be discussed in Chapter 6.

4.3.5 Variations on the Pattern Length

In the previous simulations, the pattern length of the simulated bit sequence was always set to 127 or 2^7-1 bits. This was adequate for demonstrating the general concept of the SSB systems and variations on established transmitter and link configurations. However, most experimental systems are subjected to tests with much longer pattern lengths such as $2^{23}-1$. For longer pattern lengths, the low frequency content of the signal becomes more significant in the signal spectrum. This increase in low frequency content could prove to be important in SSB systems if signal power in the low frequency content resides in the vestige portion of the transmitted SSB signal. An attempt was made to try and measure this effect and the results showed that for a smaller pattern length of 2^5-1 or 31 bits, the receiver sensitivity for most distances was better than the 2^7-1 case. This was due to the eye pattern opening up more because of fewer traces across the eye. For a longer pattern length of 2^9-1 or 511 bits, the receiver sensitivity was generally worse because of more eye closure. However, for pattern lengths even still longer than 2^9-1, the eye did not close much more and the receiver sensitivity remained constant. To examine this effect more completely, a longer pattern length would have to be tested. The problem in carrying out this measurement in simulation was that simulated pattern lengths longer than $2^{10}-1$ took an extremely long time (> 4 hours) to compute with the current program. In fact, pattern lengths of $2^{23}-1$ would take an incredibly long length of time to compute in any program running on a personal computer. Regardless, systems simulated with pattern lengths in the 2^7-1 to the $2^{10}-1$ range sufficed since even though the longer pattern length was important, it wasn't essential when measuring the implications of major changes in the SSB configuration over distances less than 500 km.

To show the effect that the pattern length could have on a SSB system with a vestige, the receiver sensitivity versus pattern length for 1000 km is shown in Figure 4.41 for two cases. The first is where a Hilbert filter with four taps is used and the second is where a Hilbert filter with an infinite number of taps is used. The infinite number of taps was simulated through an ideal frequency response representation of the Hilbert function.

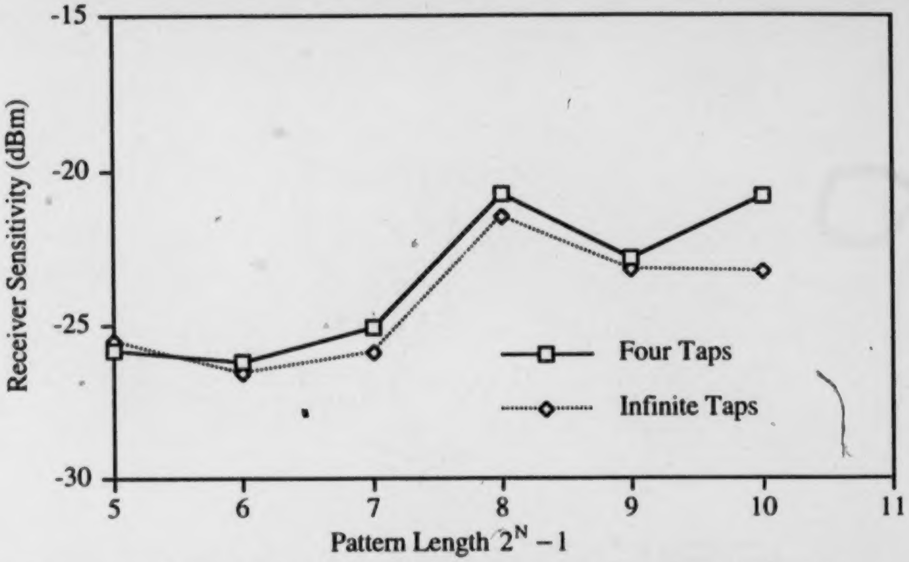

Figure 4.41 Receiver sensitivity versus pattern length for a fiber length of 1000 km

From Figure 4.41, it can be seen that the pattern length becomes significant in the system employing the four tap filter at lengths of $2^{10}-1$. This significance is seen at different fiber lengths for different pattern lengths due to the low frequency components in the vestige. The implications are a result of the dispersion limited distance of the low frequency components becoming critical. It is expected that this difference would become more pronounced with increasing pattern length. In addition, the difference would also become more significant with increasing fiber length due to increased dispersion.

4.3.6 Comparison of Normal Single Sideband with Composite Single Sideband

As outlined in section 3.5, a CSSB system provides the best SSB signal from an analytic approach. Thus, if the transmitter shown in Figure 3.24 is used to generate the optical signal, the optical electric field spectrum that is created at the output of the PM is shown in Figure 4.42.

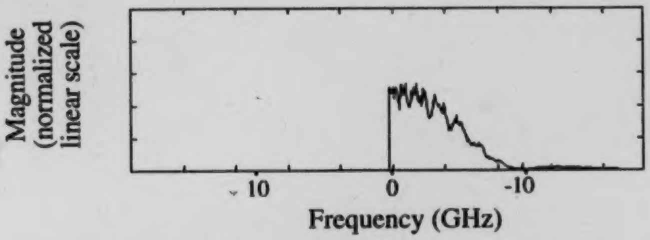

Figure 4.42 Optical electric field spectrum for CSSB

From Figure 4.42, it can be seen that this SSB spectrum provided the best sideband cancellation. As shown in the transmitter diagram in Figure 3.24, the output of the MZ modulator was used to create the Hilbert signal and thus all ordered terms were SSB. The previous cases had only the first order term in a SSB form.

In Powers' CSSB system, it is important to note that the amplitude of the modulation of the carrier is the square-root of the information signal. This way, the information is properly recovered upon square-law detection. This was not the case in the simulations using the CSSB transmitter shown in Figure 3.24. In this case, the information $m(t)$ was directly modulated onto the optical carrier with a MZ modulator in the conventional manner.

In Figure 4.43, the receiver sensitivity versus fiber length is shown for the regular SSB approach using Design 2 and the CSSB approach as shown in Figure 3.24. As can be seen in Figure 4.43, the performance is nearly the same for both cases, equalized and unequalized. This is a direct result of the fact that the information is not modulated onto the carrier in a square-root form. Thus, the level of sideband cancellation is only beneficial to a certain point. If there is a square-law detection process at the receiver, there will always be a squared term of the information providing some distortion.

This can be shown through an example. If the electric field is a perfect SSB signal of the form:

$$E = C + m(t) + j\hat{m}(t) \qquad (4.49)$$

where C is a carrier in phase with $m(t)$, the detected optical power is:

$$\left|E^2\right| = C^2 + 2Cm(t) + m^2(t) + \hat{m}^2(t) \tag{4.50}$$

Thus, as can be seen in equation 4.50, there is always distortion in the received signal due to the squaring of the information, even if there is perfect sideband cancellation. The only way this distortion is reduced is as the limit of ${}^{C}\!/_{m(t)}$ goes to infinity. However, as seen before, for noise purposes, the difference in transmitted optical powers between a one and a zero cannot be too small or else the system is less immune to noise. This translates into a higher BER at the receiver.

Implementing the CSSB system in Figure 3.24 is realistically impractical. Detecting the magnitude of the optical electric field and taking the perfect log of a 10 Gb/s digital signal impossible tasks at this time. Taking the perfect log means the log function cannot be approximated. Since the sideband cancellation process is based on analog signals, approximations to the log function would immediately create unwanted spectral components in the canceled sideband. Thus, the original designs described as Design 2 and Design 3 are good approximations to SSB operation. Benefit is seen from the nature of the SSB operation, even if there isn't perfect sideband cancellation.

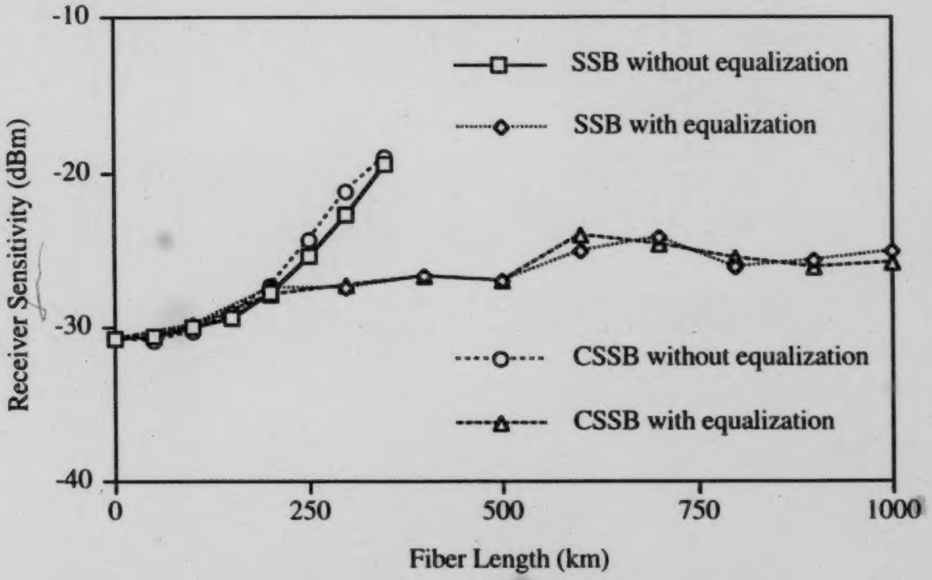

Figure 4.43 Receiver sensitivity versus fiber length for SSB and CSSB

4.3.7 Comparison of Design 2 with and without Square-Root Function

As was alluded to in the previous section, the square-root function is an important one since, in order to eliminate the distortion generating process of square-law detection, a square-root function is needed somewhere in the system. A case is examined where the regular SSB signal is created at the transmitter and a square-root function is used at the receiver such that the magnitude of the electric field is detected at the receiver rather than the magnitude of the optical power.

If a square-root function is implemented at the receiver following the square-law detector as shown in Figure 4.8, some improvements are seen in the received eye over the regular case. For example, Figure 4.44 shows the received eyes at 1000 km using a regular SSB transmitter with a normal square-law detector and with a square-law detector followed by a square-root function.

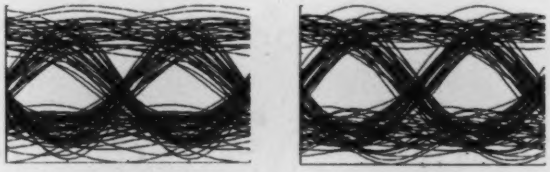
(a) (b)

Figure 4.44 Received eyes at 1000 km for (a) normal square-law detection and (b) square-law detection followed by a square-root function

From Figure 4.44, it can be seen that there is a small improvement in the eye opening when the square-root function is used. It can also be seen that the eye is also not totally distortion free. This is due to a number of factors. First, there are higher order distortion terms present from the MZ transfer function at the transmitter. Second, the square-root function follows the square-law detector plus the receiver filter frequency response. Practically, an approximation to the square-root function might be implemented experimentally by a diode.

As was shown in section 3.6, the noise processes of a random variable representing the photocurrent after square-law detection can be modeled as Gaussian. However, as was also shown, the noise processes at the output of the square-root are not Gaussian if the input random variable is Gaussian. Using the new noise derivations shown in section 3.6, the receiver sensitivity for a SSB system with square-law detection and with and without the square-root function was calculated and is shown in Figure 4.45.

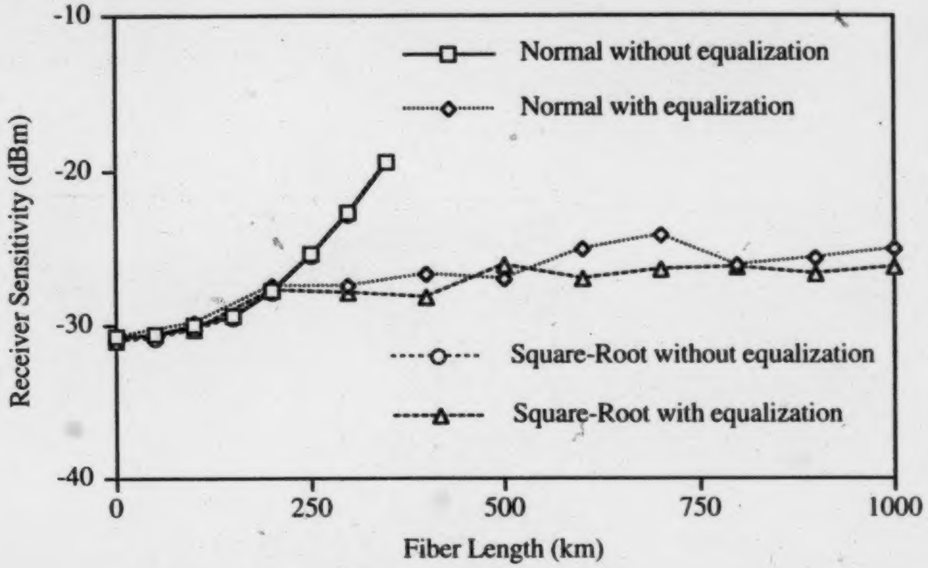

Figure 4.45 Receiver sensitivity versus fiber length for normal square-law detection and square-law detection followed by a square-root function

From Figure 4.45, it can be seen that for the unequalized case, there is no improvement in the receiver sensitivity. This is correct since putting a random variable with a certain amount of noise or a given SNR through a nonlinear function doesn't create a new random variable with a better SNR. At best, the SNR will stay the same. However, it can also be seen that if equalization is added, there is an improvement seen if the square-root function is added at the receiver. This is primarily due to the fact that the second order term of the information created upon detection is reduced with respect to the first order information which is the desired signal.

In the previous simulations, the time of calculation for the receiver sensitivity was considerably longer for the system implementing the square-root function at the receiver than the normal case. This was due to the fact that an additional integral was required at each bit to calculate a new noise variance as shown in equation 4.48. Further, at each bit, the common complementary error function (erfc) could not be used to calculate the probability of error for each bit as it is in the Gaussian case. Since the distribution is skewed as shown in Figure 4.11, another integral of the probability density function for each bit had to be carried out to determine the new probability of error. A program that uses the erfc function is considerably faster than one that numerically computes the integral since subroutines have been professionally written to speed up this calculation. Thus, it was of interest to see the comparison between the probability of error generated by using the new variance in a case where the new non-Gaussian distribution was used and one where the new variance was used but the probability density function was assumed to be approximately Gaussian so that the probability of error calculations could be speeded up by using the erfc function. The results of this comparison are shown in Figure 4.46.

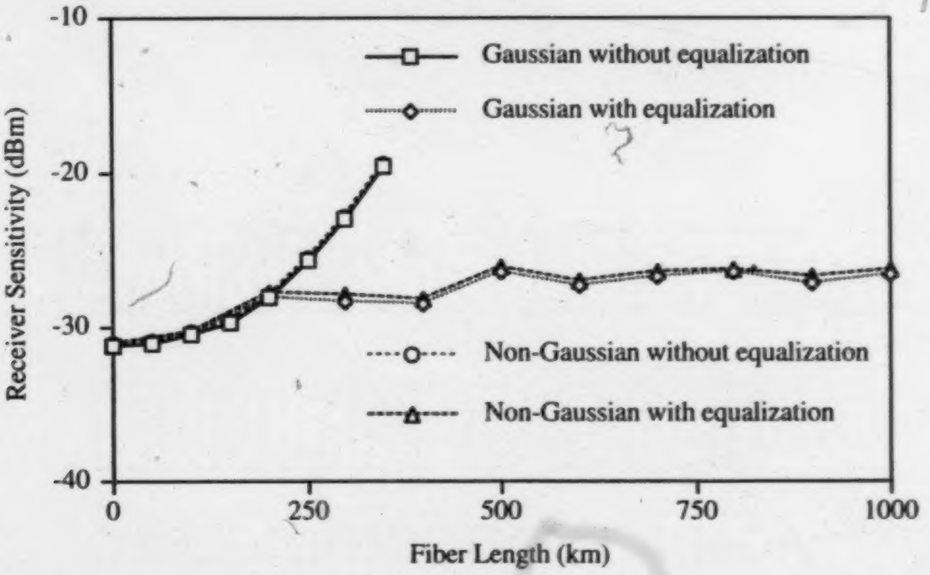

Figure 4.46 Receiver sensitivity for square-root with Gaussian and non-Gaussian noise processes

From Figure 4.46, it can be seen that for the cases of interest, the new probability density functions after the square-root function can be approximated to be Gaussian and close to the same results are obtained. The primary difference between using the two approximations lies in the optimum threshold level. Since the absolute value of the threshold is unimportant in the simulations, the substitution is acceptable.

Using a Gaussian approximation to speed up the simulations, the modulation parameter P and the bias angle θ were checked again in a system where a square-root function was employed at the receiver.

Figure 4.47 shows the receiver sensitivity versus bias angle for different modulation parameters at a fiber length of 600 km. Figure 4.48 shows the BER versus launched optical power for different modulation parameters at 600 km. Again, the BER curve for each modulation parameter is calculated at the optimal bias point, or the point that gives the best receiver sensitivity for that modulation parameter.

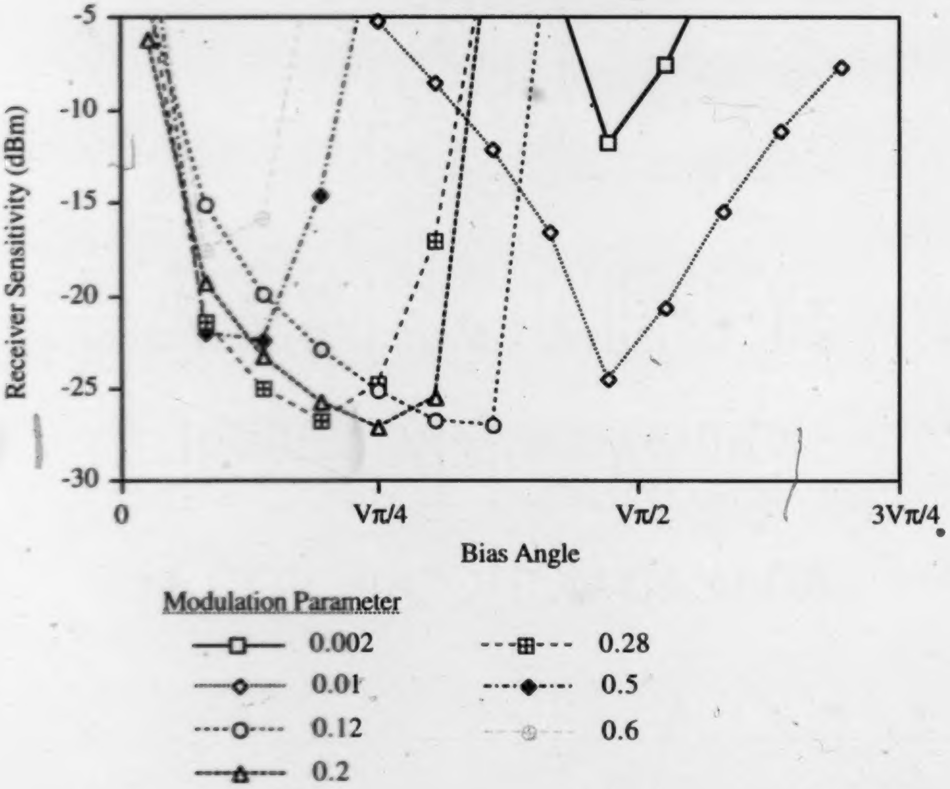

Figure 4.47 Receiver sensitivity versus bias angle for 600 km with square-root function at the receiver

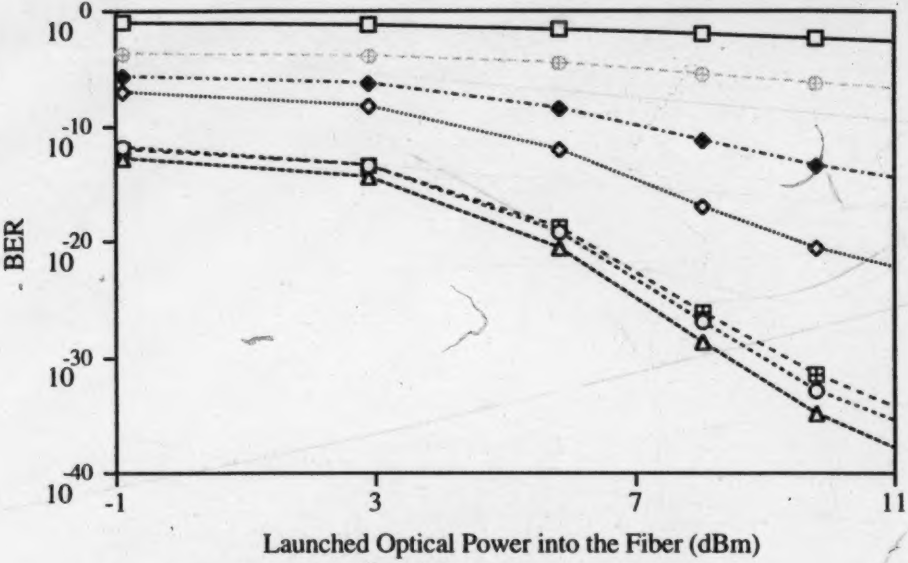

(Legend for Modulation parameters is the same as Figure 4.47)

Figure 4.48 BER versus bias angle for 600 km with square-root function at the receiver

From Figure 4.47 and 4.48, it can be seen that a modulation parameter *P* of 0.2 at a bias angle of $\theta = {}^{V_\pi}\!/_{4}$ was still the optimum case, even when the square-root function was employed at the receiver.

4.3.8 Single Sideband with Non-Zero Source Linewidth

Additional investigations showed that the laser linewidth was a primary factor in limiting the transmission distance. The inhibiting factor originating from the laser linewidth is a FM-AM noise conversion which is dependent on the laser linewidth and the amount of chromatic dispersion incurred by the fiber. Variations in the instantaneous wavelength of the source are a result of an inherent FM noise in the laser. These frequency deviations are generally classified as a source linewidth which is measured as the 3 dB spectral width of the source over a given time interval. Through the interaction of the dispersion and the square-law detection process, the FM noise is converted to an AM noise. This type of noise has minimal effects in DSB systems employing optical equalization for dispersion but it is significant in SSB systems using post detection equalization. In optically equalized systems, the dispersion is essentially zero at the point of detection and thus the FM noise is not detected. In the SSB system where the equalization is post detection, the FM noise distorts the spectral components further away from the carrier. This phase deviation incurred by the FM noise is not reversible in the post detection domain.

Investigating this noise process further, the maximum laser linewidth versus fiber length for the SSB system known as Design 2 is shown in Figure 4.49. This is the maximum source linewidth that is allowed, considering it is the only noise source in the system, that would maintain a BER of 10^{-9} at the receiver.

In order to calculate the maximum allowable linewidth in Figure 4.49, equations 4.31 to 4.33 were used. These equations described the relationship of the FM-AM noise process. As previously mentioned, this noise is dependent on the interaction of the chromatic dispersion in the fiber with the source linewidth. Thus, the additional parameters involved in this calculation were the fiber length, the dispersion coefficient, the electrical bandwidth and the wavelength of operation. For these simulations, the dispersion coefficient was again set at 17 ps/km-nm, the electrical bandwidth was set at 8 GHz and the wavelength of operation was 1.55 μm. To calculate a required linewidth for a given distance, the noise free eye was determined from simulation. From this eye, the extinction ratio of the open eye was measured and used to determine what the maximum RIN due to FM-AM noise could be in order to maintain a given BER. The relationship is given as [44]:

$$RIN = \frac{1}{Q^2}\left[\frac{k-1}{k+1}\right]^2 \tag{4.51}$$

where k is the ratio between the mean values for a one and a zero and Q is the number of standard deviations from a given level to the optimal decision threshold. For a BER of 10^{-9}, Q is 6.

It is interesting to note that the FM-AM noise penalty increased as the fiber length increased and the eye became smaller. Thus, the chromatic dispersion has a double negative impact on the system since it closes the received eye as well as increases the level of FM-AM noise. For the linewidth calculations in Figure 4.49, the dispersion effected eye for the distance of interest is used for each calculation since it is not realistic to use a 0 km eye to calculate the FM-AM noise at 1000 km.

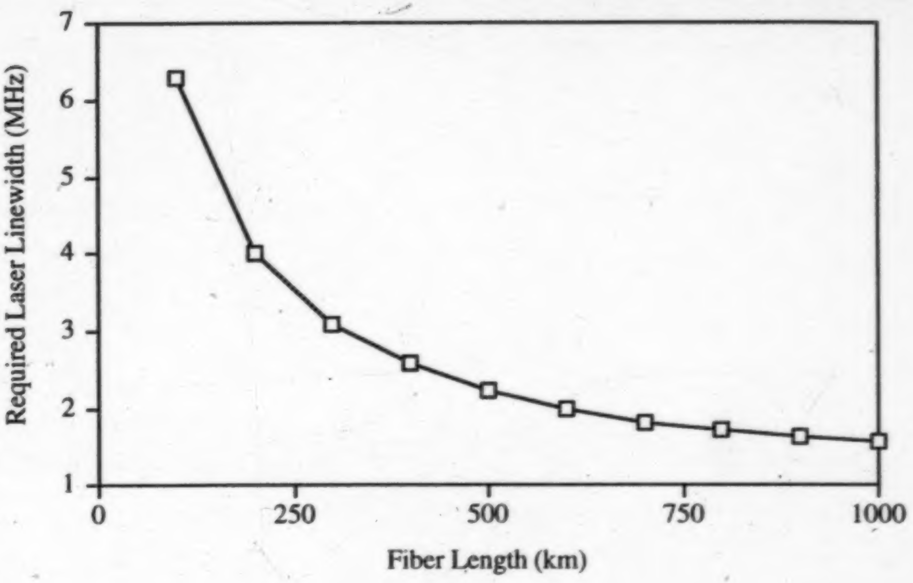

Figure 4.49 Required laser linewidth for a BER of 10^{-9} versus fiber length for a SSB system

From Figure 4.49, it can be seen that the FM-AM noise limited distance for a system using a source laser with a linewidth of 4 MHz is approximately 200 km. For systems longer than 1000 km, a source linewidth less than 1 MHz would be required.

In the next set of simulations, variations in the laser source linewidth in the context of the full EDFA cascade were examined. Thus, all of the system noise sources, including the FM-AM noise, were considered. Throughout the simulations earlier on in Chapter 4, the source linewidth was always set to zero. To show that this was the optimal value, values for the source linewidth ranging from 0 to 4 MHz were simulated for Design 2. In the following simulations, the fiber was modeled the same as in the previous simulations with the same loss and dispersion coefficient. The EDFAs were self gain regulating with a G_o of 30 dB, a P_{SAT} of 6 dBm and a N_{SP} of 2. In this simulation, the total fiber length was 540 km and the EDFAs were separated by 45 km intervals. The received BER versus launched optical power out of the EDFA post-amplifier for the varying linewidths are shown in Figure 4.50.

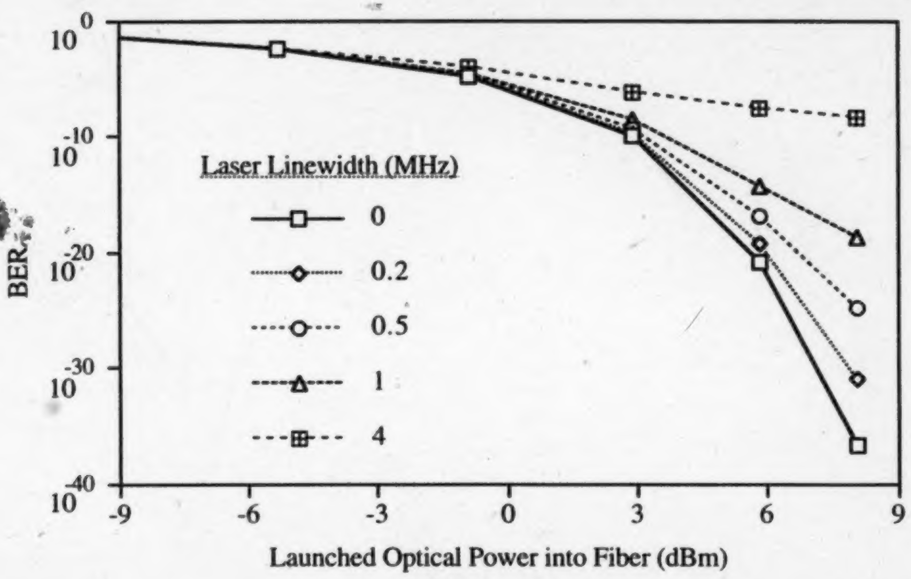

Figure 4.50 BER versus launched optical power into the fiber for 540 km fiber length for different values of source linewidth

From Figure 4.50, it can be seen that the lowest BER curve occurs when the laser source linewidth is zero. As the linewidth increases, the BER curve becomes worse and as the launched optical power increases, the curve hits a floor as predicted by the FM-AM noise theory. This theory predicts that the FM-AM noise is dependent on both the laser linewidth and the fiber length and as such, increasing either the length or the linewidth degrades the systems performance. For 540 km, it can be seen that if a BER better than 10^{-9} is to be achieved, a linewidth less than 1 MHz is required.

4.3.9 Modeled Microstrip Equalizer

In the previous simulations, ideal equalization in the form of an inverse fiber function implemented at the electrical level was used in order to demonstrate the theoretical capability of optical SSB systems. In a real experiment, the equalization must be carried out with a microstrip line or some other type of equalizer. In this simulation, the microstrip was modeled as a stripline microstrip with a frequency dependent group velocity and attenuation.

In order to show how the system performed over long distances, the modeled microstrip was used to equalize the received signal and was defined by the equations shown in section 4.1. The eye diagrams of a received signal using the modeled microstrip at distances of 300 km, 800 km and 1000 km are shown in Figure 4.51.

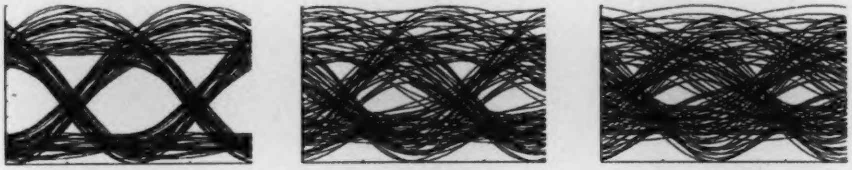
(a) (b) (c)

Figure 4.51 Received eye diagram using Design 2 for (a) 300 km and (b) 800 km and (c) 1000 km using the modeled microstrip equalizer

From Figure 4.51, it can be seen that the equalized eye at 300 km might be adequate but the eye at 1000 km is not very good.

Investigating this process further, the receiver sensitivity versus distance is shown in Figure 4.52 for the SSB system with ideal equalization represented by the inverse fiber function and a modeled microstrip equalizer. For this particular microstrip model, the previous parameters for permitivity, height and width of 10.2, 1 mm and 1 mm respectively were used. In this model, the frequency dependent conductor loss was modeled using equations 4.23 and 4.24 with σ for Copper set at 5.8e7 S/m.

From Figure 4.52, it can be seen that for distances beyond approximately 500 km, the systems performance using the microstrip equalizer degraded. This is due to two factors. First, the microstrip is only an approximation to the inverse fiber transfer function, it is not exact. Second, as also mentioned in section 4.1, the microstrip has a frequency dependent attenuation constant. This attenuation is significant when the microstrip length exceeds 40 cm which is the predicted amount of microstrip needed to equalize 500 km of standard single mode fiber. Thus, the more microstrip that is needed, the more degraded the equalized eye is from the microstrip.

Figure 4.53 shows a plot of the microstrip length needed to equalize a given length of fiber. These microstrip lengths were used for the receiver sensitivity calculations shown in Figure 4.53 and were the optimal microstrip lengths for each fiber length. The microstrip length was optimized in each case by maximizing the eye opening at the receiver for each fiber length. As can be seen from Figure 4.53, the relationship is approximately linear.

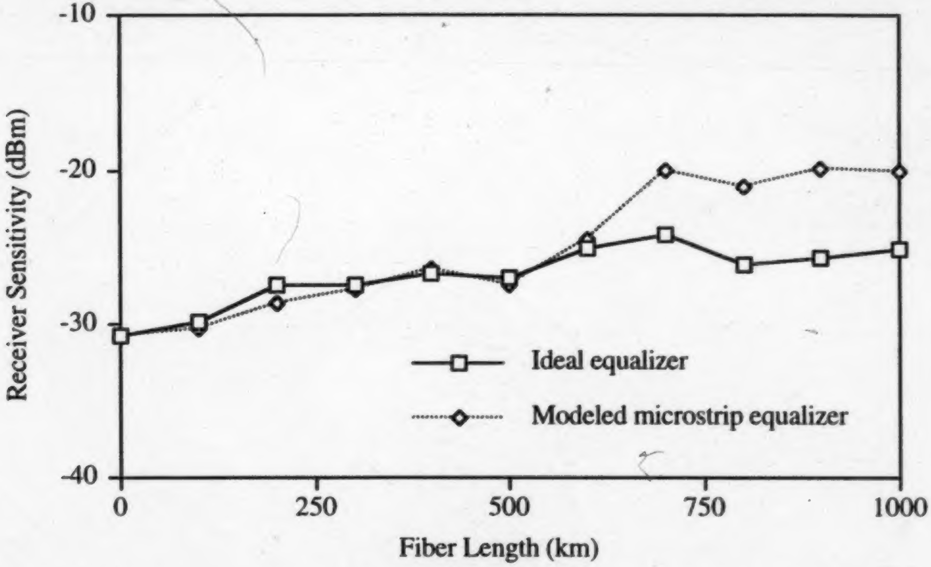

Figure 4.52 Receiver sensitivity versus fiber length using an ideal and a modeled microstrip equalizer

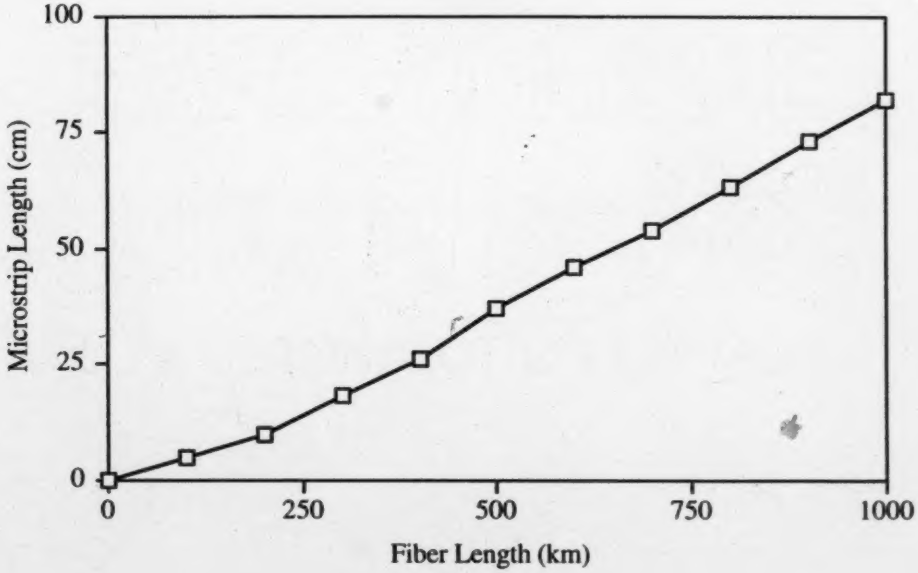

Figure 4.53 Microstrip length versus fiber length using Design 2

5. DIGITAL OPTICAL SINGLE SIDEBAND EXPERIMENTAL RESULTS

5.1 Introduction to the Experiments

As was shown in Chapter 4, a number of different transmitter designs exist for generating digital optical SSB signals. Systems with varying levels of sideband cancellation and performance were shown. These included Designs 1 through 3 and the original CSSB design. Different detection schemes were also suggested such as square law detection and also square-law detection with an additional square root function implemented post detection. Along with the different modulation formats, different Hilbert transform circuits and different modulation parameters were also suggested and simulated. Although some designs present themselves as theoretically the best alternative, they may not be the best design to implement experimentally. When it comes to implementing a circuit or system with real components, tradeoffs must be considered. These tradeoffs consist mainly of limitations of actual components versus the improvement in overall performance they create. In most cases, some theoretical functions can only be approximated and as such, the level of nonideality must be considered and weighed off against the benefit supplied in the design.

Consequently, a number of choices were made in deciding which implementation of optical SSB would be assembled and tested. First, Designs 2 and 3 were selected to be implemented experimentally due to their improved simulated performance over Design 1. Second, the tapped delay line Hilbert transform circuit was used since it was more readily implementable than any of the modified Weaver approaches. Further, the tapped Hilbert filter was approximated with four taps. Four taps were used since a 4:1 broadband combiner was readily available and as shown in the simulations, provides for adequate representation of the Hilbert signal. The true CSSB method was not implemented at the transmitter since it is not possible with today's technology to detect the envelope of the electric field and implement a perfect natural logarithm on broadband data. At the receiver, regular square-law detection was implemented with a pin detector. The square root option following the receiver was also not implemented since if it were, it would only be an approximation with a nonlinear element and probably would not offer any significant benefit. The equalizer, as already mentioned, was implemented in microstrip. As previously mentioned, the microstrip provides a good approximation to the inverse phase response of the second order dispersion in the fiber. The approximation is not exact but due to the inexpensive construction of the microstrip lines and the ease of design, were the best alternative at this time.

One of the underlining goals in the implementation of the optical SSB system was simplicity. By making minimal changes to a regular optical DSB system, conversion to an optical SSB system would seem more favorable than if major changes would be required. This is especially true for optical systems that are already installed. The optical SSB systems tested in this chapter offer a compromise between ease of implementation, realistic components and improved performance. To implement these optical SSB systems, the only changes that would have to be made to a conventional DSB system would be to modify the incoming data channels such that the modulators would be driven to give optical SSB and to add an appropriate length of microstrip in the post detection electrical circuit.

Experiments on the optical SSB system were carried out at two locations. The first was at TR Labs in Edmonton, Alberta while the second was at the Skyline lab at Nortel in Ottawa, Ontario. The majority of the developments and experiments were carried out at TR Labs while a final set of experiments were carried out at Nortel to investigate certain scenarios.

5.2 Optical Spectrum Analyzers

One of the important considerations when assembling the optical SSB transmitter is the degree of sideband cancellation. The optical SSB system will perform best when the sideband cancellation is optimized. This sideband cancellation can be nonideal for a number of reasons including improper timing of the data and it's Hilbert transform, improper timing of the taps in the Hilbert filter, improper drive levels of the modulators and improper polarization of the light entering the modulators.

The optical spectrum of the information signal cannot be properly measured by conventional optical spectrum analyzers since their lowest resolution is in the range of 0.1 nm or 12.5 GHz. To measure the information spectrum, a new optical spectrum analyzer was constructed. This was achieved by using a Fiber Fabry Perot (FFP) interferometer to sweep the optical spectrum. The acquired FFP device had a bandwidth of 100 MHz and a free spectral range (FSR) of 40 GHz. The voltage required to sweep one FSR was approximately 12V. The principle of operation of the device is that when a voltage is applied to a piezoelectric element, the effective cavity length of the device changes. Thus, the resonant frequency of light transmitted by the cavity changes proportionately. Thus, a linear sweep of applied voltage provides for a close-to-linear sweep of optical frequencies transmitted.

There were two different designs of a system that would give a spectral sweep of the optical frequencies of interest. The optical spectrum display circuit for the first design is shown in Figure 5.1.

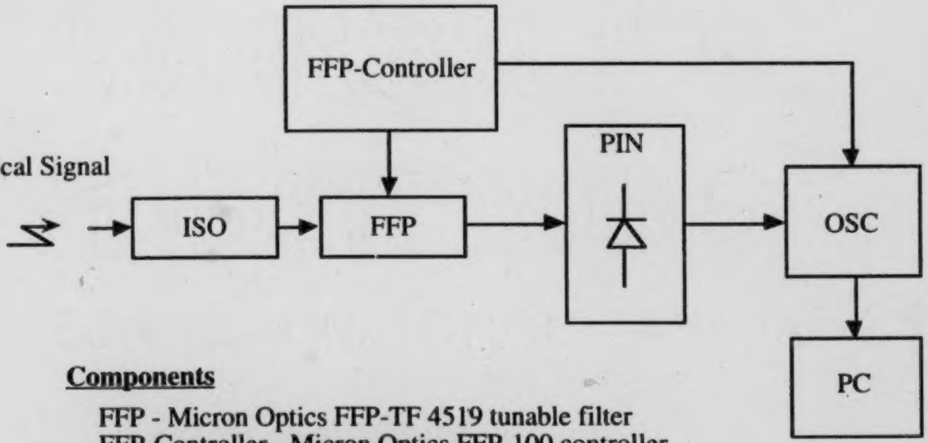

Components

FFP - Micron Optics FFP-TF 4519 tunable filter
FFP-Controller - Micron Optics FFP-100 controller
ISO - JDS IS2500 optical isolator
OSC - Tektronics 2430 digital oscilloscope
PC - Macintosh IIsi personal computer
PIN - BT&D photodetector

Figure 5.1 Optical spectrum analyzer using a FFP, a pin diode and an oscilloscope

In the first design, the FFP was driven with a triangle wave from a FFP controller. The transmitted light through the FFP device was detected with a photodiode and the received electrical signal was displayed on a digital oscilloscope. In this design, the FFP controller triggered the oscilloscope such that the optical spectrum could be continuously displayed on the oscilloscope. This was useful in phase aligning the electrical drive signal to the PM in Design 3. The display on the oscilloscope was captured on file with the use of a Labview program written on a Macintosh personal computer.

One of the problems encountered with the design shown in Figure 5.1 was that the spectral components of the data ranging from 5 to 10 GHz away from the carrier were below the noise floor of the displayed spectrum. The vertical scale on the spectral plot was linear. Thus, not only were some of the spectral components of the data buried below the noise floor but the information spectrum and the carrier could not be displayed on the screen at the same time because of the significant power in the carrier.

To partially correct for this problem and improve the quality of the spectral plots, the large dynamic range of a Hewlett Packard (HP) optical power meter was used as the detecting element. With the new power meters logarithmic scale, the spectral components of the information in the 5 to 9 GHz range away from the carrier were better displayed. In addition, the peak power of the carrier could also be displayed. The new design is shown in Figure 5.2.

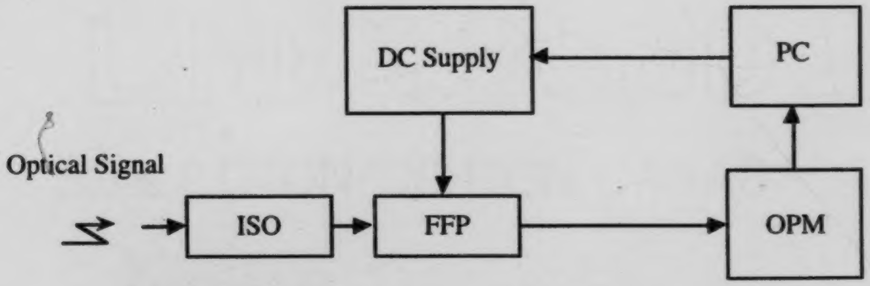

Components

FFP - Micron Optics FFP-TF 4519 tunable filter
DC Supply - Keithly 576 addressable DC supply
ISO - JDS IS2500 optical isolator
OPM - HP 8153A optical power meter
PC - Macintosh IIsi personal computer

Figure 5.2 Optical spectrum analyzer using a FFP and an optical power meter

Due to the slow response time of the optical power meter, the triangle wave generated by the FFP controller could not be used to drive the FFP in the second design. The lowest frequency wave generated by the FFP controller was too high for the optical power meter. Thus, an addressable dc power supply was used to generate the linearly increasing voltage signal. The addressable dc supply and the optical power meter were both controlled from a Labview program running on a Macintosh personal computer so that the delay time between incremental step in voltage could be set long enough to allow the optical power meter to take an accurate reading. The output of the optical power meter was logged in a file and plotted. This design provided a better measurement of the optical spectrum but the acquisition time was much slower.

5.3 Experiments at TR Labs

5.3.1 Supporting Circuits

To verify the theory developed in Chapter 3 and the simulation results presented in Chapter 4, the systems developed as Design 2 and Design 3 were assembled and tested. In addition, a standard DSB system was also assembled and tested for comparison purposes. The data rate for all of the optical systems was the OC-192 rate (~ 10 Gb/s).

A number of the subsystems used in each design were similar for all of the experiments. This included the generation of the 10 Gb/s data signals, labeled as Q and Qbar, from the 2.5 Gb/s data supplied by the Bit Error Ratio Test set (BERT), the 10 GHz clock at the transmitter, the photodetector and receiver circuit, and the 2.5 GHz clock recovery circuit at the receiver. Q and Qbar are representative of scaled versions of $m(t)$ and $-m(t)$ which have been used in the mathematical derivations in the previous chapters.

The HP pattern generator (model: 70841A) within the BERT supplied 2.5 Gb/s data and data bar signals. These signals were multiplexed (MUX) to generate a 10 Gb/s signal as shown in Figure 5.3.

In addition, in order to run the 4:1 MUX properly, a 10 GHz clock was needed as an input to the MUX. It was generated from the 2.5 GHz clock supplied by the BERT set as shown in Figure 5.4.

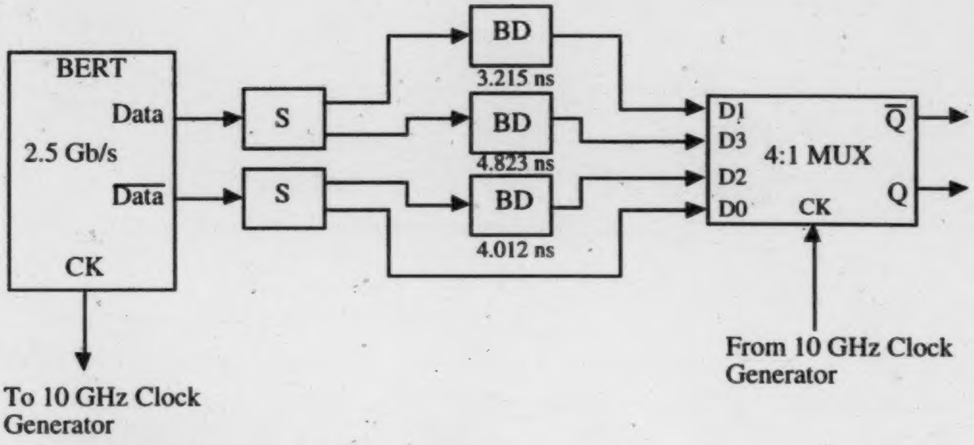

Components

BERT - HP bit error ratio test module
S - Mini-Circuits ZFSC-42 resitive splitter
BD - bulk delay
4:1 MUX - NEL NLG4219 4:1 multiplexer

Figure 5.3 Circuit to generate 10 Gb/s data from 2.5 Gb/s data supplied by the BERT

The receiver circuit for all of the optical DSB and SSB experiments is shown in Figure 5.5. In the receiver circuit, amplifiers were required post detection to boost the power of the signal to levels appropriate for the GaAs logic. The equalizer shown in Figure 5.5 is representative of the microstrip used to reverse the chromatic dispersion effects induced by the fiber in the SSB designs. At the receiver, the timing of the 2.5 GHz clock driving the D flip-flop (D-FF) was time delayed with a line stretcher such that any one of the four data channels multiplexed together could be sent to the BERT for a BER measurement. In all of the BER measurements, the channel showing the worst BER was used as the value representative of the entire system.

In addition, in order to clock the receiver decision making D-FF properly, a 2.5 GHz clock was extracted from the received data. This clock recovery from the data was essential in order to track any phase drifts in the received data incurred from the fiber. These drifts were significant in long lengths of fiber such as more than a few km. The clock recovery circuit is shown in Figure 5.6.

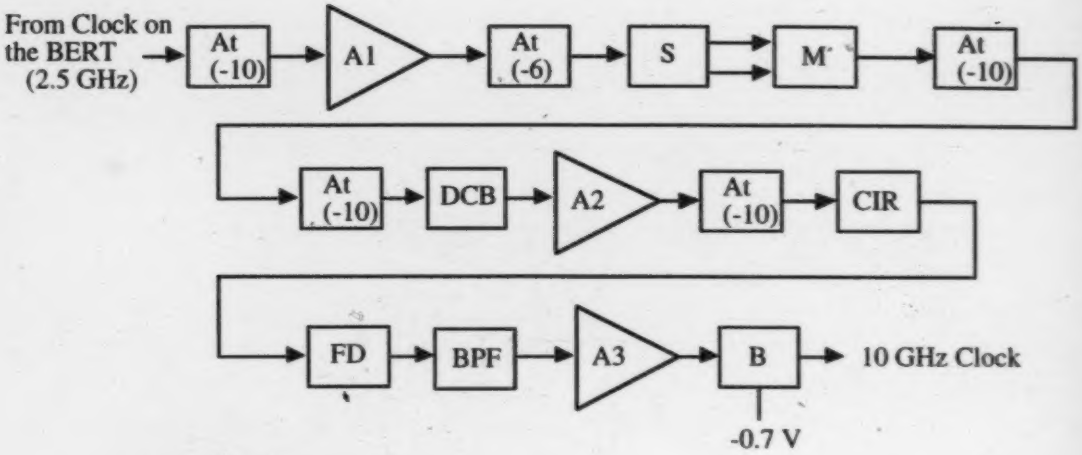
From Clock on the BERT (2.5 GHz)
At (-10)
A1
At (-6)
S
M
At (-10)
At (-10)
DCB
A2
At (-10)
CIR
FD
BPF
A3
B
10 GHz Clock
-0.7 V

Components

A1 - Mini-Circuits ZHL-1042J amplifier
A2 - Avantek AWT-8035 amplifier
A3 - Veritech VM10LA-155 limiting amplifier
At - ARRA attenuator (-x dB)
B- Picosecond Pulse Labs 5575A bias tee
BPF - K&L 5C52-9952/T20/0/0 band pass filter
CIR - Narda 4924 circulator
DCB - Picosecond Pulse Labs 5500A DC block
FD - Wilkinson Johnson FD93C frequency doubler
M - Narda 4804 mixer
S - Mini-Circuits ZFSC-42 resitive splitter

Figure 5.4 Circuit to generate 10 GHz clock from 2.5 GHz clock supplied by the BERT

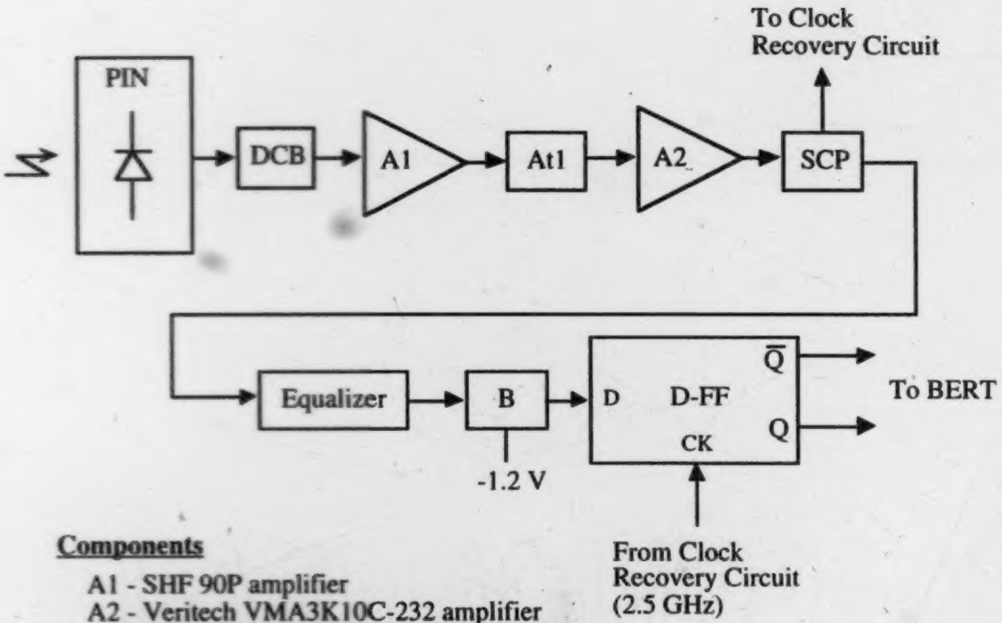
To Clock
Recovery Circuit
PIN
DCB
A1
At1
A2
SCP
Equalizer
B
-1.2 V
D
D-FF
CK
$\overline{Q}$
Q
To BERT
From Clock
Recovery Circuit
(2.5 GHz)

Components

A1 - SHF 90P amplifier
A2 - Veritech VMA3K10C-232 amplifier
At1- HP 8495B variable attenuator (0-70 dB)
B- Picosecond Pulse Labs 5575A bias tee
DCB - Picosecond Pulse Labs 5500A DC block
D-FF - NEL NLG4104 D-flip flop
Equalizer - Microstrip equalizer (used in SSB designs)
PIN - BNR PIN-Preamp module
SCP - PSPL 5520C probe

Figure 5.5 Receiver and decision circuit

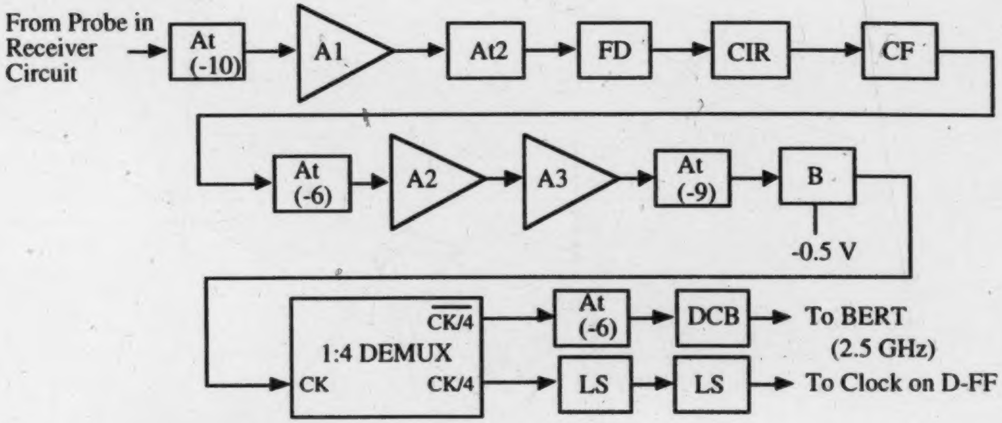
From Probe in Receiver Circuit
At (-10)
A1
At2
FD
CIR
CF
At (-6)
A2
A3
At (-9)
B
-0.5 V
1:4 DEMUX
CK
$\overline{CK/4}$
CK/4
At (-6)
DCB
LS
LS
To BERT (2.5 GHz)
To Clock on D-FF

Components

A1 - CTT APM/080-3036 amplifier
A2 - Miteq JS4-00102600-03 amplifier
A3 - Avantek LMT-12436 amplifier
At - ARRA attenuator (-x dB)
At2 - Wienschel 21-10 842 high power 10 dB attenuator
B- Picosecond Pulse Labs 5575A bias tee
CF - K&L 6C60-9953/T10-0/0 cavity filter
CIR - Narda 4924 circulator
DCB - Picosecond Pulse Labs 5500A DC block
FD - Narda 4453 frequency doubler
LS - MA/Com 2054-6103-00 line stretcher
1:4 DEMUX - NEL NLG4219 1:4 demultiplexer

Figure 5.6 Clock recovery circuit to regenerate 2.5 GHz clock from the received data at the receiver

5.3.2 Electrical Magnitude Spectra

One of the first experimental measurements taken was spectral plots of the electrical 10 Gb/s data signals $m(t)$ representing the binary information and $\hat{m}(t)$ representing the Hilbert transform of the information. The measurement of $m(t)$ is shown in Figure 5.7 and the measurement of $\hat{m}(t)$ is shown in Figure 5.8.

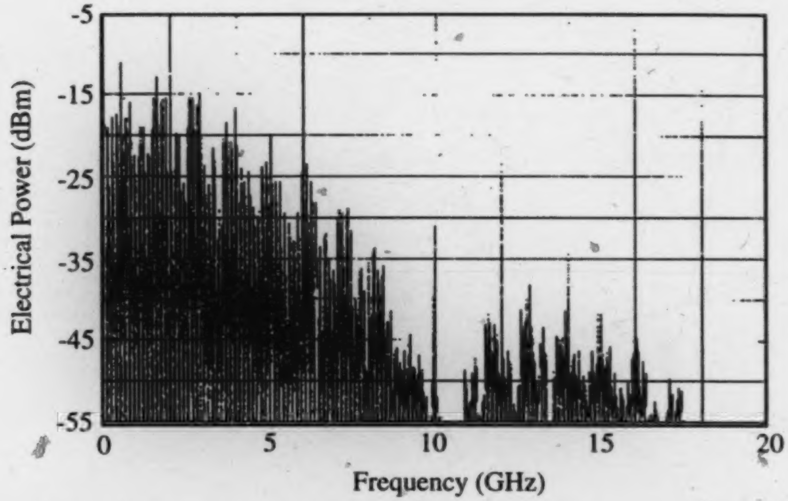

Figure 5.7 Electrical magnitude spectrum of the signal $m(t)$

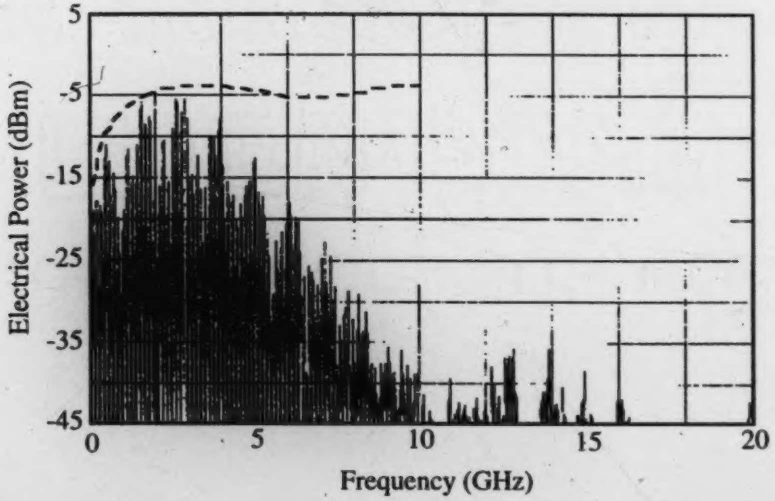

Figure 5.8 Electrical magnitude spectrum of the signal $\hat{m}(t)$ with the magnitude response of the four tap Hilbert filter overlayed as a dashed line

These spectra were measured with a HP 8565E spectrum analyzer. This spectrum analyzer could display the information spectrum from 9 kHz to 10 GHz on one screen without any discontinuities in the noise floor. Discontinuities in the noise floor can result from the spectrum analyzer using multiple local oscillators with different noise characteristics to sweep a given frequency range. This spectrum analyzer used a single local oscillator with a sweep capability from 9 kHz to 50 GHz.

The spectral response of each signal was measured at the input to the modulators. Since these signals were to be used in a transmitter configuration implementing Design 3, the signal in Figure 5.7 representing $m(t)$ would drive one arm of a MZ modulator while the signal in Figure 5.8 representing $\hat{m}(t)$ would drive the PM. In the experiment, the MZ modulator had a V_π of about 4.4 V while the PM had a V_π of about 8.9 V. Thus, this difference in V_π accounts for the increased power in $\hat{m}(t)$ shown in Figure 5.8 over $m(t)$ in Figure 5.7.

Examining the spectral response of $m(t)$ in Figure 5.7 in more detail, it can be seen that the first spectral null in frequency is at 10 GHz which is correct for a 10 Gb/s binary NRZ signal. Spectral components are evident beyond 10 GHz due to the nature of the digital information created by the signal source. However, these components are strongly attenuated after modulating the MZ modulator since the 3 dB spectral width of the MZ modulator is around 8 GHz. This bandwidth is adequate for transmitting the 10 Gb/s data.

The spectral content of $\hat{m}(t)$ in Figure 5.8 is the approximate Hilbert transform of the information $m(t)$. As previously mentioned, the Hilbert transfer function is approximated with a four tap delay line filter. In Figure 5.8, the magnitude response of the four tap filter is overlayed on the magnitude spectrum as a dashed line. Due to the magnitude response of this filter, it can be seen that the low frequency spectral components near the carrier are attenuated. This is a direct result of the low number of taps. Spectral components are also evident beyond 10 GHz but are smaller than in the case for $m(t)$ due to a number of factors such as magnitude response of the tapped delay filter and more importantly, roll-off of electrical components used to create the Hilbert signal. The frequency components above 10 GHz were also attenuated after modulation since the 3 dB spectral width of the PM was also around 8 GHz.

5.3.3 System Layouts and Results

5.3.3.1 BNR III-V Module in DSB and SSB Design 3 Configurations

In the first set of experiments, a BNR III-V module which consisted of a DFB laser and a MZ modulator integrated into one package was used as the source and modulating device. Before the acquisition of the Lucent MZ modulator, this was the only dual arm MZ modulator available with adequate electrical bandwidth. Thus, it had to be used in the first DSB and SSB systems. The linewidth of the laser mounted in the module was approximately 35 MHz. This linewidth posed a problem in the amount of FM-AM noise generated at the receiver due to the interaction of the laser phase noise with the fiber chromatic dispersion as seen in the simulated and later, experimental results. In addition, the wavelength of operation of the laser was at 1555 nm which was not compatible with the gain peak of the EDFAs at 1535 nm. However, because the laser and MZ modulator were integrated into one module, an alternate laser source could not be used.

As a baseline measurement and for comparison results to the SSB system, the first system tested was the conventional DSB system as shown in Figure 5.9. In this system, the MZ was driven in a balanced mode so as to generate a chirp free optical DSB signal. In this system, two EDFAs were cascaded at the transmitter and at the receiver. This was done as a direct result of the reduced gain provided by each EDFA at the 1555 nm wavelength. At 1555 nm, the gain provided by each EDFA was between 10 and 14 dB. By cascading two EDFAs together, the combined optical gain reached 21 dB for EDFAs #1 and #2 and 17 dB for EDFAs #4 and #5. A variable optical attenuator (VOA) was inserted before the receiver to adjust the amount of received optical power to facilitate measurements of the BER as the received optical power varied. Further information on the parameters, insertion losses and manufacturers of the optical components are listed in Appendix A. The index numbers in Appendix A correspond to the number shown below each optical element in Figure 5.9. The fiber segments are also comprised from the reels in Appendix A.

The electrical transmitter configuration for driving the DSB system is shown in Figure 5.10. This is the layout which used the data provided by the output of the 4:1 MUX to create the data signals for the MZ modulator. Due to the BNR MZ modulator material composition, the dc bias added to each arm had to be negative. Thus, the dc bias added to the right arm of the BNR MZ modulator was -3.7 V while the dc bias added to the left arm was -1.3 V. The MZ modulator also had different values of V_π for each arm and thus, different levels of attenuation were used to modify the peak to peak levels of the signals driving the left and right arms of the MZ modulator.

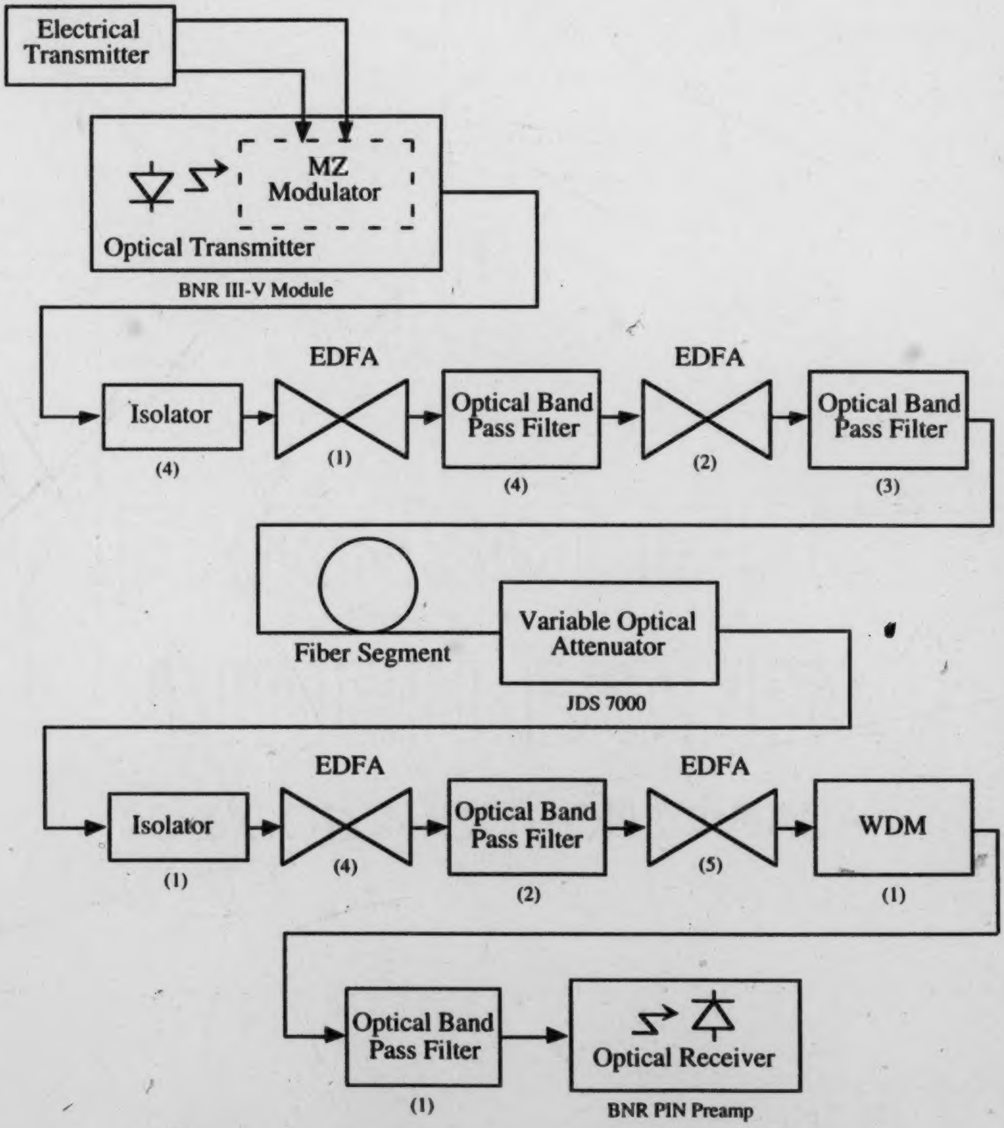
Electrical Transmitter
MZ Modulator
Optical Transmitter
BNR III-V Module
EDFA
EDFA
Isolator
(4)
(1)
Optical Band Pass Filter
(4)
(2)
Optical Band Pass Filter
(3)
Fiber Segment
Variable Optical Attenuator
JDS 7000
EDFA
EDFA
Isolator
(1)
(4)
Optical Band Pass Filter
(2)
(5)
WDM
(1)
Optical Band Pass Filter
(1)
Optical Receiver
BNR PIN Preamp

Figure 5.9 Optical DSB system using the BNR III-V module

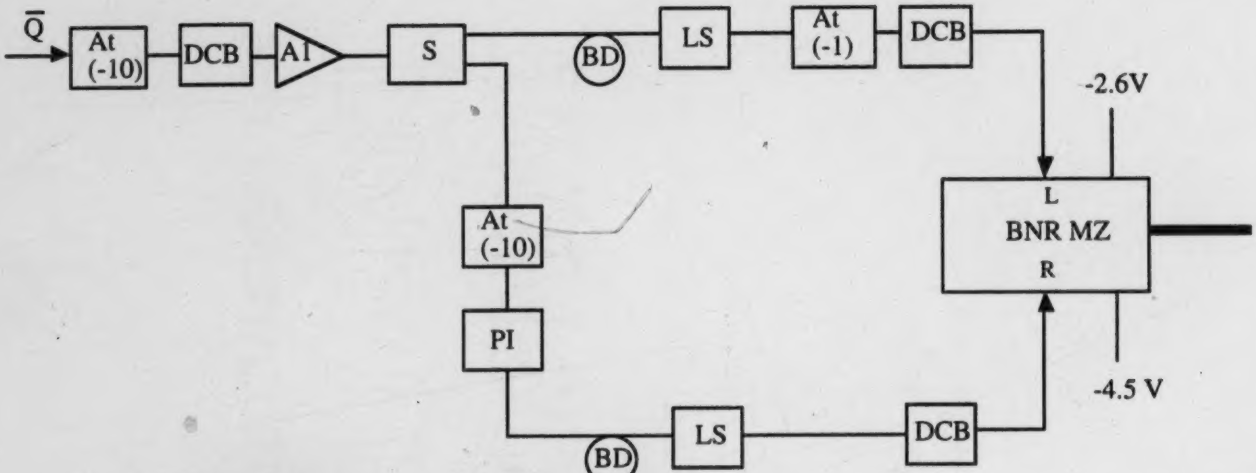
$\bar{Q}$
At (-10)
DCB
A1
S
BD
LS
At (-1)
DCB
-2.6V
L
BNR MZ
R
-4.5 V
At (-10)
PI
BD
LS
DCB

Components

A1 - B&H AC260XYH24ELL9P1 amplifier
At - ARRA attenuator (-x dB)
BD - bulk delay
BNR MZ - BNR III-V Mach Zehnder module
DCB - Picosecond Pulse Labs 5500A DC block
LS - Omni Spectra 2054-6002-00 line stretcher
PI - PSPL 5315 pulse inverter
S - Picosecond Pulse Labs 5330A resitive splitter

Figure 5.10 Electrical layout for the DSB system using the BNR III-V module

To implement the SSB design, the transmitter for the optical DSB system shown in Figure 5.9 was modified by adding the PM as shown in Figure 5.11. The driving signals for the modulators were also modified and the new electrical transmitter configuration is as shown in Figure 5.12. In the SSB case, the output of the MZ modulator is optical DSB, still but the output of the PM is now optical SSB.

In this implementation of optical SSB, Design 3 was used for reasons as outlined in Chapter 4. Some of these reasons included lower peak signal levels in the separate data and Hilbert transform data signals which reduced the amount of saturation in electrical amplifiers driving the modulators and the fact that combining four signals for a Hilbert signal is easier than combining five for a combination of the original signal it's Hilbert transform. Design 2 would eventually be tested, however, it was recognized from the start that Design 3 was easier to implement experimentally.

In the electrical transmitter layout shown in Figure 5.12, Q and Qbar were used first to drive the MZ modulator in a push-pull manner to amplitude modulate the optical carrier which generated the optical DSB signal at the output of the MZ modulator. This format was similar to the DSB case, however, the MZ modulator was not driven to full extinction in order to preserve the ability to equalize the signal post detection. Line stretchers were required for each of these signals since the Q and Qbar signals at the output of the 4:1 MUX were not phase aligned. The Hilbert transform was approximated with a four tap filter. The tap weights were implemented with broadband electrical attenuators. The delay was implemented with segments of semi-rigid coax. The tapped delay signals were summed with a broadband 4:1 combiner. The Hilbert signal was amplified with a linear amplifier by a high output power capability which was adequate for the PMs V_π of 8.9 V.

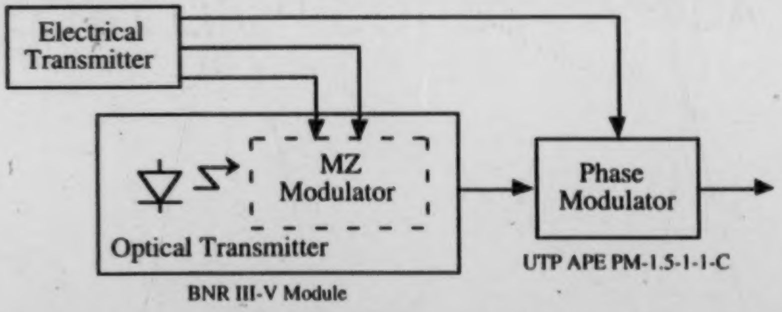

Figure 5.11 Optical SSB transmitter using the BNR III-V module and the UTP PM

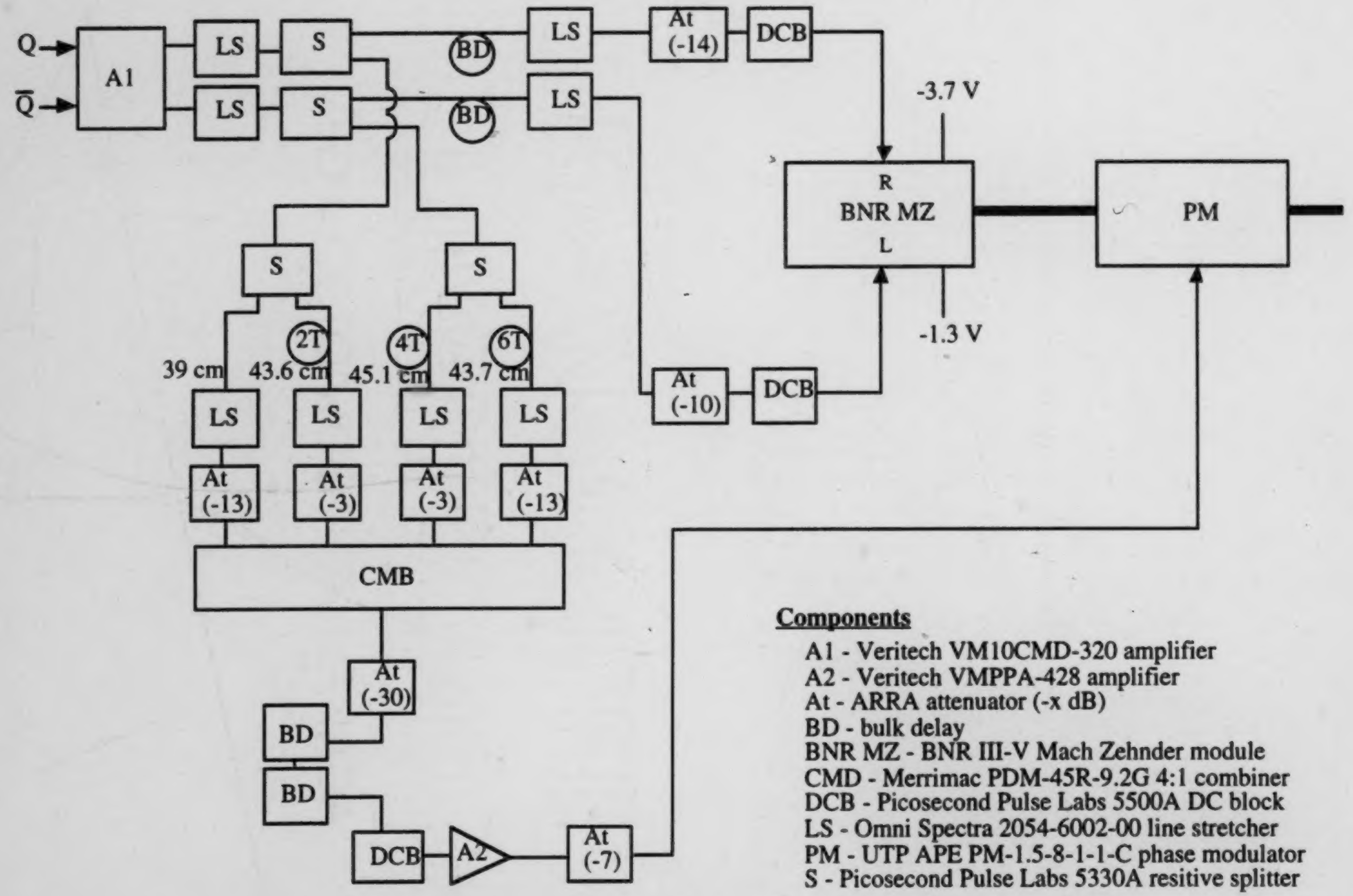
Q
Q̄
A1
LS
LS
S
S
BD
BD
LS
LS
At (-14)
DCB
At (-10)
DCB
-3.7 V
R
BNR MZ
L
-1.3 V
PM
S
S
2T
4T
6T
39 cm
43.6 cm
45.1 cm
43.7 cm
LS
LS
LS
LS
At (-13)
At (-3)
At (-3)
At (-13)
CMB
At (-30)
BD
BD
DCB
A2
At (-7)

Components

A1 - Veritech VM10CMD-320 amplifier
A2 - Veritech VMPPA-428 amplifier
At - ARRA attenuator (-x dB)
BD - bulk delay
BNR MZ - BNR III-V Mach Zehnder module
CMD - Merrimac PDM-45R-9.2G 4:1 combiner
DCB - Picosecond Pulse Labs 5500A DC block
LS - Omni Spectra 2054-6002-00 line stretcher
PM - UTP APE PM-1.5-8-1-1-C phase modulator
S - Picosecond Pulse Labs 5330A resitive splitter

Figure 5.12 Electrical layout for SSB system using the BNR III-V module and the UTP PM

After assembling the DSB and SSB optical transmitters, the optical output from each design was directed to the optical spectrum analyzer to gain a measure of the degree of single sideband that was created through the new design. The optical spectrum analyzer design used for the first DSB and SSB configurations was the first spectrum analyzer design shown in Figure 5.1.

The first set of scanned optical spectra are shown in Figure 5.13 (a) and (b). Figure 5.13 (a) is the carrier with no modulation and Figure 5.13 (b) is the same carrier with DSB modulation at full optical extinction.

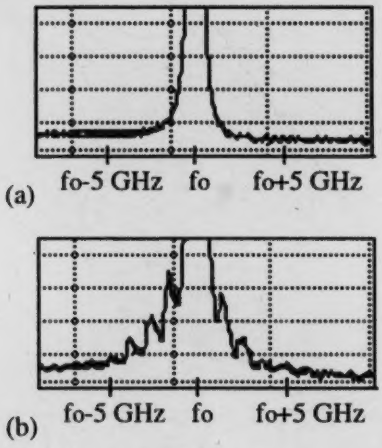

Figure 5.13 Optical spectra for the carrier (a) without and (b) with DSB modulation using the BNR III-V module (Linear vertical scale)

The second set of scanned optical spectra are shown in Figure 5.14 (a), (b) and (c). Figure 5.14 (a) is the carrier again with no modulation, Figure 5.14 (b) is the same carrier with DSB modulation at the same optical extinction level as the SSB case and Figure 5.14 (c) is the same carrier with SSB modulation. It is important to note that the optical extinction level in the DSB case in Figure 5.13 (b) is at almost 100% where in Figure 5.14 (b), it is less at a value of approximately 60%. This is required to maintain the linearity of the modulator and thus maintain the ability to equalize the SSB signal after long distances.

Comparing Figure 5.14 (b) and (c), it can be seen that by changing the modulation from DSB to SSB, there is a shift in the spectral power from the lower sideband to the upper sideband. This can readily be achieved by disconnecting and reconnecting the input to the PM in the SSB system. In the SSB case, there appears to be good sideband cancellation, however, it is hard to tell how well the components in the fo+/-5 GHz to fo+/-10 GHz region are canceled since they are below the noise floor. These high frequency components of the baseband signal are significant when trying to combat the effects of chromatic dispersion whether equalization is used or not. The problem with the optical spectrum analyzer, as outlined in section 5.2, is that the vertical scale of the optical spectrum is linear in Figures 5.13 and 5.14. Despite this, the SSB implementation with the BNR III-V module was found to be ineffective in terms of BER performance.

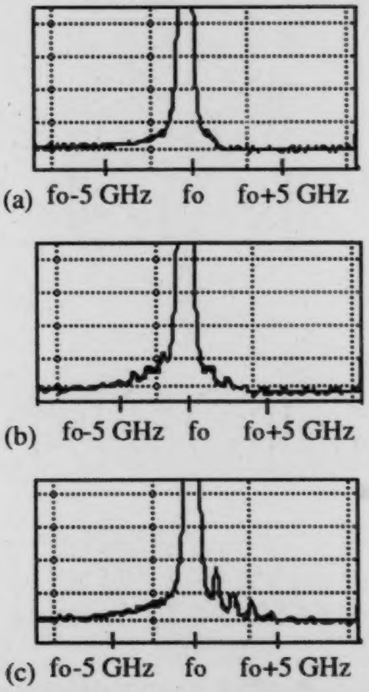

Figure 5.14 Optical spectra for the carrier (a) without modulation, (b) with DSB modulation and (c) with SSB modulation using the BNR III-V module (Linear vert. scale)

For the DSB and SSB cases, the ineffectiveness of the BNR III-V module is shown in the measured receiver sensitivity versus distance plots shown in Figure 5.15. The receiver sensitivity is a measure of the required optical power at the input to the EDFAs at the receiver to give a BER of 10^{-9} at the receiver. In this case, the EDFAs used at the transmitter as well as the receiver were included in the measured BER as opposed to just the EDFA at the receiver as was done in the simulations of receiver sensitivity versus fiber length in Chapter 4. This is unavoidable in the experimental case since the optical loss of the fiber, which was neglected in the simulations for receiver sensitivity, must be overcome. However, as long as the received optical power is not too low and the SNR does not degrade too far, the ASE noise effects from the EDFAs prior to the EDFA used at the receiver will be minimal. At the short fiber lengths, the transmitter EDFAs were not needed to recover loss but were left in the link so that the receiver sensitivity measurements for the different lengths could be compared.

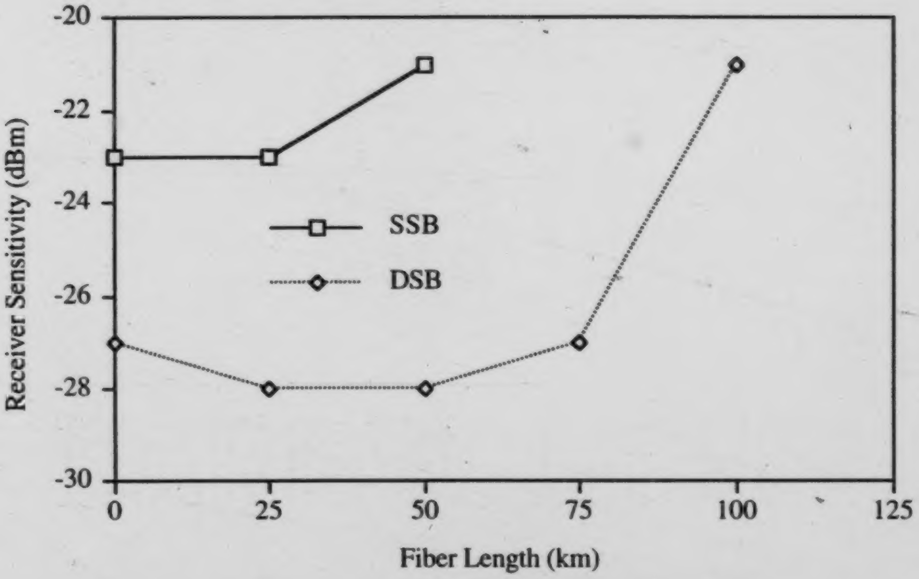

Figure 5.15 Receiver sensitivity versus fiber length for BNR III-V module

In Figure 5.15, the SSB receiver sensitivity curve only extended to 50 km. Beyond this distance, a BER floor worse than 10^{-9} was measured. This BER floor was due to a combination of eye closure and the FM-AM noise induced by the interaction of the laser phase noise and the chromatic dispersion induced by the fiber. This noise floor could be reduced by narrowing the linewidth of the laser. Another problem existed in both the SSB and the DSB systems in that at fiber lengths approaching 150 km, there was not enough optical power to recover from the fiber loss. This was primarily due to the fact that the wavelength of the laser in the BNR III-V module was at approximately 1555 nm and the gain peak of the EDFAs were around approximately 1535 nm. Thus, gain provided by the

EDFAs was substantially lower than what was needed to maintain an acceptable BER. During this implementation, only four EDFAs were available. Thus, it was obvious that a separate laser and MZ modulator would have to be used to improve the system. The linewidth and wavelength of the laser could then be optimized for the system.

To show the BER floor in the SSB system more effectively, the BER versus received optical power for the SSB case at 75 km without equalization is shown in Figure 5.16. At this distance, a BER of 10^{-9} could not be achieved for any amount of received optical power.

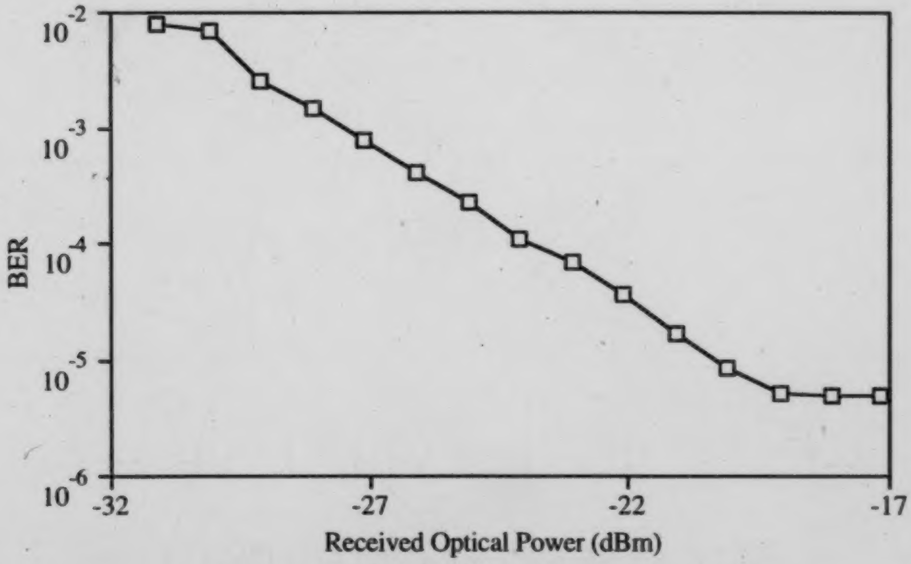

Figure 5.16 BER versus received optical power for SSB case at 75 km with the BNR III-V module and the UTP PM

5.3.3.2 Lucent Modulator in SSB Design 2 Configuration

To alleviate the problem of the linewidth of the laser and the mismatched wavelength of the source within the BNR III-V module and the EDFA gain peak, a separate MZ modulator was acquired. It was a Lucent dual arm $LiNbO_3$ external modulator with an electrical bandwidth of 8 GHz. This facilitated the use of an independent laser source with a linewidth of 3.8 MHz at a more beneficial wavelength of 1533 nm.

The next design under test with the Lucent MZ was the configuration of Design 2. The optical system for this SSB layout is shown in Figure 5.17.

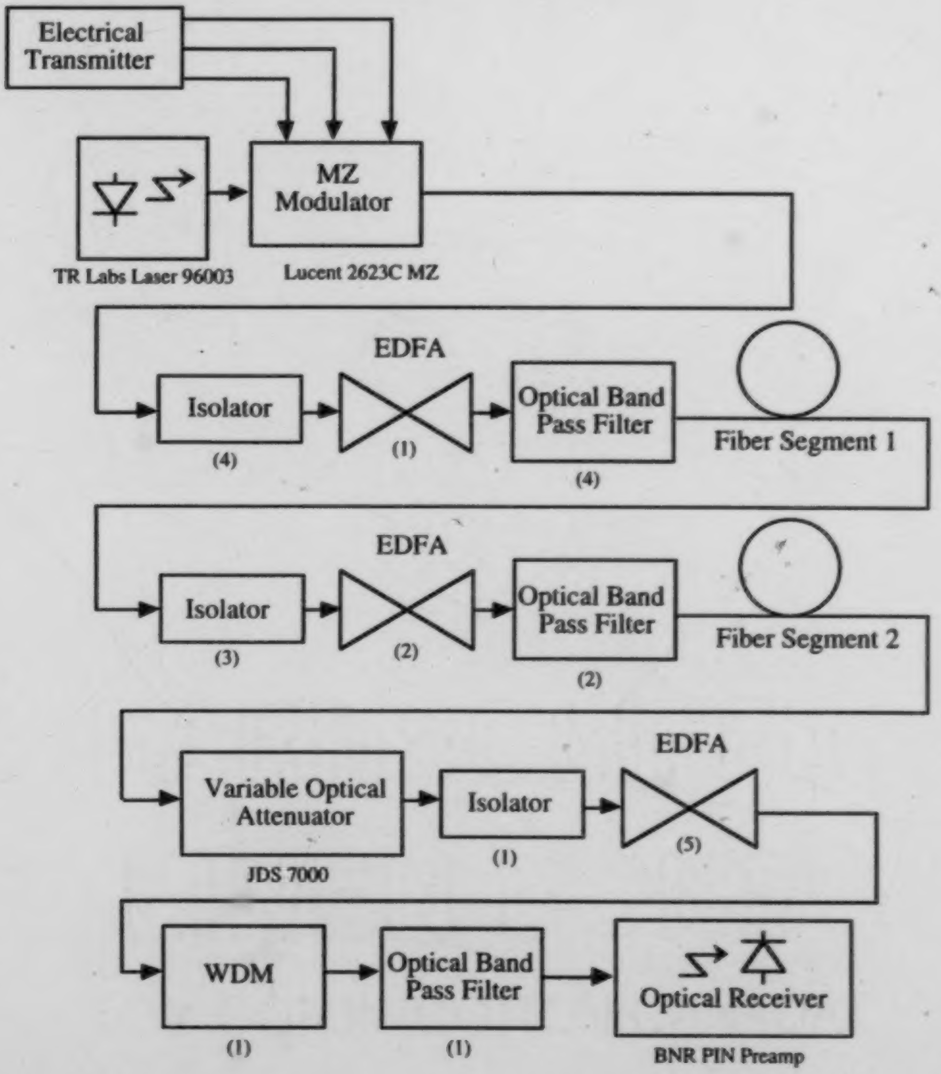
Electrical Transmitter
MZ Modulator
TR Labs Laser 96003
Lucent 2623C MZ
EDFA
Isolator
(4)
(1)
Optical Band Pass Filter
(4)
Fiber Segment 1
EDFA
Isolator
(3)
(2)
Optical Band Pass Filter
(2)
Fiber Segment 2
EDFA
Variable Optical Attenuator
JDS 7000
Isolator
(1)
(5)
WDM
(1)
Optical Band Pass Filter
(1)
Optical Receiver
BNR PIN Preamp

Figure 5.17 Optical SSB system using Lucent modulator in the Design 2 configuration

At this new wavelength of 1533 nm, the gain provided by each of the EDFAs was in the range of 23 to 31 dB. This was more than 10 to 14 dB at 1555 nm. The full EDFA parameters for each EDFA at the 1533 nm wavelength are given in Appendix A. At this new wavelength, the EDFAs provided enough gain that they no longer had to be placed back to back as in Figure 5.9. It was expected that this design would reach 150 km so three EDFAs were used in the link. Fiber segments 1 and 2 consist of reels listed in Appendix A.

The electrical transmitter configuration for driving the MZ modulator for the SSB system is shown in Figure 5.18. In this configuration, a five channel broadband combiner was not available to combine the information signal plus the four taps to create the Hilbert transform of the signal. Thus, Design 2 was implemented in a different configuration than was suggested in Chapter 4. In the new implementation, a four to one combiner was used to create the Hilbert signal. The Hilbert signal was then split and recombined with the information driving each arm of the MZ through a resistive splitter. There were a couple of inherent problems with using resistive splitters as combiners. One is that is there is a strong reflected signal into each input arm. These reflections can be limited by putting attenuators in each arm. This way, reflected signals are attenuated twice while the original information signal is only attenuated once. The additional drawbacks of this type of implementation are that electrical amplifiers are needed before the MZ to boost the signal to an appropriate level to drive the MZ and that the reflected signals can still cause distortion of the transmitted information. A further drawback of this design was the availability of linear amplifiers. The choice of amplifiers to drive the MZ was restricted to the B&H amplifiers. These amplifiers have a poor frequency response and thus they seriously degraded the transmitted signal.

When this system was tested, measurements showed that the received BER hit a floor at an even shorter distance than the previous Design 3 using the BNR MZ modulator and a PM. This was a result of the transmitted eye being even smaller in this case. This smaller eye was a direct result of the frequency response of the electrical components at the transmitter used to create the $m(t)+\hat{m}(t)$ and $-m(t)+\hat{m}(t)$ signals. In particular, the B&H amplifiers used to boost the signals in order to drive the MZ modulator. Thus, with a smaller eye, the effects of the FM-AM noise conversion were even more critical even in light of a narrower linewidth source. As a result, the testing of this system configuration was discontinued and the more successful implementation of Design 3 was continued with the Lucent MZ modulator. In order to make Design 2 comparable to Design 3, two very linear high power amplifiers would need to be purchased in order to properly amplify the driving signals at the input to the modulator. Further, improvements in the method used to create the driving signals would also be needed.

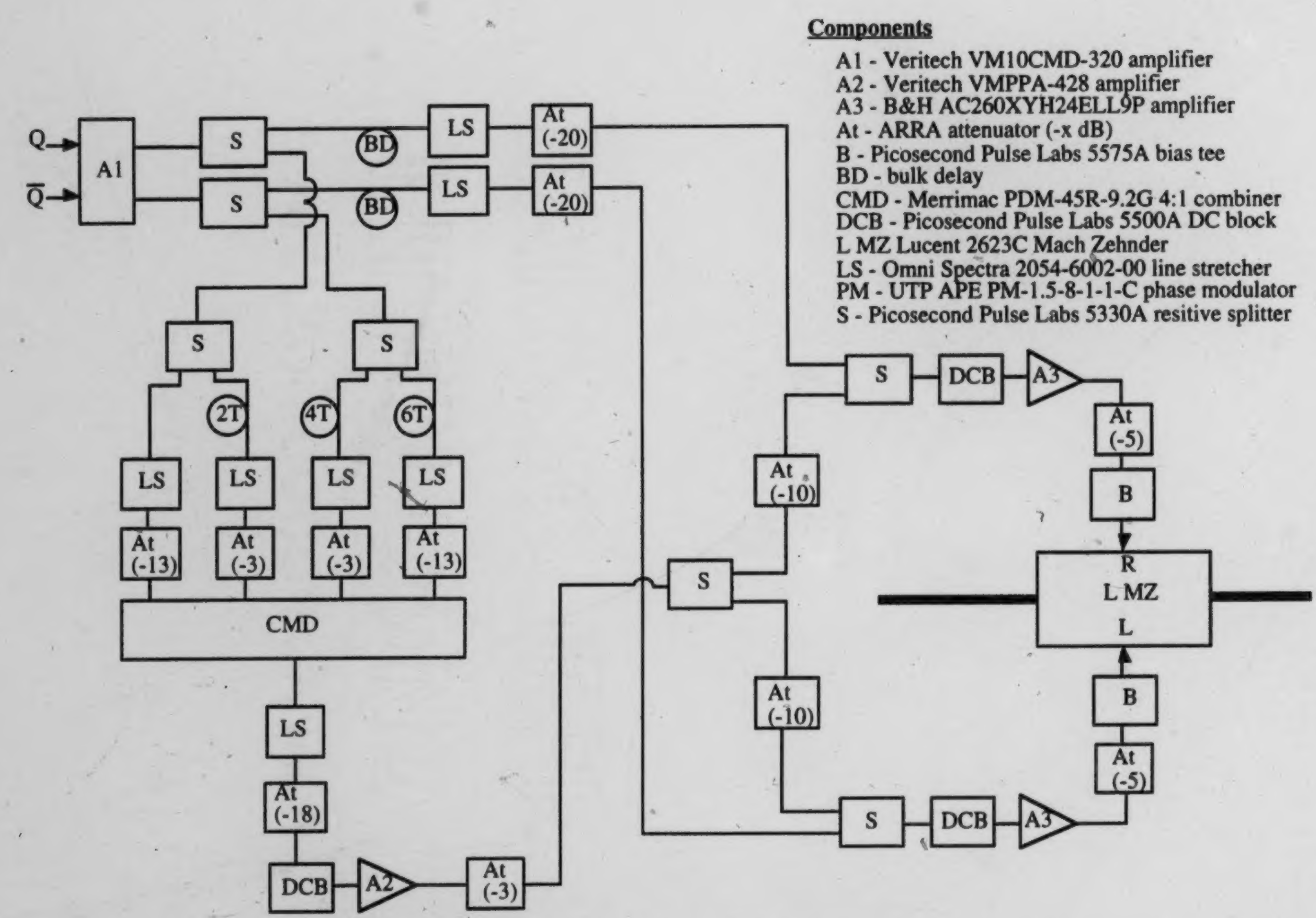

Components

- A1 - Veritech VM10CMD-320 amplifier
- A2 - Veritech VMPPA-428 amplifier
- A3 - B&H AC260XYH24ELL9P amplifier
- At - ARRA attenuator (-x dB)
- B - Picosecond Pulse Labs 5575A bias tee
- BD - bulk delay
- CMD - Merrimac PDM-45R-9.2G 4:1 combiner
- DCB - Picosecond Pulse Labs 5500A DC block
- L MZ Lucent 2623C Mach Zehnder
- LS - Omni Spectra 2054-6002-00 line stretcher
- PM - UTP APE PM-1.5-8-1-1-C phase modulator
- S - Picosecond Pulse Labs 5330A resitive splitter

Q
$\overline{Q}$
A1
S
S
BD
BD
LS
LS
At (-20)
At (-20)
S
S
2T
4T
6T
LS
LS
LS
LS
At (-13)
At (-3)
At (-3)
At (-13)
CMD
LS
At (-18)
DCB
A2
At (-3)
S
At (-10)
At (-10)
S
DCB
A3
S
DCB
A3
At (-5)
B
At (-5)
B
R
L MZ
L

Figure 5.18 Electrical layout using the Lucent modulator in the Design 2 configuration

5.3.3.3 Lucent Modulator in DSB and SSB Design 3 Configurations

After determining that Design 3 was the best SSB implementation to test experimentally, Design 3 was assembled with Lucent MZ modulator, the PM and the DFB laser with the 3.8 MHz laser linewidth. Once again, as a baseline measurement, the conventional DSB system as shown in Figure 5.19 was tested. In the SSB case, four EDFAs were required to cover the fiber loss and thus, for comparative purposes, four EDFAs were used for the DSB system even though it required less than four to recover the loss incurred by the fiber at certain distances. In these new systems, the wavelength of operation of the laser was at 1533 nm which was compatible with the gain peak of the EDFAs at around 1535 nm.

The VOA was again inserted before the receiver to adjust the amount of received optical power to facilitate measurements of the BER as the received optical power varied. The BPFs were strategically placed after each EDFA to limit the amount of ASE in the optical link and so that the BPF with the narrowest optical bandwidth was closest to the receiver. This way, the smallest amount of ASE noise would be incident on the photodetector. A WDM was again used after the last EDFA to filter out any residual pump left in the signal before photodetection. Fiber segments 1, 2 and 3 are again from the reels listed in Appendix A.

The electrical transmitter configuration for driving the DSB system is shown in Figure 5.20. The transmitter configuration for this DSB case was slightly different than the previous DSB system tested. In this case, the Q and Qbar outputs from the 4:1 MUX are used to drive the MZ modulator in a push pull manner as opposed to using just Q and a pulse inverter. The Lucent MZ modulator had a specified V_π of 4.4 V. This value of V_π was the same for both arms and thus the peak to peak values for the signals on each arm were approximately the same. The receiver circuit and clocking circuits for both the DSB and the SSB systems were the same as in the previous cases.

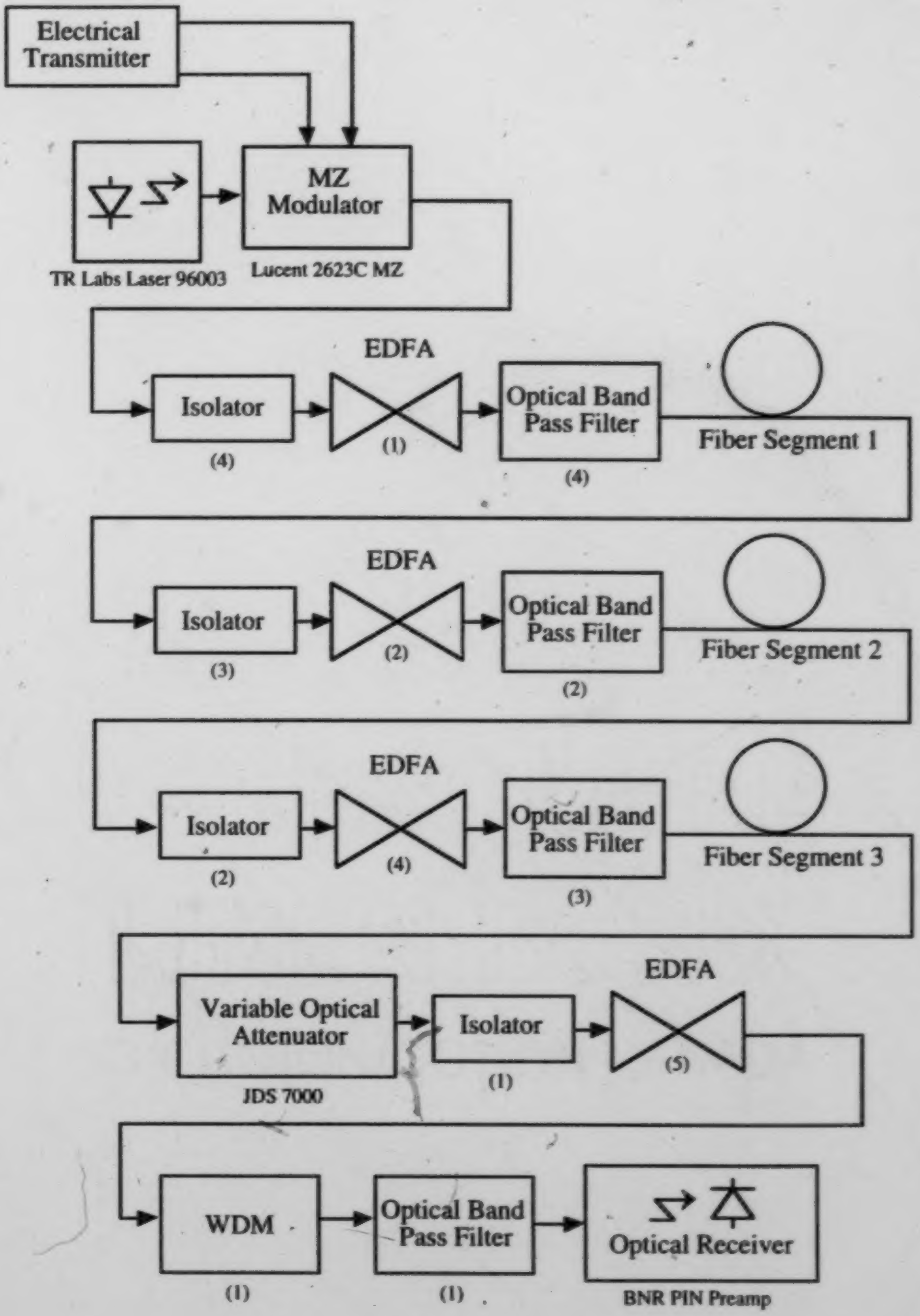
Electrical Transmitter
MZ Modulator
TR Labs Laser 96003
Lucent 2623C MZ
EDFA
Isolator
(4)
(1)
Optical Band Pass Filter
(4)
Fiber Segment 1
EDFA
Isolator
(3)
(2)
Optical Band Pass Filter
(2)
Fiber Segment 2
EDFA
Isolator
(2)
(4)
Optical Band Pass Filter
(3)
Fiber Segment 3
Variable Optical Attenuator
JDS 7000
Isolator
(1)
EDFA
(5)
WDM
(1)
Optical Band Pass Filter
(1)
Optical Receiver
BNR PIN Preamp

Figure 5.19 Optical DSB system using the Lucent modulator

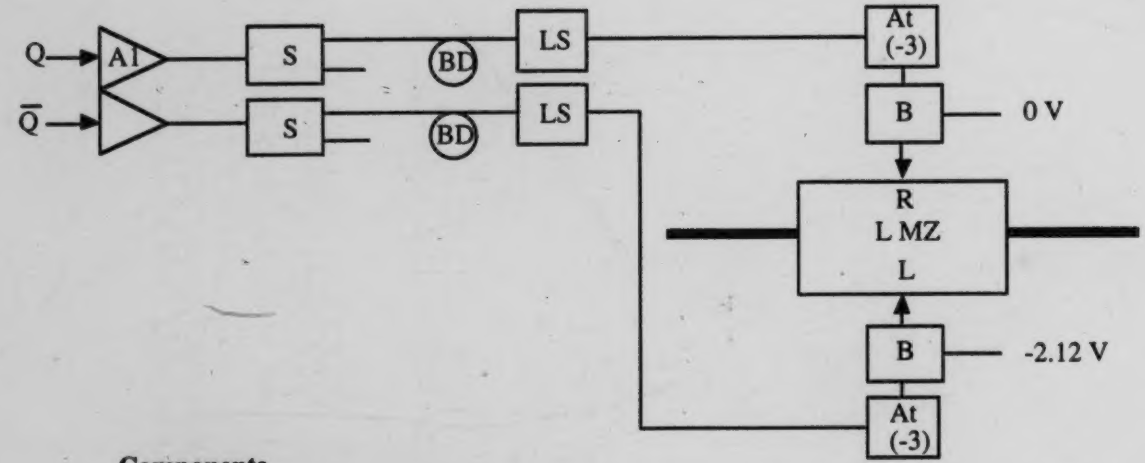
Q
$\overline{Q}$
A1
S
S
BD
BD
LS
LS
At
(-3)
B
0 V
R
L MZ
L
B
-2.12 V
At
(-3)

Components

A1 - Veritech VM10CMD-320 amplifier
At - ARRA attenuator (-x dB)
B - Picosecond Pulse Labs 5575A bias tee
BD - bulk delay
L MZ - Lucent 2623C Mach Zehnder
LS - Omni Spectra 2054-6002-00 line stretcher
S - Picosecond Pulse Labs 5330A resitive splitter

Figure 5.20 Electrical layout for DSB system using the Lucent modulator

To implement the SSB design, the transmitter for the optical DSB configuration shown in Figure 5.19 was modified by adding the PM and a polarization rotator as shown in Figure 5.21. In the SSB case, a polarization rotator had to be added between the MZ modulator and the PM. Since the PM was polarization sensitive and the fiber pigtail on the output of the Lucent MZ modulator was not polarization maintaining fiber, the polarization rotator was required.

The driving signals for the modulators were also modified and the new electrical transmitter configuration is as shown in Figure 5.22. In the SSB case, the output of the MZ modulator is again optical DSB with the output of the PM is now optical SSB.

In the electrical transmitter layout shown in Figure 5.22, Q and Qbar were used first to drive the MZ modulator in a push-pull manner to amplitude modulate the optical carrier which generated the optical DSB signal at the output of the MZ modulator. This format was similar to the DSB case, however, the MZ modulator was not driven to full extinction in order to limit its operation to the linear range and preserve the ability to equalize the signal post detection. The previous Hilbert transform circuit with four taps was used.

For some of the SSB tests, equalization in the form of microstrip was added at the receiver. In these cases, the microstrip was added to the receiver circuit just following the last Veritech amplifier and just before the bias tee which adds a dc offset to the signal before it is applied to the D-FF as shown in Figure 5.5.

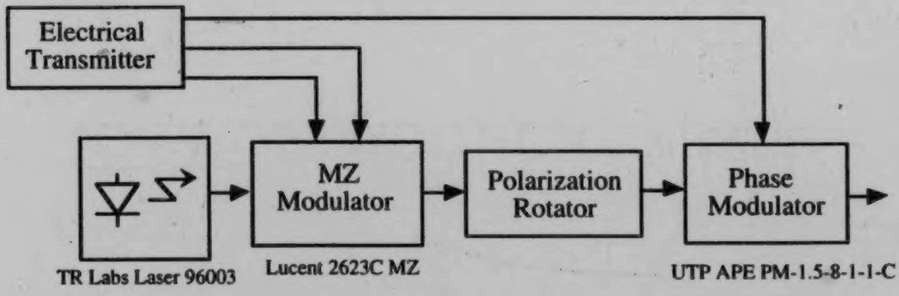

Figure 5.21 Optical SSB transmitter using the Lucent modulator and UTP PM

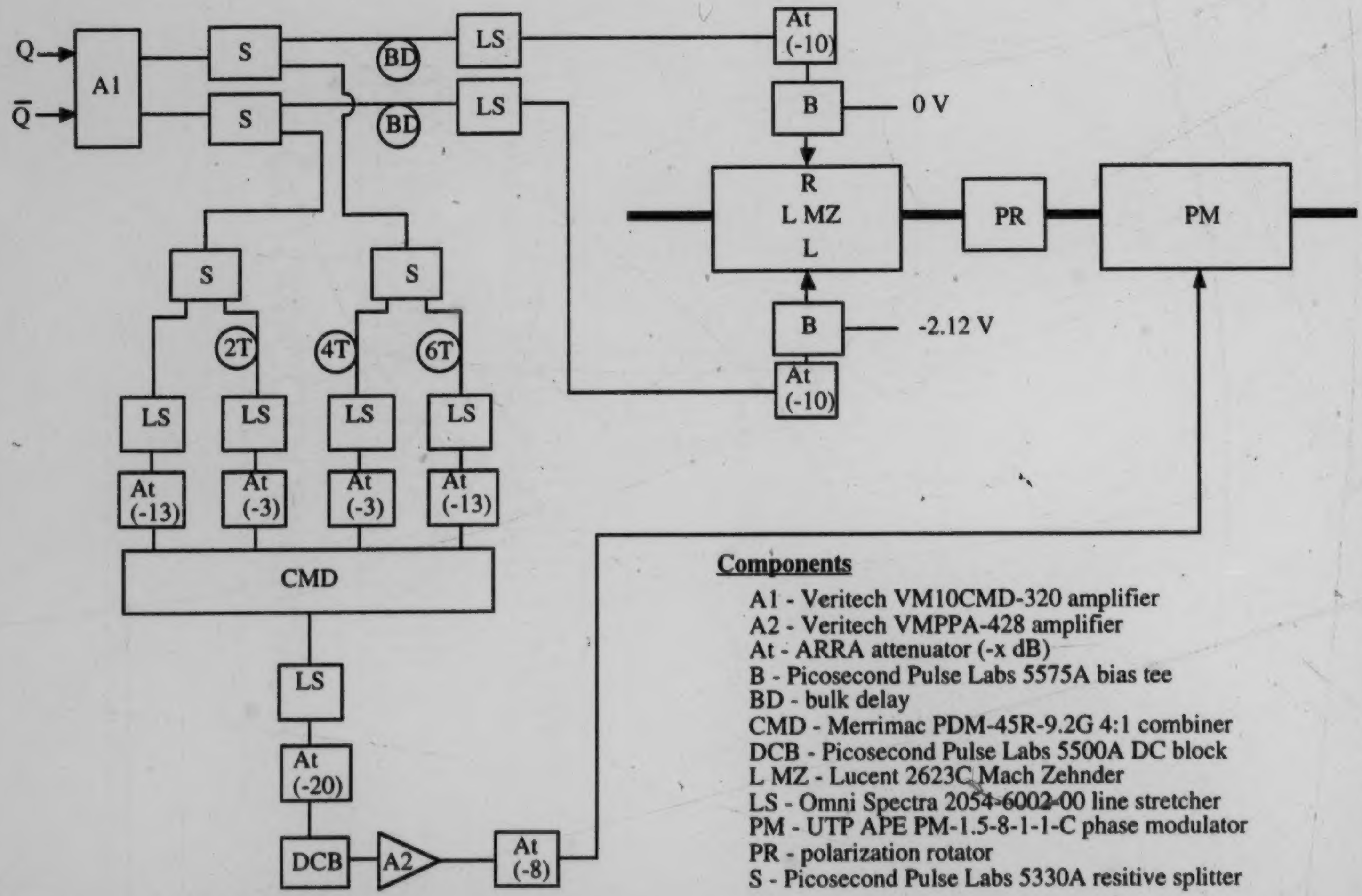
Q
Q̄
A1
S
S
BD
BD
LS
LS
At (-10)
B
0 V
R
L MZ
L
B
-2.12 V
At (-10)
PR
PM
S
S
2T
4T
6T
LS
LS
LS
LS
At (-13)
At (-3)
At (-3)
At (-13)
CMD
LS
At (-20)
DCB
A2
At (-8)

Components

- A1 - Veritech VM10CMD-320 amplifier
- A2 - Veritech VMPPA-428 amplifier
- At - ARRA attenuator (-x dB)
- B - Picosecond Pulse Labs 5575A bias tee
- BD - bulk delay
- CMD - Merrimac PDM-45R-9.2G 4:1 combiner
- DCB - Picosecond Pulse Labs 5500A DC block
- L MZ - Lucent 2623C Mach Zehnder
- LS - Omni Spectra 2054-6002-00 line stretcher
- PM - UTP APE PM-1.5-8-1-1-C phase modulator
- PR - polarization rotator
- S - Picosecond Pulse Labs 5330A resitive splitter

Figure 5.22 Electrical layout for SSB system using the Lucent modulator and the UTP PM

Using the first optical spectrum analyzer design, the scanned optical spectra for the first set of scanned spectra are shown in Figure 5.23 (a) and (b). Figure 5.23 (a) is the carrier with no modulation and Figure 5.23 (b) is the same carrier with DSB modulation at full optical extinction.

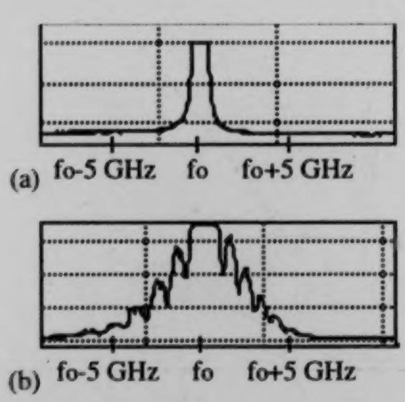

Figure 5.23 Optical spectra for the carrier with (a) no modulation and (b) with DSB modulation using the Lucent modulator (Linear vertical scale)

The second set of scanned optical spectra are shown in Figure 5.24 (a) and (b). Figure 5.24 (a) is the carrier with DSB modulation at the same optical extinction level as the SSB case and Figure 5.24 (b) is the same carrier with SSB modulation. As in the SSB case with the BNR III-V module, a shift in spectral power from the LSB to the USB occurs as the optical signal is transformed from a DSB signal to a SSB signal.

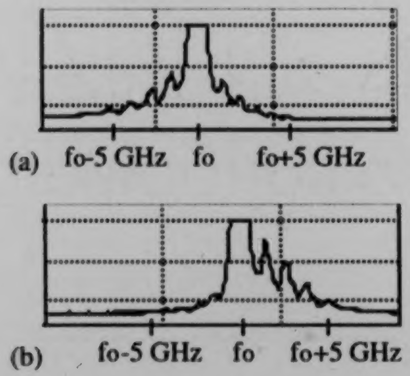

Figure 5.24 Optical spectra for the carrier with (a) DSB modulation and (b) SSB modulation using the Lucent modulator (Linear vertical scale)

The first optical spectrum analyzer design was useful in phase aligning the optical and electrical signals entering the PM. Since the optical spectrum was continuously displayed on the oscilloscope screen, the timing could be adjusted quickly. Critical to making the transmitted signal optical SSB was the fact that the bits in the optical stream entering the optical port of the PM had to be critically phase aligned with the corresponding Hilbert transform of those bits entering the PM through the electrical port.

In order to gain a better measure of the level of sideband cancellation, especially in the 5-10 GHz region away from the carrier, the second optical spectrum analyzer design shown in Figure 5.2 was utilized. The measurement time on this analyzer was quite slow (~5 minutes) because of the large amount of time required by the optical power meter to make an accurate reading. In spite of this slow response time, this design provided the ability to fine tune the timing and also show a larger dynamic range of the optical spectrum.

Figure 5.25 shows the optical spectra for three different cases as measured using the FFP interferometer in the second design. Figure 5.25 (a) shows just the optical carrier, (b) shows a regular DSB spectrum with the same modulation depth as the SSB case, and (c) shows the SSB spectrum. Figure 5.25 (c) appears as a LSB, however, due to the orientation of the applied voltage to the FFP, it is actually a USB. The laser used as the source in these spectral plots had a linewidth of 3.8 MHz. Since this linewidth was much smaller than the bandwidth of the FFP interferometer, the spectral shape of the carrier in (a) is really the shape of the FFP filter response. Thus, the shape of the FFP filter partially distorts the spectrums in (b) and (c) as well.

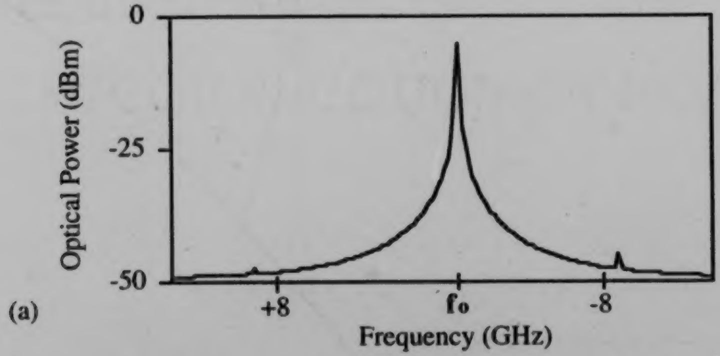

Figure 5.25 Optical signal spectra for (a) carrier

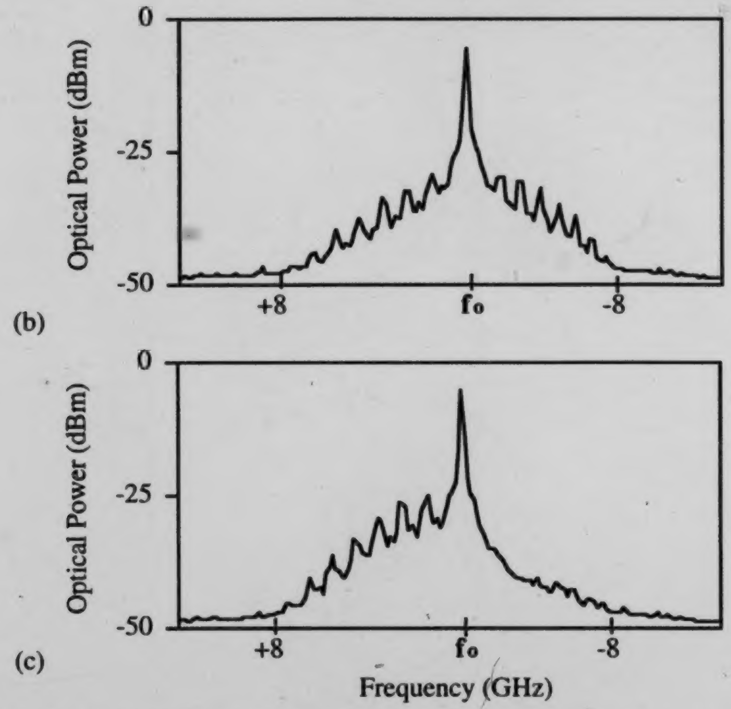

Figure 5.25 (continued) Optical signal spectra for (b) DSB and (c) SSB

Recognizing that the spectral shape of the FFP distorts the measured spectra of information, the FFP spectrum, which is approximate to the carrier spectrum in Figure 5.25 (a), was deconvolved out of the spectra in Figures 5.25 (b) and (c) to give the more realistic spectra in Figures 5.26 (a) and (b). The orientation of the USB in Figure 5.25 (c) is corrected for, mathematically, in Figure 5.26 (b).

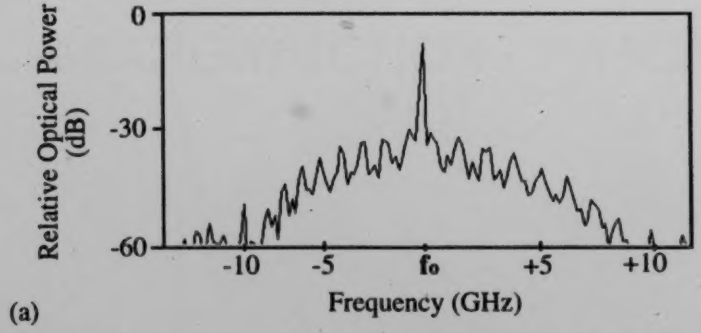

Figure 5.26 Deconvolved optical signal spectra for DSB modulation

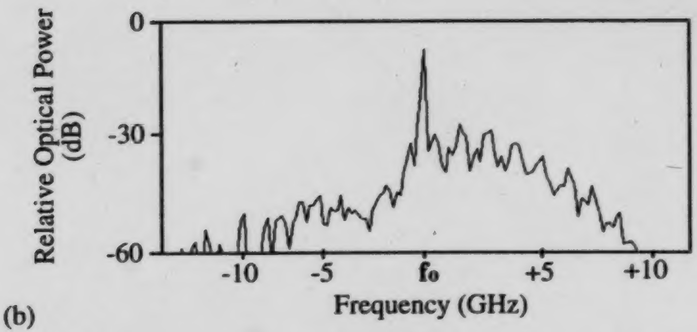

Figure 5.26 (continued) Deconvolved optical signal spectra for SSB modulation

From Figure 5.26, it can be seen that the spectral components in the 5-8 GHz region are better displayed with the second optical spectrum analyzer design than they were in the plots provided by the first design. Beyond 8 GHz, the spectrum in Figure 5.26 (a) and (b) is not well shown due to a combination of the roll-off of the information spectrum and the spectrum being attenuated by the frequency response of the modulators.

It can also be seen in Figure 5.26 (b) that the SSB spectrum does not have a completely canceled sideband. The sideband cancellation is close to 20 dB at some frequencies which is fairly good, however, not perfect. This is due to a number of nonidealities in the transmitter configuration. Since the sideband cancellation process is an analog one, it is essential that the signal driving the PM is the Hilbert transform of the optical signal entering the PM. As shown in section 4.3.6, this is never achieved with this design. In addition, the signal source generating the 10 Gb/s data labeled as Q and Qbar is nonideal. In the experiment, the signals $m(t)$ and $-m(t)$ driving the MZ modulator were generated from the GaAs logic signals of Q and Qbar out of the 4:1 MUX. Q and Qbar out of the 4:1 MUX are not the exact inverse of each other in terms of analog signals, even though digitally they are the inverse of each other. More specifically, ripples and rise/fall times of the bits in Q and Qbar do not match up. This results in imperfect sideband cancellation since the signals used to generate the Hilbert transform and ultimately cancel one of the sidebands are analog for this purpose. As will be shown later, this nonideal signal source will prove to be one of the major limitations in extending the transmission distance of this SSB system.

The ripples in the magnitude spectra in Figure 5.26 are due to the nature of the information signals. The 10 Gb/s data was created by multiplexing four 2.5 Gb/s data channels. These ripples are a result of the multiplexing operation. The ripples are analogous to the ripples shown in the electrical magnitude spectra of the data shown in Figure 5.7.

Figure 5.27 shows the experimental receiver sensitivity versus fiber length for a BER of 10^{-9} for the conventional DSB case as well as the new optical SSB case implementing Design 3 [72].

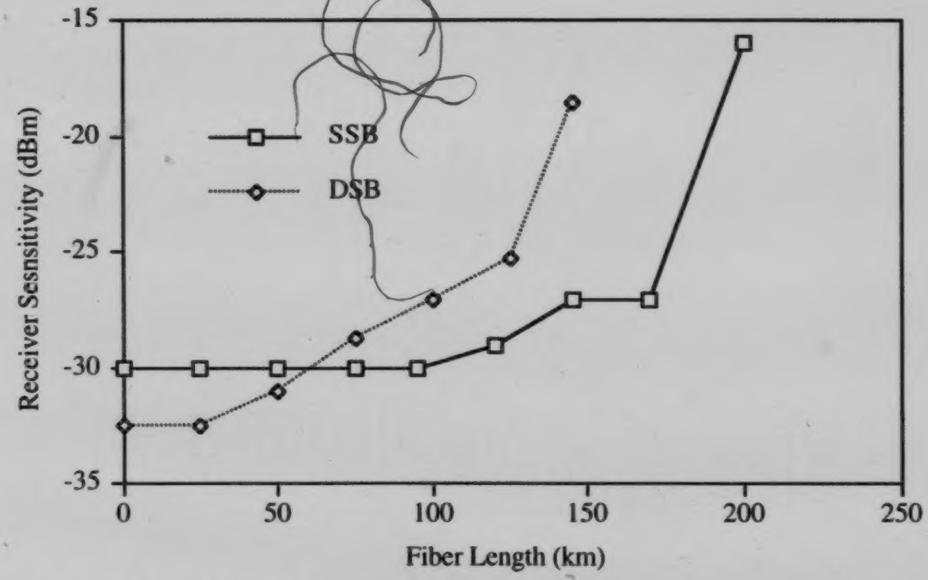

Figure 5.27 Receiver sensitivity versus fiber length for the four EDFA link

From Figure 5.27 it can be seen that the DSB case was operating with a small residual chirp on the MZ modulator thus allowing the DSB case to reach 150 km. It can also be seen that the experimental optical SSB case degraded very rapidly at distances greater than 170 km and a BER of 10^{-9} could only be maintained to 200 km. It was determined through simulation that this limitation in the SSB case arose from FM-AM noise conversion generated by the interaction of the source linewidth and the fiber chromatic dispersion with a partially closed eye. In the simulations, a laser with a 3.8 MHz linewidth was used as the source, similar to the one used in the experiments. In the simulations, it was determined that a BER floor worse than 10^{-8} would be encountered for any distance longer than 200 km. The FM-AM noise conversion penalty can be substantially eliminated if a source linewidth less than 1 MHz is used.

As a result of this limitation, the experimental optical SSB system could not be thoroughly tested with an electrical equalizer. However, for a distance of 270 km, the BER floor dropped from about 10^{-3} to 10^{-5} when the received optical power was -18 dBm and a 32 cm microstrip equalizer was added at the receiver. To show the nature of this BER floor, the BER versus received optical power for the SSB case with microstrip equalization at 270 km is shown in Figure 5.28.

Distances beyond 270 km could not be tested at the time since additional EDFAs, isolators and BPFs were unavailable at the time to recover the loss incurred by the fiber.

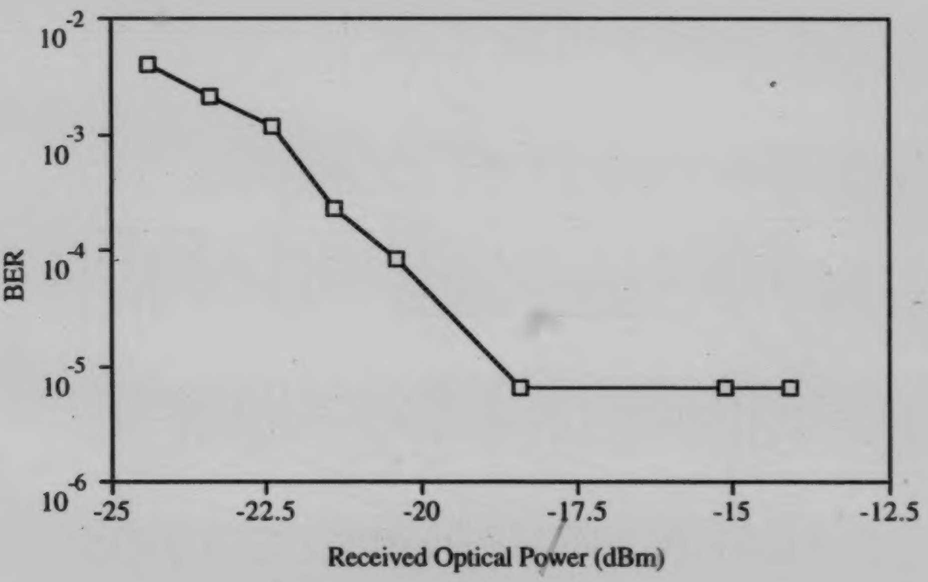

Figure 5.28 BER versus received optical power for SSB Design 3 at 270 km of fiber and 32 cm of microstrip

To further show the effects of the FM-AM noise as a result of the interaction of the laser phase noise with the chromatic dispersion incurred by the fiber, the BER versus received optical power at a distance of 200 km with no microstrip equalization for source linewidths of 3.8 MHz and 6.2 MHz are shown in Figure 5.29. The wavelength of each source is 1533 nm and the output power of each source is +5 dBm. Thus, the only major difference between the lasers was their linewidths. From Figure 5.29, it can be seen that the BER is generally worse when the laser with the 6.2 MHz linewidth is used as opposed to when the laser with the 3.8 MHz linewidth is used.

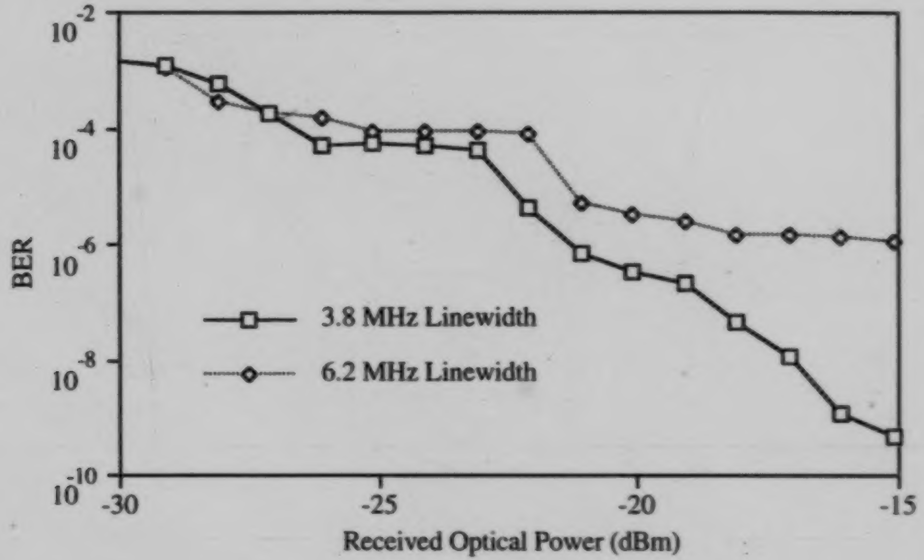

Figure 5.29 BER versus received optical power at 200 km with two different source linewidths

To show the nature of the degradation of the DSB system beyond 150 km due to chromatic dispersion, the measured eyes for the DSB case at distances of 0 km, 100 km and 170 km are shown in Figure 5.30. To show the improvement that the SSB system provides over the DSB system, the measured eyes for the SSB case at distances of 0 km, 120 km and 195 km are shown in Figure 5.31. These eyes were measured by a digital oscilloscope measuring the signal at the input to the D-FF. These eyes include all of the noise present in the system. This noise can be averaged out by acquiring a large number of samples for each instant in time, however, this is hard to do over fiber lengths longer than 100 km since the effective length of the fiber changes and as a result, the received pattern drifts in time. This change in effective length is a direct result of temperature fluctuations along the fiber length. This drift becomes more pronounced with longer lengths of fiber. Thus, some of the long distance eyes appear to be more closed and distorted than they actually are as a result of this temporal drift. Regardless, a degree of eye closure related to the effects of chromatic dispersion is still dominant in these traces.

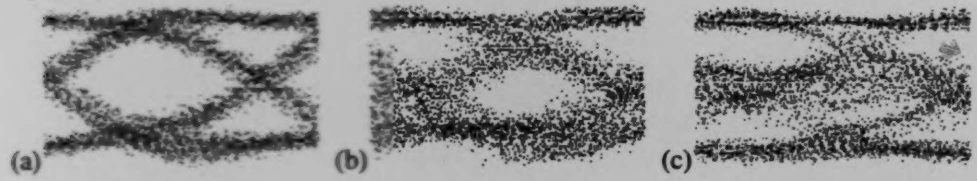

Figure 5.30 Experimental DSB eyes at (a) 0 km, (b) 100 km and (c) 170 km

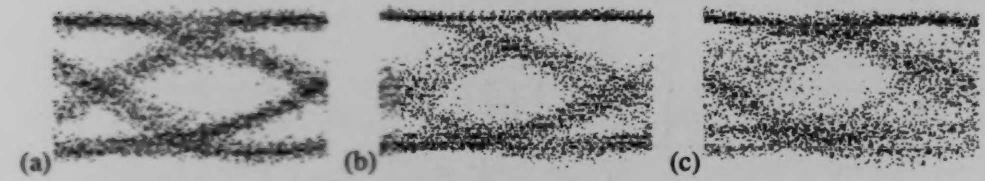

Figure 5.31 Experimental SSB eyes at (a) 0 km, (b) 120 km and (c) 195 km

To show the improvement that adding the 32 cm section of microstrip to the receiver has on the received eye, the measured eyes for the SSB case at a distance of 270 km with no equalization and with equalization are shown in Figure 5.32. In the equalized case, 32 cm of microstrip is added to the receiver circuit prior to the decision circuit. The eyes are quite noisy as a result of the FM-AM noise but the improvement as a result of the microstrip is still visible.

Pictures of a 16 cm section of microstrip along with some of the other experimental equipment such as the BERT set, the EDFAs, the fiber reels and the transmitter and receiver electronics are shown in Appendix B.

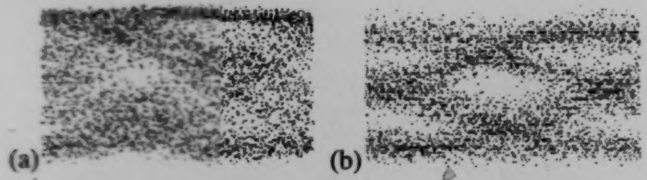

Figure 5.32 Experimental SSB eyes at 270 km for (a) unequalized and (b) equalized using 32 cm microstrip

In the experiment, an improvement in the received eye in terms of a noticeable improvement in receiver sensitivity was not noticed at the receiver using a microstrip equalizer until the fiber length reached 270 km. According to the ideal simulations shown in Chapter 4, at any distance beyond approximately 200 km, an improvement should be noticed. Upon further investigation of these results, it was determined that one of the amplifiers used in the receiver circuit (Veritech VMA3K10C-232) had a phase response similar to that for a 10 to 13 cm section of microstrip. In other words, the amplifier was already providing an amount of equalization before any microstrip was added. Thus, a benefit from additional microstrip was not seen until 270 km. At distances above 200 km but below 270 km, equalization was provided by the amplifier. Beyond 270 km, improvements as a result of adding microstrip could not be measured since the optical loss incurred by the fiber could not be recovered with only four EDFAs.

The nonlinear phase response of this amplifier was measured with a network analyzer. It is shown in Figure 5.33 along with the inverse phase response of 100 km of fiber. Comparing the phase response of this amplifier to that of the fiber, it can be seen that it has a nonlinear phase response similar to that of the microstrip which is specifically designed for equalizing the effects induced by the fiber. Thus, a certain amount of equalization is always present in this SSB system. As for the DSB system, the nonlinear phase response of the amplifier only degrades the quality of the received signal.

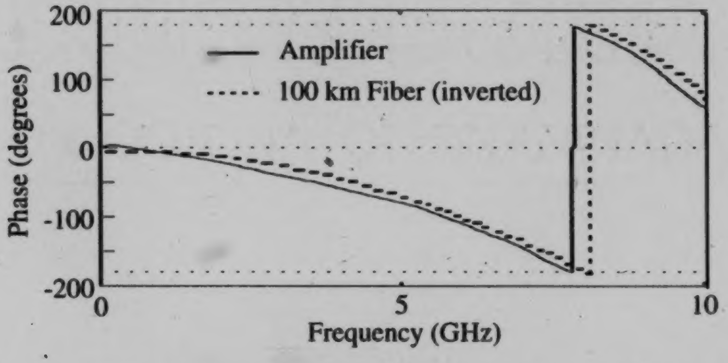

Figure 5.33 Phase response of the Veritech (VMA3K10C-232) amplifier and 100 km of standard single mode fiber

Recognizing through experiments and simulation that the major impediments to extending the transmission distance was the linewidth of the laser, a new laser from Photonetics was brought in and tested. In the previous system, the laser linewidth at 3.8 MHz was the major reason why the system hit a BER floor beyond 200 km. To solve this problem, a tunable laser source with a linewidth of 150 kHz was used for the next set of experiments. Since the new source was tunable, its wavelength of operation was set at 1533 nm to take advantage of the improved gain of the EDFAs at this wavelength.

It was also determined through simulation that this new system with the new laser should be able to transmit just over 300 km with a BER better than 10^{-9}. However, in order to achieve this distance, more than four EDFAs would be needed in the link. To meet this requirement, four additional EDFAs were built. The parameters for these additional EDFAs are also shown in Appendix A.

Using the new tunable laser and three of the new EDFAs, a new successful experiment was demonstrated. With the implementation of the new equipment, 10 Gb/s data was transmitted up to 320 km with a BER better than 10^{-10}. The setup for this experiment is shown in Figure 5.34. Figure 5.34 shows the 320 km link with six EDFAs. The fiber length between each EDFA varied between 75 km and 50 km, however, due to the differing losses of each fiber reel, the link loss between each EDFA was approximately the same. Again, Design 3 was used as the optical SSB transmitter configuration. A picture of the entire system is shown in Figure B.4 in Appendix B.

In Figure 5.34, the number under each isolator, EDFA and BPF corresponds to the number used for each element listed in Appendix A. Further, the average optical power at various points in the system is shown with a dashed line and an arrow. This power was measured with an optical power meter. It is essential to this system's successful operation that the optical power at any point in the fiber not be above +9 dBm in order to avoid serious implications from self phase modulation or other forms of nonlinear distortion [73]. In standard single mode fiber, the refractive index can change as the optical power becomes large. Thus, information within a pulse at a high optical power can travel at a different velocity than information within a pulse at a lower power. As can be seen in Figure 5.34, the average optical power at any point along the fiber is not higher than +7 dBm.

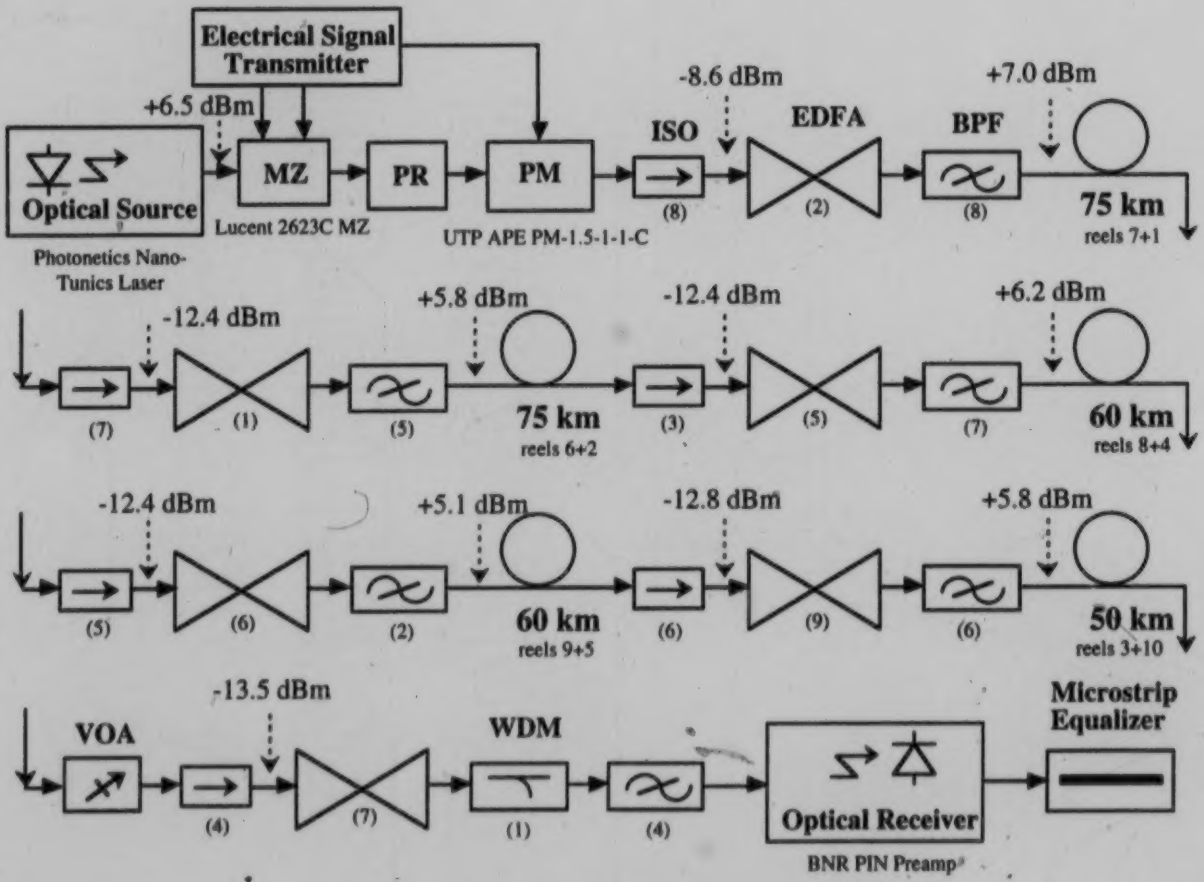
Electrical Signal Transmitter
+6.5 dBm
Optical Source
Photonetics Nano-Tunics Laser
MZ
Lucent 2623C MZ
PR
PM
UTP APE PM-1.5-1-1-C
ISO
(8)
-8.6 dBm
EDFA
(2)
BPF
(8)
+7.0 dBm
75 km
reels 7+1
(7)
-12.4 dBm
(1)
(5)
+5.8 dBm
75 km
reels 6+2
(3)
-12.4 dBm
(5)
(7)
+6.2 dBm
60 km
reels 8+4
(5)
-12.4 dBm
(6)
(2)
+5.1 dBm
60 km
reels 9+5
(6)
-12.8 dBm
(9)
(6)
+5.8 dBm
50 km
reels 3+10
VOA
(4)
-13.5 dBm
(7)
WDM
(1)
(4)
Optical Receiver
BNR PIN Preamp
Microstrip Equalizer

Figure 5.34 320 km SSB optical system

To gain a measure of the effects of chromatic dispersion using the new source, a plot of receiver sensitivity versus fiber length is shown in Figure 5.35 for the DSB and SSB cases. In each case, all six EDFAs were left in the link to isolate the effects of chromatic dispersion. Again, to test the shorter distances, fiber links were replaced with optical attenuation to keep the amount of ASE noise constant at the receiver. In Figure 5.35, three plots are shown, SSB without equalization, SSB with equalization and DSB. For equalization in the SSB case, sections of microstrip were used. In the DSB case, the optical extinction ratio was increased over the SSB case as in the previous system using the 3.8 MHz linewidth source. The pattern length of the 2.5 Gb/s PR sequence was $2^{10}-1$ so the length of the 10 Gb/s PR sequence was $2^{12}-4$. Longer pattern lengths were tested in the new system but this was the longest pattern length that would give acceptable BERs.

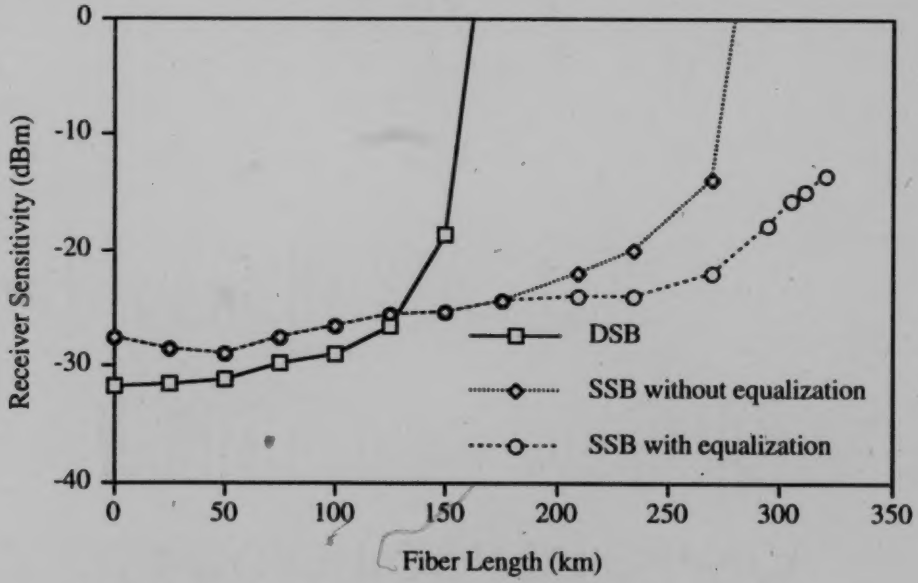

Figure 5.35 Receiver sensitivity versus fiber length for six EDFA link

From Figure 5.35, it can be seen that the DSB case can only extend to approximately 150 km. Beyond this distance, the eye closes. In addition, the receiver sensitivity at 0 km is -31.8 dBm which is slightly higher than the -32.5 dBm value measured in the previous system with four EDFAs. This is a direct result of using two more EDFAs in the new system. In the SSB case, the plot without equalization extends to approximately 270 km before the eye closes so much that the BER is something worse than

10^{-9}. In the SSB case with equalization, the transmission length can be extended to 320 km at a BER of 10^{-9} after which the eye closes to a point where the BER can no longer reach 10^{-9} no matter how high the received optical power is.

The slight improvement in the receiver sensitivity of the SSB curves at 50 km over the value at 0 km is a result of the phase response of the Veritech amplifier used at the receiver. As was alluded to earlier, the phase response of this amplifier is similar to approximately 10-13 cm of microstrip and thus supplies a certain amount of equalization.

The degradation of the receiver sensitivity beyond 250 km in the equalized SSB case is a result of a number of nonidealities of which the main one is the nonideal signal source. As was previously mentioned, sideband cancellation is limited due to the lack of similarity between Q and Qbar. The frequency responses of the transmitter and receiver electronics, especially the microstrip equalizer, play a role in this degradation as well.

To demonstrate how the BER changes as a function of the received power, plots are shown for the distances of 0 km, 100 km, 210 km and 320 km in Figure 5.36. The 210 km system has 8 cm of microstrip in the receiver circuit while the 320 km system has 32 cm of microstrip in the receiver circuit.

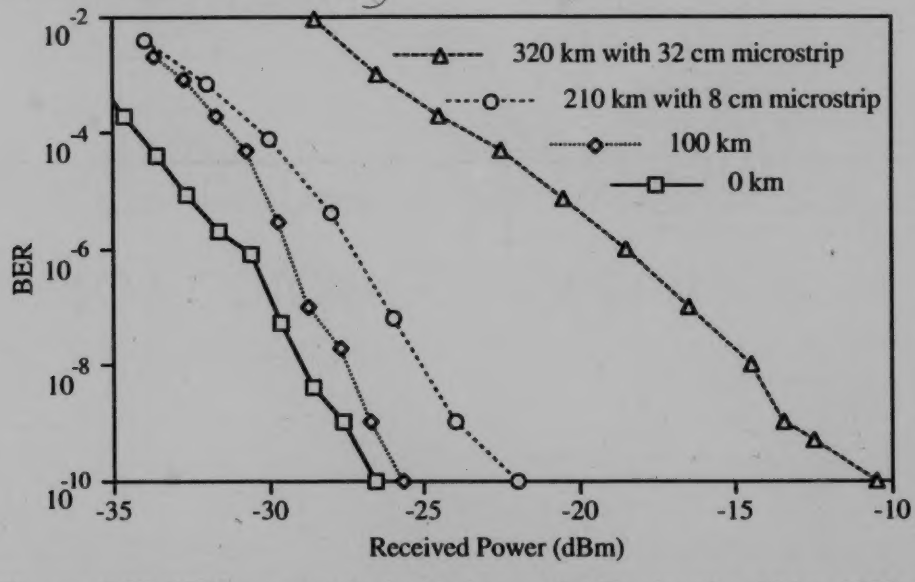

Figure 5.36 BER versus received optical power for fiber lengths of 0 km, 100 km, 210 km with 8 cm microstrip and 320 km with 32 cm microstrip equalization for six EDFAs

As can be seen from Figure 5.36, as the received power decreases, the BER becomes worse. This is a direct result of the degradation of the SNR. In optical systems of this type, when the received power decreases, the system becomes more and more dominated by receiver noise.

Figure 5.37 shows the BER versus received optical power for the SSB case at 270 km with and without microstrip equalization. As can be seen from Figure 5.37, adding the 24 cm of microstrip equalization at the receiver improves the BER. The microstrip equalizer does not reduce the total amount of noise but rather opens the received eye further thus improving the received SNR.

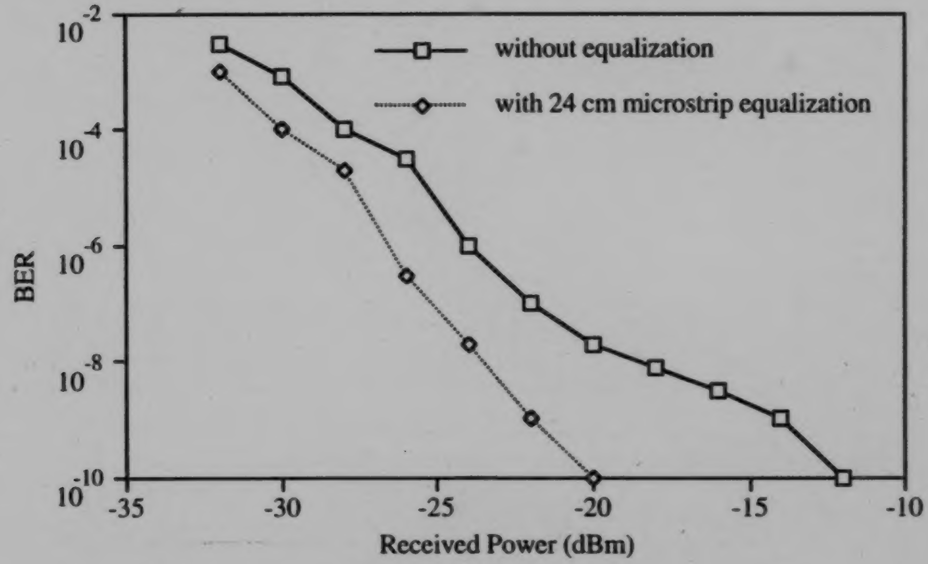

Figure 5.37 BER versus received optical power for 270 km with and without 24 cm microstrip equalization for six EDFAs

To further demonstrate the effect that the microstrip has on opening the received eye and improving the received BER, BER versus microstrip length is plotted for three distances of 305 km, 320 km and 330 km and shown in Figure 5.38.

From Figure 5.38, it can be seen that there is an optimal amount of microstrip that should be used for each fiber length in order to maximize the eye opening and received BER. The received BER is not extremely sensitive to the length of microstrip used for equalization (i.e. +/- 1 cm), however, extreme changes in the microstrip length (i.e. +/- 30 cm) will eventually degrade the system's performance.

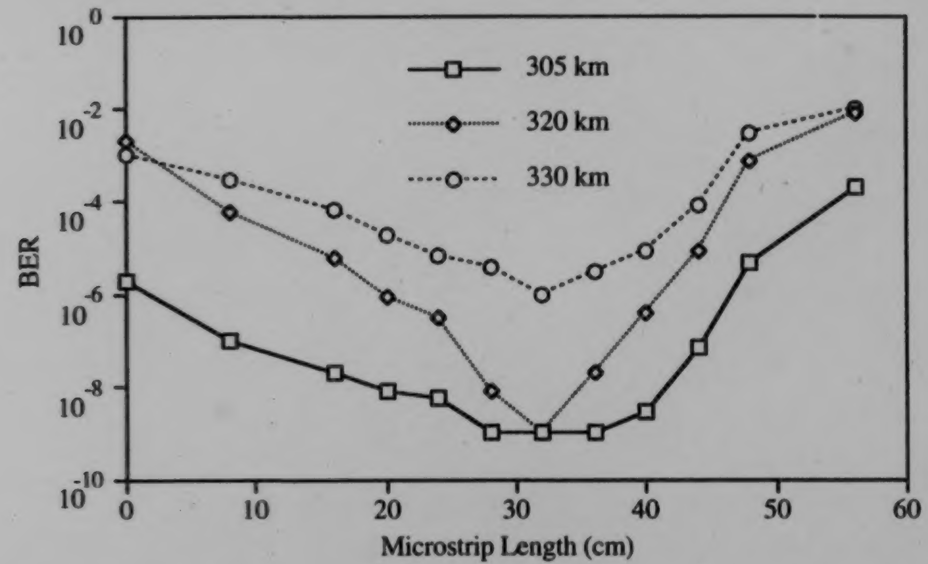

Figure 5.38 BER versus microstrip length for an optical SSB system with six EDFAs in the link

Figure 5.38 also shows the BER floor reached at 330 km. The best achievable BER at 330 km was around 10^{-6}. As previously mentioned, this experimental system could not transmit 10 Gb/s beyond 320 km with a BER of 10^{-10} or better.

As a further measure of performance of the DSB and SSB systems, eye diagrams of the received signal were measured with a digital oscilloscope. The time acquired eyes were sampled for a number of different distances. The eyes were measured with the noise sources. As was mentioned previously, this noise is hard to average out of the plot, especially at longer fiber lengths, due the timing drift of the received sequence as a result of temperature fluctuations along the length of the fiber. Some of the eyes acquired for the longer fiber lengths are slightly corrupted by this drift, however, the improvements obtained by using an optical SSB system with equalization over a conventional DSB system without optical equalization are clearly demonstrated.

The measured eyes for the DSB case at fiber lengths of 0 km, 100 km and 175 km are shown in Figure 5.39.

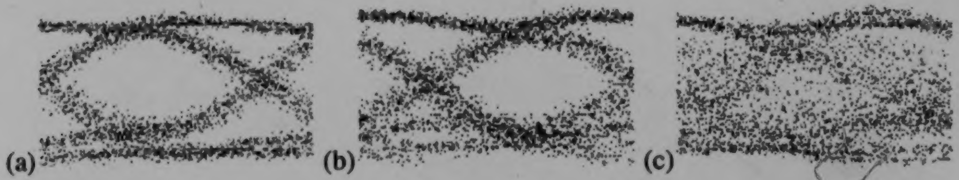

Figure 5.39 Experimental DSB eyes at fiber lengths of (a) 0 km, (b) 100 km and (c) 175 km

The measured eyes forthe SSB case at fiber lengths of 0 km, 100 km and 175 km without microstrip equalization are shown in Figure 5.40.

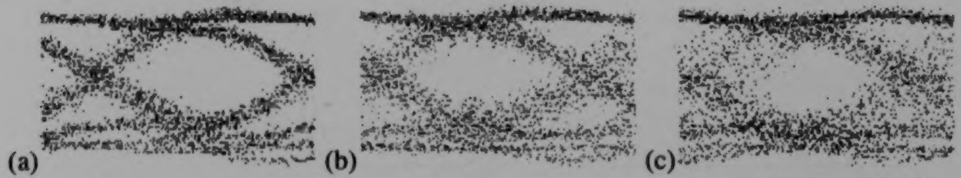

Figure 5.40 Experimental SSB eyes at fiber lengths of (a) 0 km, (b) 100 km and (c) 175 km

The measured eyes for the SSB case at fiber lengths of 210 km, 270 km and 320 km with microstrip equalizers of length 8 cm, 24 cm and 32 cm respectively are shown in Figure 5.41.

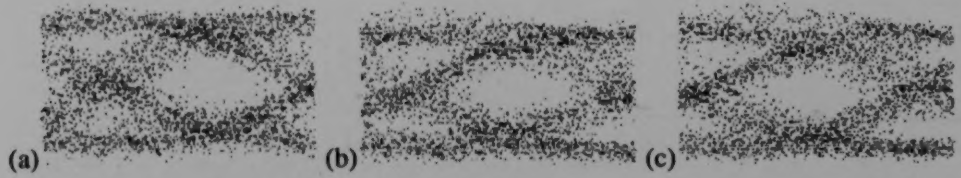

Figure 5.41 Experimental SSB eyes at fiber lengths of (a) 210 km with 8 cm microstrip, (b) 270 km with 24 cm microstrip and (c) 320 km with 32 cm microstrip

While the previous eyes are of signals which would give BER as good or better than 10^{-9}, the next set of eyes are representative of signals which gave BER worse than 10^{-9}. The measured eyes for the SSB case at distances of 270 km without equalization, 270 km with the old source linewidth of 3.8 MHz with 24 cm microstrip and 330 km with 32 cm microstrip are shown in Figure 5.42. These eyes were acquired to demonstrate the degraded system performance when either no equalization is used, a large laser linewidth or at a fiber length beyond equalization.

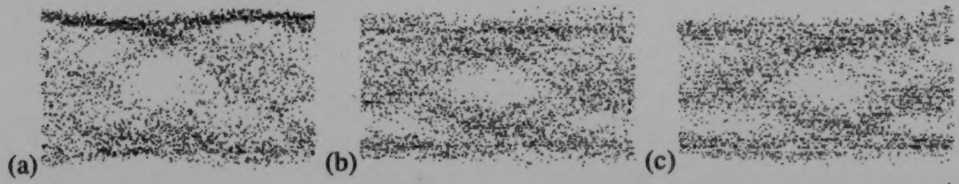

Figure 5.42 Experimental SSB eyes at fiber lengths of (a) 270 km with no equalization (b) 270 km with 24 cm microstrip with the old source linewidth of 3.8 MHz and (c) 330 km with 32 cm microstrip

5.3.4 Comparison of Simulated and Experimental Results

In order to gain a better understanding of the limitations of the SSB system that was tested in the lab, in particular Design 3, a more detailed and accurate simulation of the system was carried out as compared to the simulations of the ideal systems in Chapter 4. In the new simulations, the models and parameters from the Design 3 simulation presented in Chapter 4 were modified and the frequency response of a number of critical electrical components was included in simulation to more accurately model the real experiment. This provided insight into what modifications could be made to the experimental system in order to improve its performance.

In the simulation of the experimental system, a number of changes were made to the ideal system. First, the ideal pseudo-random bit sequence at the input to the transmitter was replaced with the time acquired data traces out of the Veritech dual channel amplifier (VM10CMD-320). These signals represented the actual Q and Qbar signals which would ultimately drive the MZ and the Hilbert transform circuit. These data signals were then filtered through the frequency responses of a Picosecond Pulse Labs bias tee (5575A) and the Lucent modulator left and right arms before driving the MZ. In addition, these signals were applied to the Hilbert transform circuit where the Hilbert signal was passed through the frequency responses of the Veritech high power amplifier (VMPPA-428), the Merrimac 4:1 combiner (PDM-45R-9.2G) and a Picosecond Pulse Labs DC block (5500A) before driving the UTP PM. This was the most accurate representation of the transmitter configuration and thus the most accurate simulation of the transmitted optical electric field.

At the receiver, the detected optical signal was passed through the frequency responses of the BNR PIN-Preamp, the SHF amplifier (SHF90P), the Veritech amplifier (VMA3K10C-232) and a Picosecond Pulse Labs DC block (5500A) before determining the optimal decision time and threshold thus giving the BER of the received data.

Making these changes to the ideal system allowed simulation of Design 3 for the two experimental systems of Design 3. The major differences between these two systems was the laser linewidth and the optical link parameters such as the component loss and the EDFA parameters. Four EDFAs were used in the first system with the 3.8 MHz linewidth source and six were used in the second with the 150 kHz linewidth source.

As a first measure of performance, the received eyes of the simulated experimental system were plotted. The eyes were simulated for the three cases, DSB, SSB without equalization and SSB with equalization. For the simulated eyes, the noise was not included in the plots.

The simulated eyes for the DSB case at fiber lengths of 0 km, 100 km and 175 km are shown in Figure 5.43.

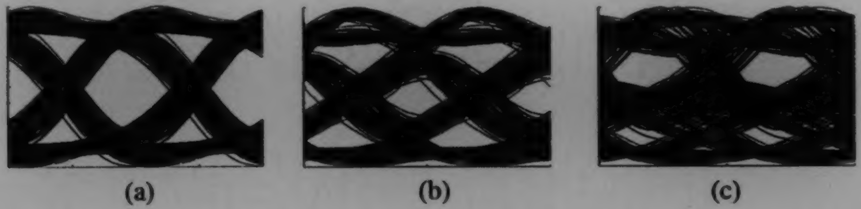
(a) (b) (c)

Figure 5.43 Simulated DSB eyes at fiber lengths of (a) 0 km, (b) 100 km and (c) 175 km

The simulated eyes for the SSB case at fiber lengths of 0 km, 100 km and 175 km without microstrip equalization are shown in Figure 5.44.

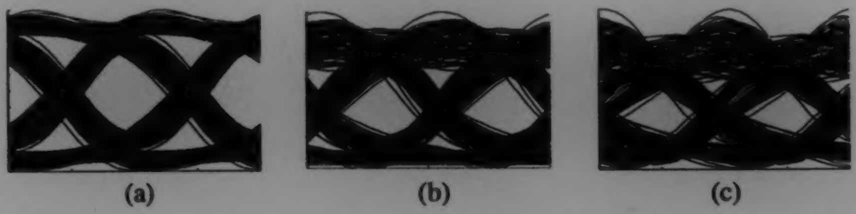
(a) (b) (c)

Figure 5.44 Simulated SSB eyes at fiber lengths of (a) 0 km, (b) 100 km and (c) 175 km

The simulated eyes for the SSB case at fiber lengths of 210 km, 270 km and 320 km with microstrips of length 8 cm, 24 cm and 32 cm respectively are shown in Figure 5.45.

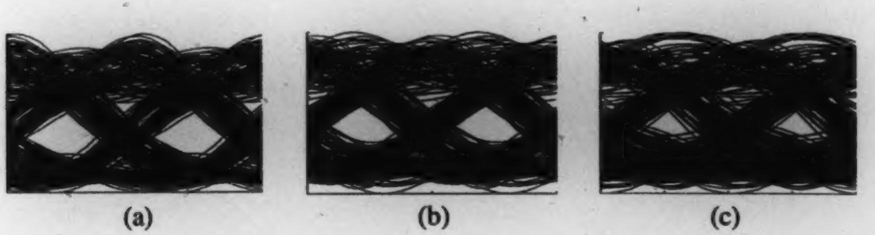
(a) (b) (c)

Figure 5.45 Simulated SSB eyes at fiber lengths of (a) 210 km with 8 cm microstrip, (b) 270 km with 24 cm microstrip and (c) 320 km with 32 cm microstrip

Comparing the simulated eyes in Figures 5.43 through 5.45 to the experimental eyes in Figures 5.39 to 5.41, it can be seen that the simulated eyes follow the same general trend as the corresponding experimental eyes. The DSB eye closes beyond 150 km while the SSB eye at the same distance is still open. Further, the SSB eye at 320 km is still discernible if equalization is used. The major difference between the experimental and simulated eyes is that the experimental eyes have noise while the simulated eyes do not.

As a further measure of performance, the received eyes of the simulated system for the SSB case at distances of 270 km without equalization and 330 km with 32 cm of microstrip are shown in Figure 5.46. These eyes can be compared to the experimental ones shown in Figure 5.42.

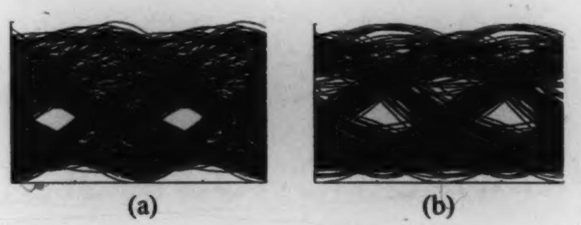
(a) (b)

Figure 5.46 Simulated SSB eyes at fiber lengths of (a) 270 km with no equalization (b) 330 km with 32 cm microstrip

The simulated frequency spectrums for the DSB and SSB optical systems are shown in Figure 5.47. In these plots, the vertical scale is linear and, as such, the carrier is removed to better show the spectral side lobes. As a result of these spectra being simulated and not experimentally measured, the system is not subjected to noise and thus the spectral content beyond 10 GHz is clearly visible. The spectral spikes shown in these plots are analogous to the spikes in the plots in Figures 5.7 and 5.8.

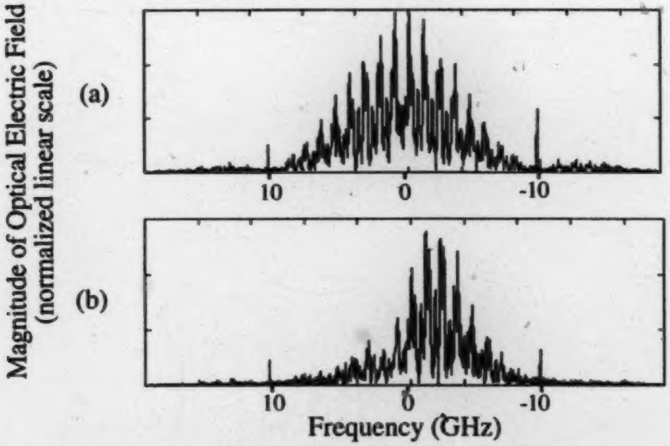

Figure 5.47 Simulated DSB and SSB optical spectra

Adding the EDFAs to the link, the receiver sensitivity versus received optical power can be simulated and compared to the experimental results. The first system tested is the first implementation of Design 3 where the laser with the 3.8 MHz linewidth is used and four EDFAs are used in the link. The EDFAs used in the simulation correspond to those shown in Figure 5.19. In this system, the first four EDFAs built at TR Labs were used. Their parameters are shown in Appendix A. The simulated and experimental plots for the receiver sensitivity versus fiber length are shown in Figure 5.48. The experimental plot is the same information as was shown in Figure 5.27. In this SSB system, no equalization was used since the system hit a BER floor beyond 200 km due to the FM to AM noise. Equalization was not an issue at distances less than 200 km. Again, the receiver sensitivity is the required optical power at the input to the receiver EDFA needed to maintain a BER of 10^{-9} at the receiver.

In Figure 5.49, the receiver sensitivity versus fiber length is shown for the second case of Design 3 where the laser with the 150 kHz linewidth was used and six EDFAs were used in the link. The EDFA placement in the system correspond to those shown in Figure 5.34. The parameters for the EDFAs are also shown in Appendix A.

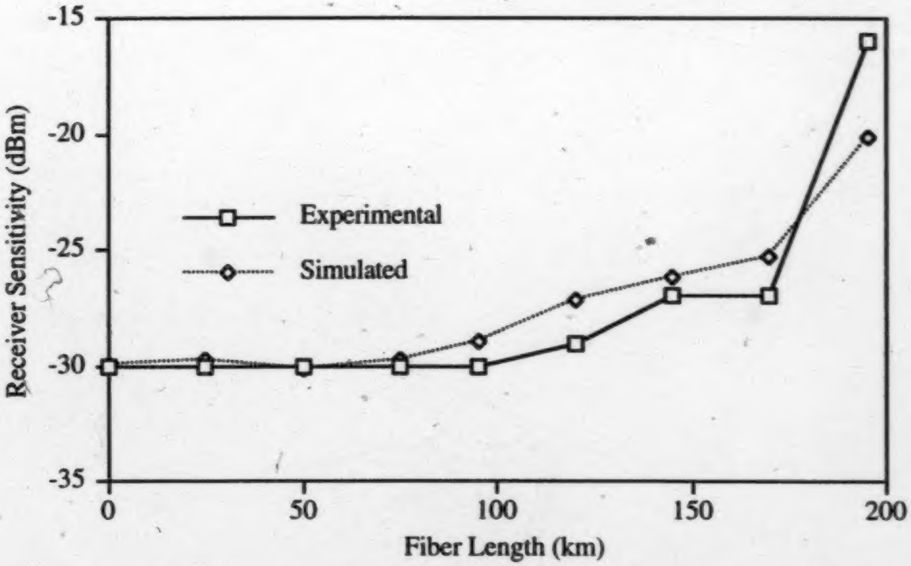

Figure 5.48 Receiver sensitivity versus fiber length for the experimental and the simulated optical SSB system with four EDFAs

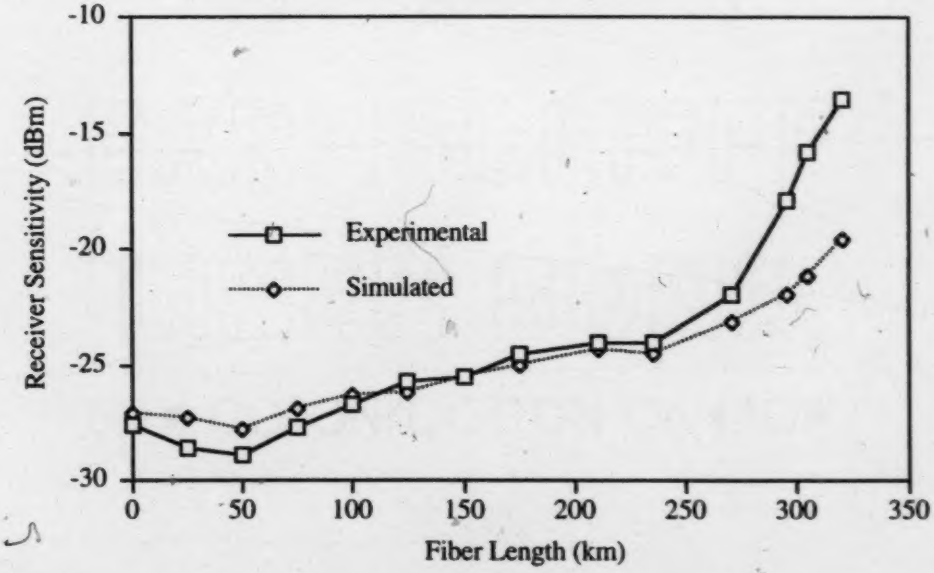

Figure 5.49 Receiver sensitivity versus fiber length for the experimental and the simulated optical SSB system with six EDFAs

From Figures 5.48 and 5.49, it can be seen that the simulated system performs closely to the experimental system. The differences lie in a few areas. One is that not all of the frequency responses of components in the receiver have been included in the simulation. For example, the transmission path connecting the input of the D-FF used for the decision circuit is slightly mismatched to the actual chip. This is suspected of causing slight problems. Another area of inconsistency lies in the fact that the amplitude and phase response of the modulators can never be separated from the detector's frequency response since there is the optical medium between the two. Another area of inconsistency is the optical connector loss. It is assumed to be negligible or a fixed value in the simulations, however, in the experiment, it changes every time a connection is broken and reconnected. Connections were broken frequently during the experiment in order to measure the optical power at various points in the optical link. A last area of inconsistency lies in the fact that the simulated system measures the BER always at an optimal decision time and threshold while the experimental case is dependent on a manual adjustment of the decision time and threshold level. These values were optimized in the experiment but are known to drift over time.

Based on the previous comparison of simulated and experimental results, it can be concluded that if enough detail is added to the simulation, the experimental system can be accurately represented.

Using this simulation capability, a better understanding of where improvements could be made in the experimental system was sought. In order to do this, simulations of the nonideal components in the experiment were isolated within the system to determine which nonidealities had the most significant impact on the system's performance. More specifically, the ideal system as shown in Chapter 4 was subjected, independently, to nonideal components to determine which ones had the most negative impact on the system's performance. The ideal system under test consisted of the Design 3 configuration outlined in Chapter 4 with an EDFA cascade of 13 units that covered 540 km of fiber.

In the simulations, the individual effects of four major items were measured: the nonideal source laser linewidth of 4 MHz, the microstrip equalizer, the frequency responses of the electrical components at the transmitter and the receiver, and the nonideal signal source out of the BERT set.

In the system, the link EDFAs in the cascade were modeled with an output saturation power P_{SAT} of 5 dBm, a spontaneous noise factor N_{SP} of 1.73 and a small signal gain G_o of 25 dB. The EDFA post-amplifier used at the transmitter had an output saturation power of 7 dBm, a small signal gain of 15 dB and a spontaneous noise factor of 1.73. The EDFAs were separated by 45 km sections of normal single mode fiber. As a result, the optical loss per stage was 17 dB (11 dB fiber loss, 2 dB splice loss and 4 dB insertion loss due to an isolator at the input of the EDFA and an optical BPF at the output of the EDFA). The received BER versus launched optical power out of the EDFA post-amplifier is shown in Figure 5.50. Each plot is representative of the ideal system with one nonideal component added.

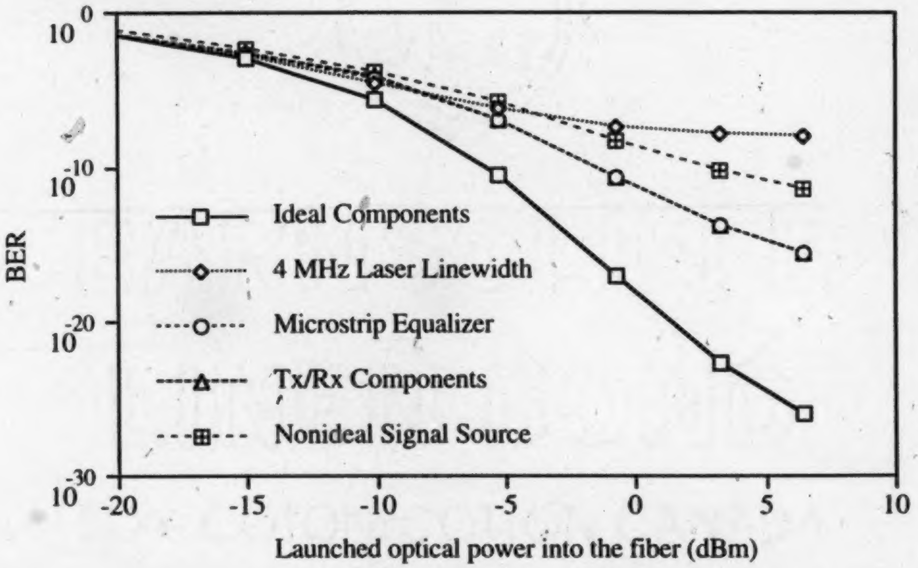

Figure 5.50 BER versus launched optical power into the fiber for the ideal system with nonideal components at 540 km with 45 km EDFA spacings

From Figure 5.50 it can be seen that the laser source linewidth of 4 MHz had the most negative impact on the system. The nonideal signaling source had the second most negative impact on the system. The frequency responses of the transmitter and receiver components along with the microstrip equalizer had the next most negative impact on the system. In the case of the microstrip, an 80 cm long section was used to equalize the 540 km section of fiber. In the experiments, the source linewidth was reduced to 150 kHz which eliminated it as the bottleneck in the system. Improving the signal source is now the component with the most negative impact on the system. By matching the rise/fall characteristics and the corresponding ripples in the Q and Qbar signals, the impact of the nonideal signal source can be reduced, if the quality of the signal source were improved, transmission up to 400 km with a BER better than 10^{-10} should be possible. To extend the distance beyond 400 km, the equalizer would have to be redesigned. The microstrip could be replaced with a tapped delay filter. The tapped delay filter could provide a better match to the inverse phase function of the fiber since the tap weights could be adjusted. Further, the tap delay filter would not have to be subject to frequency dependent attenuation which is seriously detrimental in long sections of microstrip.

As a last comparison of simulated versus experimental results, the simulated and experimental loss and phase delay of the microstrip at 10 GHz are shown. In Figure 5.51, the attenuation versus microstrip length for both the simulated and experimental case at 10 GHz is shown.

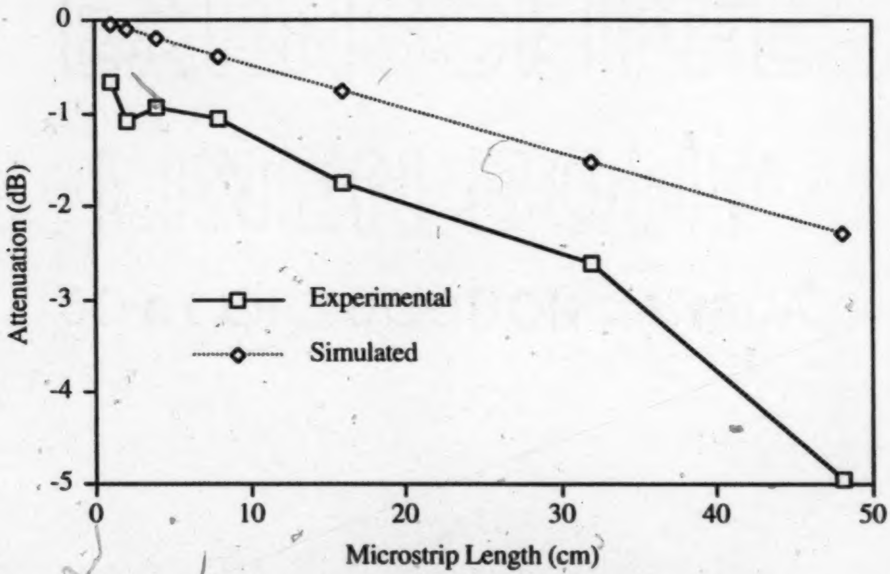

Figure 5.51 Attenuation versus microstrip length at 10 GHz

The attenuation in the microstrip is frequency dependent. For example, at 0 Hz, the microstrip has effectively no attenuation while at 10 GHz it is maximum over the 0 to 10 GHz range. This frequency dependent attenuation proved to be a critical limiting element in the ability of the microstrip to equalize long lengths of fiber. The equations used to model the microstrip are shown in section 4.1 in equations 4.8 to 4.19.

From Figure 5.51, it can be seen that the attenuation coefficient α chosen for the simulations was too small. Additional loss from the connection between the SMA connector and the microstrip was also a factor. The connector loss could be excessively large in the 48 cm long section of microstrip as is evident in Figure 5.51.

Figure 5.52 shows the phase delay provided from the microstrip at 10 GHz for the actual and simulated versions of microstrip. The phase response of the simulated and experimental microstrip is of a second order nature. Thus, the phase difference between the simulated and experimental microstrip is different for each frequency. The largest difference, which is at 10 GHz, was chosen as the measured parameter.

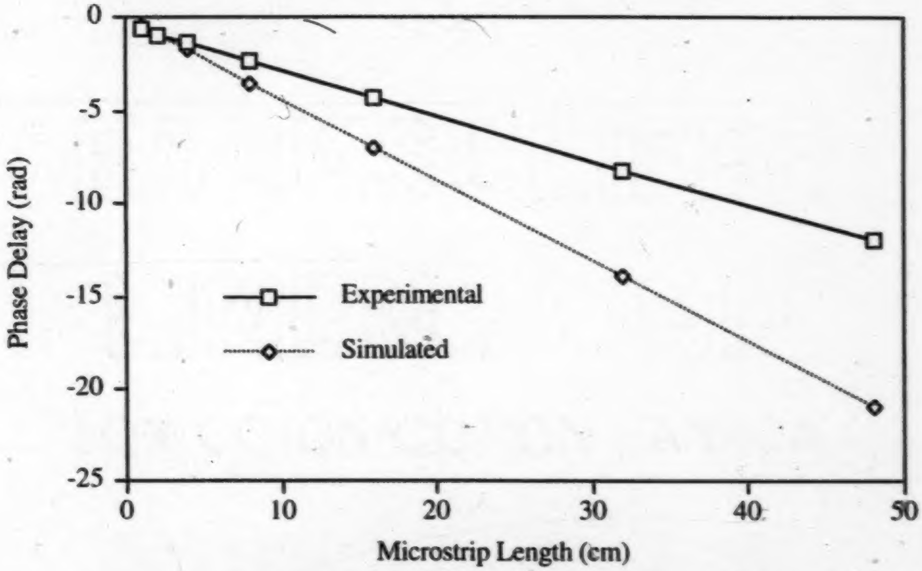

Figure 5.52 Phase delay versus microstrip length at 10 GHz

In Figure 5.52, it can be seen that the amount of phase delay in the simulated case is larger than the actual case. Thus, the amount of phase correction provided by the modeled microstrip was overestimated. This means that for a given fiber length, more microstrip is needed than expected for equalization. For example, to equalize 100 km of fiber, 12 cm of microstrip is needed as opposed to 9 cm which was used in simulation. The negative implications of this are that more attenuation from the microstrip will result when equalizing a given length of fiber. Overall, the result of more attenuation from more microstrip leads to the conclusion that the microstrip will eventually have to be replaced with some other form of equalization if fiber lengths longer than 400 km are to be experimentally demonstrated.

5.4 Experiments at Nortel

After the completion of the tests at TR Labs in Edmonton, additional experiments were organized at Nortel's Skyline lab in Ottawa. In these experiments, the first goal was to demonstrate the operation of the optical SSB system using the Design 3 transmitter configuration consisting of a MZ modulator and the concatenated PM. The second goal of the experiments was to try and improve upon the maximum transmitted distance of the optical SSB system. At TR Labs, the maximum transmission distance was 320 km. There were a number of experimental nonidealities which limited the effective operating distance as was shown in the previous section. One of the major ones was the nonideal signal source. The mismatch between the Q and Qbar signals at the output of the 4:1 MUX was fairly significant. Improved quality of Q and Qbar was expected at the Nortel site by using an Anritsu MP1763B 12.5 Gb/s pattern generator. According to simulation, an improvement in the signal source should extend the effective operating distance beyond 320 km.

The optical SSB transmitter layout used at Nortel is shown in Figure 5.22. There were two differences between the transmitter setup at TR Labs and the one setup at Nortel. The first difference was that the 10 Gb/s data signals of Q and Qbar for the Nortel experiment were generated directly from the Anritsu pattern generator. The second difference was that the Lucent MZ modulator was replaced. A Lucent MZ modulator with the same model number was used in the Nortel experiments. The reason for this change was the original MZ modulator was slightly damaged subsequent to the last experiment carried out at TR Labs.

Using the optical spectrum analyzer layout shown in Figure 5.2, the optical spectra at the output of the PM were measured. The measured spectra of the DSB and SSB modulation formats were again deconvolved with the measured spectra of the carrier. The deconvolution process removed the frequency response of the FFP from the measured spectra. Figure 5.54 (a) shows the experimental DSB spectrum with the same modulation depth as the SSB case and (b) shows the experimental SSB spectrum.

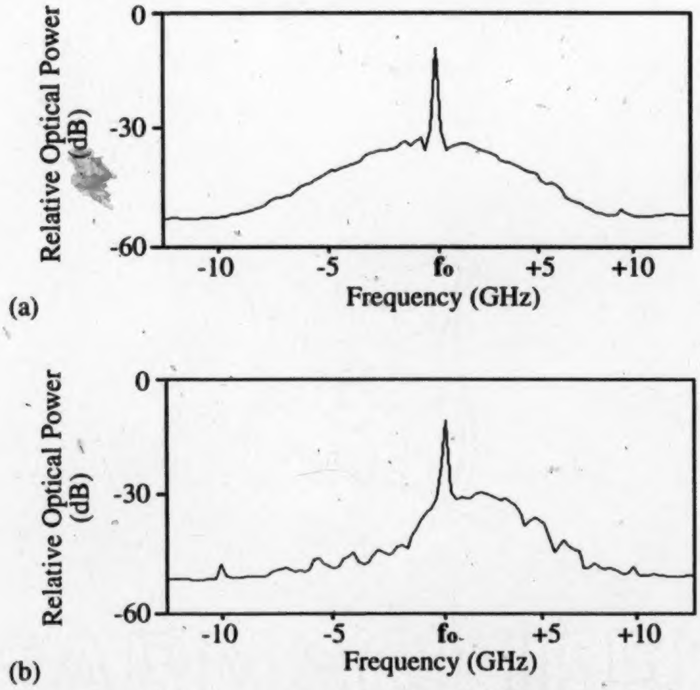

Figure 5.53 Optical signal spectra for (a) DSB and (b) SSB

From Figure 5.53 (a), it can be seen that the information sidebands in the DSB case are more continuous and have less ripples than the sidebands measured at TR Labs shown in Figure 5.26 (a). This difference is due to the fact that the 10 Gb/s data at Nortel was created directly from a pattern generator and was not a multiplexed version of four 2.5 Gb/s channels.

Comparing Figure 5.53 (b) with (a), it can be seen that there is significant sideband cancellation. Further, it can be seen that the Hilbert transform filter, which is comprised of a four tap delay filter, creates it's own ripples in the optical SSB magnitude spectrum.

The optical SSB transmitter was connected to a full optical system and the performance of the system was measured for a number of different fiber lengths. For each fiber length, the span between EDFAs varied between 60 to 80 km. The 290 km system is shown in Figure 5.54.

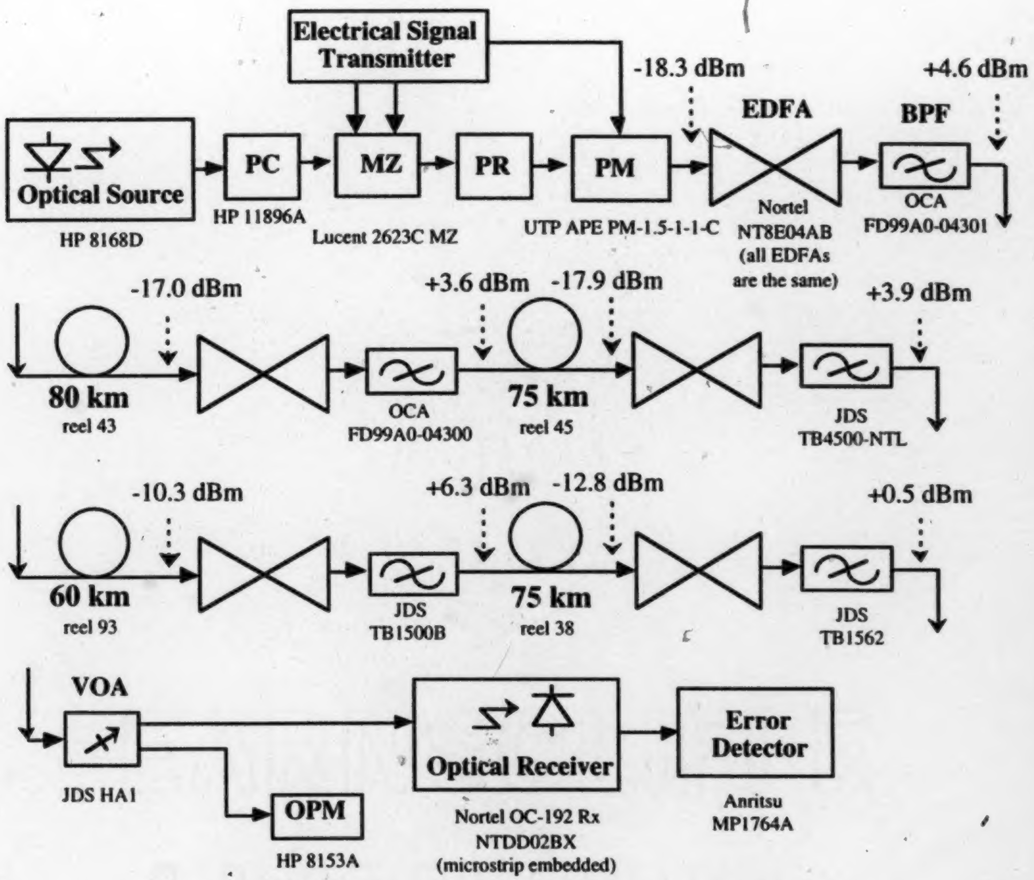
Electrical Signal Transmitter
-18.3 dBm
+4.6 dBm
EDFA
BPF
Optical Source
HP 8168D
PC
HP 11896A
MZ
Lucent 2623C MZ
PR
PM
UTP APE PM-1.5-1-1-C
Nortel
NT8E04AB
(all EDFAs
are the same)
OCA
FD99A0-04301
-17.0 dBm
+3.6 dBm
-17.9 dBm
+3.9 dBm
80 km
reel 43
OCA
FD99A0-04300
75 km
reel 45
JDS
TB4500-NTL
-10.3 dBm
+6.3 dBm
-12.8 dBm
+0.5 dBm
60 km
reel 93
JDS
TB1500B
75 km
reel 38
JDS
TB1562
VOA
JDS HA1
OPM
HP 8153A
Optical Receiver
Nortel OC-192 Rx
NTDD02BX
(microstrip embedded)
Error Detector
Anritsu
MP1764A

Figure 5.54 Nortel 290 km optical SSB system

In all of the experiments at Nortel, the source laser was a tunable narrow linewidth source. The linewidth was 80 kHz and the chosen wavelength of operation was 1549 nm to be compatible with OCA bandpass filters which had a fixed passband wavelength. As previously mentioned, the transmitter configuration was the same as shown in Figure 5.22. The receiver used in the experiments was the Nortel OC-192 receiver module. This receiver module had the optical signal as an input and provided a 1:N demultiplexed output channel. Due to the $2^N - 1$ pattern length of the PR sequence created by the pattern generator, the demultiplexed channel could be sent to the Anritsu error detector and an accurate representation of the BER on the 10 Gb/s data would be measured and displayed.

The Nortel receiver circuit handled all of the required receiver functions. The variations in the received optical power were compensated for by an adaptive gain circuit. Functions handled on board included the clock recovery required for the decision circuit, the optimal decision time, and optimal threshold level. These decision levels were continuously updated based on any changes in the received optical signal.

BER versus received optical power at the input to the receiver module for fiber lengths of 0 km, 155 km, 215 km and 290 km are shown in Figure 5.55. The distances of 0 km, 155 km and 215 km are for the optical SSB system without equalization. The 290 km system had 24 cm of microstrip equalization.

The 0 km system used only one EDFA, the 155 km system used a 80 km and a 75 km fiber segment along with three EDFAs, the 215 km system used 80 km, 75 km and 60 km fiber segments with four EDFAs, and the 290 km system was as shown in Figure 5.54 with five EDFAs.

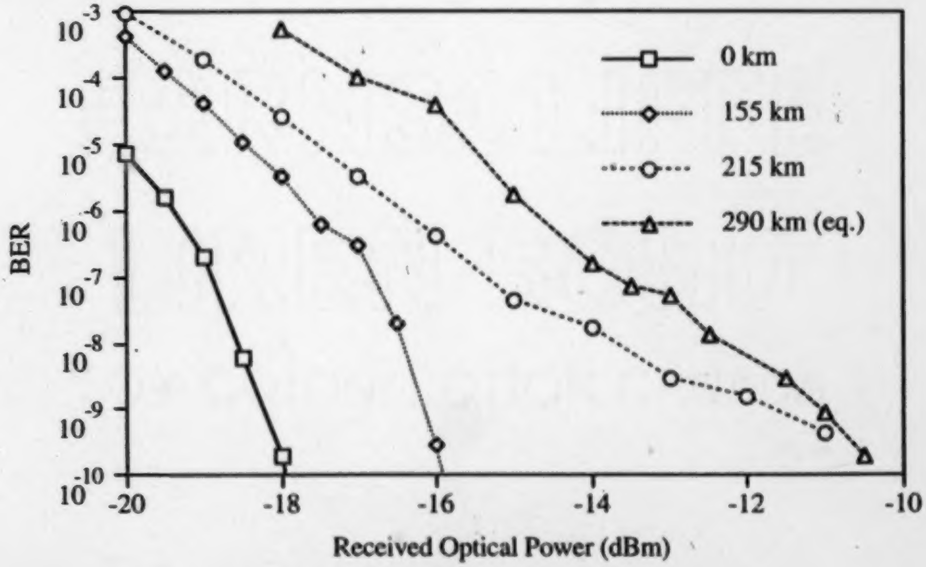

Figure 5.55 BER versus received optical power for SSB systems at 0, 155, 215 and 290 km (with 24 cm microstrip equalization)

From Figure 5.55, it can be seen that the threshold for a BER in the neighborhood of 10^{-10} is -17.5 dBm for the optical SSB system operating back to back. This value was close to the expected value for the SSB transmitter in conjunction with the Nortel receiver.

It can also be seen that the nonequalized limit on transmission distance for the SSB system is around 215 km. This value is lower than the nonequalized limit of 270 km in the latest TR Labs experiments. This is directly due to the Veritech amplifier (VMA3K10C-232) which was used in the TR Labs receiver circuit. As was shown in Figures 5.33, this amplifier provided compensation for approximately 100 km of fiber. For the equalized case at 290 km, the BER versus received power hit a floor near 2×10^{-10}. Increasing the received power beyond -11 dBm had little effect on shifting operation into an error free zone. This is due to a combination of eye closure and system noise before the receiver.

Initial expectations of the experiments at Nortel were that the successful transmission distance of 320 km established at TR Labs would be surpassed. It was expected that the Anritsu pattern generator would provide better quality Q and Qbar data signals than was provided by the 4:1 MUX used at TR Labs. As it turned out, the overall performance of the system at Nortel was comparable to the TR Labs system but not better. This can be seen in comparing the receiver sensitivity penalty of the 290 km length to the 0 km length. The penalty in both the Nortel experiment and the TR Labs experiment was around 7 dB.

This lack of improvement is attributable to a number of reasons. First, even though the quality of the data out of the Anritsu pattern generator was better than the data out of the 4:1 MUX, it still had ripples in the logic levels. It can never be expected that actual 10 Gb/s data will be as good as an ideally simulated sequence on a computer. Second, the optical link was less than optimal. Connecting the EDFAs located in one bay to the fiber reels in another bay required the use of specific patchcords. Some of these patchcords had losses as high as 3 dB. Depending on where these losses occur in the link, the loss can have minimal effect in the received optical power, however, the SNR is still degraded. Third and finally, the Veritech amplifier which provided the equalization at the receiver at TR Labs worked better than a section of microstrip since the amplifier had a fairly flat magnitude response while the microstrip had a substantial frequency dependent attenuation.

One additional problem that occurred at the Nortel site, but was eventually controlled, was the drift in polarization of the light entering the MZ modulator and the PM. Polarization rotators were used at the input to each modulator but this served to optimize the polarization instantaneously. After a period of a few hours, the polarization of the light into the modulators drifted and the polarization rotators had to be reset.

This polarization drift had two effects. First, the electro-optic effect of the modulator was diminished. This reduced the modulation depth in the MZ modulator and the level of sideband cancellation in the PM. As the modulation depth decreased and the optical signal became more DSB, the system's performance at distances beyond 150 km seriously fluctuated. Second, the insertion loss of the modulator also changed with the change in polarization of the light entering the modulator. This translated to changes in the transmitted power and thus affected the received BER. The polarization was primarily stabilized with the introduction of a HP 11896A polarization controller before the MZ modulator, however, the polarization into the PM still had to be retuned every few hours.

A measurement was made of the optical SSB system's dependence on pattern length. The pattern length for the BER curves shown in Figure 5.55 was 2^7-1. Figure 5.56 shows BER versus pattern length for the 290 km link with a received power of -11 dBm.

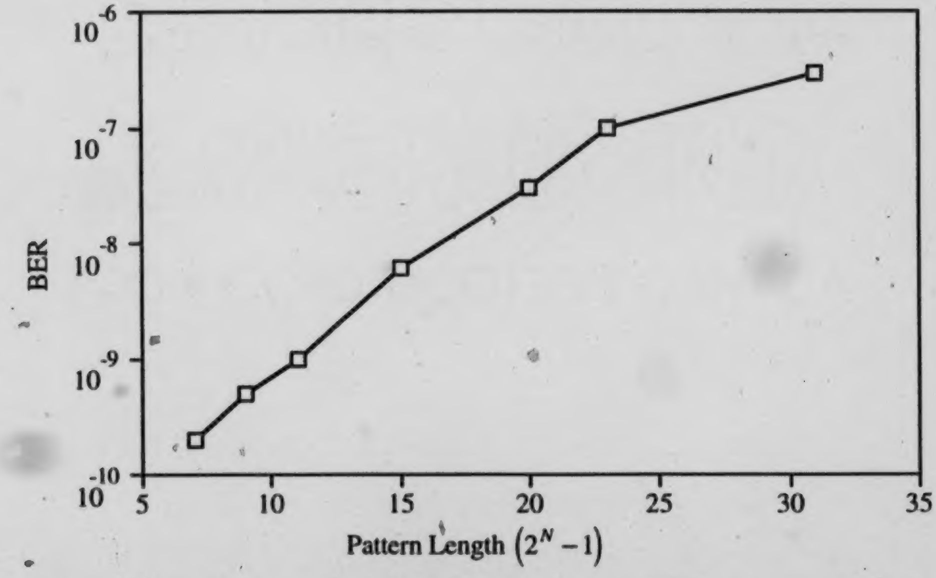

Figure 5.56 BER versus pattern length for the optical SSB system at 290 km

From Figure 5.56, it can be seen that there is a dependence on the pattern length. This dependence is more prominent at longer fiber lengths since sideband cancellation was more important. Further, the Merrimac 4:1 combiner used in creating the Hilbert transform had a low frequency cutoff at 170 MHz. This limited certain lower frequencies from propagating through the Hilbert transform circuit.

As a verification that the pattern length dependence was a result of the Hilbert path, the Hilbert signal into the PM was disconnected and a conventional DSB system over 80 km of fiber was tested for pattern dependence. Measurements showed that this DSB system had no visible pattern length dependence over the pattern length range of $2^7 - 1$ to $2^{31} - 1$.

6. CONCLUSION

6.1 Conclusion

There were four main objectives of the research described in this thesis. The first objective was to review the previously published approaches which have been either developed or proposed to reverse or limit the effects of chromatic dispersion in standard single mode fiber in the 1.55 μm wavelength region. Focus was given to digital systems at the OC-192 data rate. The second objective was to develop a new method or technique which could be used in baseband digital optical systems which would reverse or limit the effects of chromatic dispersion. In this case, the new method was SSB modulation of an optical carrier with a digital signal. The third objective was to simulate this technique by modeling the optical SSB system on a computer and verify that the new technique was effective. The fourth and final objective was to build and test this new optical SSB system in the lab and verify experimentally the effectiveness of the new technique.

In Chapter 2, a brief review on the background of the problems created by chromatic dispersion in standard single mode fiber was presented. As well, the previous approaches used to reverse or limit the effects of chromatic dispersion were reviewed. These approaches fell into three general categories. The first category consisted of techniques which used equalization in the optical domain. In these approaches, optical elements with the inverse phase characteristic of the fiber were used to reverse the effects of the chromatic dispersion incurred by the fiber. Some typical optical elements included chirped Bragg gratings and dispersion compensating fiber. Prechirping the optical signal with an external modulator also offered a small amount of optical compensation. The second category consisted of techniques which used post detection equalization. In these approaches, equalization was implemented with an electrical component after the light was detected. Some typical electrical elements were microstrip lines and microwave waveguides. Electrical equalization could not be used on conventional optical DSB transmission with self-homodyne detection because of the destruction of the phase information upon detection. Thus, electrical equalization had to be used with alternate transmission or detection formats such as heterodyne detection. The third and final category consisted of techniques which modified the transmission format of the information such that the required optical transmission bandwidth used to transmit the information was reduced. By reducing this effective bandwidth, the transmission distance could be partially extended. Some typical formats include multilevel transmission and AM-PSK duobinary transmission.

The second objective of this research was to try to develop a new method or technique which could be used in baseband digital optical systems which would reverse or limit the effects of chromatic dispersion. SSB systems were shown to be candidates for dispersion compensation. Chapter 3 presented a theoretical derivation and analysis of a number of optical SSB modulation systems that could be used in a digital transmission system. Three different transmission designs were outlined in this chapter of which two were shown to be superior candidates for experimental implementation. In order to create a SSB signal, the Hilbert transform of the original information had to be derived. A number of different methods for generating a Hilbert transform signal were presented. The tapped delay approach with four taps was selected as the best experimental implementation.

In Chapter 4, simulation results of the new optical SSB systems were presented. The performance of these systems in terms of extending the transmission distance of the OC-192 data rate on standard single mode fiber was the focus. Simulations were performed for ideally modeled components. From these simulations, it was determined that the new optical SSB system could offer an improvement over a conventional optical DSB system. The new optical SSB system was optimized in terms of transmission parameters and link conditions. The equalization, which was done post detection, would be implemented with sections of microstrip. The microstrip was also modeled. Based on the simulations, the optical SSB system showed the ability to equalize the dispersion induced by almost any length of fiber as long as the one sideband was effectively canceled and the inverse fiber transfer function could be accurately represented with an electrical component.

Experimental limitations such as FM-AM noise, improper sideband cancellation and nonideal equalization post detection were recognized in the simulations.

Chapter 5 presented the experimental results of the tested optical SSB systems. Again, performance of these systems in terms of extending the transmission distance of the OC-192 data rate was the focus. In these experiments, 10 Gb/s data was transmitted over 320 km of fiber with a BER better than 10^{-10}. Transmission beyond 320 km was not possible without reaching an error floor worse than 10^{-8}. This was a result of a number of nonideal components in the experimental setup. A comparison of the simulated and experimental results was also given with comments given on similarities and differences between the two results. The simulations were used to determine which of the nonideal components within the experimental setup were the most detrimental to extending the transmission distance. At this point of development, inadequate sideband cancellation and improper equalization from the microstrip are the major limiting factors in extending the transmission distance.

6.2 Future Work

As was shown experimentally, the optical SSB system currently works effectively up to 320 km. However, if this distance is to be extended, a number of improvements and changes would have to be made to the existing system. First, work on simulating the optical SSB system could be extended. The more detail that is added into the simulation, the closer the simulation is to representing the experimental system. The bottlenecks in the system performance at this point have been recognized, however more work on predicting future problems such as nonlinear optical effects [73] in SSB modulation could be carried out.

Two major improvements in the experimental SSB system were undertaken during the course of the thesis work. The first was to reduce the linewidth of the source. Initially, the laser in use had a linewidth of 4 MHz. With the existing technology, the FM-AM noise penalty limited the error free transmission to about 200 km. When the linewidth was reduced to 150 kHz, the FM-AM noise penalty was determined to be insignificant until well beyond 1000 km. As a result, a laser with a linewidth of 150 kHz or lower was used in the latest experiments. The second improvement that was implemented was to improve the quality of the bit stream entering the transmitter. This improvement was not critical to go beyond 200 km, however, it is critical to go beyond 320 km. In the initial system setup at TR Labs, the data signal and it's complement are generated from a NEL 4:1 MUX. Thus, the data and it's complement are not always the exact inverse of each other as there are spurious fluctuations throughout the bit in each data stream. Thus, the quality of the transmitted amplitude modulated signal was reduced and more importantly, the quality of the Hilbert transform of the data was also reduced. This lead to reduced sideband cancellation and thus, reduced equalization of the chromatic dispersion.

An attempt was made at Nortel to use a 10 Gb/s pattern generator that would improve the quality of the bit stream entering the transmitter. The Anritsu pattern generator offered an improvement over the NEL 4:1 MUX however there were still some slight mismatches between the data and it's complement. What is required to correct this problem is to integrate all of the signal generating processes into an integrated circuit. If the layout is carefully designed, the driving signals can be closely matched and the Hilbert transform can be accurately constructed. Further, the optical SSB design labeled as Design 2 might be more practically implementable in this form.

Pending improvements in transmitter design, transmission over 400 km should be possible, however, transmission beyond 400 km is questionable unless another form of equalizer is designed. The microstrip currently used to perform the equalization has a frequency dependent loss. More specifically, the 10 GHz frequencies are attenuated more than the 10 Hz frequencies. This seriously limits the microstrip's ability to equalize the transmitted signal. Thus, work could be done on developing a multiple tap equalizer in an integrated circuit form which would be designed to have a more flat magnitude response than the microstrip and an effective phase response.

Pending development of a new equalizer, transmission up to 1000 km is feasible, however, beyond this mark is unpredictable simply because the frequency response of the transmitter and receiver electronics may have significant effects that would destroy the SSB quality of the signal and as such, limit the equalizer's ability to reverse the effects of chromatic dispersion. Since this method reduces the spectral content of one sideband through phase cancellation of frequencies, anything that alters the phase of the original signal before sideband cancellation but after the signals have been directed to the Hilbert path will reduce the amount of cancellation thus reducing the ability to equalize. Thus, the next area of improvement would be to improve the quality of the frequency response of the transmitter and also the receiver components. At this time, most of the electrical components at the transmitter and receiver are already of high quality and it is unlikely that electrical components with perfectly flat amplitude responses will ever exist. However, improvements in RF electronics are steady and may prove to be beneficial.

Uses of optical SSB transmission are also being proposed in WDM systems where the spacing of the optical carriers could be as low as the bit rate B in a SSB transmission format as opposed to 2B in a DSB format. Thus, experiments of optical SSB signaling in a WDM system could be carried out and the performance of different signaling formats in a closely spaced WDM system could be studied. It is interesting to note that modulating the signal in the AM-PSK format previously described offers the same bandwidth reduction as SSB. However, the AM-PSK format has to be equalized optically beyond approximately 200 km.

6.3 Additional Comments

As a result of the work presented in this thesis, it is evident that optical SSB modulation does provide dispersion compensation. However, if the SSB systems use electrical equalization, they will probably not be used in 10 Gb/s systems longer than 1000 km in the near future. The inherent problems with the design and the effects that nonideal components have on this design will limit the optical SSB system's capability. In light of the new optical SSB system that has been developed, the best form of equalization that could be used for extending the transmission distance of digital systems expected to be longer than 400 km at a bit rate of 10 Gb/s appears at this time to be optical equalization in the form of dispersion compensating fiber. Further, the DSB systems with optical equalization are not subject to FM-AM noise problems like the SSB systems are. On the other hand, the optical SSB systems may be useful in a 10 Gb/s system with a fiber length somewhere between 100 km and 400 km. The ultimate decision will lie in a cost analysis of the proposed compensating schemes.

In the analysis, the cost of an optical equalizing element and the penalty caused by it's insertion loss will have to be weighed against the cost of implementing a complete optical SSB transmitter along with an equalizer at the receiver. The optical SSB system has no added optical insertion loss, however, the MZ modulator cannot be driven to full extinction in the optical SSB case in order to maintain the ability to equalize post detection. As shown in simulations, the reduced optical extinction has a strong negative impact in terms of SNR.

The feasibility may also be affected by whether or not the optical link is already installed. The optical SSB system offers the advantage of being able to transform an existing DSB system by modifying only the transmitter and receiver electronics. Optical equalization with elements such as dispersion compensating fiber or chirped Bragg gratings may have to be placed at the transmitter or the receiver if the system is already installed. It is hard to determine at this point whether DSB modulation with optical equalization or SSB modulation with electrical equalization is more feasible since the cost can vary greatly depending on the specifics of the system.

REFERENCES

[1] J. S. Cook, O. I. Szentesi, "North American field trials and early applications in telephony," *IEEE Journal on Selected Areas in Communications,* vol. SAC-1, pp. 393-397, Apr. 1983.

[2] E. F. O'Neill, ed., *A History of Science and Engineering in the Bell System,* AT&T Bell Laboratories, 1985.

[3] P. S. Henry, "Lightwave primer," *IEEE Journal of Quantum Electronics*, vol. QE-21, no. 12, pp. 1862-1879, Dec. 1985.

[4] K. Yonenaga, A. Matsuura, S. Kuwahara, M. Yoneyama, Y. Miyamoto, K. Hagimoto, K. Noguchi, "Dispersion-compensation-free 40 Gb/s x 4-channel WDM transmission experiment using zero-dispersion-flattened transmission line," OFC '98 Post-deadline Papers, PD-20, San Jose, CA. Feb. 1998.

[5] Y. Yano, T. Ono, K. Fukuchi, T. Ito, H. Yamazaki, M. Yamaguchi, K. Emura, *Proceedings of ECOC '96*, paper ThB.3.1, Oslo, Norway, 1996.

[6] A. F. Elrefaie, R. E. Wagner, D. A. Atlas, D. G. Daut, "Chromatic dispersion limitations in coherent lightwave transmission systems," *IEEE Journal of Lightwave Technology*, vol. 6, no. 5, pp. 704-709, May 1988.

[7] A. Vengsarkar, "Tutorial on dispersion compensation," OFC '98, Paper TuL, San Jose, CA. Feb. 1998.

[8] B. E. A. Saleh, M. C. Teich, *Fundamentals of Photonics*, John Wiley and Sons Inc., New York, 1991.

[9] J. Conradi, EE 683 Course Notes, University of Alberta, Edmonton, Alberta, 1997.

[10] C. Lin, H. Kogelnik, L. Cohen, "Optical-pulse equalization of low-dispersion transmission in single-mode fibers in the 1.3-1.7-μm spectral region," *Optics Letters*, vol. 5, p. 476, 1980.

[11] M. Onishi, Y. Koyano, M. Shigematsu, H. Kanamori, M. Nishimura, "Dispersion compensation fibre with a high figure of merit of 250 ps/nm/dB," *Electronics Letters*, vol. 30, no. 2, pp. 161-163, Jan. 1994.

[12] J. M. Duggan, A. J. Price, M. Ramadan, D. L. Wolfe, E. F. Murphy, A. J. Antos, D. K. Smith, D. W. Hall, "All-optical, fiber-based 1550 nm dispersion compensation 10 Gb/s, 150 km transmission experiment over 1310 nm optimized fiber," *Proceedings of OFC '92*, paper PD-12, San Jose, CA, 1992.

[13] A. Goel, R. K. Shevgaonkar, "Wide-band dispersion compensating optical fiber," *IEEE Photonics Technology Letters*, vol. 8, no. 12, pp. 1668-1670, Dec. 1996.

[14] K. I. White, B. P. Nelson, "Zero total dispersion in step-index monomode fibres at 1.3 and 1.55 μm," *Electronics Letters,* vol. 15, no. 13, pp. 396-397, June 1979.

[15] H. Tsuchiya, N. Imoto, "Dispersion-free single mode fibre in 1.5 μm wavelength region," *Electronics Letters,* vol. 15, no. 15, pp. 476-478, July 1979.

[16] L. Jeunhomme, "Dispersion minimization in single-mode fibres between 1.3 μm and 1.7 μm," *Electronics Letters,* vol. 15, no. 15, pp. 478-479, July 1979.

[17] R. M. Jopson, A. H. Gnauck, R. M. Derosier, "10 Gb/s 360-km transmission over normal-dispersion fiber using mid-system spectral inversion," *Proceedings of OFC '93,* paper PD-3, 1993.

[18] W. H. Loh, R. I. Laming, N. Robinson, A. Cavaciuti, F. Vaninetti, C. J. Anderson, M. N. Zervas, M. J. Cole, "Dispersion compensation over distances in excess of 500 km for 10 Gb/s systems using chirped fiber gratings," *IEEE Photonics Technology Letters*, vol. 8, no. 7, pp. 944-946, July 1996.

[19] Authors from British Telecom, *Proceedings of ECOC '96*, postdeadline paper ThB.3.2, Oslo, Norway, 1996.

[20] K. Okamoto, Y. Hibino, M. Ishii, "Guided-wave optical equalizer with α-power chirped grating," *IEEE Journal of Lightwave Technology*, vol. 11, no. 8, pp. 1325-1330, Aug. 1993.

[21] F. Ouellette, J. Cliche, S. Gagnon, "All-fiber devices for chromatic dispersion compensation based on chirped distributed resonant coupling," *IEEE Journal of Lightwave Technology*, vol. 12, no. 10, pp. 1728-1738, Oct. 1994.

[22] N. M. Litchinitser, D. B. Patterson, "Analysis of fiber bragg gratings for dispersion compensation in reflective and transmissive geometries," *IEEE Journal of Lightwave Technology*, vol. 15, no. 8, pp. 1323-1328, Aug. 1997.

[23] N. M. Litchinitser, B. J. Eggleton, D. B. Patterson, "Fiber bragg gratings for dispersion compensation in transmission: theoretical model and design criteria for nearly ideal pulse recompression," *IEEE Journal of Lightwave Technology*, vol. 15, no. 8, pp. 1303-1313, Aug. 1997.

[24] D. Garthe, R. E. Epworth, W. S. Lee, A. Hadjifotiou, C. P. Chew, T. Bricheno, A. Fielding, H. N. Rourke, S. R. Baker, K. C. Byron, R. S. Baulcomb, S. M. Ohja, S. Clements, "Adjustable dispersion equalizer for 10 and 20 Gb/s over distances up to 160 km," *Electronics Letters,* vol. 30, no. 25, pp. 2159-2160, Dec. 1994.

[25] R. I. Laming, N. Robinson, P. L. Scrivener, M. N. Zervas, S. Barcelos, L. Reekie, J. A. Tucknott, "A dispersion tunable grating in a 10-Gb/s 100-220-km-step index fiber link," *IEEE Photonics Technology Letters*, vol. 8, no. 3, pp. 428-430, Mar. 1996.

[26] F. Ouellette, P. A. Krug, T. Stephens, G. Dhosi, B. Eggleton, "Broadband and WDM dispersion compensation using chirped sampled fibre bragg gratings," *Electronics Letters,* vol. 31, no. 11, pp. 899-901, May 1995.

[27] A. H. Gnauck, C. R. Giles, L. J. Cimini, Jr., J. Stone, L. W. Stulz, S. K. Korotky, J. J. Veselka, "8-Gb/s-130 km transmission experiment using Er-doped preamplifier and optical dispersion equalization," *IEEE Photonics Technology Letters*, vol. 3, no. 12, pp. 1147-1149, Dec. 1991.

[28] T. Ozeki, "Optical equalizers," *Optics Letters*, vol. 17, no. 5, pp. 375-377, Mar. 1992.

[29] M. Sharma, H. Ibe, T. Ozeki, "Optical circuits for equalizing group delay dispersion of optical fibers," *IEEE Journal of Lightwave Technology*, vol. 12, no. 10, pp. 1759-1765, Oct. 1994.

[30] K. Takiguchi, K. Okamoto, S. Suzuki, Y. Ohmori, "Planar lightwave circuit optical dispersion equalizer," *IEEE Photonics Technology Letters*, vol. 6, no. 1, pp. 86-88, Jan. 1994.

[31] S. Walklin, *Frequency chirping in a mach-zehnder modulator*, TR Labs Internal Report, Edmonton, AB., July, 1995.

[32] A. H. Gnauck, S. K. Korotky, J. J. Veselka, J. Nagel, C. T. Kemmerer, W. J. Minford, D. T. Moser, "Dispersion penalty reduction using an optical modulator with adjustable chirp," *IEEE Photonics Technology Letters*, vol. 3, no. 10, pp. 916-918, Oct. 1991.

[33] J. C. Cartledge, R. G. McKay, "Performance of 10 Gb/s lightwave systems using an adjustable chirp optical modulator and linear equalization," *IEEE Photonics Technology Letters*, vol. 4, no. 12, pp. 1394-1397, Dec. 1992.

[34] A. Djupsjöbacka, O. Sahlén, "Dispersion compensation by differential time delay," *IEEE Journal of Lightwave Technology*, vol. 12, no. 10, pp. 1849-1853, Oct. 1994.

[35] K. Iwashita, N. Takachio, "Chromatic dispersion compensation in coherent optical communications," *Journal of Lightwave Technology*, vol. 8, no. 3, pp. 367-375, Mar. 1990.

[36] N. Takachio, S. Norimatsu, K. Iwashita, "Optical PSK synchronous heterodyne detection transmission experiment using fiber chromatic dispersion equalization," *IEEE Photonics Technology Letters,* vol. 4, no. 3, pp. 278-230, Mar. 1992.

[37] N. Takachio, K. Iwashita, "Compensation of fibre chromatic dispersion in optical heterodyne detection," *Electronics Letters,* vol. 24, no. 2, pp. 108-109, Jan. 1988.

[38] J. H. Winters, "Equalization in coherent lightwave systems using microwave waveguides," *Journal of Lightwave Technology*, vol. 7, no. 5, pp. 813-815, May 1989.

[39] J. H. Winters, "Equalization in coherent lightwave systems using a fractionally spaced equalizer," *Journal of Lightwave Technology,* vol. 8, no. 10, pp. 1487-1491, Oct. 1990.

[40] G. May, A. Solheim, J. Conradi, "Extended 10 Gb/s fiber transmission distance at 1538 nm using a duobinary receiver," *IEEE Photonics Technology Letters*, vol. 6, no. 5, pp. 648-650, May 1994.

[41] K. Yonenaga, S. Kuwano, S. Norimatsu, N. Shibata, "Optical duobinary transmission system with no receiver sensitivity degradation," *Electronics Letters,* vol. 31, no. 4, pp. 302-304, Feb. 1995.

[42] W. H. Loh, R. I. Laming, A. D. Ellis, D. Atkinson, "10 Gb/s transmission over 700 km of standard single-mode fiber with 10-cm chirped fiber grating compensator and duobinary transmitter," *IEEE Photonics Technology Letters*, vol. 8, no. 9, pp. 1258-1260, Sept. 1996.

[43] K. Ennser, R. I. Laming, M. N. Zervas, "Phase-encoded duobinary transmission over non-dispersion shifted fibre links using chirped grating dispersion compensators," *Electronics Letters,* vol. 33, no. 1, pp. 72-74, Jan. 1997.

[44] S. Walklin, "Multilevel signaling for increasing the capacity of high-speed optical communication systems," Ph. D. Thesis, University of Alberta, Edmonton, Alberta, Fall 1997.

[45] K. H. Powers, "The compatibility problem in single-sideband transmission," *Proceedings of the IRE*, vol. 48, pp. 1431-1435, Aug. 1960.

[46] O. G. Villard, "Composite amplitude and phase modulation," *Electronics*, vol. 21, pp. 86-89, Nov. 1948.

[47] G. B. Lockhart, "A spectral theory for hybrid modulation," *IEEE Transactions on Communications*, pp. 790-800, July 1973.

[48] B. F. Logan, M. R. Schroeder, "A solution to the problem of compatible single-sideband transmission," *IRE Transactions on Information Theory*, vol. IT-8, pp. S 252-S 259 , Sept. 1962.

[49] M. A. M. A. Zaid, "Envelope detection and correction of SSB," *Electronics Letters,* vol. 20, no. 22, pp. 901-902, Oct. 1984.

[50] B. P. Lathi, *Modern Digital and Analog Communication Systems*, Holt, Rinehart and Winston, Philadelphia, PA, 1989.

[51] M. Izutsu, S. Shikama, T. Sueta, "Integrated optical SSB modulator / frequency shifter," *IEEE Journal of Quantum Electronics*, vol. QE-17, no. 11, pp. 2225-2227, Nov. 1981.

[52] R. Olshansky, "Single sideband optical modulator for lightwave systems," U. S. Patent No. 5,301,058, 1994.

[53] J. Park, A. F. Elrefaie, K. Y. Lau, "Fiber chromatic dispersion effects on multichannel digital millimeter-wave transmission," *IEEE Photonics Technology Letters*, vol. 8, no. 12, pp. 1716-1718, Dec. 1996.

[54] G. H. Smith, D. Novak, Z. Ahmed, "Technique for optical SSB generation to overcome dispersion penalties in fibre-radio systems," *Electronics Letters*, vol. 33, no. 1, pp. 74-75, Jan. 1997.

[55] J. Conradi, B. Davies, M. Sieben, D. Dodds, S. Walklin, "Optical single sideband (OSSB) transmission for dispersion avoidance and electrical dispersion

compensation in microwave subcarrier and baseband digital systems," OFC '97 Post-deadline Papers, PD-29, Dallas, Tx. Feb. 1997.

[56] M. J. Wale, R. G. Walker, C. Edge, "Single-sideband modulator in GaAs integrated optics for microwave frequency operation," *Integrated Photonics Research, OSA Technical Digest Series*, no. 10, post-deadline paper PD-8, 1992.

[57] K. Yonenaga, N. Takachio, "A fiber chromatic dispersion compensation technique with an optical SSB transmission in optical homodyne detection systems," *IEEE Photonics Technology Letters*, vol. 5, no. 8, pp. 949-951, Aug. 1993.

[58] K. Yonenaga, N. Takachio, "Dispersion compensation for homodyne detection systems using a 10 Gb/s optical PSK-VSB signal," *IEEE Photonics Technology Letters*, vol. 7, no. 8, pp. 929-931, Aug. 1995.

[59] D. K. Weaver, Jr., "A third method of generation and detection of single sideband signals," *Proceedings of the IRE,* vol. 44, pp. 1703-1705, Dec. 1956.

[60] E. A. Lee, D. G. Messerschmidt, *Digital Communications,* Kluwer Academic Pub., pp. 239-240, 1988.

[61] A. J. Price, N. Le Mercier, "Modulation with improved chromatic dispersion tolerance," *Electronics Letters*, vol. 31, no. 1, pp. 58-59, Jan. 1995.

[62] A. J. Price, L. Pierre, R. Uhel, V. Harvard, "210 km repeaterless 10 Gb/s transmission experiment through nondispersion-shifted fiber using partial response scheme," *IEEE Photonics Technology Letters*, vol. 7, no. 10, pp. 1219-1221, Oct. 1995.

[63] S. Walklin, *Modeling the extinction ratio of a lithium niobate mach zehnder modulator in the electric-field domain*, TR Labs Internal Report, Edmonton, AB., July, 1995.

[64] S. Walklin, *Chromatic dispersion and the fiber transfer function for single mode fiber*, TR Labs Internal Report, Edmonton, AB., Oct., 1995.

[65] J. C. Cartledge, A. F. Elrefaie, "Effect of chirping-induced waveform distortion on the performance of direct detection receivers using traveling-wave semiconductor optical preamplifiers," *IEEE Journal of Lightwave Technology*, vol. 9, no. 2, pp. 209-219, Feb. 1991.

[66] C. R. Giles, E. Desurvire, "Propagation of signal and noise in concatenated erbium-doped fiber optical amplifiers," *Journal of Lightwave Technology,* vol. 9, no. 2, pp. 147-154, Feb. 1991.

[67] D. M. Pozar, *Microwave Engineering*, Addison-Wesley, Reading, MA, 1990.

[68] E. Hammerstad, O. Jensen, "Accurate models for microstrip computer-aided design," *IEEE Microwave Techniques and Theory International Microwave Symposium Digest,* pp. 407-409, 1980.

[69] N. A. Olsson, "Lightwave systems with optical amplifiers," *IEEE Journal of Lightwave Technology*, vol. 7, no. 7, pp. 1071-1081, July 1989.

[70] S. Yamamoto, N. Edagawa, H. Taga, Y. Yoshida, H. Wakabayashi, "Analysis of laser phase noise to intensity noise conversion by chromatic dispersion in intensity modulation and direct detection optical-fiber transmission," *Journal of Lightwave Technology,* vol. 8, no. 11, pp. 1716-1722, Nov. 1990.

[71] N. S. Bergano, C. R. Davidson, M. Ma, A. Pilipetskii, S. G. Evangelides, H. D. Kidorf, J. M. Darcie, E. Golovchenko, K. Rottwitt, P. C. Corbett, R. Menges, M. A. Mills, B. Pederson, D. Peckham, A. A. Abramov, A. M. Vengsarkar, "320 Gb/s WDM transmission (64x5 Gb/s) over 7,200 km using large mode fiber spans and chirped return-to-zero signals," OFC '98 Post-deadline Papers, PD-12, San Jose, CA. Feb. 1998.

[72] M. Sieben, J. Conradi, D. Dodds, B. Davies, S. Walklin, "10 Gb/s optical single sideband system," *Electronics Letters*, vol. 33, no. 11, pp. 971-973, May 1997.

[73] G. P. Agrawal, *Nonliner Fiber Optics*, Academic Press, Boston, MA, 1991.

APPENDIX A

Parameters and Losses of Optical Components used in the Experiments at TR Labs

Table A.1 Fiber Loss at 1533 nm

Reel	Company	Model	Length (km)	Loss (dB)
1	Corning	Stan. Single Mode	25	4.7
2	Corning	Stan. Single Mode	25	6.2
3	Corning	Stan. Single Mode	25	8.1
4	Corning	Stan. Single Mode	10	1.9
5	Corning	Stan. Single Mode	10	1.7
6	Nortel	Stan. Single Mode	50	11.6
7	Nortel	Stan. Single Mode	50	11.9
8	Corning	Stan. Single Mode	50	13.0
9	Corning	Stan. Single Mode	50	12.5
10	Corning	Stan. Single Mode	25	7.5
11	Corning	Stan. Single Mode	10	2.8
12	Corning	Stan. Single Mode	6	4.0

Table A.2 Isolator Loss at 1533 nm

Isolator	Company	Model	Serial No.	Loss (dB)
1	JDS	IS2500	26016	1.6
2	-	-	3664	2.3
3	JDS	IS2500	26014	0.6
4	JDS	IS2500	26015	0.6
5	MP	IU15PLAA11	716475	0.3
6	MP	IU15PLAA11	716463	0.7
7	MP	IU15PLAA11	716410	0.7
8	Qualop	ISP15	300596	0.7

Table A.3 Band Pass Filter Loss at 1533 nm

BPF	Company	Model	Serial No.	Loss (dB)
1	JDS	TB-1500B	901181	3.5
2	JDS	TB-1500B	901182	1.7
3	JDS	TB-1570	901041	2.0
4	JDS	TB-1500B	901675	1.7
5	JDS	TB-1500B	CA000042	1.7
6	JDS	TB-1500B	CA000043	2.7
7	JDS	TB-1500B	CA000041	1.6
8	JDS	TB-1500B	CA000044	2.2

Table A.4 Wavelength Division Multiplexer Loss at 1533 nm

WDM	Company	Model	Serial No.	Loss (dB)
1	JDS	WD915F	Y179	0.8

Table A.5 Erbium Doped Fiber Amplifier Parameters at 1533 nm

EDFA	Company	G_o	N_{SP}	P_{SAT}
1	TRLabs	29.9	1.7	5.6
2	TRLabs	29.8	1.6	6.7
4	TRLabs	23.2	2.0	2.0
5	TRLabs	30.5	2.1	6.0
6	TRLabs	31.6	2.3	3.6
7	TRLabs	30.6	2.7	4.3
8	TRLabs	27.2	2.0	1.0
9	TRLabs	31.8	2.1	4.5

APPENDIX B

Pictures of Components and the Full System used in the Experiments at TR Labs

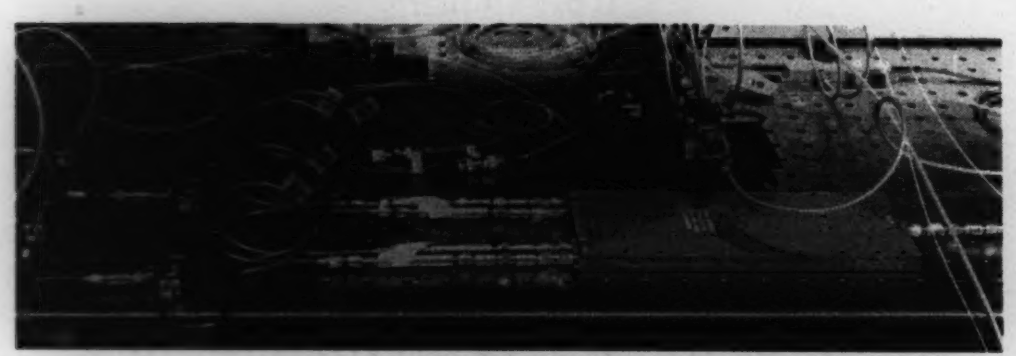

Figure B.1 Hilbert transform circuit (showing splitters, delay lines, attenuators, broadband combiner, amplifier and phase modulator)

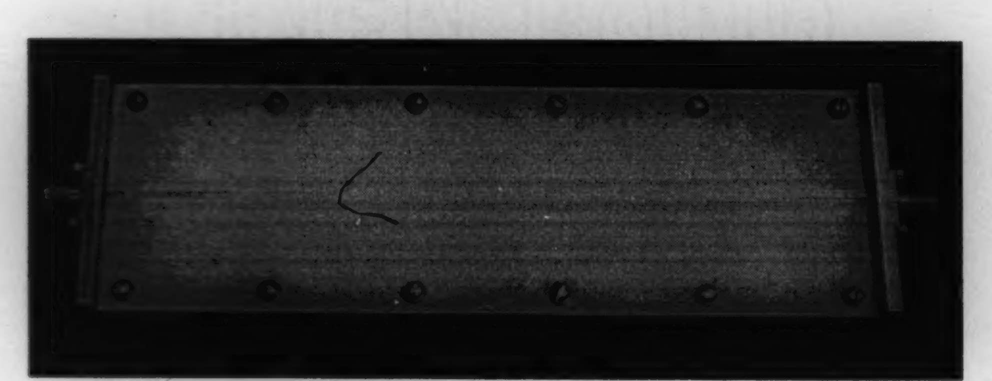

Figure B.2 16 cm microstrip equalizer

Figure B.3 Erbium doped fiber amplifiers and fiber reels

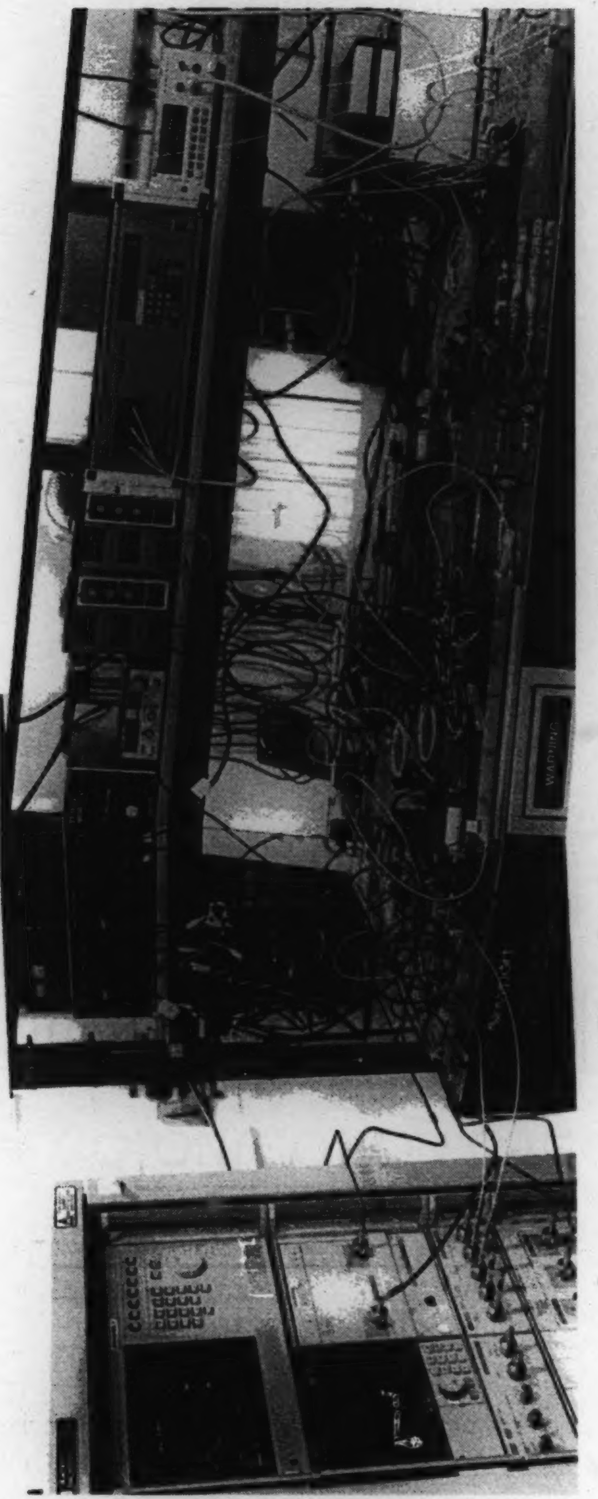

Figure B.4 System layout showing Bit Error Ratio Test set

APPENDIX C

The Erbium Fiber Laser

As part of a future test strategy, a fiber laser was purchased and assembled. Fiber lasers can have extremely narrow linewidths due to their long cavity length. As was identified in the thesis, a narrow linewidth source is required in an optical SSB system to minimize the level of FM-AM noise created by the interaction of the source linewidth with the chromatic dispersion in the fiber. Thus, a fiber laser would be useful in future experiments of optical SSB systems.

A system diagram of the fiber laser that was assembled is shown in Figure C.1. The system is comprised first of a 980 nm laser which provides the pump power for the fiber laser. The following fiber laser converts part of the 980 nm light into the desired 1550 nm light. The pump laser has an output power of approximately 100 mW so there is a significant amount of 980 nm power still remaining in the output following the fiber laser. This pump power is utilized by a subsequent section of Erbium fiber. Thus, following the fiber laser is a WDM which splits the 1550 nm light and the 980 nm residual pump. The 980 nm light bypasses an isolator and is then recombined with the 1550 nm light before they are launched into a section of Erbium fiber. The isolator helps reduce back reflections into the fiber laser. The final section of Erbium fiber utilizes the residual 980 nm pump to amplify the desired 1550 nm light from the fiber laser.

The performance of this fiber laser is satisfactory for use in an optical SSB system. The linewidth is specified at 20 kHz, the RIN at the output of the Erbium fiber was measured to be -140 dB/Hz, the wavelength at 25 degrees Celsius was measured to be 1550.87 nm and the final optical power at the output of the Erbium fiber can be set as high as +10.1 dBm with full pump current.

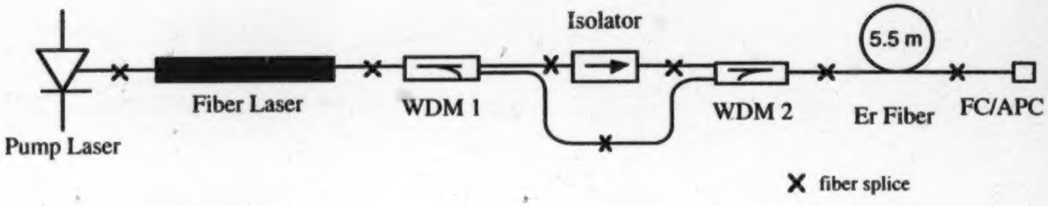

Components

Pump Laser - 980 nm SDL Pump Laser	Model: SDLO-2400-100	Serial: 77613
Fiber Laser - Ionas DFB Fiber Laser	Model: IF01W1E-T	Serial: DFB0030
WDM1 - Sifam WDM	Model: L2SWM98/15AA	Serial: HC048
Isolator - MP Isolator	Model: IU15PLAA00	Serial: 716287
WDM2 - Sifam WDM	Model: L2SWM98/15AA	Serial: HC045
Er Fiber - NOI Erbium doped fiber	Model: Er68	
FC/APC - Optical connector		

Figure C.1 Erbium Fiber Laser

This laser was completed in time for use at the Nortel site, however, it was not used in any of the experiments at Nortel since Nortel had a tunable narrow linewidth source. The Nortel source had a satisfactory linewidth of 80 kHz and a RIN lower than -155 dB/Hz. Further, the flexibility provided in tuning the Nortel source wavelength was more appealing due to variations in the optimal operating wavelength of the optical band pass filters and optical amplifiers at the Nortel site.

It is expected that this laser will be useful in optical SSB experiments and other experiments requiring a narrow linewidth source that might be carried out at TR Labs in the future.